APPLIED COMPUTATIONAL ELECTROMAGNETICS SOCIETY JOURNAL

Special Issue on Bio-Electromagnetic Methods and Applications

Guest Editors
Lei Zhao
Yongxin Guo
Joe Wiart
Wenhua Yu

June 2016
Vol. 31 No. 6
ISSN 1054-4887

The illustrations on the front cover have been obtained from the research groups at the Department of Electrical Engineering, The University of Mississippi.

THE APPLIED COMPUTATIONAL ELECTROMAGNETICS SOCIETY

JOURNAL

TABLE OF CONTENTS

A Single-Channel Non-Orthogonal I/Q RF Sensor for Non-Contact Monitoring of Vital Signs

Hongrui Bo [1], Lisheng Xu [1], Liling Hao [1], Yuanzhu Dou [2], Lei Zhao [3], and Wenhua Yu [3]

[1] Department of Electrical Engineering, Sino-Dutch Biomedical and Information Engineering School
Northeastern University, Shenyang, Liaoning Province, 110819, China
xuls@bmie.neu.edu.cn

[2] XIKANG ALPS Technology Co. Ltd.
Shenyang, Liaoning Province, 110179, China

[3] Center for Computational Science and Engineering
School of Mathematics and Statistics, Jiangsu Normal University, Xuzhou, China

Abstract ─ In order to remotely monitor the activities of heartbeat, respiration and body movement, this article designed and implemented a single-channel non-orthogonal in-phase/quadrature (I/Q) RF sensor, which works at the central frequency of 2.4 *GHz*. The designed RF sensor is based on a printed circuit board (PCB) antenna. Taking into account low cost, simple structure and easy fabrication, the antenna is designed and implemented with a special broad-band microstrip-to-coplanar strip line Balun structure by combining the transmitter with the receiver on a PCB to form one single antenna system. The gain of the sensor is 7.7 *dB*. The return loss is -22.7 *dB* at 2.4 *GHz* and the directionality of the antenna is satisfactory for monitoring vital signs. It has been validated that the designed sensor can detect the respiration, heartbeat and body movement accurately in comparison with the signals acquired by respiration sensor and pulse sensor.

Index Terms ─ Non-contact RF sensor, non-orthogonal I/Q signals, vital signs monitoring, Yagi antenna.

I. INTRODUCTION

The cost in healthcare is an important portion of each government's budget, and it is increasing rapidly every year. In America, it is estimated that one hundred million Americans suffer from chronic diseases including heart diseases, lung disorders, and diabetes. The expense for these conditions accounts for three-fourths of total US healthcare expense [1]. If there is a way that the diseases can be prevented at early stage, the costs of healthcare will be significantly reduced. With the advent of big data era, daily vital signs become essential for prevention and diagnosis of diseases. By analyzing daily physiological parameters, doctors are able to diagnose the illness accurately. Monitoring sleep

information of infants can reduce the mortality of sudden infant death syndrome (SIDS) [2]. Consequently, there is a growing market for application, which allows monitoring vital signs for convenience and at low cost [3].

Although most of the wearable devices can detect our daily physiological parameters, it is not convenience for our daily life and has low accuracy. Furthermore, most people may be shameful to wear equipment every day [4].

Therefore, there is a great demand for monitoring physiological parameters conveniently with low costs in our daily lives [5-6]. Since the 1970s, microwave Doppler radar has drawn attention for new applications in human healthcare because it offers a non-contact alternative for healthcare monitoring, such as physiologic movement, volume change sensing [7], life detection for finding human subjects trapped in earthquake rubble [8], and cardiopulmonary monitoring for sleep apnea syndrome detection [9-10], remote non-contact detection of vital signs, and so on.

The respiration and heartbeat, based on microwave Doppler phase modulation technique, has been studied for many years [11]. Nevertheless, Doppler radar used for detecting vital signs has not been commoditized and is still under being investigated. The most important limitation in Doppler radar measurement of periodic motion is the presence of the null demodulation points [12]. When vital signs become weak with a lot of background noise caused by walking and talking of the people nearby, it will be hard for the radar sensor to detect the relative weak vital signs from strong background noise, unless shorter carrier wavelength is used to improve the sensitivity [13]. In consequence, single-channel receiver cannot be used and a multiple antenna system is required, which means this kind of

Doppler radar system is complex [14-15].

In summary, there is a huge market for a new kind of sensor with simple structure and accurate detection. Compared with Doppler radar, this article analyzes and designs an RF sensor working at the frequency of 2.4 *GHz* for monitoring physiological parameters, which can form a single-antenna system. In principle, our antenna detects body movements by the shift of phases; however Doppler radar detects the body movements by the change of frequency [16]. Therefore, our antenna can form a single-antenna system and provide a more accurate detection method with low noise [17]. Due to the ease production of PCB antenna, our design also ensures the possibility of mass production with low cost.

II. PRINCIPLE OF DETECTING MOTION BY MICROWAVE

According to the principle of microwave, the phase of signal and the location of the time-varying moving target will be modulated in a linear scale and reflected again by a time-varying moving target whose rate close to zero. In comparison with the speed of electromagnetic wave, the speed of human body's breathing almost close to zero in quiet state. Therefore, a microwave radar targets in thoracic will receive the phase modulation signal with time varying movement of thoracic position similar to launch signal. This signal contains information of respiration, heartbeat and body movements. Therefore, the signal of single frequency microwave radars can be expressed as follows:

$$S(t) = A_0 \, cos[2\pi ft + \phi(t)], \qquad (1)$$

where, A_0 is the amplitude of the transmitted signal; $\phi(t)$ is the phase of the transmitted signal; f is the frequency of the signal.

The total distance that radar signal comes from the transmitting antenna to the receiving antenna is $2d(t) = 2d_0 + 2x(t)$, where d_0 is the distance between the transmitting antenna and the subject, $x(t)$ is the distance caused by thoracic motion. In order to simplify the computation, the amplitude A_0 is equal to 1. Therefore, the echo signal is launched by the body as follows:

$$S_F(t){=}cos[2\pi f(t - \frac{2d(t-\frac{d(t)}{c_0})}{c_0}) + \phi(t - \frac{2d(t-\frac{d(t)}{c_0})}{c_0})], \quad (2)$$

where, c_0 is the speed of light, the cycle of chest movement caused by respiration is $T \gg \frac{d_0}{c_0}$, so in $x(t - \frac{d(t)}{c_0})$, $\frac{d(t)}{c_0}$ can be neglected. Thus, the received echo signal can be expressed as follows:

$$S_F(t) \approx cos[2\pi f(t - \frac{4\pi d_0}{\lambda} - \frac{4\pi x(t)}{\lambda}) + \Phi(t - \frac{2d_0}{c_0})]. \quad (3)$$

Having compared this function with Equation (1), the received radar echo signal is similar with the transmitting signal. The reason is that the phase of the echo signal is modulated by the movement of the thorax, as well as the delay caused by the distance between

subject and radar.

Mixing the echo signal with the local oscillator signal results in a conversion directly to baseband signal $BD(t)$:

$$BD(t) = cos(\theta + \frac{4\pi x(t)}{\lambda} + \Delta\phi(t)), \qquad (4)$$

where, $\Delta\phi(t) = \phi(t) - \phi\left(t - \frac{2d_0}{c_0}\right)$ is the rest of the phase noise, $\theta = \frac{4\pi d_0}{\lambda} + \theta_0$ is the inherent phase shift, which is determined by d_0. θ_0 is caused by the phase shift of the reflection plane, mixer and the distance between the antennas and so on.

If θ is an odd number of times of $\frac{\pi}{2}$, and $x(t) \ll \lambda$, where λ is the wavelength of light. According to the principle of small angle approximation, baseband signal can be approximated into the following equation,

$$BD(t) = \frac{4\pi x(t)}{\lambda} + \Delta\phi(t). \qquad (5)$$

In this case, the optimum demodulation point will occur. When we ignore the influence of the remainder term $\Delta\phi(t)$, the baseband signal and the periodic thoracic movement displacement $x(t)$ will form a linear ratio.

When θ is an even multiple of $\frac{\pi}{2}$, baseband signal can be approximated as Equation (6):

$$BD(t) = 1 - \left[\frac{4\pi x(t)}{\lambda} + \Delta\phi(t)\right]^2. \qquad (6)$$

In this case, the baseband signal and time-varying displacement cannot form a linear ratio. A null demodulation point will occur when the vibration signal and echo signal are in 0-degree phase or 180-degree phase shift. It could be solved by obtaining two signals that have a 90-degree phase difference to eliminate the disturbed redundancy. Therefore, the echo signal contains the information of respiration, heartbeat and body movement. This article designs a special circuit that could produce the non-orthogonal I/Q signals to solve this problem. And it will be introduced in next part.

III. DESIGN AND IMPLEMENTATION

This article designed and implemented an RF sensor. The block diagram is presented in Fig. 1. Parts of circuits of the sensor will be introduced in this part.
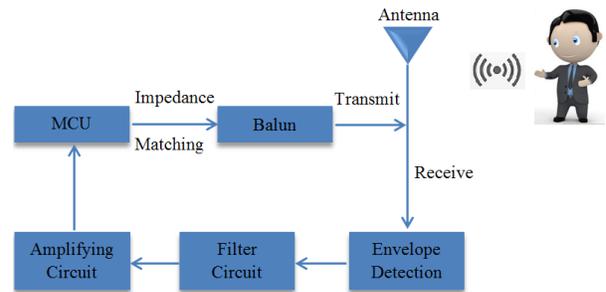
Fig. 1. Block diagram of our designed sensor.

A. Yagi antenna design

The Yagi patch antenna has a high directivity, low profile and it has attracted more interest in recent years. Considering the simple structure and high directivity, Yagi patch antenna is selected for detecting physiological parameters such as the heartbeat, respiration in daily life.

According to the principle of Yagi antenna design, a higher gain is associated with a larger size. It is balanced between the gain and the size of this sensor. The transmission distance is also taken into account. The designed Yagi antenna, which consisted of two dipole elements, a reflector and three director patch elements, is shown in Fig. 2. The length of two dipole elements is equal to the half of the wavelength. For the sake of size and universal feasibility, the antenna was designed for working at 2.4 *GHz*, which belongs to industrial scientific medical (ISM) band [18].
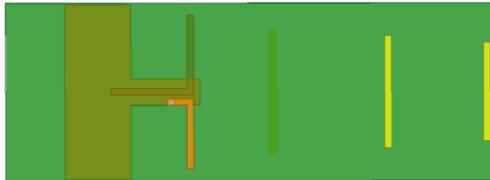
Fig. 2. The configuration designed Yagi antenna.

According to the working frequency f_0 and the speed of light C_0, we could get the wavelength in vacuum:

$$\lambda = \frac{C_0}{f_0}. \tag{7}$$

The original antenna patches are based on the FR4 (a kind of level code of fire resistant) substrate with the thickness of 1.2 *mm*. The permittivity (ε_r) of FR4 substrate is 4.4. When the electromagnetic wave transmits in the medium whose permittivity is ε_r, the speed of light will change to:

$$c = \frac{C_0}{\sqrt{\varepsilon_r}}. \tag{8}$$

Therefore, the length of the two dipole elements should be shorter than the half of the wavelength. Using electromagnetism simulation software-HFSS (Version 14.0), this article designed a Yagi patch antenna based on the FR4 substrate with the thickness of 1.2 *mm*, and size of 154.5*54 *mm²*.

Compared with five or more director elements in other literature, this paper achieved the high gain of 7.7 *dB* with using three director elements, which reduced the size of Yagi antenna. A special broad-band microstrip-to-coplanar strip line (CPS) Balun structure was also designed to make the antenna's impedance equal 50 *ohm* instead of using the CPS Balun and impendence converter in the common Yagi design [19-22] as shown in Fig. 3. According to the microwave radiation principle, the currents in the two dipole elements have opposite direction and the same amplitude [23]. We designed one

via hole connecting one of dipole elements with the reflector to simply the structure of antenna and reduce the size of the antenna as shown in Fig. 3 (b). The Port1 connects directly with the output of the radio frequency (RF) as the input of RF signals. Adjusting the distance of the Port2 connecting with the microstrip and the Port3 connecting with the reflector by the vial hole can change the amount of coupling between the coplanar strip lines. This paper adjusted the distance to make the currents in two dipole elements have the same amplitude.

(a)

(b)
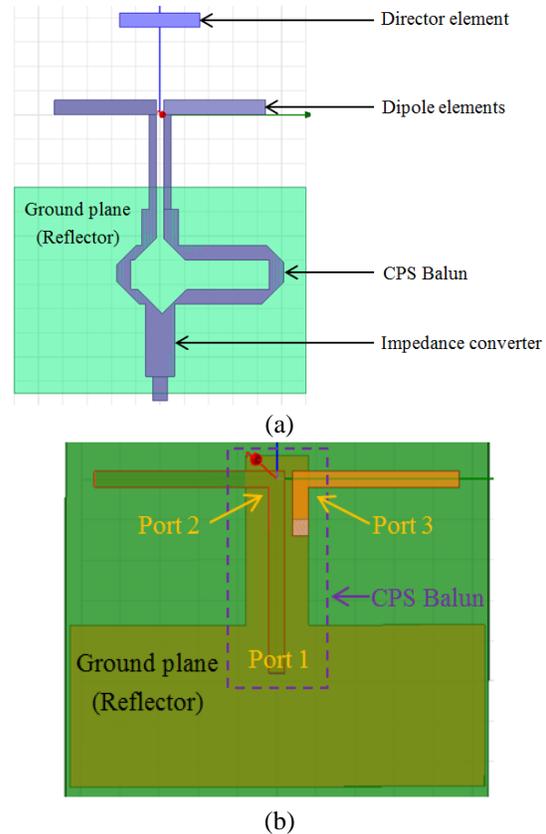
Fig. 3. Structure of Yagi antenna. (a) Structure of common Yagi antenna [19]; (b) structure of our designed Yagi antenna.

In this article, the Yagi antenna and the circuits are printed on a PCB. In order to have enough space to place the circuits, this paper increased the width of the reflector from 2 *mm* to 20 *mm*, resulting in influencing the performance of the RF sensor. For a satisfied directivity and higher gain, this paper increased the length of the reflector and reduced the distance between reflector and dipole element at the same time.

B. Circuit design

At present, an RF micro control unit (MCU) of Nordic company is employed in our sensor. The features of this MCU are low consumption and embedded

transmission protocol. The sensor was designed for working long time in our daily life, which means low power consumption. Those features are suitable for monitoring daily vital signs.

Design of high frequency circuit is different from low frequency circuit design. There might be a variety of unexpected issues emerged because of inappropriate high frequency circuit design. This sensor is an integration of antenna and circuit, which means that the circuits will be disturbed by the high frequency part. Therefore, it is of vital importance to reduce the disturbance caused by high frequency.

Considering the polarization of the Yagi antenna, the direction of current flowing on the PCB is perpendicular to the direction of microwave propagation. One of the most effective ways is Balun (balanced-to-unbalanced). Usually, the transmitter is regarded as unbalanced and the antenna is regarded as balanced. Balun is a converter to get the resistance matched. Furthermore, the standing wave will be reduced obviously by the Balun. It is represented on the MCU datasheet about how to design a Balun for this MCU. However, this paper has designed a new Balun to match our antenna. As Fig. 4 depicted, the layout of components were arranged elaborately to lower power dissipation.
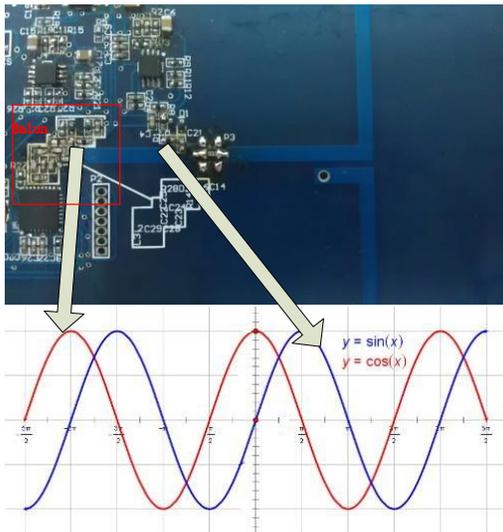
Fig. 4. Special circuits design.

As shown in Fig. 4, this paper designed a wire whose length is equal to one-eighth of the wavelength. And it was mounted between the MCU and the Yagi antenna. When the MCU transmits and receives a signal through this wire, two signals with 90-degree phase difference will be acquired at its two ends. According to the contents described in the "principle of detecting body motion by microwave" section, a new signal without the null demodulation point will be generated after reconstruction.

This paper produced RF signals by downloading program into the chip rather than producing it by some high frequency analog circuits, such as a voltage controlled oscillator (VCO) circuit, a mixers circuit in other literatures. The high frequency circuits are a Balun circuit and an envelope detection circuit, which reduce the loss of the high frequency and the influence of the circuits.

As shown in Fig. 5, the RF chip was set to transmit a pulse-square wave whose period is 10 *ms* at the carrier frequency of 2.4 *GHz*. According to the previously described, the echo signal contains some information about body movement. The envelope detection circuit can remove high frequency components and demodulate the human dynamic information of low frequency component. Then the signals were filtered and amplified. Using an analog to digital converter (ADC) converts analog signal into 8 hex decimal number coding and encodes it into a pulse by Gauss frequency shift keying (GFSK). Finally, the signal is sent at the carrier frequency of 2.4 *GHz*.
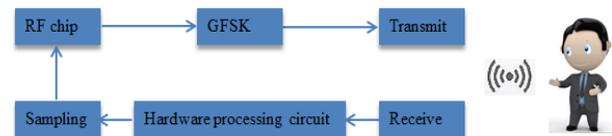
Fig. 5. Block diagram of software design.

In high frequency circuits, the phase of signal changes with the length of the wire. This article has taken advantage of this special characteristic to get two echo signals in one sensor.

C. RF sensor implementation

Well-implemented PCB antennas have similar performance with that of a ceramic antenna. However, the performance of the antenna will be changed after adding circuits to the board. In order to make it work at 2.4 *GHz* properly and have a high gain at the same time, this paper adjusted the length of dipole element and rebuilt ground for the circuits. Adding circuits to the original antenna makes the simulation more complex. The wires in these circuits are subtle and the components are different in irregularity shapes and sizes, which add a lot of burden to the simulation, especially increase the amount of calculation. However the compute capability of the computer is limited. In order to improve the simulation performance and the computational complexity meanwhile, this paper simulated the long wires, all the large size via holes and components close to the antenna. On the contrary, we ignored the influences of the rest of components and wires to simplify the model. While simulation results are slightly

affected due to simplification, so we increase the area of reflector and adjust the distance between the reflector and the dipole element. However, via holes are remained since via holes on the reflector may produce the parasitic capacitance and inductance and change the characteristic impedance, which influences the result of the RF sensor.

If the distance (D1) between dipole element and the first wave-guider is shorter than the distance (D2, D3)

between the other wave-guiders, the antenna will have a higher gain. Figure 6 and Table 1 show the main parameters of the designed RF sensor.

Table 1: Main parameters of the Yagi antenna

Parameter	L1	L2	L3	L4	D1	D2	D3
Size (mm)	42.6	39.7	36.0	29.5	24.0	32.0	28.45
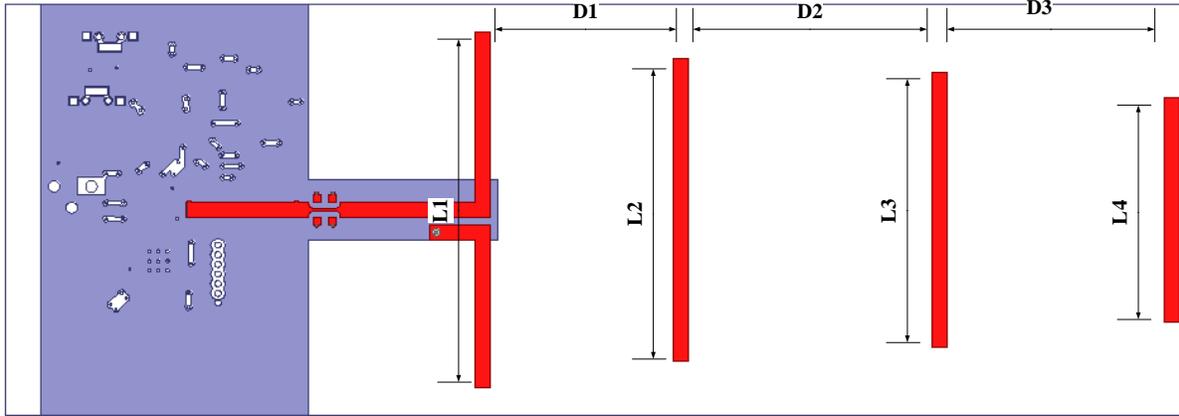
Fig. 6. Main parameters of the designed antenna and circuits.

IV. RESULTS AND DISSCUSSIONS

A. Parameter S11

When the impedance mismatches the antenna from the fed line of transmitter or receiver, the system performance will be declined due to the reflection. The sensor is an integration of the antenna and circuits, so it is important to examine the return loss of this design. Parameter S11 is a distinct factor to examine the performance of an RF component.

The HFSS solver was employed to simulate and process the data. Figure 7 (a) shows the simulated S11 parameters at different frequencies with a single Yagi antenna. The value of S11 is -15.30 *dB* in 2.4 *GHz* and resonance point is placed exactly at 2.4 *GHz* as demonstrated. This value is a considerable result which means most of the electromagneticwave is transmitted by designed antenna and only few are returned. The results demonstrate that the Yagi patch antenna has a nice match in 50 *Ω*.

Figure 7 (b) shows the experimental S11 results of designed sensor measured by a network analyzer. These are the final results after some experiments. By analyzing the simulated results, some improvements

were achieved. For instance, the resonance point was deviated from 2.4 *GHz* thus this article enlarged the area of the ground to make the sensor working at the frequency of 2.4 *GHz* properly. Table 2 shows the return loss (RL) of the original antenna and the integrate system at different frequencies.

Table 2: Return loss of simulation and experiment.

Frequency (*GHz*)	2.400	2.450	2.485
RL of integration (*dB*)	-15.30	-10.32	-7.21
RL of real sensor (*dB*)	-22.77	-14.72	-10.27

From Table 2, the return loss of the sensor evidently shows our improvements' effect. At the frequency of 2.4 *GHz*, the return loss of the sensor reaches -22.77 *dB*. The experimental results are better than simulated results after our adjustment, although the resonance frequency of experiments is not exactly at 2.4 *GHz*.

(a)

(b)
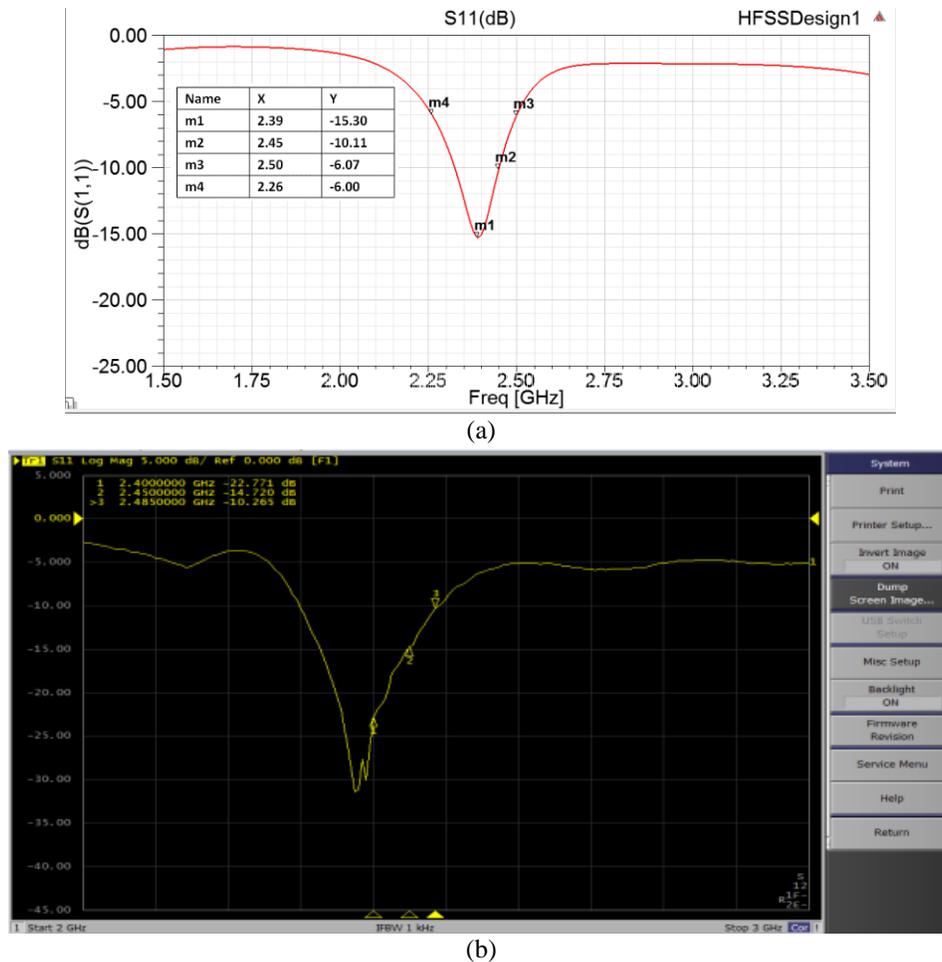
Fig. 7. S11 of simulation and experimental results. (a) Simulated results; (b) the experimental result.

B. Radiation pattern

Radiation pattern is another indicator which can depict the performance of an antenna. The results about radiation pattern of sensor were obtained by using software-HFSS to get the simulated results. And the experimental results were obtained at a professional chamber for microwave measurement. Figure 8 shows the environment of the experiment.

Figure 9 (a) shows the simulated result about co-polarization at electricfield plane from the sensor. It can be found that there is a maximum gain of 7.71 dB in the front. And the directionality which concentrates most power in the front and is satisfactory for detecting physiological parameters.

Considering the different methods and standard of measurement between the real experiment and HFSS, Fig. 9 (b) shows the experimental result about co-polarization at electricfield plane from the sensor.

The parameters of the original antenna were settled after simulating, however, the performance of the antenna was changed totally after adding circuits to it. And the practical implementation is performed with some uncertainty factors, such as the wires, components and soldering, may influence the antenna profoundly. This paper took some adjustments to improve the performance by adjusting the Balun circuit and other improvements as it is said in the circuit design section. The S11 parameter was placed at the first position thus there will be a compromise about radiation pattern.

Fig. 8. Experimental environment of our testing.

(a)

(b)
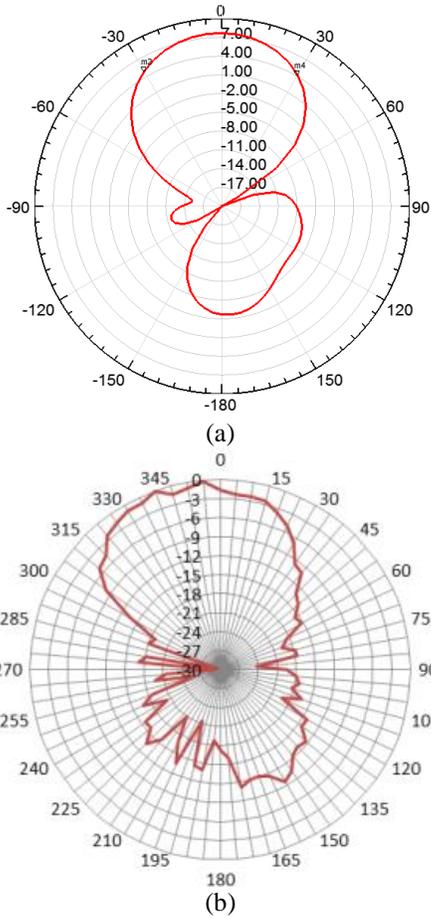
Fig. 9. Radiation pattern of the sensor. (a) Simulated result; (b) experimental result.

The simulated result and experiment result both have a huge front lobe. That means the sensor could concentrate more power on the front and will promote sensitivity effectively. The back lobe of the sensor is larger than simulated result, which might be caused by electronic components. The result is under our consideration and acceptability for monitoring vital signs. Figure 10 shows the designed RF sensor.
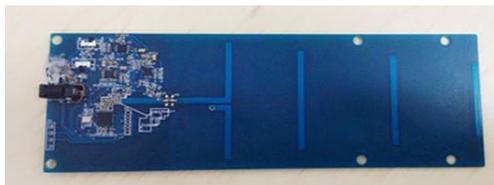
Fig. 10. Our designed RF sensor.

C. Experiment results

All the results were obtained by the sensor directly and transmitted to PC with a receiver. The performances of designed RF sensor are compared with the pulse

sensor, and respiration sensor as a reference. Figure 11 shows the signals collected by RF sensor without any processing. The signals were collected at the distance of 20 *cm* from Yagi antenna with objects facing towards the Yagi antenna and wearing the pulse sensor and respiration sensor at the same time. The duration of the data collection was 60 seconds for each dataset. Figure 11 (a) shows the original signal collected by designed RF sensor. According to the Doppler principle, echo signal consists of information on heartbeat, respiration and body movement as shown in the Fig. 11 (b).

(a)

(b)
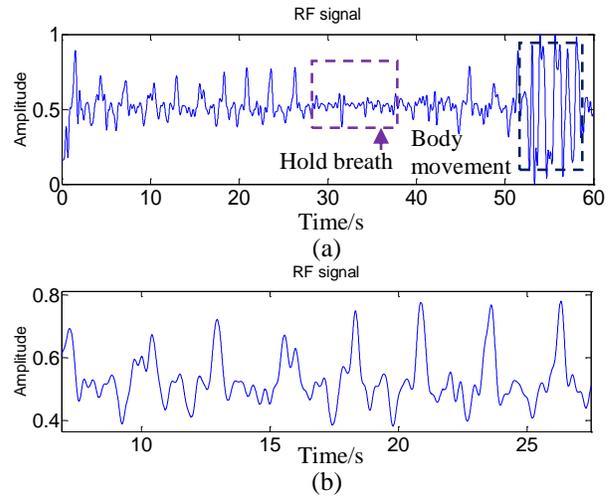
Fig. 11. Signals collected by RF sensor. (a) Original signals collected by RF sensor; (b) local amplification of original information.

The extraction of heartbeat and respiration is achieved by digital filter to filter some noise and wavelet transform. Comparing with the signals collected by the pulse sensor and respiration sensor, our designed RF sensor is able to monitor the vital signs. Figure 12 shows the respiration signal and heartbeat signal collected by the respiration sensor (Fig. 12 (a) TOP) and heartbeat sensor (Fig. 12 (b) TOP) as a reference signal in comparison with the signal collected by signals collected by RF sensor. It is notable that the heartbeat signal and respiration signal obtained from RF sensor closely agree with that of the reference.

(a)
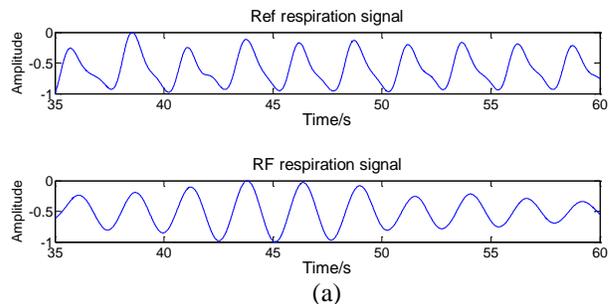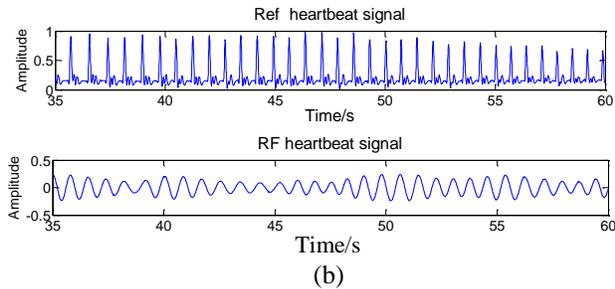
Fig. 12. Signals acquired by RF sensor, respiration sensor and pulse sensor. (a) Respiration from respiration sensor and RF sensor; (b) heartbeat signal from pulse sensor and RF sensor.

V. CONCLUSIONS

A single-channel non-orthogonal I/Q RF sensor was designed for non-contact monitoring of vital signs. The maximum gain of our designed sensor in the front is 7.7 *dB*. And the chip separates the transmitted signals and received signals by our designed program. Also, the directionality of the antenna is satisfactory. After simulation, experiment and compared with the respiration, heartbeat sensor, it was validated that the sensor could monitor the respiration, heartbeat and body movements accurately.

ACKNOWLEDGMENTS

REFERENCES

[1] M. K Rajagopal and E. Rodriguez-Villegas, "Towards wearable sleep diagnostic systems for point-of-care applications," *IEEE Point-of-Care Healthcare Technologies*, vol. 25, pp. 26-29, 2013.

[2] Y. Nijsure and W. P. Tay, "An impulse radio ultra-wideband system for contactless noninvasive respiratory monitoring," *IEEE Transactions on Biomedical Engineering*, vol. 60, pp. 1059-1517, 2013.

[3] C. Hoffman, D. Rice, et al., "Persons with chronic conditions: their prevalence and costs," *Journal of the American Medical Association*, vol. 276, pp. 1473-1479, 1996.

[4] Y. Yan, C. Li, et al., "Verification of a non-contact vital sign monitoring system using an infant simulator," *2009 Annual International Conference of the IEEE Engineering in Medicine and Biology Society*, pp. 4836-4839, 2009.

[5] J. C. Lin, "Microwave sensing of physiological movement and volume change: A review," *Bioelectromagnetics*, vol. 13, pp. 557-565, 1992.

[6] D. Zito, D. Pepe, and M. Mincica, et al., "Wearable system-on-a-chip UWB radar for contact-less cardiopulmonary monitoring: Present status," *Conf. Proc. IEEE Eng. Med. Bio. Soc. 2008*, vol. 14, pp. 5274-5277, 2008.

[7] M. Mincica, D. Pepe, et al., "Enabling technology for heart health wireless assistance," *The 12th IEEE Int. Conf. on e-Health Networking Applications and Services*, pp. 36-42, 2010.

[8] A. Droitcour, V. Lubecke, et al., "A microwave radio for Doppler radar sensing of vital signs," *IEEE MTT-S Int. Microw. Symp. Digest*, vol. 5, pp. 175-178, 2001.

[9] A. D. Droitcour, O. Boric-Lubecke, et al., "Range correlation and I/Q performance benefits in single-chip silicon Doppler radars for non-contact cardiopulmonary monitoring," *IEEE Transactions on Microwave Theory and Techniques*, vol. 52, pp. 838-848, 2004.

[10] V. Vasu, C. Heneghan, et al., "Signal processing methods for non-contact cardiac detection using Doppler radar," *IEEE Workshop on Signal Processing Systems*, pp. 368-373, 2010.

[11] C. Li and J. Lin, "Non-contact measurement of periodic movements by a 22-40 GHz radar sensor using nonlinear phase modulation," *IEEE/MTT-S International Microwave Symposium*, pp. 579-582, 2007.

[12] Y. Xiao, C. Li, et al., "Accuracy of a low-power Ka-band non-contact heartbeat detector measured from four sides of a human body," *IEEE MTT-S International Microwave Symposium Digest*, pp. 1576-1579, 2006.

[13] D. Girbau, A. Lazaro, et al., "Remote sensing of vital signs using a Doppler radar and diversity to overcome null detection," *IEEE Sensors Journal*, vol. 12, pp. 512-518, 2012.

[14] S. A. Bokhari, J. F. Zuercher, et al., "A small micro-strip patch antenna with a convenient tuning option," *IEEE Transactions on Antennas and Propagation*, vol. 44, pp. 1521-1528, 1996.

[15] C. Li, J. Cummings, et al., "Radar remote monitoring of vital signs - from science fiction to reality," *IEEE Microwave Magazine*, vol. 10, pp. 47-56, 2009.

[16] H. J. Kim, K. H. Kim, et al., "Measurement of human heartbeat and respiration signals using phase detection radar," *Review of Scientific Instruments*, vol. 78, pp. 104703, 2007.

[17] A. D. Droitcour, O. Boric-Lubecke, et al., "Signal-to-noise ratio in Doppler radar system for heart and respiratory rate measurements," *IEEE Transactions on Microwave Theory and Techniques*, vol. 57, pp.

2498-2507, 2009.

[18] J. Zhao, L. Xu, et al., "Analysis and design of a printed Yagi antenna working at the frequency of 2.4 GHz for monitoring physiological parameters," *The 11th World Congress on Intelligent Control and Automation*, pp. 543-547, 2014.

[19] W. R. Deal, N. Kaneda, et al., "A new quasi-Yagi antenna for planar active antenna arrays," *IEEE Transactions on Microwave Theory and Techniques*, vol. 48, pp. 910-918, 2000.

[20] A. Abbosh, "Ultra-wideband quasi-Yagi antenna using dual resonant driver and integrated Balun of stepped impedance coupled structure," *IEEE Transactions on Antenna and Propagation*, vol. 61, pp. 3885-3888, 2013.

[21] Y. Chen, C. Zhang, et al., "Modified quasi-Yagi antenna," *Modern Radar*, vol. 31, pp. 60-62, 2009.

[22] G. Ni, W. Ni, et al., "Design of planar UWB quasi-Yagi microstip antenna," *Modern Radar*, vol. 35, pp. 48-51, 2013.

[23] J. Venkatesan, "Novel version of the double-Y Balun: Microstrip to coplanar strip transition," *IEEE Antennas and Wireless Propagation Letters*, vol. 5, pp. 172-174, 2006.

H. R. Bo received the B.S. degree in Biomedical Engineering from Northeastern University, Shenyang, China, 2014, and is currently working toward the M.S. degree at the Northeastern University, Shenyang, China.

His research interests include antenna structures and arrays, digital signal processing and electronic circuits.

L. S. Xu (SM'15) received the B.S. degree in Electrical Power System Automation, the M.S. degree in Mechanical Electronics, and the Ph.D. degree in Computer Science and Technology from Harbin Institute of Technology, Harbin, China, in 1998, 2000 and 2006, respectively.

His current research interests include nonlinear medical signal processing, computational electromagnetic simulation, medical imaging, and pattern recognition.

AMC Integrated Textile Monopole Antenna for Wearable Applications

A. Alemaryeen and S. Noghanian

Department of Electrical Engineering
University of North Dakota, Grand Forks, ND 58202-7165, USA
ala.alemaryeen@my.und.edu, sima.noghanian@engr.und.edu

Abstract ─ In this paper, performance of monopole textile antenna integrated with a flexible artificial magnetic conductor (AMC) surface is presented. The integrated antenna is designed for operating within the 2.45 GHz Industrial, Scientific and Medical (ISM) band. The addition of AMC is to reduce the backward radiation toward the human body and increase the antenna gain. Characteristics of the AMC antenna based on simulation and measurement results under different bending conditions have been studied and presented to validate the antenna for its usefulness in wearable applications. Besides, the causes that lead to the discrepancies between simulations and measurements are discussed.

Index Terms ─ Artificial Magnetic Conductor (AMC), Coplanar Waveguide (CPW), monopole antennas, wearable antennas.

I. INTRODUCTION

Recently, industrial and academic researchers have shown significant interest in the field of wearable antennas, especially for medical applications. In general, wearable antennas possess light-weight and low-profile characteristics, while they can be easily worn and conformed to the body. Such properties are considered as one of the key components in many applications such as health monitoring for military, firefighting, and space applications.

Extensive research has been carried out on the usage of flexible materials, spatially textile materials, as a part of planar antennas [1-3]. Moreover, the effect of different electro-textile materials on the performance of wearable antenna has been studied [4,5].

In wearable applications, antennas are worn in close proximity to the human body. Frequency-detuning problems might arise because of the high dielectric properties of the human body. Besides, reducing the radiation towards the body is desirable, [6]. It is well known that AMCs and Electromagnetic Bandgap (EBG) structures have the potential to reduce both effects, thereby improve the antenna's radiation characteristics.

In [7], reflector patch element was utilized in order to decrease the back radiated field. The performance of this technique is highly dependent on the reflector size, furthermore, antenna design is based on a stack of multiple layers which leads to a high profile antenna system. In [8], inkjet-printed EBG array on paper substrate was designed for gain enhancement of microstrip monopole antenna. Despite that the proposed design is efficient on human body phantom, substrate material puts limitations on the compactness of the proposed antenna for wearable antenna applications. In [9], enhancement in the backward radiation and gain of a coplanar-waveguide (CPW) fed monopole antenna is obtained using AMC reflector. However, another limitation imposed by wearable antenna applications in terms of antenna flexibility has been faced in the proposed antenna system.

In this paper, we provide results from a study of CPW fed monopole textile antenna integrated with 4×4 flexible AMC array to cover ISM 2.45 GHz. The proposed antenna is flexible and compact which makes it suitable for wearable antenna applications. Bending analysis is performed to validate wearable antenna as in [2,6]. The prototype provides stable reflection coefficient characteristics under different bending conditions.

II. DESIGN OF MONOPOLE ANTENNA

The proposed monopole antenna configuration is based on the proposed design in [9], and is optimized using commercial electromagnetic simulation software CST Microwave Studio [10]. The radiating element and the CPW feeding line are printed on the same side of a Pellon fabric substrate having a thickness of 3.6 mm, dielectric constant $\varepsilon_r = 1.08$ and loss tangent $\tan\delta = 0.008$. Figure 1 depicts dimension details and fabricated prototype of the monopole antenna. Pellon fabric is chosen as the antenna's substrate since it exhibits a low profile and flexible characteristics, which enable stacking multiple layers to control the thickness of the substrate.

Figure 2 presents simulated and measured reflection coefficient (S_{11}) of the monopole antenna. Reflection coefficient measurements are carried out using Agilent E5071C Network Analyzer. Simulation result yields a -10 dB impedance bandwidth of 2.58 GHz (1.75 GHz - 4.33 GHz) with a good impedance matching at 2.45 GHz ($S_{11} = -16.01$ dB). On the other hand, measurement result (see Antenna 1) shows a wider impedance bandwidth of 3.58 GHz (1.28 GHz - 4.86 GHz) with a better matching

characteristic at 2.45 GHz (S_{11}= -20.97 dB). Discrepancies between simulations and measurements (see Antenna 1) were observed in the obtained results. This may be attributed due to errors during simulation, fabrication, and measurement phases of our investigation. It is worth mentioning that the textile monopole antenna was made by hand. Therfore, we first looked at the errors due to fabrication process. We thus decided to fabricate a new monopole antenna in order to avoid the effect of fabrication errors on the obtained results. We found out that errors due fabrication process didn't explain the discrepancies between simulations and measurements (see Antenna 2). However, the precision of the fabrication process has been increased in the second fabrication phase and the new fabricated antenna was used in the following investigations.

(a)   (b)
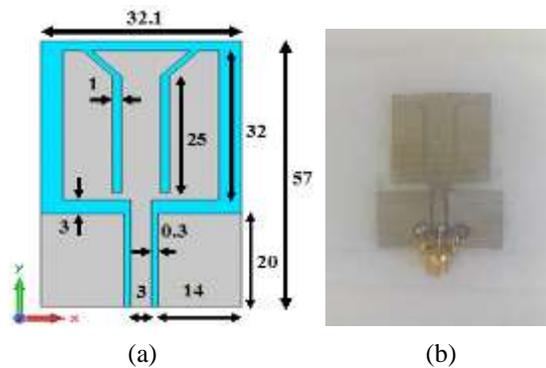
Fig. 1. CPW-fed monopole antenna: (a) dimension details are given in mm, and (b) fabricated prototype.
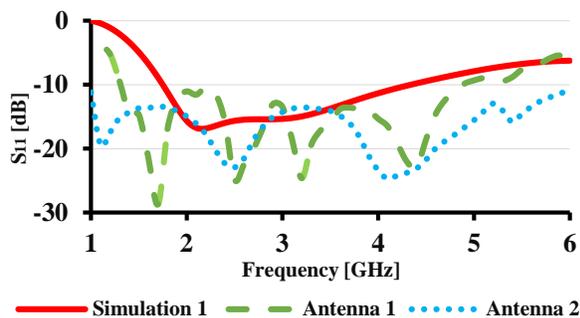
Fig. 2. Reflection coefficient of monopole antenna.

Another possible cause we found for discrepancies between simulations and measurements is the errors in material properties that used during the simulation phase of our investigation. In the first simulation, we have assumed the used conductive material in monopole antenna is copper material (σ = 5.8×10^7 S/m) for simplicity. However, the conductivity of the electro-textile materials is different from that for a good conductor such as copper. To validate this conclusion, a parametric study on the conductivity of the electro-

textile material was carried out based on simulations. As shown in Fig. 3, S_{11} results when the conductivity of electro-textile material is 500 S/m (see Simulation 2) are with a good agreement with the measurement results, as expected. Thus, we can conclude from the above discussion that the conductivity of the textile material is one of the error sources in our investigation.
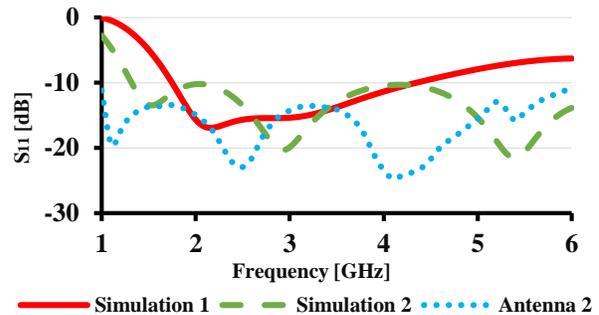
Fig. 3. S_{11} of monopole antenna using different conductive material.

Radiation patterns measurements have been performed using the anechoic chamber in Antenna Measurements Laboratory at University of North Dakota. Figure 4 shows the normalized E-plane radiation pattern of the monopole antenna at 2.45 GHz based on simulation and measurement results. The simulated cross-pole component isn't shown in the figure since it is less than -60 dBi. The simulated antenna gain is 2.45 dBi while the measured value is 3.39 dBi.
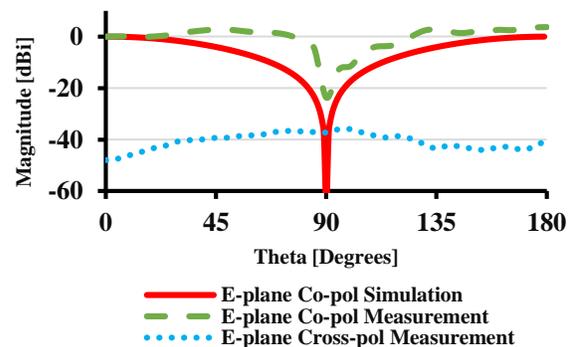
Fig. 4. E-plane radiation pattern of CPW-fed monopole antenna at 2.45 GHz.

III. DESIGN OF AMC GROUND SURFACE

The proposed antenna is placed on a symmetric 4×4 AMC array measuring 124×124 mm². To determine the array size, it was increased by one row and one column at a time until satisfactory performance in terms of high gain within the frequency range of interest was achieved, while maintaining a relatively small size. The geometry of the AMC unit cell is based on the proposed design in

[10] and optimized using CST MWS software. AMC cell measures 31×31 mm^2, and it is printed on 1.52 mm thick RO3003 flexible material with ε_r= 3 and $\tan\delta$ = 0.0013. Figure 5 shows dimension details of the proposed AMC unit cell and the prototype of the fabricated AMC array.

(a) (b)
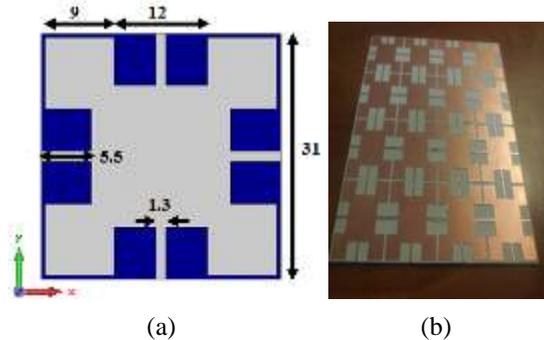
Fig. 5. Geometry of AMC structure: (a) dimension details are given in mm, and (b) fabricated prototype.

AMC reflector is designed by means of reflection phase characterization. The AMC reflection phase characterization procedure follows the same methodology applied in [11]. In the proposed cell, the exact point of zero phase is located at 2.45 GHz, having a narrow bandwidth of 138 MHz (2.34 GHz to 2.48 GHz) within ±90 phase values, as shown in Fig. 6.
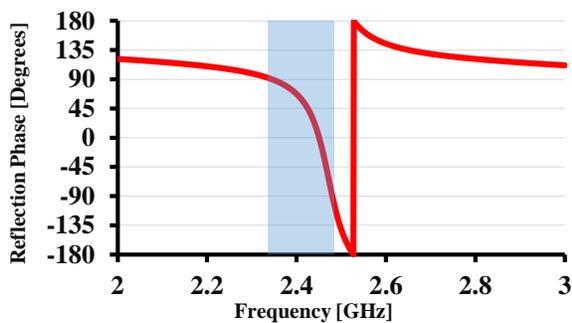
Fig. 6. Reflection phase diagram of an AMC unit cell.

S_{11} results of monopole antenna integrated on AMC reflector, which is defined as AMC antenna, using both copper material (see Simulation 1) and material of 500 S/m conductivity (see Simulation 2) are shown in Fig. 7 along with the measurement results. In general, a significant reduction in the impedance bandwidth by about 2.31 GHz (based on measurements) is obtained due to the use of AMC ground plane. However, the obtained bandwidth of AMC antenna is obviously sufficient for ISM-2.45 GHz operation with a good matching characteristics. Moreover, changing the

conductivity of the monopole antenna has an effect of increasing the bandwidth of AMC antenna by about 2.5%, based on simulations. However, changing the material didn't explain the discrepancy in the obtained results. Many challenges were faced during the measurement phase due to the stiffness of the vector network analyzer cables and the softness of the designed textile antenna. We could not firmly fix the antenna and we noticed a large variation in the resonances and S_{11} level when we changed the position of the antenna and cables during the setup of the test. Also, a large variation in S_{11} with the pressure on the antenna connector while moving the cable was confirmed. Hence, problems in terms of misalignment of the monopole antenna on the AMC structure and air gap between monopole antenna and AMC structure were faced.
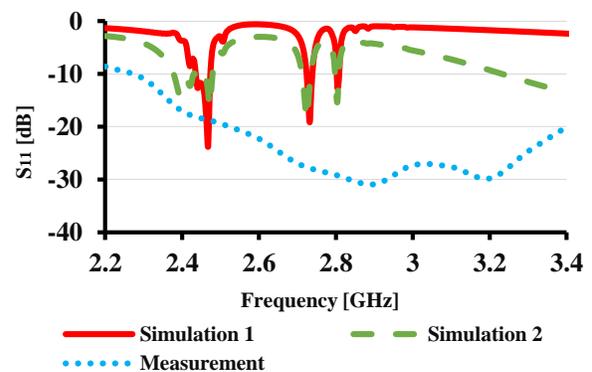
Fig. 7. Reflection coefficient of AMC antenna.

Normalized radiation patterns in E- and H-plane of AMC antenna based on simulation and measurement results at 2.45 GHz are shown in Fig. 8. Cross-pole components of both planes aren't shown here since they are less than -40 dB. The measured AMC antenna gain is 6 dBi while the simulation-based value is 8.41 dBi. This reduction might be due to error sources discussed previously.

(a)

(b)
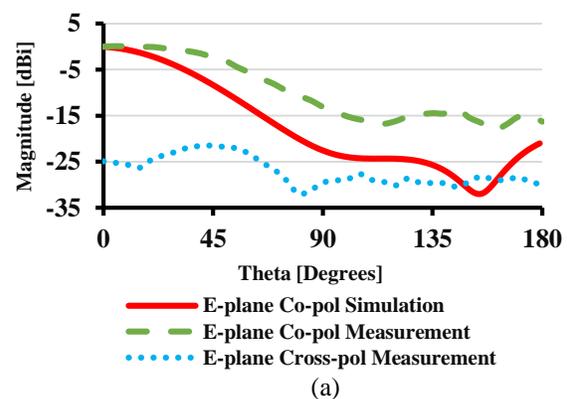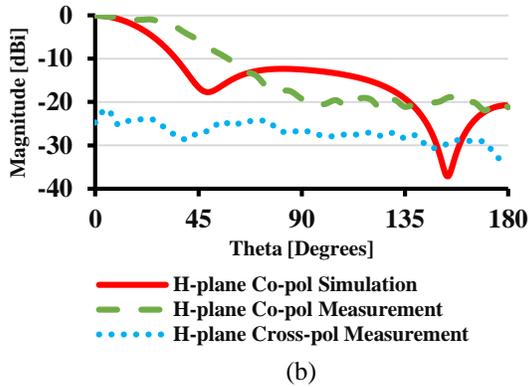
Fig. 8. Radiation patterns of AMC antenna at 2.45 GHz:
(a) E-plane and (b) H-plane.

IV. PERFORMANCE OF AMC ANTENNA UNDER BENDING CONDITIONS

In wearable antenna system, it is difficult to keep the antenna flat all the time, especially when the antenna is made out of flexible material. Moreover, the wearable antenna will be subject to several shape distortion forms due to the human body movements. Therefore, investigation of the antenna's performance on the dynamic body environment such as under bending conditions due to the antenna conformability with the surface of the body is one of the important factors to be studied. Bending radii (R) chosen in our investigation are: 40 mm, 100 mm and 140 mm to approximate a human adult's arm, leg and thigh. Moreover, investigations of antenna performance were executed for two bending directions: E- and H-plane, illustrated in Figs. 9 (a) and (b), respectively.

(a)   (b)
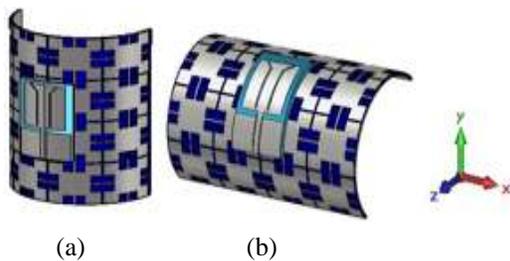
Fig. 9. AMC antenna bent around cylinders for different directions: (a) E-plane and (b) H-plane.

A. Reflection coefficient

Reflection coefficient results of AMC antenna based on simulations and measurements in flat form and under different bending conditions in E- and H-plane are depicted in Figs. 10 and 11, respectively. It is worth mentioning that it is impossible to reach a specific bending in the measurements as accurately as in the simulations. Hence, errors in bending radii are unavoidable. In addition, S_{11} measurement results for

$R = 40$ mm are not shown here due to the difficulty to get to that bending degree accurately. However, simulation results are shown to test the flexibility of the design based on simulations.

Despite best efforts, discrepancies between simulations and measurements still exist. However, bending AMC antenna resulted in shifting the resonance frequency toward lower values for both bending directions, which is independent from the bending radius, based on simulations and measurements. In addition, based on measurement results, bending AMC antenna in H-plane direction has changed its matching properties dramatically in terms of impedance bandwidth and S_{11} level compared to bending conditions in E-plane direction.

(a)

(b)
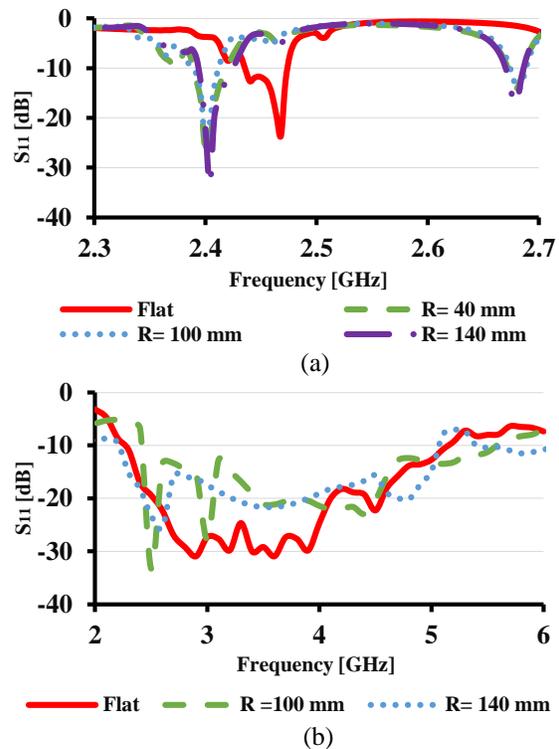
Fig. 10. S_{11} for different bending radius at the E-plane direction: (a) simulations and (b) measurements.

(a)

(b)
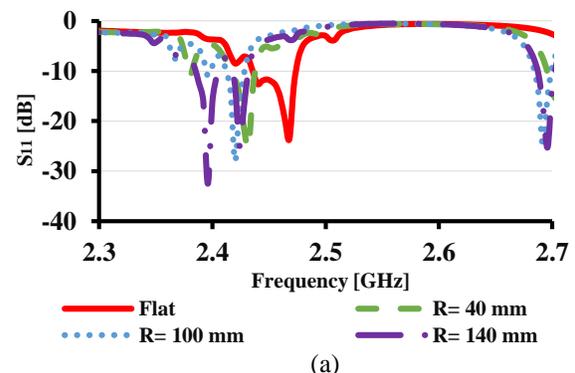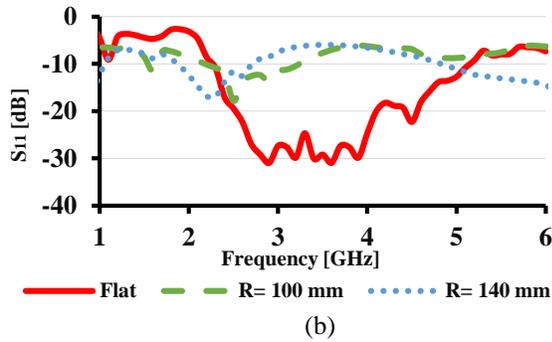
Fig. 11. S_{11} for different bending radius at the H-plane direction: (a) simulations and (b) measurements.

B. Radiation patterns

Radiation patterns at the resonance frequency of E- and H-plane bent AMC antenna are shown in Figs. 12 and 13, respectively. In general, it can be observed that as the AMC antenna is bent more and more (bending radius gradually decreased), antenna gain and directivity have been decreased due to both E- and H-plane bending conditions. The least value of AMC antenna gain of 3.4 dBi is obtained due to $R = 100$ mm bending in H-plane direction. Moreover, the power level of the cross-pol components has been increased under bending conditions in H-plane direction, while less deformation has been achieved due to bending in E-plane direction.
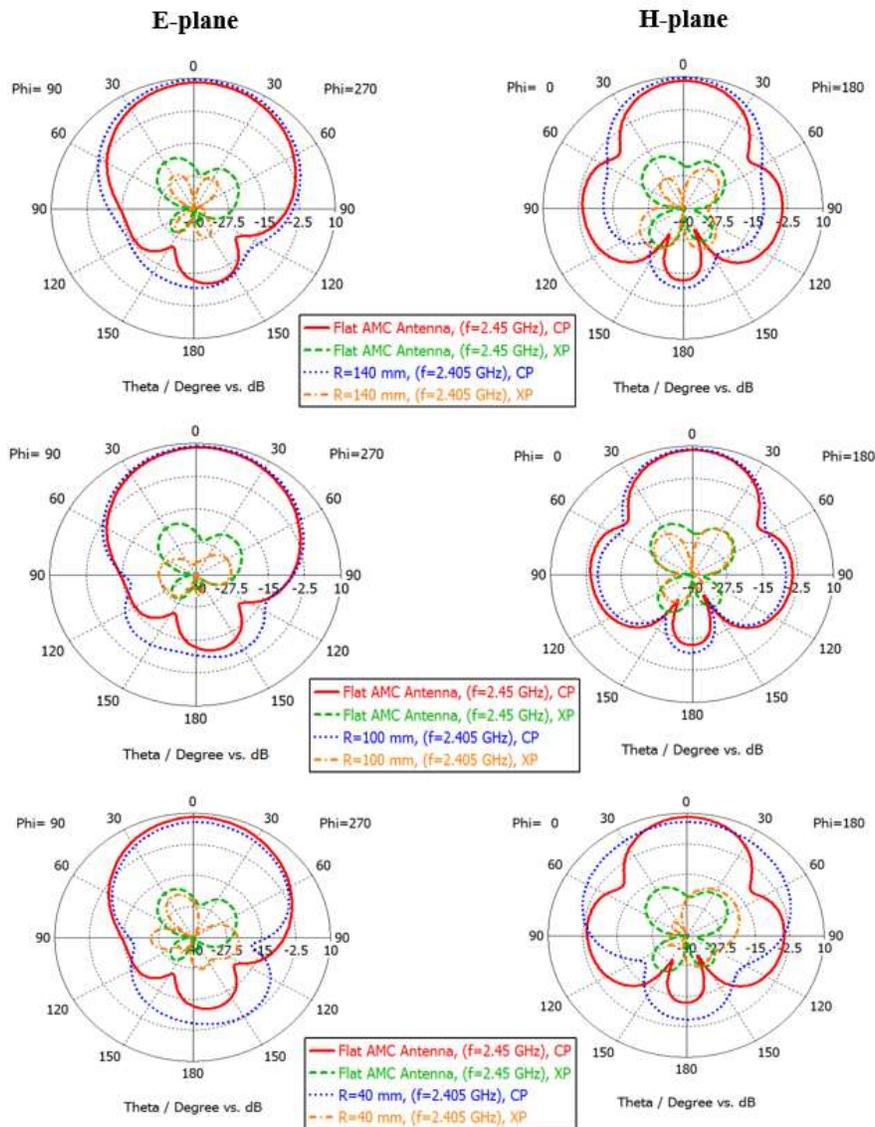
Fig. 12. Simulated radiation patterns of AMC antenna bent in E-plane at f_r: (left) E-plane and (right) H-plane; Co Polarization (CP) and Cross Polarization (XP).
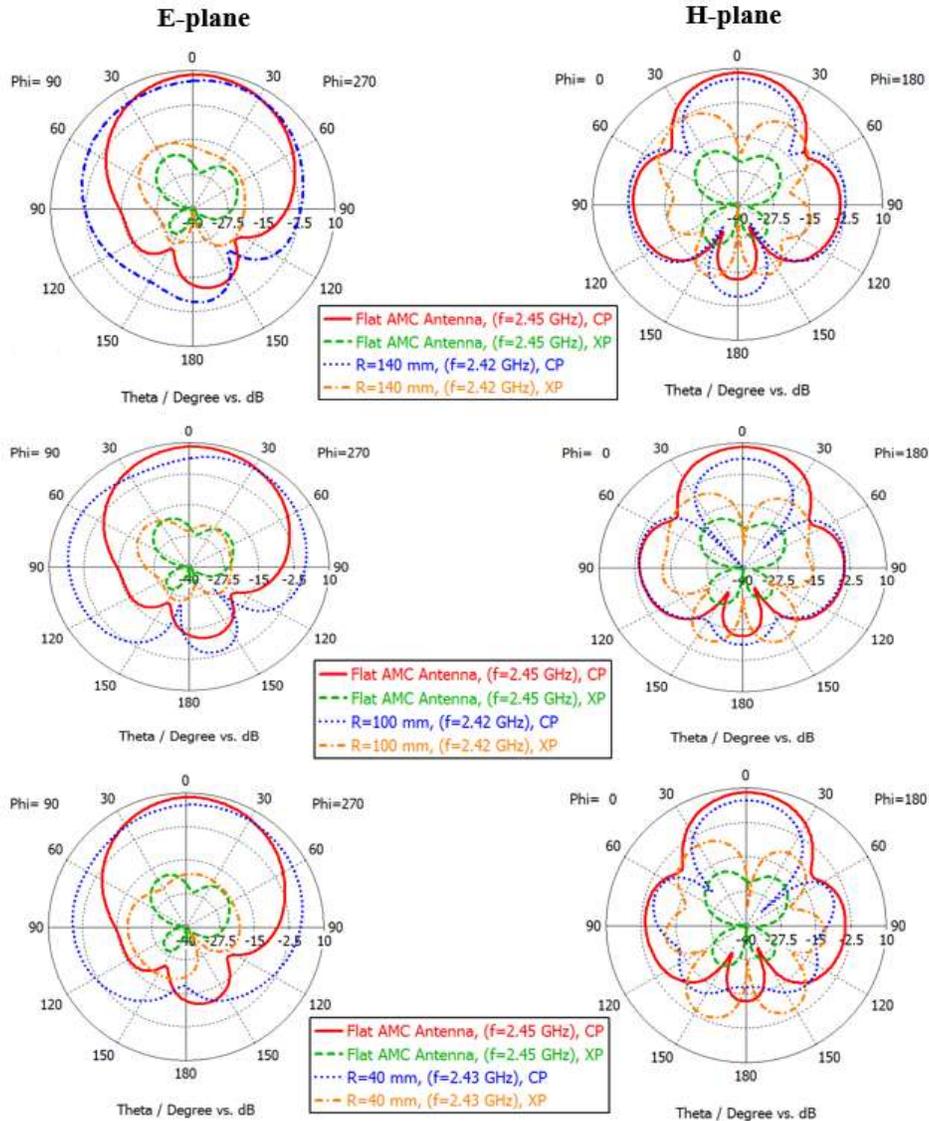
Fig. 13. Simulated radiation patterns of AMC antenna bent in H-plane at f_r: (left) E-plane and (right) H-plane; Co Polarization (CP) and Cross Polarization (XP).

In order to explain AMC antenna gain degradation due to bending conditions, effect of AMC antenna bending on the point of zero phase reflection was investigated based on simulations and summarized in Table 1. It can be concluded that bending AMC antenna has an effect of shifting the point of zero phase reflection, which is no more at the resonance frequency of the AMC antenna.

Table 1: Zero reflection point of AMC structure bent in E- and H-plane directions

Bending Radius	E-plane	H-plane
$R = 40$ mm	2.4868 GHz	2.4775 GHz
$R = 100$ mm	2.4776 GHz	2.4679 GHz
$R = 140$ mm	2.4902 GHz	2.4763 GHz

V. CONCLUSION

Textile monopole antenna integrated with flexible AMC surface operating in ISM 2.45 GHz band is investigated for wearable applications under different bending conditions. A detailed description about the design has been presented. Results demonstrated improvement in the antenna gain of the integrated antenna, which implies enhancement in the radiation characteristics, and reduction in the backward radiation toward the human body. Furthermore, measurement results showed that AMC antenna bending in H-plane direction has changed its matching properties dramatically in terms of impedance bandwidth and S_{11} level compared to bending conditions in E-plane direction.

REFERENCES

[1] P. Salonen, Y. Rahmat-Samii, M. Schaffrath, and M. Kivikoski, "Effect of textile materials on wearable antenna performance: A case study of GPS antennas," in *Proc. IEEE AP-S Int. Symp.*, pp. 459-462, 2004.

[2] S. Zhu and R. Langley, "Dual-band wearable textile antenna on an EBG substrate," *IEEE Trans. Antennas Propag.*, vol. 57, no. 4, pp. 926-935, 2009.

[3] S. Sankaralingam and B. Gupta, "Development of textile antennas for body wearable applications and investigations on their performance under bent conditions," *Progress in Electromagnetics Research B*, vol. 22, pp. 53-71, 2010.

[4] Y. Ouyang, E. Karayianni, and W. J. Chappell, "Effect of fabric patterns on electrotextile patch antennas," in *Proc. IEEE AP-S Int. Symp.*, Washington DC, vol. 2B, pp. 246-249, Jul. 2005.

[5] I. Locher, M. Klemm, T. Kirstein, and G. Troster, "Design and characterization of purely textile patch antennas," *IEEE Trans. Adv. Package*, vol. 29, no. 4, pp. 777-788, Nov. 2006.

[6] S. Velan, E. Sundarsingh, M. Kanagasabai, A. Sharma, C. Raviteja, and R. Sivasamy, "Dual-band EBG integrated monopole antenna deploying fractal geometry for wearable applications," *IEEE Antennas Wireless Propag. Lett.*, vol. 14, pp. 249-252, Feb. 2014.

[7] W. S. T. Rowe and R. B. Waterhouse, "Reduction of backward radiation for CPW fed aperture stacked patch antennas on small ground planes," in *IEEE Trans. Antennas Propag.*, vol. 51, no. 6, pp. 1411-1413, June 2003.

[8] S. Kim, Y.-J. Ren, H. Lee, A. Rida, S. Nikolaou, and M. M. Tentzeris, "Monopole antenna with inkjet-printed EBG array on paper substrate for wearable applications," *IEEE Antennas Wireless Propag. Lett.*, vol. 11, pp. 663-666, 2012.

[9] M. Mantash, A.-C. Tarot, S. Collardey, and K. Mahdjoubi, "Investigation of flexible textile antennas and AMC reflectors," *International Journal of Antennas and Propagation*, vol. 2012, 2012, Article ID 236505, 10 pages, http://dx.doi.org/10.1155/2012/236505

[10] CST Microwave Studio [Online]. Available: http/www.cst.com

[11] F. Yang and Y. Rahmat-Samii, "Reflection phase characterizations of the EBG ground plane for low profile wire antenna applications," *IEEE Trans. Antennas Propag.*, vol. 51, no. 10, pp. 2691-2703, Oct. 2003.

Ala Alemaryeen received the B.Sc. degree in Electrical Engineering from Mutah University, Karak, Jordan, in 2012, and the M.Sc. in Electrical Engineering in the field of Applied Electromagnetics with focus on Artificial Magnetic Conductors and Wearable Antennas, from University of North Dakota (UND), North Dakota, USA, in 2015. She is working towards the Ph.D. degree in Electrical Engineering at UND. Her research interests are in wearable antennas and metamaterial.

Sima Noghanian received the B.Sc. degree in Electrical Engineering from the Sharif University of Technology, Tehran, Iran, in 1992, and the M.Sc. and Ph.D. degrees both in Electrical Engineering, from the University of Manitoba, Winnipeg, Canada, in 1996 and 2001, respectively. In 2001, she was a Researcher at YottaYotta Corporation, Edmonton, Canada. She received a Postdoctoral Fellowship from Natural Sciences and Engineering Research Council of Canada in 2002, which she took at the University of Waterloo.

She was an Assistant Professor in the Department of Electrical Engineering, Sharif University of Technology, Iran, during 2002-2003. From 2003 to 2008, she was an Assistant Professor in the Department of Electrical and Computer Engineering, University of Manitoba, Canada. She is currently an Associate Professor of the Department of Electrical Engineering, University of North Dakota, USA. Her research interests include antenna design and modeling, wireless channel modeling, ultra-wideband antennas, and microwave imaging. Noghanian is a Senior Member of IEEE and served as the IEEE Winnipeg Waves Chapter (joint Chapter of Antenna & Propagation, Microwave Theory & Techniques, and Vehicular Technology societies) Chair during 2004-2005. She is a Member of Eta Kappa Nu, a Member of International Union of Radio Science URSI Commission B, and a Member of the Applied Computational Electromagnetics Society. She is currently an Area Editor for AEU - International Journal of Electronics and Communications.

A Communication Link Analysis Based on Biological Implant Wireless Body Area Networks

Yangzhe Liao, Mark S. Leeson, and Matthew D. Higgins

School of Engineering
University of Warwick, Coventry, CV4 7AL, UK
{yangzhe.liao, mark.leeson, m.higgins}@warwick.ac.uk

Abstract ─ The rapid growth in remote healthcare services and biomedical demands has seen novel developments in wireless body area networks (WBANs). The WBAN can be seen as an integration of intelligent networks, which permits devices and sensors to work together to obtain a series of critical physiological parameters, such as blood flow velocity and heartbeat frequency. Analysis of WBAN radio frequency communication systems is the key factor and the critical research challenge that determines system performance, such as achievable transmission distance, data rate and so forth. The human head is an area of particular potential in WBAN design that is worthy of attracting more attention than its limited literature to date. This paper is primarily focused on the one of the most detailed comprehensive multi-modal imaging-based anatomical human head models. This is a multimodal imaging-based detailed anatomical model, denoted by the acronym MIDA, this features 153 structures at a high resolution of up to 500 μm, including numerous distinct muscles, bones and skull layers in the license-free 2.4 GHz industrial, scientific, and medical (ISM) band. It presents and compares a set of advanced simulation methods and then proposes a path loss simulation flat phantom, semi-empirical path loss models for typical homogeneous tissues and the anatomical human head MIDA model. The bit error rate (BER) performances of the MIDA model fading channel using binary phase shift keying (BPSK) and pulse-amplitude modulation (PAM) are obtained. Furthermore, achievable transmission distances for several data rates for predetermined acceptable BERs are accomplished. The results show that PAM promises longer transmission distances than BPSK when using both high and low data rates. The proposed communication systems can be applied to optimize implantation communication system scenarios and biotelemetry applications.

Index Terms ─ MIDA human head model, path loss, system margin, WBANs.

I. INTRODUCTION

Wireless body area networks (WBANs) are becoming increasingly significant for numerous applications in e-health and biosensor technology for a number of reasons, including low power consumption, simple structure requirements and potentially fast transmission data rates [1-3]. A typical WBAN can be regarded as a healthcare network system, which consists of sensors and other devices on, near or inside the human body as shown in Fig. 1. Recently, implant WBANs for biomedical applications have brought about a revolutionary change due to the development of antenna technologies and wireless communication systems [4]. However, surprisingly little work has been published to date on the proposed use of WBANs for the human cephalic section, which is the most significant and urgent area that can cooperate with future telemedicine technology and electronic medical services [4, 5].

An important feature in the development of WBANs is the characterization of the physical layer [4-7]. The majority of the literature has been concerned with on-body propagation while fewer studies have been focused on the modeling of intra-body propagation subjects [8-10]. Since the human body area is a natural lossy environment, signals propagating from the transmitter are attenuated considerably before reaching the receiver; hence an essential step in the understanding of implant WBANs is to comprehend the propagation loss process [11-15]. A path loss (PL) model is an advantageous approach to help with the design of wireless communication systems between nodes located within the human body [13-18]. In [16], the performance of PL in muscle and fat tissues individually is obtained using insulated dipole antennas at 2.45 GHz through a Method of Moments program, FEKO from EMSS in South Africa. In [17], PL results have been obtained for an in-body propagation model in saline water with a Hertzian dipole. A multi-implant setup at 2.4 GHz has been investigated in [18] using insulated dipole antennas for specific locations including the liver, heart, spleen and

kidneys.
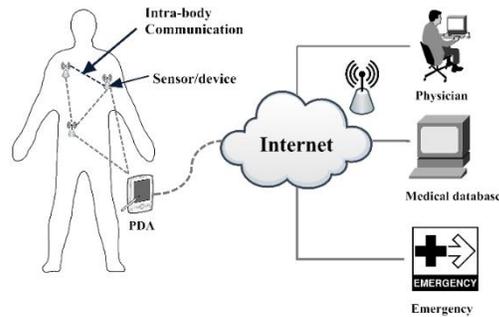
Fig. 1. Typical architecture of an implant WBAN system.

Due to the difficulty of specific absorption rate (SAR) measurements in an actual human head for electromagnetic (EM) radio-frequency exposure, the second challenge lies in the examination of human tissue safety [19, 20]. This involves evaluating health risks related to exposure to electromagnetic (EM) fields and making sure that these satisfy the international SAR compliance regulations, for example those of the Institute of Electrical and Electronics Engineers (IEEE) [21] and the International Commission on Non-Ionizing Radiation Protection (ICNIRP) [22].

Implant WBAN analysis includes propagation loss, energy consumption, transmission rate, and quality transmission distance issues [1-5]. Shadow fading characterizes the variations in the implant WBAN channel power loss caused by obstacles in the propagation path [23]. Also, essential requirements within an implant WBAN channel model are the capability to support long transmission distances and high transmission data rates that can effectively connect and work with future medical servers [24, 25].

The work described in the present paper is intended to provide valuable insight into implantable communication systems research. The rest of the paper is organized as follows. Frequency selection and EM simulation methods are discussed and selected in Section II [23, 24, 26-28]. In Section III, a PL simulation flat phantom is proposed and semi-empirical PL models for typical homogeneous tissues as well as the MIDA cephalic model are given. A flat phantom is utilized to obtain the properties of various typical homogeneous tissues, in which the signal propagation attenuation is determined using a transmitting dipole antenna (Tx) and receiving dipole antenna (Rx). Then semi-empirical PL models for several typical human tissues are proposed as well as the MIDA human head model [29]. This is followed by calculation of the maximum 10-g SAR distribution [21, 22]. In Section IV, several performance indicators are determined using binary phase shift keying (BPSK) and pulse-amplitude modulation (PAM), and the

MIDA cephalic model fading channel. The indicators are the bit error rate (BER) performance, the minimal signal-to-noise ratio (SNR) requirement, the system margins and the achievable transmission distances for several data rates at a given BER. Finally, Section V presents conclusions and suggestions for further work.

II. RELATED WORK

Selecting the frequency for the WBAN system can profoundly influence tissue dielectric characterization as well as implanted antenna size [23-28]. WBAN channels are primarily proposed in the medical implant communication service (MICS), industrial, scientific, and medical (ISM) and the ultra wideband (UWB) frequency bands or in multi-bands [5]. The MICS frequency band allows the transmitted signal to suffer lower attenuation when propagating along an implanted communication path than the UWB and ISM bands, and was thus accepted for the IEEE 802.15.6 standard [29]. However, the MICS band is less likely to satisfy future high data transmission demands; it results in antennas that are too large and complex to employ in realistic situations [6, 29-31]. The UWB frequency band is a promising candidate due to its simple structure, multi-path fading, and high data speed. Nevertheless, the weaknesses of UWB are that it only offers short-range of coverage and it experiences higher energy attenuation [2, 6, 26, 32]. In this paper, the 2.4 GHz band is selected because it can support higher data rate applications and is accepted worldwide [6]. The results indicate that higher transmitted power within safety guidelines can be obtained. It is also much more likely to be embedded within the human body due to its small antenna size.

Numerous advanced electromagnetic simulation technologies have been applied in WBANs [13, 15, 16, 33-35]. In [33], it was pointed out that the method of moments (MoM) is the most effective technology for planar antenna structures (for example, PCB layers). The finite element method (FEM) is a useful scheme for helical antennas along with some simple 3D constructions [34]. Unlike the MoM and FEM algorithms, the finite difference time domain (FDTD) approach [35] is very efficient for solving complex problems, such as the characterization of antenna performance when embedded inside multi-layer surroundings. In addition, FDTD 3D model meshes are built from Yee Cells so as to deliver high processing capabilities and reduced memory resources for large 3D structures [35]. It is important to note that, unlike much other work, which uses conductivity and relative permittivity to simulate tissues in the High Frequency Structure Simulator (HFSS) and other commercial software [4-5, 12, 16, 41-43], here we employ the CST Studio Suite® 2015 (Computer Simulation Technology, Darmstadt, Germany) [36] which takes the loss tangent parameter into account. Moreover, at the same time relatively permittivity is automatically

considered in the simulation process, thus allowing the
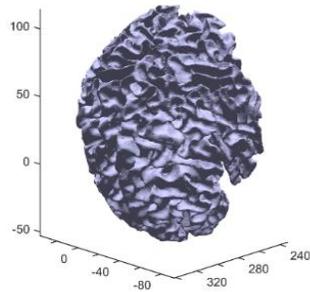
simulation results to be more accurate [3, 36-39].
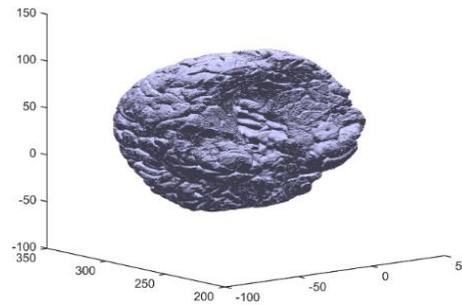
Fig. 2. MIDA 3D model structures of brain white matter (left) and brain gray matter (right). (Units in millimeters).

Given the difficulty of experimental investigation of signal power loss on a real human body, the CST program has been investigated for solving electromagnetic issues in this paper. The multimodal imaging-based detailed anatomical or MIDA model [29] was obtained by scanning a healthy 29-year old female volunteer head and neck down to the level of the fifth cervical vertebra at the Institute for Biomedical Engineering Laboratory (ETH, Zurich, Switzerland). It is a detailed anatomical computer model, including 153 kinds of different organs and tissues, with a highest resolution of 0.5 mm; it is thus more advanced and accurate than the Virtual Family models [38-40]. The advances of the MIDA model are not limited to computational modeling research, but also can be applied to computational simulations to investigate the safety and efficacy of medical devices located in, on or around the head [29]. Figure 2 shows the brain white matter and brain gray matter of the MIDA model.

III. PL MODELING AND HUMAN SAFETY ANALYSIS

A. Simulation setup

For traditional wireless communication, radio propagation refers to the process of radio waves suffering from reflection, diffraction and scattering when they propagate from the Tx to the Rx [1-4]. However, the scenario of in-body communication channel is more complicated and less predictable as the intensity varies with the lossy environment at diverse locations. As we are mainly aiming to design communication links within a human head model, the antenna design issue is not the central focus of this paper. To the best of our knowledge, the majority of the proposed antennas for in-body communication systems use a homogenous tissue (single layer structure), and are unable to work accurately when embedded in the brain, which is a multi-layer structure [16, 17, 42]. Kurup et al. proposed a novel insulated dipole antenna rather than bare dipoles for WBANs at 2.45 GHz [16]. The method improves the leakage of conducting charge as well as reducing sensitivity of the current distribution within the ambient medium. However,

the dielectric parameters of the insulator material polytetrafluoroethylene are similar to those of human muscle tissue and can thus affect the simulation results. In this paper, two identical dipoles are selected because dipole antennas are simple and well-understood in free space communications. Additionally, the dimensions of such antennas are appropriate for them to be implanted in the body [16, 41]. The two arms of the dipole antenna (shown in Fig. 3) are both made of perfect electric conducting (PEC) material with a diameter $\lambda_1 = 1$ mm. The resonance occurs when the antenna is equal to a half wavelength in a transmission medium, and $\lambda_2 = 6.25$ cm for 2.4 GHz. The simulations use a voltage source, and the dimensions and simulation methods are the same for all the cases examined. The proposed flat phantom is beneficial to understand and compare the PL performance between several typical human head tissues Also, antenna design mechanisms can be applied to the MIDA model. The dielectric parameters are frequency dependent and can be obtained from thorough survey published by Andreuccetti et al. [44]. This was compiled using both data from a range of published papers and comprehensive measurements by the authors using several experimental techniques. Figure 4 demonstrates that tissue conductivity is monotonically increasing while the loss tangent goes through a minimum close to 2.5 GHz. The dielectric parameters of several typical human tissues at 2.4 GHz, such as conductivity σ, loss tangent $\tan \delta$ and relative permittivity ϵ_r, are summarized in Table 1 [44].
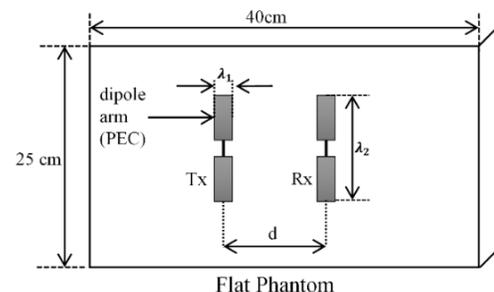
Fig. 3. Simulation platform design.
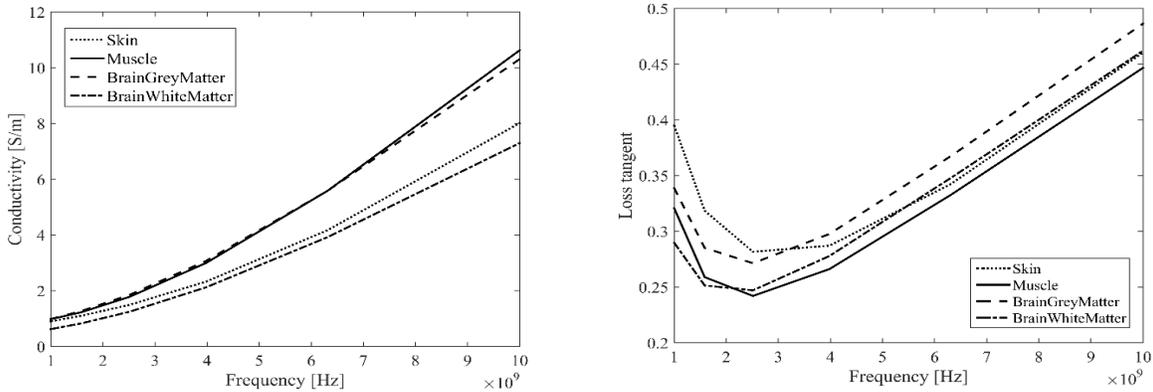
Fig. 4. (left) Conductivity of skin, muscle, brain gray matter and brain white matter from 1-10 GHz. (right) Loss tangent of skin, muscle, brain gray matter and brain white matter from 1-10 GHz.

B. PL analysis

We first investigate wave propagation at 2.4 GHz in human homogeneous tissues, using simulations for the proposed implantable antennas. The dielectric parameters used are those summarized in Table 1. The simulations in this paper are all performed using the 3D CST FDTD electromagnetic solver introduced above. The maximum grid step in the homogeneous tissues and heterogeneous MIDA human head model is 1 mm. The simulations are carried out using the implantable antennas up to 5 cm apart for homogeneous tissues.

Table 1: Dielectric properties of human body typical tissues at 2.4 GHz [44]

Tissue	σ	ϵ_r	$\tan\delta$
Dry skin	1.441	38.063	0.2385
Muscle	1.705	52.791	0.2419
Brain gray matter	1.773	48.994	0.2710
Brain white matter	1.190	36.226	0.2460

Figure 5 shows that the direction of the Tx and Rx dipole antennas are both set to be aligned in the MIDA model. The Tx transmitting dipole is fixed in the skin tissue while the Rx receiving dipole horizontally moves from the reference location ($d = 0.5$ cm) up to a distance of 7 cm (from the skin area to the deep head area). The scenario of the simulated PL of MIDA (heterogeneous model) is more complex than homogeneous tissues because energy attenuation becomes considerable and antenna coupling occurs when penetrating other tissues alone. The PL is derived as a function of the distance between Tx and Rx when the antennas are aligned for homogeneous tissues and a heterogeneous human head model. A semi-empirical in-body distance-based PL model in dB based on the Friis formula [16, 24, 44] is proposed:

$$PL_{dB}(d) = \alpha + 10n\log_{10}(d) + S, \qquad (1)$$

where α denotes the PL value at d_{ref} (set as 0.05 cm). The variable d is the separation distance between the Tx and Rx antennas. The PL model allows the receiving antenna at the same distance d to have a different PL, which varies with a normally distributed, zero mean random shadowing effect $S \sim \mathcal{N}(0, \sigma^2)$. The value of the variance for the MIDA model may be taken from the standard deviations given in Table 2. This contribution thus explicitly includes the stochastic effect of shadow fading that is imposed on the deterministic contribution to the PL. The parameter n represents the standard PL exponent; this varies with the transmission medium, with a value of two corresponding to free space and higher values including situations with more obstructions. To assess the accuracy of the parameter estimates, a least square fit method and MATLAB curve fitting toolbox were applied to determine PL [42] with the detailed information summarized in the last row of Table 2. The coefficients of determination values R^2, representing the fitting degree between PL and the antenna separation distances, are higher than those mentioned in [16, 44] indicating a better fit.

Figure 6 shows PL results illustrating that the highest PL value is achieved by muscle, followed by brain gray matter, brain white matter and then skin. The simulation starts at $d = 5$ mm from the transmitting antenna and ranges up to a distance of 5 cm for homogeneous tissues in order to limit antenna coupling effects [42]. The results are similar to those seen previously in the literature [5, 6], although previous work used insulated or helical antennas. As expected, the PL increases when the separation distance between Tx and Rx increases. Figure 7 shows the PL as a function of the distance of the proposed heterogeneous MIDA model. The PL is derived as a function of the distance between Tx and Rx when the antennas are aligned for homogeneous tissues and a heterogeneous human head model.
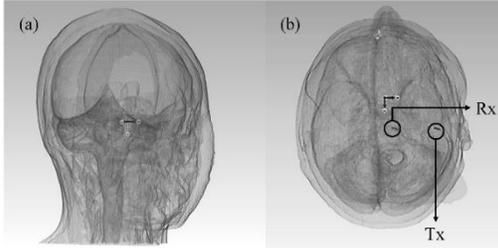
Fig. 5. MIDA model and dipole antennas. (a) side view, and (b) front view.

Table 2: Parameters for PL models for homogeneous tissues and the MIDA model

Tissue	α	n	σ	R^2
Dry skin	30.17	1.608	1.534	0.9941
Muscle	37.08	1.964	3.623	0.9911
Brain gray matter	37.97	1.631	0.658	0.9972
Brain white matter	36.97	1.644	1.101	0.9954
MIDA model	43.95	2.552	1.079	0.9728
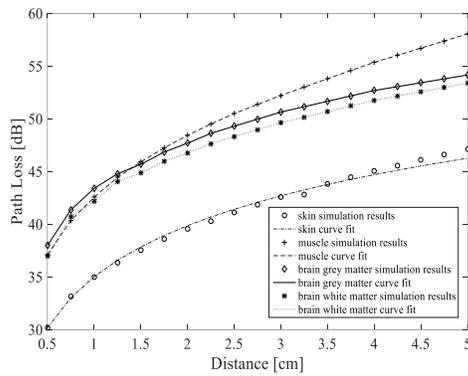
Fig. 6. PL versus separation distance between antennas for homogeneous tissues.
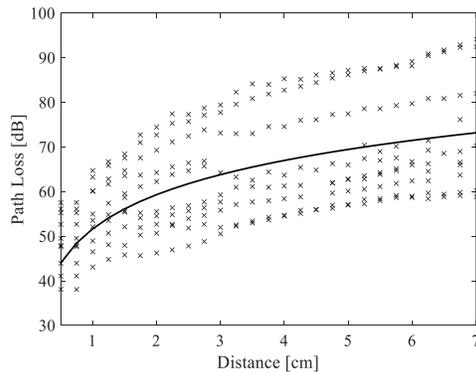
Fig. 7. PL versus distance between antennas for heterogeneous human body model.

C. Human tissues safety

As the human head is an extremely sensitive environment with tissues absorbing electromagnetic power from the antenna [19], safety is paramount. Therefore, we undertook numerical SAR calculations for comparison to latest regulatory authority provisions. For example, the IEEE standard regulates the SAR averaged over 10g of tissue to no more than 1.6 W per kg in the shape of a cube [21]. The ICNIRP regulations state that the limit of the average SAR of 10g contiguous tissue should be less than 2 W per kg [22].

It can be seen from Fig. 8 that the maximum SAR 10g W per kg changes with the distance. SAR values have been calculated by moving the Rx antenna position in the human head. The maximum value is 0.14 W per kg at the nearest point of skin tissue and the lowest SAR value is 0.045 W per kg at a distance of approximately 2 cm from the reference point.

Figure 9 presents the relationship between absorbed that the maximum power is 3.8 mW at the reference point while the minimum value of 1.9 mW occurs between 2 and 2.5 cm from the reference point. These SAR and absorbed power results reveal that the antenna design and simulation methods are suitable and meet the safety requirements of the ICNIRP and IEEE standards [21, 22].
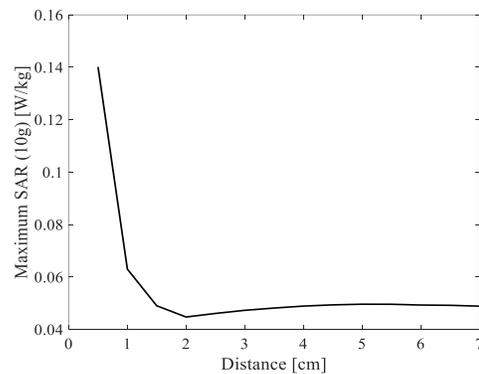
Fig. 8. Influence of the distance on the maximum SAR over 10g.
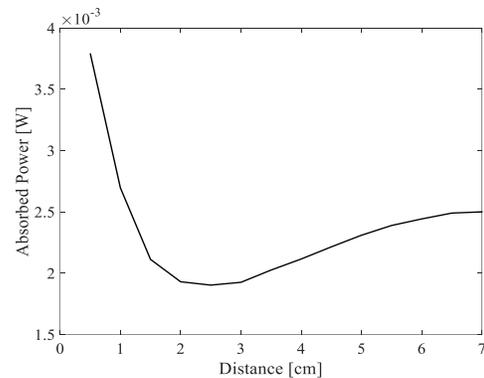
Fig 9. The absorbed power versus antennas separation distance.

IV. SHADOW FADING CHANNEL MODELING AND SYSTEM MARGIN

It is difficult to analytically derive the probability density function of the combined SNR at the receiver output. Therefore, we employ an approximation based on curve fitting and the results are shown by the solid line on Fig. 7 based on the least square error [44]. As can be seen from that figure, there is a large fluctuation in the simulated path loss values around the fitted mean path loss. The fluctuation of the simulated path loss is mainly due to the shadowing effect of the different brain tissues. The shadowing is induced by the diffraction in the shadowed regions of the body [45-46].

Since body motions are not considered in this paper, a static human body model is assumed. Shadowing can be regarded as directly resulting in the variations of the received signal at the receiver front-end. The amplitude variation caused by shadowing is often defined as the difference between calculated path loss values and the mean path loss. The mean PL is denoted by PL_{dB}^{ave}, which based on the empirical power decay law is a potential PL model for fitting to the calculated results [6, 16, 24, 44]:

$$PL_{dB}^{ave}(d) = \alpha + 10n \, \log_{10}\left(\frac{d}{d_{ref}}\right), d \geq d_{ref}, \quad (2)$$

where α is the PL at the reference point (0.5 cm) andequals 43.95 dB; the PL exponent n is here 2.552.

The shadow fading effect S can be derived from Equations (1) and (2):

$$S_{dB} = PL_{dB}(d) - PL_{dB}^{ave}(d). \quad (3)$$

The in-body communication channel might have a different PL since the surrounding environments may vary with the location of the receiver in practice. However, the majority of published PL models do not take this particular situation into account [1-3, 16]. A log-normal shadowing model is appropriate when dealing with a more realistic situation and the shadow fading S follows a lognormal distribution, which can be expressed as [13, 44, 46-47]:

$$p(S) = \frac{1}{\sqrt{2\pi}\sigma S} exp\left[-\frac{(\log_{10}(S)-\mu)^2}{2\sigma^2}\right], \quad (4)$$

where S has mean μ and standard deviation σ. Here, we take $\mu = 0$ and $\sigma = 1.079$. The average BER of the human head shadow fading channel can be expressed as [13, 19]:

$$P_b(\bar{\gamma}) = \int_0^\infty P_0(\gamma)P(\gamma)d\gamma, \quad (5)$$

where $\bar{\gamma}$ is the mean signal-to-noise ratio, $P_0(\gamma)$ denotes the BER performance of the additive white Gaussian noise (AWGN) channel, and $P(\gamma)$ is the probability density function of γ which follows a lognormal distribution with the same standard deviation as the BER performance for this shadow fading channel using BPSK and binary orthogonal PAM using the MIDA model is shown in Fig. 10.

In common with previous work on in-body communication systems [16, 18], to provide acceptable quality for communication, the predetermined threshold

BER is set as 10^{-3} for both BPSK and binary orthogonal PAM optimum receivers [15-17, 44]. With this value of BER, it can be seen from Fig. 10 that the minimum required SNR_{min} of binary orthogonal PAM is around 10.5 dB, while for BPSK it is nearly 17 dB.
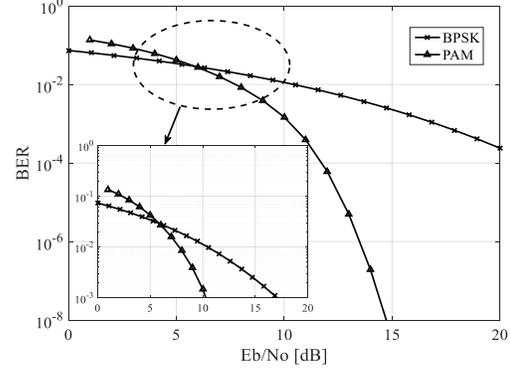
Fig. 10. SNR versus BER under the MIDA human head model fading channel under the BPSK and binary orthogonal PAM modulation schedules.

It is then necessary to take into account the wireless communication systems link budget. According to the existing literature [3, 4, 9, 45], AWGN noise at the receiver side is the only noise source which needs to be considered, basically representing thermal noise. The one-sided power spectral density of the noise in Watts per Hertz (dimensionally equivalent to Joules) is given by:

$$N_0 = k[T_a + (N_F - 1)T_0], \quad (6)$$

where T_a and T_b are the noise temperature of the receiving dipole antenna and of the environment, respectively, k is the Boltzmann constant and N_F is the noise factor at the receiver side. This is defined via the noise figure in dB by:

$$N_{F,dB} = 10\log_{10}(N_F), \quad (7)$$

where the noise factor of an intra-body device is related to its noise temperature T_e by:

$$N_F = 1 + \frac{T_e}{T_0}. \quad (8)$$

We assume the temperatures of the Tx and Rx antennas are the same since they are both located in the human head. Noise temperature (thermal noise), which depends on the temperature of the intra-body device, thus can be seen as the same as T_0:

$$T_a = T_0, \quad (9)$$
$$T_0 = T_e. \quad (10)$$

The mean temperature of the human head over baseline is 36.56 °C (equal to 309K), with a standard deviation of 0.36 °C and a range from 36.16 °C to 37.02 °C [48]. Equation (6) can be rewritten in dB scale as:

$$N_{0,dB} = 10\log_{10}(kT_0) + N_{F,dB}. \quad (11)$$

The SNR in dB thus can be expressed as:

$$SNR_{dB} = P_{r,dBW} - 10\log_{10}(R_b) - N_{0,dB}, \quad (12)$$

where $P_{r,dBW}$ is the received power and R_b is the communication transmission data rate.

A system margin M_s [49] is introduced to evaluate the quality of the communication system channel; it is also an effective way of evaluating system performance when a predetermined BER (10^{-3}) is selected. This system margin M_s can be taken as:

$$M_s = SNR_{dB} - SNR_{min} \geq 0, \qquad (13)$$

where SNR_{min} is the minimal SNR value that promises a reliable communication transmission in the predetermined BER situation.

Figure 11 illustrates the achievable quality transmission distance at a number of data rates of 1 Mbps, 10 Mbps and 20 Mbps employing BPSK and binary orthogonal PAM modulation. It can be seen that the implanted communication link can achieve higher data rates at shorter distances. For BPSK, 20 Mbps can be reliably transmitted at a distance of around 4.5 meters and 10 Mbps can be transmitted at approximately 5.5 meters; using 1 Mbps extends the distance to more than 10 meters. The performance of PAM at those three transmission data rates can reach longer distances than BPSK, and 20 Mbps high speed data transmission rate can be conveyed for up to 8 meters.
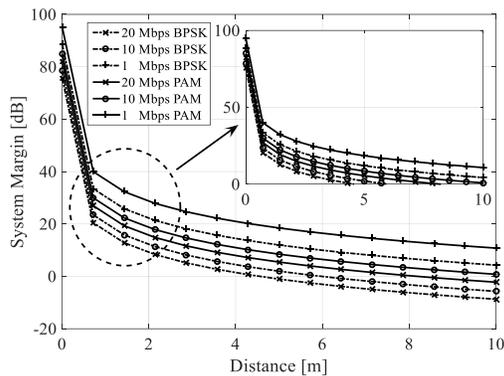
Fig. 11. System margin versus distance at different data rates.

V. CONCLUSION

Implanted WBAN technology is one of the most promising emerging applications in future healthcare services that allows a wide range of applications to function inside the human body. However, there is a limited amount of literature focused on the communication systems for within the human brain. In this paper, a communication link for the human cephalic area has been proposed for implant WBAN communications and analysed using the FDTD method. The BER performances have been obtained using binary orthogonal PAM and BPSK modulation, and the minimal required SNR values for predetermined BER conditions of 10^{-3} are 10.5 dB and 17 dB, respectively. The achievable

distances to deliver the target BER are greater with PAM than BPSK for both a higher data rate of 20 Mbps and a relatively lower data rate of 1 Mbps. The results show that a data rate of 20 Mbps to 8 meters can be covered using binary orthogonal PAM but only up to 4.5 meters when employing BPSK. These results point towards future work in the area of in-body cephalic area circuit design and experimental validation.

REFERENCES

[1]   T. Tuovinen, et al., "Effect of the antenna-human body distance on the antenna matching in UWB WBAN applications," in *7th Medical Information and Communication Technology (ISMICT) International Symposium*, Tokyo, Japan, pp. 193-197, 2013.

[2]   M. Seyedi, B. Kibret, D. T. Lai, and M. Faulkner, "A survey on intrabody communications for body area network applications," *IEEE Transactions on Biomedical Engineering*, vol. 60, no. 8, pp. 2067-2079, 2013.

[3]   S. Ullah, et al., "A comprehensive survey of wireless body area networks," *Journal of Medical Systems*, vol. 36, pp. 1065-1094, 2012.

[4]   S. Woo, J. Baek, D. Kang, J. Tak, and J. Choi, "A compact UWB MIMO antenna with enhanced isolation for WBAN applications," in *2014 International Symposium on Antennas and Propagation (ISAP)*, Kaohsiung, Taiwan, pp. 413-414, 2014.

[5]   K. Y. Yazdandoost, "UWB loop antenna for in-body wireless body area network," in *7th European Conference on Antennas and Propagation (EuCAP)*, Gothenburg, Sweden, pp. 1138-1141, 2013.

[6]   B. Choi, et al., "Narrowband physical layer design for WBAN system," in *2010 First International Conference on Pervasive Computing Signal Processing and Applications (PCSPA)*, Harbin, China, pp. 154-157, 2010.

[7]   A. Pantelopoulos and N. G. Bourbakis, "A survey on wearable sensor-based systems for health monitoring and prognosis," *IEEE Transactions on Systems, Man, and Cybernetics, Part C: Applications and Reviews*, vol. 40, no. 1, pp. 1-12, 2010.

[8]   C. Lee, et al., "Physical layer designs for WBAN systems in IEEE 802.15.6 proposals," in *9th International Symposium on Communications and Information Technology*, Incheon, Korea, pp. 841-844, 2009.

[9]   H. Wang, X. Tang, C. Choy, and G. Sobelman, "Cascaded network body channel model for intra-body communication," *IEEE Journal of Biomedical and Health Informatics*, Available online, Doi:10.1109/JBHI.2015.2448111, 2015.

[10] X. M. Chen, S. H. Pun, Y. M. Gao, P. U. Mak, M. I. Vai, and M. Du, "Study on transfer function of intra-body communication based on quasi-static electric field modeling," in *IEEE-EMBS International Conference on Biomedical and Health Informatics (BHI)*, Hong Kong, China, pp. 388-391, 2012.

[11] K. Takizawa et al., "Channel models for wireless body area networks," in *30th Annual International Conference of the IEEE Engineering in Medicine and Biology Society*, Vancouver, Canada, pp. 1549-1552, 2008.

[12] K. L. L. Roman, G. Vermeeren, A. Thielens, W. Joseph, and L. Martens, "Characterization of path loss and absorption for a wireless radio frequency link between an in-body endoscopy capsule and a receiver outside the body," *EURASIP Journal on Wireless Communications and Networking*, vol. 2014, pp. 1-10, 2014.

[13] D. Kurup, et al., "Simulation of path loss between biocompatible antennas embedded in homogeneous human tissues and comparison of their specific absorption rate," in *IEEE Antennas and Propagation Society International Symposium (APSURSI)*, Toronto, Canada, pp. 1-4, 2010.

[14] M. Pourhomayoun, Z. Jin, and M. L. Fowler, "Accurate localization of in-body medical implants based on spatial sparsity," *IEEE Transactions on Biomedical Engineering*, vol. 61, no. 2, pp. 590-597, 2014.

[15] B. Blaszczyszyn, M. K. Karray, and H. P. Keeler, "Wireless networks appear Poissonian due to strong shadowing," *IEEE Transactions on Wireless Communications*, vol. 14, no. 8, pp. 4379-4390, 2015.

[16] D. Kurup, W. Joseph, G. Vermeeren, and L. Martens, "In-body path loss model for homogeneous human tissues," *IEEE Transactions on Electromagnetic Compatibility*, vol. 54, no. 3, pp. 556-564, 2012.

[17] S. K. S. Gupta, Y. Prakash, E. Elsharawy, and L. Schwiebert, "Towards a propagation model for wireless biomedical applications," *Proc. IEEE Int. Conf. Commun.*, Anchorage, AK, pp. 1993-1997, 2003.

[18] D. Kurup, W. Joseph, G. Vermeeren, and L. Martens, "Specific absorption rate and path loss in specific body location in heterogeneous human model," *IET Microwaves, Antennas & Propagation*, vol. 7, no. 1, pp. 35-43, 2013.

[19] S. Wolf, D. Diehl, M. Gebhardt, J. Mallow, and O. Speck, "SAR simulations for high-field MRI: How much detail, effort, and accuracy is needed?," *Magnetic Resonance in Medicine*, vol. 69, no. 4, pp. 1157-1168, 2013.

[20] H. Homann, et al., "Local SAR management by RF shimming: A simulation study with multiple human body models," *Magnetic Resonance Materials in Physics, Biology and Medicine*, vol. 25, no. 3, pp. 193-204, 2012.

[21] "IEEE recommended practice for radio frequency safety programs, 3 kHz to 300 GHz," *IEEE Std. C95.7-2005*, pp. 1-52, 2006.

[22] International Commission on Non-ionizing Radiation Protection, "Guidelines for limiting exposure to time-varying electric and magnetic fields (1 Hz to 100 kHz)," *Health Physics*, vol. 99, no. 6, pp. 818-836, 2010.

[23] M. S. Uddin, N. B. Z. Ali, and N. H. Hamid, "Wave propagation and energy model for dynamic wireless body area networks," in *International Conference on Electrical, Control and Computer Engineering (INECCE)*, Kuantan, Malaysia, pp. 160-165, 2011.

[24] A. Kiourti and K. S. Nikita, "A review of implantable patch antennas for biomedical telemetry: challenges and solutions [Wireless Corner]," *IEEE Antennas and Propagation Magazine*, vol. 54, no. 3, pp. 210-228, 2012.

[25] T. Dissanayake, K. P. Esselle, and M. R. Yuce, "Dielectric loaded impedance matching for wideband implanted antennas," *IEEE Transactions on Microwave Theory and Techniques*, vol. 57, no. 10, pp. 2480-2487, 2009.

[26] K. Y. Yazdandoost and R. Kohno, "UWB antenna for wireless body area network," in *Asia-Pacific Microwave Conference*, Yokohama, Japan, pp. 1647-1652, 2006.

[27] A. Alomainy and H. Yang, "Modeling and characterization of biotelemetric radio channel from ingested implants considering organ contents," *IEEE Transactions on Antennas and Propagation*, vol. 57, no. 4, pp. 999-1005, 2009.

[28] M. L. Scarpello, et al., "Design of an implantable slot dipole conformal flexible antenna for biomedical applications," *IEEE Transactions on Antennas and Propagation*, vol. 59, no. 10, pp. 3556-3564, 2011.

[29] M. I. Iacono, et al., "MIDA: A multimodal imaging-based detailed anatomical model of the human head and neck," *PloS One*, vol. 10, no. 4, 2015.

[30] N. Cho, T. Roh, J. Bae, and H. J. Yoo, "A planar MICS band antenna combined with a body channel communication electrode for body sensor network," *IEEE Transactions on Microwave Theory and Techniques*, vol. 57, no. 10, pp. 2515-2522, 2009.

[31] J. Abadia, et al., "3D-spiral small antenna design and realization for biomedical telemetry in the

MICS band," *Radio Engineering*, vol. 18, no. 4, pp. 359-367, 2009.

[32] D. Porcino and W. Hirt, "Ultra-wideband radio technology: Potential and challenges ahead," *IEEE Communications Magazine*, vol. 41, no. 7, pp. 66-74, 2003.

[33] V. Vahrenholt, et al., "Fast EMC analysis of systems consisting of PCBs and metallic antenna structures by a hybridization of PEEC and MoM," *IEEE Transactions on Electromagnetic Compatibility*, vol. 52, no. 4, pp. 962-973, 2010.

[34] N. Neveu, et al., "Miniature hexaferrite axial-mode Helical antenna for unmanned aerial vehicle applications," *IEEE Transactions on Magnetics*, vol. 49, no. 7, pp. 4265-4268, 2013.

[35] F. Demuynck and M. Petersen, "Choosing the right EM simulation technology for antenna design and analysis," in *6th European Conference on Antennas and Propagation (EUCAP)*, Prague, Czech, pp. 1296-1300, 2012.

[36] https://www.cst.com/products/cstmws

[37] K. Kyung Sup, S. Ullah, and N. Ullah, "An overview of IEEE 802.15.6 standard," in *3rd International Symposium on*, *Applied Sciences in Biomedical and Communication Technologies (ISABEL)*, pp. 1-6, 2010.

[38] M. Iacono, et al., "A computational model for bipolar deep brain stimulation of the sub thalamic nucleus," in *36th Annual International Conference of the IEEE Engineering in Medicine and Biology Society*, Chicago, IL, pp. 6258-6261, 2014.

[39] E. Neufeld, et al., "Simulation platform for coupled modeling of EM-induced neuronal dynamics and functionalized anatomical models," in *7th International IEEE/EMBS Conference on Neural Engineering*, Montpellier, France, pp. 517-520, 2015.

[40] M. C. Gosselin, et al., "Development of a new generation of high-resolution anatomical models for medical device evaluation: The virtual population 3.0," *Physics in Medicine and Biology*, vol. 59, no. 18, pp. 5287, 2014.

[41] H. Y. Lin, M. Takahashi, K. Saito, and K. Ito, "Performance of implantable folded dipole antenna for in-body wireless communication," *IEEE Transactions on Antennas and Propagation*, vol. 61, no. 3, pp. 1363-1370, 2013.

[42] D. Kurup, W. Joseph, G. Vermeeren, and L. Martens, "Path loss model for in-body communication in homogeneous human muscle tissue," *Electronics Letters*, vol. 45, no. 9, pp. 453-454, 2009.

[43] G. Noetscher, Y. Xu, and S. Makarov, "Body area antenna link modeling using MATLAB engine," in *35th Antenna Applications Symposium*, Monticello, IL, pp. 20-22. 2011.

[44] D. Andreuccetti, R. Fossi, and C. Petrucci, "An internet resource for the calculation of the dielectric properties of body tissues in the frequency range 10 Hz-100 GHz," Online: http://niremf.ifac.cnr.it/tissprop/

[45] R. Chavez-Santiago, K. Sayrafian-Pour, A. Khaleghi, K. Takizawa, J. Wang, I. Balasingham, and H. B. Li, "Propagation models for IEEE 802.15.6 standardization of implant communication in body area networks," *IEEE Communications Magazine*, vol. 51, no. 8, pp. 80-87, 2013.

[46] G. D. Ntouni, A. S. Lioumpas, and K. S. Nikita, "Reliable and energy-efficient communications for wireless biomedical implant systems," *IEEE Journal of Biomedical and Health Informatics*, vol. 18, no. 6, pp. 1848-1856, 2014.

[47] M. Cheffena, "Performance evaluation of wireless body sensors in the presence of slow and fast fading effects," *IEEE Sensors Journal*, vol. 15, no. 10, pp. 5518-5526, 2015.

[48] B. Harris, P. Andrews, I. Marshall, T. Robinson, and G. Murray, "Forced convective head cooling device reduces human cross-sectional brain temperature measured by magnetic resonance: A non-randomized healthy volunteer pilot study," *British Journal of Anesthesia*, vol. 100, no. 3, pp. 365-372, 2008.

[49] D. B. Smith, D. Miniutti, L. W. Hanlen, D. Rodda, and B. Gilbert, "Dynamic narrowband body area communications: Link-margin based performance analysis and second-order temporal statistics," in *IEEE Wireless Communications and Networking Conference*, Sydney, Australia, pp. 1-6, 2010.
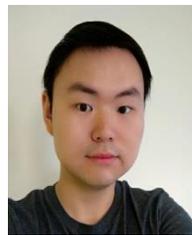
Yangzhe Liao received his B.S. degree in Measurement and Control Technology from the Northeastern University, China in 2013 where he was also an exchange student in the Electrical and Computer Engineering Department of the University of Illinois at Chicago during his final year. Currently he is a Ph.D. student in the School of Engineering, University of Warwick, UK. His research interests include Wireless body area networks, Mathematical modeling, Error correction and detection codes and communication systems, Multi-input Multi-output systems.

Mark S. Leeson received the degrees of B.Sc. and B.Eng. with First Class Honors in Electrical and Electronic Engineering from the University of Nottingham, UK, in 1986. He then obtained a Ph.D. in Engineering from the University of Cambridge, UK, in 1990. From 1990 to 1992 he worked as a Network Analyst for National Westminster Bank in London. After holding academic posts in London and Manchester, in 2000 he joined the School of Engineering at Warwick, where he is now a Reader. His major research interests are coding and modulation, nanoscale communications and evolutionary optimization. To date, Leeson has over 230 publications and has supervised fifteen successful research students. He is a Senior Member of the IEEE, a Fellow of Both the Institute of Physics and the UK Higher Education Academy.

Matthew D. Higgins received his M.Eng. in Electronic and Communications Engineering and Ph.D. in Engineering from the School of Engineering at the University of Warwick in 2005 and 2009 respectively. Remaining at the University of Warwick, he then progressed through several Research Fellow positions with leading defense and telecommunications companies before undertaking two years as a Senior Teaching Fellow. From July 2012 until February 2016, he was an Assistant Professor in the School of Engineering. As of March 2016, Higgins holds the position of Associate Professor in the Warwick Manufacturing Group (WMG), University of Warwick. His major research interests include the modelling of optical propagation characteristics in underwater, indoor and atmospheric conditions as well as investigating new areas such as nano-communications. Higgins is a Member of the IEEE.

An Efficient Algorithm for SAR Evaluation from Anatomically Realistic Human Head Model Using DGTD with Hybrid Meshes

Lei Zhao [1,2], Geng Chen [1], and Wenhua Yu [1]

[1] Center for Computational Science and Engineering, School of Mathematics and Statistics
Jiangsu Normal University, Xuzhou, China
leizhao@jsnu.edu.cn, gengchn@163.com, yuwenhua@jsnu.edu.cn

[2] State Key Laboratory of Millimeter Waves, Southeast University, Nanjing, China

Abstract ─ In this paper, an efficient and fast algorithm is proposed to analyze the specific absorption rate (SAR) in the anatomically realistic human head model with voxel data format exposed a handset antenna. The algorithm is based on the discontinuous Galerkin time-domain (DGTD) method with conformal region division and hybrid meshes. The proposed algorithm is done by dividing the computational domain into a sub-region with head model and a sub-region with handset antenna. As the realistic head model is voxel data format, the voxel-based meshes are used to divide the sub-region with head model. The tetrahedral meshes are used to divide the antenna, and are suitable for antennas with curved features and thin objects. And the pyramid meshes are used to connect voxel-based mesh and tetrahedral mesh regions. The accuracy and efficiency of the proposed algorithm are verified by comparing numerical results with analytical solutions.

Index Terms ─ Anatomically realistic human head model, discontinuous Galerkin time-domain (DGTD), hybrid meshes, specific absorption rate (SAR).

I. INTRODUCTION

Electromagnetic energy absorption in human body exposed to electromagnetic radiation has brought about tremendous concerns for the possible consequences of electromagnetic radiation on human health in the past few decades. Many studies have been performed for calculating the RF specific absorption rate (SAR) in a human body exposed to the electromagnetic (EM) field [1-4]. The uncertainty of the calculated SAR distribution exists and is contributed by a number of factors including the implementation of numerical algorithm, the modeling of radiating source and the human head model. In the late 1970s, the human body was approximated as the composition of homogenous prolate spheroids, ellipsoids and cylinders. Then, the layered tissue models consisting of a few tissue types with different dielectric properties were used to approximate the human anatomy. Recently, a number of realistic partial or whole body human models have been created. Those voxel models can be constructed from cross-sectional images generated by computer tomography (CT) or magnetic resonance imaging (MRI), and the feature size and the number of tissues, and resolution of the model play an important role in the SAR calculation.

For voxel human body models, the finite difference time domain (FDTD) [5] is widely used to analyze the SAR in head model exposed to antennas. However, the FDTD method with Yee grid suffers from serious accuracy degradation for dealing with the curved objects or treating curved material interfaces [6]. A number of finite difference methods have been proposed in the past for the treatment of curved interfaces or complex objects [7-9]. Indeed, the so-called stair-casing approximation may lead to local zeroth-order and at most first-order accuracy, which may also produce locally non-convergent results. DGTD algorithm has most of the advantages of FDTD. Besides and contains the adaptability of the unstructured meshes and spatial super-convergence, which allows us to effectively handle many practical electromagnetic (EM) problems where the required precision is different over the entire domain, or when the solution lacks smoothness [10-13]. For SAR evaluation, Hassan uses DGTD method to calculate SAR of human head with tetrahedral mesh in their paper, the head model contains four kinds of tissues [14].

In this paper, the electromagnetic scattering problem from a high resolution 3D anatomically realistic head model was considered. The DGTD with hybrid meshes is proposed to analyze the SAR in the anatomically realistic head model exposed to a handset antenna. In the proposed algorithm, the computational domain is divided into two sub-regions. One sub-region includes head model and voxel-based grids are used for the simulation. Another sub-region includes the antenna and the tetrahedral meshes are used to describe the antenna with curved features and thin objects. And the pyramid meshes are used to connect voxel-based mesh

with tetrahedral mesh regions. We have verified the accuracy and efficiency of the algorithm by comparing the numerical results with analytical results. Numerical results show that the proposed method has a better performance than the conventional techniques.

II. THEORY AND METHOD

A. Governing equations and DGTD formulation

We consider the time-domain Maxwell equations in three space dimensions for heterogeneous linear isotropic media:

$$\varepsilon \frac{\partial \mathbf{E}}{\partial t} = \nabla \times \mathbf{H} - \sigma \mathbf{E} + \mathbf{J} , \tag{1}$$

$$\mu \frac{\partial \mathbf{H}}{\partial t} = -\nabla \times \mathbf{E} , \tag{2}$$

where $\mathbf{E}(\mathbf{x},t) = (E^x, E^y, E^z)$, $\mathbf{H}(\mathbf{x},t) = (H^x, H^y, H^z)$ are the electric and magnetic fields, ε, μ, σ denote dielectric permittivity, magnetic permeability and conductivity respectively, and $\mathbf{J}$ represents the current density. This system of equations is supplemented with appropriate boundary conditions. Two different boundary conditions are involved in the examples considered in this work: perfect electrical conductor (PEC) and non-reflecting boundary. On the PEC surface, the tangential component of the electric field vanishes and the condition $\mathbf{n} \times \mathbf{E} = 0$ is applied, where $\mathbf{n}$ denotes the unit normal vector to the PEC surface. For problems posed on unbounded domains, the computational domain is truncated and a uniaxial perfectly matched layer (UPML) is imposed on the truncated boundary [13].

We first discretize the computational domain Ω into a set of elements τ_i and,

$$\Omega \approx \Omega_h = \bigcup_{i=1}^{N_h} \tau_i . \tag{3}$$

For each element τ_i, the local electric and magnetic fields $\mathbf{E}_i$ and $\mathbf{H}_i$ are expressed as linear combination of linearly independent vector Φ_{il} ($1 \le l \le 3d_i$):

$$\mathbf{E}_i(\mathbf{x},t) = \sum_{l=1}^{3d_i} E_{il}(t) \Phi_{il}(\mathbf{x}) , \tag{4}$$

$$\mathbf{H}_i(\mathbf{x},t) = \sum_{l=1}^{3d_i} H_{il}(t) \Phi_{il}(\mathbf{x}) , \tag{5}$$

where d_i is the local number of degrees of freedom and associates to the interpolation degree of p_i, and E_{il}, H_{il} denote the nodal values of $\mathbf{E}_i$ and $\mathbf{H}_i$, respectively. The global solution of Maxwell's Eqs. (1)–(2) is given by:

$$\mathbf{E}(\mathbf{x},t) \approx \mathbf{E}_h(\mathbf{x},t) = \bigoplus_{i=1}^{N_h} \mathbf{E}_i(\mathbf{x},t) , \tag{6}$$

$$\mathbf{H}(\mathbf{x},t) \approx \mathbf{H}_h(\mathbf{x},t) = \bigoplus_{i=1}^{N_h} \mathbf{H}_i(\mathbf{x},t) . \tag{7}$$

To avoid any ambiguity, we introduce the following notations:

$$(\Phi_{il})_{1 \le l \le 3d_i} = \left[\begin{pmatrix} \varphi_{i1} \\ 0 \\ 0 \end{pmatrix}, \begin{pmatrix} 0 \\ \varphi_{i1} \\ 0 \end{pmatrix}, \begin{pmatrix} 0 \\ 0 \\ \varphi_{i1} \end{pmatrix}, \cdots, \begin{pmatrix} \varphi_{id_i} \\ 0 \\ 0 \end{pmatrix}, \begin{pmatrix} 0 \\ \varphi_{id_i} \\ 0 \end{pmatrix}, \begin{pmatrix} 0 \\ 0 \\ \varphi_{id_i} \end{pmatrix} \right] , \tag{8}$$

$$(E_{il})_{1 \le l \le 3d_i} = \left(E_{i1}^x, E_{i1}^y, E_{i1}^z, \cdots, E_{id_i}^x, E_{id_i}^y, E_{id_i}^z \right) , \tag{9}$$

and similarly for the sequence $(H_{il})_{1 \le l \le 3d_i}$.

Multiplying Eqs. (1)-(2) by the test function Φ, we get:

$$\int_{\tau_i} \varepsilon \frac{\partial \mathbf{E}}{\partial t} \cdot \Phi d\mathbf{x} = \int_{\tau_i} \nabla \times \mathbf{H} \cdot \Phi d\mathbf{x} - \int_{\tau_i} \sigma \mathbf{E} \cdot \Phi d\mathbf{x} , \tag{10}$$

$$\int_{\tau_i} \mu \frac{\partial \mathbf{H}}{\partial t} \cdot \Phi d\mathbf{x} = \int_{\tau_i} -\nabla \times \mathbf{E} \cdot \Phi d\mathbf{x} . \tag{11}$$

Integrating by part Eqs. (10)-(11), we have:

$$\int_{\tau_i} \varepsilon \frac{\partial \mathbf{E}_h}{\partial t} \cdot \Phi d\mathbf{x} = \int_{\tau_i} \nabla \times \Phi \cdot \mathbf{H}_h d\mathbf{x} - \int_{\partial \tau_i} \Phi \cdot (\mathbf{H}_h \times \mathbf{n}) ds - \int_{\tau_i} \sigma \mathbf{E}_h \cdot \Phi d\mathbf{x} , \tag{12}$$

$$\int_{\tau_i} \mu \frac{\partial \mathbf{H}_h}{\partial t} \cdot \Phi d\mathbf{x} = -\int_{\tau_i} \nabla \times \Phi \cdot \mathbf{E}_h d\mathbf{x} + \int_{\partial \tau_i} \Phi \cdot (\mathbf{E}_h \times \mathbf{n}) ds , \tag{13}$$

where $\mathbf{n}$ is the unit outward normal vector of faces on τ_i. In the DGTD method $\mathbf{E}_i$ and $\mathbf{H}_i$ on element boundary can be discontinuous across the boundary. For two distinct elements τ_i and τ_k in Ω_h, then let $a_{ik} = \tau_i \bigcap \tau_k$ be the common interface of τ_i and τ_k. Here we use the central flux, which is defined as follows:

$$\mathbf{E}_h \mid a_{ik} = \frac{\mathbf{E}_i \mid a_{ik} + \mathbf{E}_k \mid a_{ik}}{2}, \mathbf{H}_h \mid a_{ik} = \frac{\mathbf{H}_i \mid a_{ik} + \mathbf{H}_k \mid a_{ik}}{2} . \tag{14}$$

Evaluating the volume integrals and surface integrals in Eqs. (12)-(13) with central flux and re-integrating by parts, we can obtain:

$$\int_{\tau_i} \varepsilon \frac{\partial \mathbf{E}_h}{\partial t} \cdot \Phi d\mathbf{x} = \frac{1}{2} \int_{\tau_i} \nabla \times \Phi \cdot \mathbf{H}_h + \int_{\tau_i} \nabla \times \mathbf{H} \cdot \Phi d\mathbf{x} - \int_{\partial \tau_i} \Phi \cdot (\mathbf{H}_h \times \mathbf{n}) ds - \int_{\tau_i} \sigma \mathbf{E}_h \cdot \Phi d\mathbf{x} , \tag{15}$$

$$\int_{\tau_i} \mu \frac{\partial \mathbf{H}_h}{\partial t} \cdot \Phi d\mathbf{x} = -\frac{1}{2} \int_{\tau_i} \nabla \times \Phi \cdot \mathbf{E}_h + \nabla \times \mathbf{E} \cdot \Phi d\mathbf{x} + \frac{1}{2} \sum_{k \in v_i} \int_{\partial a_{ik}} \Phi \cdot (\mathbf{E}_h \times \mathbf{n}) ds . \tag{16}$$

Replace $\mathbf{E}_h$, $\mathbf{H}_h$ and Φ in Eqs. (15)-(16) by $(E_{il})_{1 \le l \le 3d_i}$, $(H_{il})_{1 \le l \le 3d_i}$ and $(\Phi_{il})_{1 \le l \le 3d_i}$, respectively, we can get an equivalent system:

$$M_i^\varepsilon \partial_t E_i = K_i H_i - \sum_{k \in v_i} S_{ik} H_k - D_i E_i , \tag{17}$$

$$M_i^\mu \partial_t H_i = -K_i E_i + \sum_{k \in v_i} S_{ik} E_k , \tag{18}$$

in which M_i^{ε} and M_i^{μ} are the symmetric positive definite mass matrices, K_i, S_{ik} and D_i are stiffness matrix, rectangular interface matrices and conduction matrix, respectively. They are defined as:

$$\left(M_i^{\varepsilon}\right)_{jl} = \int_{\tau_i} \Phi_{ij}^T \varepsilon_i \Phi_{il} d\mathbf{x} \qquad (1 \le j,l \le 3d_i), \quad (19)$$

$$\left(M_i^{\mu}\right)_{jl} = \int_{\tau_i} \Phi_{ij}^T \mu_i \Phi_{il} d\mathbf{x} \qquad (1 \le j,l \le 3d_i), \quad (20)$$

$$\left(K_i\right)_{jl} = \frac{1}{2}\int_{\tau_i} \Phi_{ij}^T \nabla \times \Phi_{il} + \Phi_{il}^T \cdot \nabla \times \Phi_{ij} d\mathbf{x} \left(1 \le j,l \le 3d_i\right), \quad (21)$$

$$\left(S_{ik}\right)_{jl} = \frac{1}{2}\int_{\tau_i} \Phi_{ij}^T \left(\Phi_{kl} \times \mathbf{n}_{ik}\right) ds \left(1 \le j \le 3d_i, 1 \le l \le 3d_k\right), \quad (22)$$

$$\left(D_i\right)_{jl} = \int_{\tau_i} \Phi_{ij}^T \sigma_i \Phi_{il} d\mathbf{x} \quad (1 \le j,l \le 3d_i). \quad (23)$$

The set of local system of ordinary differential equations for each τ_i can be formally transformed in a global system. We suppose that all electric and magnetic fields are gathered in a column vector $\mathbb{E}$ and $\mathbb{H}$ with size of $d = \sum_{i=1}^{N_h} d_i$. Then Eqs. (17)-(18) can be rewritten as:

$$\mathbb{M}_{\varepsilon} \frac{d\mathbb{E}}{dt} = \mathbb{K}\mathbb{H} - \mathbb{A}\mathbb{H} - \mathbb{B}\mathbb{H} - \mathbb{C}^E \mathbb{E} - \mathbb{D}\mathbb{E}, \quad (24)$$

$$\mathbb{M}_{\mu} \frac{d\mathbb{H}}{dt} = -\mathbb{K}\mathbb{E} + \mathbb{A}\mathbb{E} - \mathbb{B}\mathbb{E} + \mathbb{C}^H \mathbb{H}, \quad (25)$$

where $\mathbb{M}_{\varepsilon}$, $\mathbb{M}_{\mu}$ and $\mathbb{K}$ are $3d \times 3d$ block diagonal mass and stiffness matrices with diagonal blocks equal to M_i^{ε}, M_i^{μ} and K_i respectively. $\mathbb{A}$ is a block sparse matrix whose non-zero blocks are equal to S_{ik} when a_{ik} is an internal interface. $\mathbb{C}^E$ and $\mathbb{C}^H$ are the block diagonal matrices associated with boundary integral terms. $\mathbb{D}$ is a positive semi-definite block diagonal matrix with diagonal blocks equal to D_i.

The semi-discrete system Eqs. (24)-(25) is time integrated using a second order leap-frog scheme as:

$$\mathbb{M}_{\varepsilon} \left(\frac{\mathbb{E}^{n+1} - \mathbb{E}^n}{\Delta t / 2}\right) = \mathbb{S}\mathbb{H}^{n+\frac{1}{2}} + \mathbb{C}^E \mathbb{E}^n - \frac{1}{2}\mathbb{D}\left(\mathbb{E}^{n+1} + \mathbb{E}^n\right), (26)$$

$$\mathbb{M}_{\mu} \left(\frac{\mathbb{H}^{n+\frac{3}{2}} - \mathbb{H}^{n+\frac{1}{2}}}{\Delta t / 2}\right) = -\mathbb{S}^T \mathbb{E}^{n+1} + \mathbb{C}^H \mathbb{E}^n, \quad (27)$$

where $\mathbb{S} = \mathbb{K} - \mathbb{A} - \mathbb{B}$ and $\Delta t = t_n - t_{n-1}$ denotes the time step size. This algorithm is conditionally stable with a critical time step size proportional to h^{-1}. And the time step is determined by the smallest grid element as:

$$\Delta t \le \frac{2}{\sqrt{\rho\left(\left(\left(\mathbb{M}_{\mu}^{-1}\right)^{\frac{1}{2}}\right)^T \mathbb{S}\left(\mathbb{M}_{\varepsilon}^{-1}\right)^{\frac{1}{2}}\right)}}. \quad (28)$$

B. Hybrid meshes and basis functions

For the SAR calculation from anatomically realistic human head model exposed handset antenna, as shown in Fig. 1, a hybrid mesh approach [15, 16] is adopted in which an unstructured tetrahedral or pyramid mesh is used to discretize the sub-region containing the handset model, a structured Cartesian mesh is used to discretize the remainder of the computation domain containing the voxel head model. In three dimensions, the nodal distribution proposed in [10] for the tetrahedron and in [16] for the pyramid is used. A tensor product of one-dimensional Gauss-Lobatto points is used for hexahedron. Figure 2 shows the reference tetrahedron, pyramid and hexahedron with a nodal distribution corresponding to polynomial order $p = 2$.

For tetrahedron meshes, the basis function on reference element is described as:

$$\varphi_{i,j,k} = P_i^{0,0}\left(\frac{2x}{1-y-z}-1\right)\left(1-y-z\right)^i P_j^{2i+1,0}\left(\frac{2y}{1-z}-1\right) .(29)$$
$$\left(1-z\right)^j P_k^{2i+2j+2,0}\left(2z-1\right)\left(2z-1\right), i+j+k \le r$$

For pyramid meshes, the basis function on reference element is:

$$\varphi_{i,j,k} = P_i^{0,0}\left(\frac{x}{1-z}\right)P_j^{0,0}\left(\frac{y}{1-z}-1\right)\left(1-z\right)^{\max(i,j)} . (30)$$
$$P_k^{2\max(i,j)+2,0}\left(2z-1\right), 0 \le i,j \le r-k, k \le r$$

And the following basis function is used for hexahedron meshes:

$$\varphi_{i,j,k} = \psi_i(x)\psi_j(y)\psi_k(z), \quad (31)$$

where $\psi_i(x) = \frac{\prod_{i \ne j} x - \xi_j}{\prod_{i \ne j} \xi_i - \xi_j}$ is the Lagrange interpolation function.

With this approach, the benefits of using affine elements can be exploited, not only for tetrahedral but also for the hexahedral and pyramidal elements. Moreover, compared to tetrahedral meshes, the use of hexahedral meshes results in a significant reduction in the number of internal faces. It can be expected that hybrid meshes will lead to a reduction in the CPU time requirements, as the computational cost of integration over element faces is an important portion of the DGTD scheme.
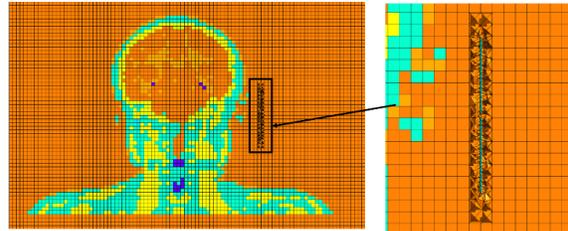
Fig. 1 Human head model exposed in dipole antenna.
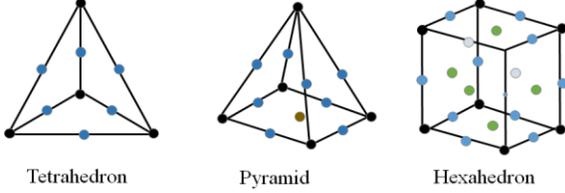
Fig. 2. Reference elements with showing the location of the nodes: (a) tetrahedron, (b) pyramid, and (c) hexahedron.

III. NUMERICAL RESULTS

To illustrate the accuracy and efficiency of the proposed DGTD with hybrid meshes, we first consider the EM propagation of a mode inside a perfect metallic cubic cavity. The cavity is a cube with a PEC boundary, the edge length of the cube is $1m$ with the center at $x = y = z = 0$. We evaluate the field at a test-point $x = y = z = -0.167m$. The propagative mode is given by following formulations:

$$E_x = 0,$$
$$E_y = 0,$$
$$E_z = \sin(m\pi x)\sin(m\pi x)\cos(\omega t),$$
$$H_x = \frac{1}{\omega\mu_0} n\pi \sin(m\pi x)\cos(m\pi x)\sin(\omega t), \quad (32)$$
$$H_y = \frac{1}{\omega\mu_0} m\pi \cos(m\pi x)\sin(m\pi x)\sin(\omega t),$$
$$H_z = 0.$$

The comparison of numerical results of the internal electric fields obtained by using DGTD with hexahedron mesh, the FDTD method and analytical results $(m = n = 2)$ is illustrated in Fig. 3, where the mesh size for DGTD and FDTD is $\lambda/10$. From Fig. 3, we clearly observe a very good agreement between the DGTD method and analytical results, which is much better than the FDTD results. We have also computed the electric fields at the observation point $x = y = z = -0.167m$ using DGTD with tetrahedron meshes and hybrid meshes, and the FDTD method with mesh size $\lambda/30$, as demonstrated in Fig. 4. Good agreements can be obtained between the GDTD results and analytic results. Comparing with analytic results, the FDTD method with mesh size $\lambda/30$ is much better than the FDTD results with mesh size $\lambda/10$, as shown in Fig. 3 and Fig. 4. However, the FDTD method with $\lambda/30$ cannot still get a good agreement with the analytic results. The detailed computational parameters such as mesh size, degrees of freedom, time step and computational time are listed in Table 1. The benefit of using hexahedron elements can be clearly seen in Table 1 by comparing the computational cost. The reason for the benefit obtained is that tetrahedral meshes possess more elements and

more internal faces than hexahedral meshes for a given number of degrees of freedom in DG framework. Meanwhile, the computation of numerical fluxes at internal faces represents an important part of the overall computational cost of the algorithm. For the EM problems from simple 3D geometries, the potential computational advantages of hexahedral elements can often be exploited. However, this is totally unfeasible for complex geometries. For this reason, it is a good choice to use hybrid meshes, employing tetrahedral elements near objects of complex geometrical shape, with affine hexahedral elements used to fill the remainder of the computational domain.
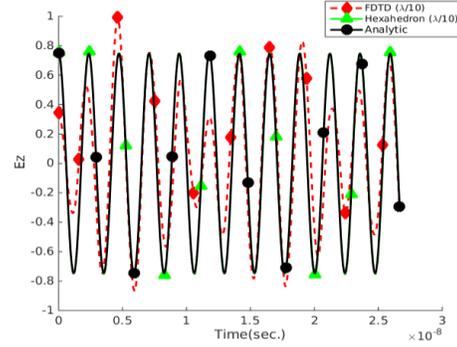
Fig. 3. Electric field distribution at point $x = y = z = -0.167m$.
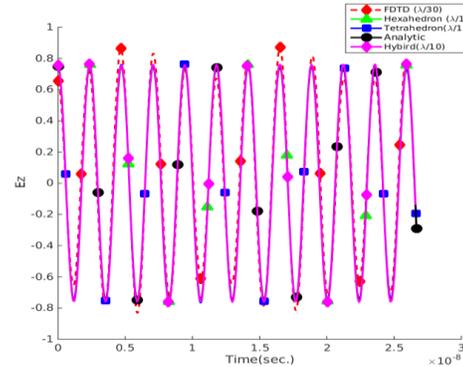
Fig. 4. Electric field distribution at point $x = y = z = -0.167m$.

Table 1: Mesh size, degrees of freedom, time step and computational time

Mesh Type	Mesh Size	Δt (s)	Dofs	CPU Time(s)
Tetrahedron	$\lambda/10$	0.021	18240	36.8
Hexahedron	$\lambda/10$	0.047	3375	1.2
Hybrid meshes	$\lambda/10$	0.028	5550	6.2
FDTD	$\lambda/10$	0.025	8000	0.2
FDTD	$\lambda/30$	0.01	216000	16.1

After verification of the accuracy and efficiency, we apply the proposed DGTD method with hybrid meshes to study the scattering problem from 3D anatomically realistic human head model exposed to a handset antenna, as shown in Fig. 5. The Chinese electromagnetic human model (CMODEL) used in the simulation setup is voxel format model, in which 15 different biological tissues can be identified, as shown in Fig. 6. The electromagnetic properties (ε_r and σ) of 15 different tissues in the model can be obtained from FCC directly [17], as listed in Table 2. The resolution of this model is 5 mm. The handset antenna is a half wave dipole working at 2.1 GHz, and the distance between head model and antenna is15 mm. To accurately describe the antenna, tetrahedral meshes are used for the sub-region containing the antenna. As the head model is voxel-based format, the hexahedral meshes are used to describe the sub-region containing the human head model. And two parts are connected by affine pyramid meshes.

As the dipole antenna has 15 degrees rotation, it is hard for the computational methods with cube grids to solve the problem. DGTD method with tetrahedral meshes is suitable to handle the EM problem from complex and thin objects. Figure 7 shows the return loss of the dipole antenna with 15 degree rotation, a good agreement can be obtained for different antenna postures.

To evaluate the performance of different elements employed for the numerical solution of the Maxwell's equations in three dimensions using a DGTD formulation, the tetrahedral and hybrid meshes are used to solve the EM problem of 3D anatomically realistic human head model exposed to an antenna, respectively. Table 3 shows the number of degrees of freedom and CPU time for solving the same problem with tetrahedral and hybrid meshes, where the mesh distributions are generated by using the same mesh size. It is observed that the reduction in number of degrees of freedom is translated into a corresponding reduction in computational cost. For an order of approximation p=2, hybrid elements provide the same accuracy as tetrahedral elements by reducing the CPU time by a factor of about 5, as shown in Table 3. Figure 8 shows the electric field distribution on the head surface, bone, brain and blood. The electric field distribution on slices of x=200 mm and y=170 mm is demonstrated in Fig. 7. The following definition of the point SAR value is used in this work [2]:

$$SAR = \frac{\sigma}{\rho}|\mathrm{E}|^2 , \tag{33}$$

where σ is the electric conductivity, ρ the density of the tissue, and E the computed electric field intensity. The SAR distribution is shown in Fig. 9.
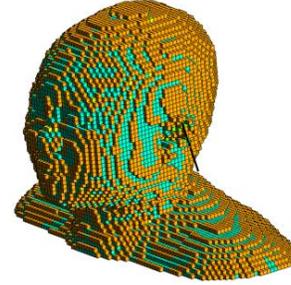
Fig. 5. CMODEL exposed to a dipole antenna working at 2.1 GHz.
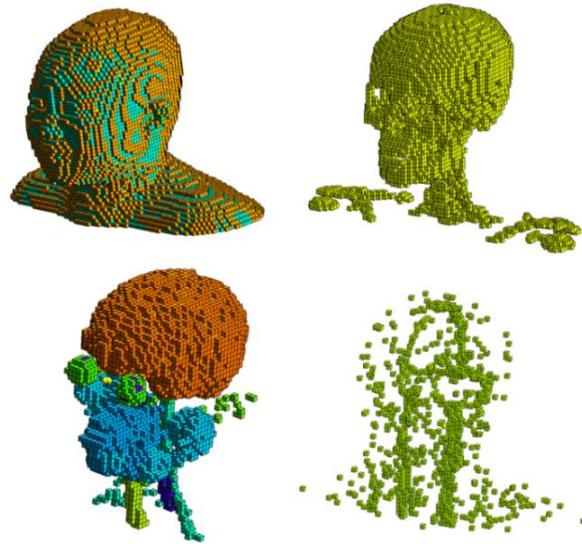
Fig. 6. CMODEL with 15 tissues.

Table 2: Dielectric properties of human head tissues at 2.1 GHz

Tissue	ε_r	σ
Skin	38.871857	1.184768
Fat	5.349368	0.078385
Muscle	55.335312	1.437796
Cartilage	40.215481	1.286782
Cerebro spinal fluid	68.638336	2.412575
Eye tissue	53.567787	1.601727
Vitreous humour	68.573364	2.032478
Lens nucleus	34.649647	0.787477
Grey matter	50.078876	1.391190
White matter	37.010921	0.914969
Spinal chord	32.530067	0.573612
Thyroid thymus	58.142151	1.500878
Tongue	53.567787	1.371193
Bone cancellous	19.343237	0.588224
Blood	59.372261	2.043690
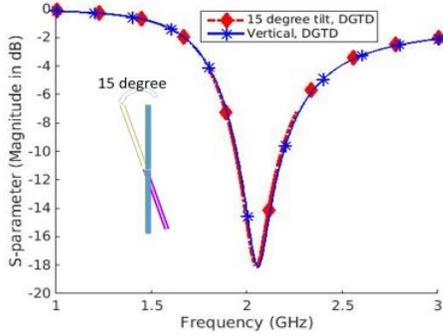
Fig. 7. Return loss for dipole antenna.

Table 3: Comparison of Dofs and computational cost with tetrahedron and hybrid meshes

Mesh Type	Δt (sec.)	Dofs	CPU Time(sec.)
Tetrahedron	0.53	24714168	60801
Hybrid Meshes	1.40	13355664	12819
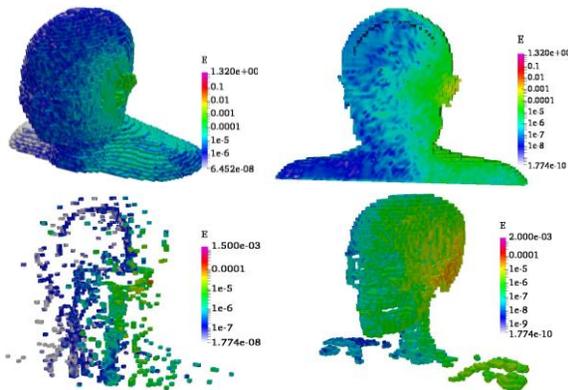
Fig. 8. Electric field distribution on tissues.
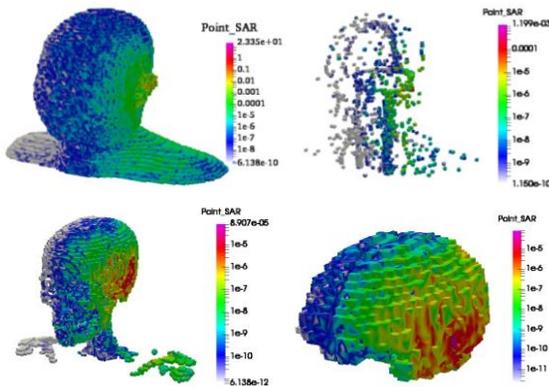
Fig. 9. Point SAR distribution.

IV. CONCLUSION

The efficiency of the DGTD method with hybrid mesh for the realistic human head SAR evaluation has been studied. Using an unstructured mesh around complex geometric objects, geometric flexibility is achieved. And computational efficiency is then improved by using a Cartesian mesh of affine hexahedra to fill the remainder of the domain.

REFERENCES

[1] A.-K. Lee, H.-D. Choi, and J.-I. Choi, "Study on SARs in head models with different shapes by age using SAM model for mobile phone exposure at 835 MHz," *IEEE Trans. Electromagnetic Compatibility*, vol. 49, pp. 302-312, 2007.

[2] A. Schiavoni, P. Bertotto, G. Richiardi, and P. Bielli, "SAR generated by commercial cellular phones-phone modeling, head modeling, and measurements," *IEEE Trans. Microwave Theory and Techniques,* vol. 48, pp. 2064-2071, 2000.

[3] L. Zhao and K.-L. Wu, "A Hybrid NFM/MoM full-wave analysis of layered proflate head model exposed to handset antenna," *Progress In Electromagnetics Research*, vol. 123, pp. 205-225, 2012.

[4] B. B. Beard, W. Kainz, T. Onishi, T. Iyama, S. Watanabe, O. Fujiwara, et al., "Comparisons of computed mobile phone induced SAR in the SAM phantom to that in anatomically correct models of the human head," *IEEE Trans. Electromagnetic Compatibility*, vol. 48, pp. 397-407, 2006.

[5] A. Taflove and S. Hagness, *Computational Electromagnetics: The Finite-Difference Time-Domain Method*, 3rd ed., Artech House, Norwood, MA, 2005.

[6] A. Ditkowski, K. Dridi, and J. S. Hesthaven, "Convergent Cartesian grid methods for Maxwell's equations in complex geometries," *Journal of Computational Physics*, vol. 170, pp. 39-80, 2001.

[7] T. Xiao and Q. H. Liu, "A staggered upwind embedded boundary (SUEB) method to eliminate the FDTD staircasing error," *IEEE Trans. Antennas and Propagation*, vol. 52, pp. 730-741, 2004.

[8] S. Chaillou, J. Wiart, and W. Tabbara, "A subgridding scheme based on mesh nesting for the FDTD method," *Microwave and Optical Technology Letters*, vol. 22, pp. 211-214, 1999.

[9] A. Yefet and P. G. Petropoulos, "A staggered fourth-order accurate explicit finite difference scheme for the time-domain Maxwell's equations," *Journal of Computational Physics*, vol. 168, pp. 286-315, 2001.

[10] J. S. Hesthaven and T. Warburton, "High–order nodal discontinuous Galerkin methods for the Maxwell eigenvalue problem," *Philosophical Transactions of the Royal Society of London A: Mathematical, Physical and Engineering Sciences*, vol. 362, pp. 493-524, 2004.

[11] G. Cohen, X. Ferrieres, and S. Pernet, "A spatial high-order hexahedral discontinuous Galerkin method to solve Maxwell's equations in time domain," *Journal of Computational Physics*, vol. 217, pp. 340-363, 2006.

[12] S. Pernet and X. Ferrières, "Hp a-priori error estimates for a non-dissipative spectral discontinuous Galerkin method to solve the Maxwell equations in the time domain," *Mathematics of Computation*, vol. 76, pp. 1801-1832, 2007.

[13] X. Ji, T. Lu, W. Cai, and P. Zhang, "Discontinuous galerkin time domain (DGTD) methods for the study of 2-D waveguide-coupled microring resonators," *Journal of Lightwave Technology*, vol. 23, pp. 3864, 2005.

[14] H. Fahs, A. Hadjem, S. Lanteri, J. Wiart, and M.-F. Wong, "Calculation of the SAR induced in head tissues using a high-order DGTD method and triangulated geometrical models," I*EEE Trans. Antennas and Propagation*, vol. 59, pp. 4669-4678, 2011.

[15] R. Sevilla, O. Hassan, and K. Morgan, "The use of hybrid meshes to improve the efficiency of a discontinuous Galerkin method for the solution of Maxwell's equations," *Computers and Structures*, vol. 137, pp. 2-13, 2014.

[16] M. Bergot, G. Cohen, and M. Duruflé, "Higher-order finite elements for hybrid meshes using new nodal pyramidal elements," *Journal of Scientific Computing*, vol. 42, pp. 345-381, 2010.

[17] https://transition.fcc.gov/oet/rfsafety/dielectric.html.
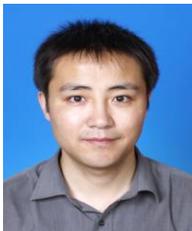
Lei Zhao joined the Jiangsu Normal University in September 2009. He is the Director of the Center for Computational Science and Engineering, and the Vice Dean of School of Mathematics and Statistics. He received the B.S. degree in Mathematics from Jiangsu Normal University, China, 1997, the M.S. degree in Computational Mathematics, and the Ph.D. degree in Electromagnetic Fields and Microwave Technology from Southeast University, China, in 2004 and 2007, respectively. From Aug. 2007 to Aug. 2009, he worked in Department of Electronics Engineering, The Chinese University of Hong Kong as a Research Associate. From Feb. 2011 to Apr. 2011, he worked in Department of Electronics and Computer Engineering, National University of Singapore as a research Fellow.

Zhao has published over 20 technical papers in PRE, APL, IEEE APM etc., international journals and conferences. His current research interests include computational electromagnetics, electromagnetic radiation to human's body, and numerical methods for partial differential equations.

Geng Chen received the B.S. degree and Master degree in Computational Mathematics from Jiangsu Normal University in 2012 and 2015, respectively. He is currently working at University of Illinois at Urbana-Champaign, USA, as a Research Assistant. His research interests include parallel-processing techniques, numerical methods, and software development.

Wenhua Yu joined the Jiangsu Normal University as a Distinguished Professor in May, 2014. He is the Director of the Jiangsu Key Laboratory for Education Big Data Science and Engineering. He worked at the Department of Electrical Engineering of the Pennsylvania State University and has been a Group Leader of the Electromagnetic Communication Lab between 1996 and 2013. He received his Ph.D. in Electrical Engineering from the Southwest Jiaotong University in 1994. He worked at the Beijing Institute of Technology as a Postdoctoral Research Associate from February 1995 to August 1996. He has published five books related to the FDTD method, parallel-processing techniques, software-development techniques, and simulation techniques, from 2003 to 2009. He has published over 150 technical papers and four book chapters. He founded the Computer and Communication Unlimited company, and serves as President and CEO. He is a Senior Member of the IEEE. His research interests include computational electromagnetic methods, software-development techniques, parallel-processing techniques, simulation and design of antennas, antenna arrays, and microwave circuits.

Assessment of the Electric Field Induced by Deep Transcranial Magnetic Stimulation in the Elderly Using H-Coil

Serena Fiocchi [1], Yiftach Roth [2], Abraham Zangen [2], Paolo Ravazzani [1], and Marta Parazzini [1]

[1] Consiglio Nazionale delle Ricerche
Istituto di Elettronica e di Ingegneria dell'Informazione e delle Telecomunicazioni, Milan, 20133, Italy
serena.fiocchi@ieiit.cnr.it, paolo.ravazzani@ieiit.cnr.it, marta.parazzini@ieiit.cnr.it

[2] Department of Life Sciences
Ben-Gurion University of the Negev, Be'er Sheva, 84105, Israel
yiftah@Brainsway.com, azangen@bgu.ac.il

Abstract ─ The recent advancements in the design of TMS coils to reach specific cortical and subcortical regions have allowed the treatment of various neuropsychiatric disorders, whose prevalence increases with age. This could be also due to the anatomical and morphological changes with age of the brain tissues, such as the atrophy that characterizes the elderly cortex. This study provides a description of the electric field, the main engine of the stimulation, distribution induced in specific cerebral tissues. That was performed by comparing, making use of computational electromagnetic techniques, the **E** distributions in two human models of different ages (34 and 84 years-old males), the older one showing cortical atrophy in the prefrontal lobe. The analysis of the parameters describing the spread of the electric field distribution shows that the H1 coil is able to induce in the prefrontal cortex an **E** amplitude higher than the neural threshold and with a widespread distribution in both models, with a slight prevalence on the younger one. On the contrary, the maximum **E** penetration depth and the consequent capability to reach deeper targets in the brain, is slightly higher for the elderly model.

Index Terms ─ Bioelectromagnetics, deep transcranial magnetic stimulation, elderly, H-coils, neuropsychiatric disorders.

I. INTRODUCTION

In the last few years, the possibility to approach the treatment of pathological conditions with noninvasive techniques of neurostimulation, such as transcranial magnetic stimulation TMS and transcranial direct current stimulation tDCS, has become more and more appealing to neuroscientists. In parallel, their use moved from the merely diagnosis of damage, to the therapy of many neuropsychiatric disorders and spinal injuries [1]-[8]. The efficacy of these techniques is associated to the induction of electric field (**E**), which acts by modulating the electrical activity of the target neural region of interest. That can take place in a direct way as in transcranial electrical stimulation, through electrodes placed over the skin close to the target of interest, or else in an indirect way as in the case of TMS, through coils placed in proximity to the scalp.

Lately, the knowledge of the role of different cortical and subcortical structures in the development of specific neuropsychiatric pathologies has moved the interest of researchers to develop new TMS coils able to stimulate deep brain structures rather than only the cortex, giving birth to the deep TMS (dTMS). For example, in the major depressive disorder (MDD), some functional neuroimaging studies have shown the presence of alterations in the prefrontal cortex (PFC) and in areas belonging to the reward circuit linked with the dorsal and ventral lateral PFC, i.e., the nucleus accumbens and the ventral tegmental area [9,10]. The dorsolateral prefrontal cortex (DLPFC) was found to be critically involved in both mood and reward mechanisms and was found to be dysfunctional in both MDD and substance-abuse patients [11]-[13]. Also, it was indicated, together with the hippocampus, as the dTMS target for the treatment of schizophrenia [13] and of dysthymic disorder [15]. The medial prefrontal cortex (MPFC) was identified as target region for the treatment of the post-traumatic stress disorder [16]. The role of the PFC in the regulation of mood and anxiety was confirmed by a study in which repetitive TMS of the right DLPFC was associated with disrupted PFC–amygdala connectivity [17]. Lastly, it is well known that midbrain and sub-thalamic structures are strictly involved in the progress of subcortical dementias, such as Parkinson disease

(PD), Huntington's disease and vascular dementia [18].

Many of these pathologies also affect elderly people, that present a prefrontal atrophy related to the age [19], and hence, in these patients, the capability to effectively reach deeper brain regions could be even more critical.

dTMS is administered by specific coils, designed at the precise scope to improve the penetration depth of the stimulation. Among those ones, the so-called Hesed family (H-) coils have been exploited in several studies [20]-[28] with significant outcomes. They have larger dimension with respect to the conventional TMS coils and a complex three-dimensional structure, which allows to minimize the non-tangential element in the coil and to slower the decay of electric field with distance.

Although these techniques are becoming more and more popular in neuroscience, little is known about the actual distribution of the **E** field induced within the cerebral tissues by dTMS coil configurations. Although some estimations of the induced **E** in dTMS have been performed in adult or in simplified models [30]-[33], so far, no investigation has addressed the issue of the **E** distribution in elderly people.

This study, therefore, addresses precisely this topic through a computational approach. In detail, we assessed, by using numerical electromagnetic techniques, the **E** distributions induced by a particular coil of the H-coil family (the H1 coil) in an anatomical head model of an 84 years old man with a pronounced age related prefrontal atrophy. Then it was compared with the **E** distribution in an adult male model, stimulated with the same coil configuration. The purpose is to investigate and quantify the **E** distributions in different brain regions in the elderly, with particular attention to the cerebral targets for the treatment of neuropsychiatric disorders, i.e., as stated above, the prefrontal cortex and related areas and the deeper tissues. The comparison with the stimulation of an adult head with identical coil configuration, will also allow exploring the change with age of the **E** distribution.

II. MATERIALS AND METHOD

A computational approach as implemented by the simulation platform SEMCAD X [34] was used to build the simulations and then to assess the distribution of the electric field **E** inside specific brain target tissues. In detail, we used the magneto quasi-static low-frequency solver to solve the Biot-Savart law. It is based on the scalar potential finite element (SPFE) method. Since in the low frequency band, the appropriate dimensions of the computational domain are smaller than the free space wavelength, the magnetic vector potential **A** is decoupled from **E**. Given here the dominance in the human body of the conduction currents, **E** can be calculated from the scalar potential Φ, which is given by:

$$-\nabla \cdot \sigma \nabla \Phi = j\omega \nabla \cdot (\sigma \mathbf{A}). \qquad (1)$$

Simulations were conducted over two realistic anatomical models of the Virtual Population [35]. They are based on high-resolution magnetic resonance (MR) images of two volunteers (a 34 and a 84 years-old male adult models, named "Duke" and "Glenn", respectively). Both models distinguish up to 84 tissues within the whole body and up to 20 different tissues at the head level. With the aim to analyse the induced **E** distributions inside specific brain target areas, in both human models, we identified the prefrontal cortex (PFC), and within this, the dorsolateral prefrontal cortex (DLPFC) and the medial prefrontal cortex (MPFC), and the deeper neuronal regions of the reward-related pathways such as amygdala, nucleus accumbens and ventral tegmental area (VTA), by comparison with MR images based brain atlas.

To all the tissues we assigned the dielectric properties based on data at low frequency collected by the studies of Gabriel and colleagues [36], [37].

A hexahedral uniform meshing algorithm at 1 mm of resolution, performed by the computational software [34], was used to discretize the computational domain, limited to the upper region of the body at the shoulder level.

Among the Hesed coils family [38], we chose the H1 coil, recently used in some dTMS studies ([20]-[29]) for the treatment of neuropsychiatric diseases. It is built on a complex three-dimensional structure, which is supposed to reach the deep brain tissues as well as to enhance the PFC stimulation. In detail, it is composed of 12 windings that form a base portion, a protruding return portion and a contacting return portion, indicated as α, β and γ respectively in Fig. 1.

The base portion (α) has a curved shape along its length axis in order to wrap the subject's scalp and it provides electrical current flow in a direction tangential to prefrontal and orbitofrontal regions [38]. The protruding (β) and the contacting (γ) return portions are arranged to carry returning current in a direction opposite to the one in the brain target area. The coil model was built to accommodate the anatomy of the head on which it is placed, as it happens during the experiments. The current flows clockwise and in the same direction in each winding. As to the coil positioning, we followed a procedure mimicking what is currently done in neurophysiological experiments making use of H-family coils for stimulating the PFC (see e.g., [13], [15], [22], [24]-[26], [28], [29]]). For both human models, the coil was first placed on the scalp and the coil current at a frequency of 5 kHz was adjusted in order to achieve a level of **E** equals to the 120 % of the motor threshold (i.e., in our case, 120 V/m, considering a threshold equals to 100 V/m) in the area of the motor cortex corresponding to the right hand abductor policies brevis (APB). The 100 V/m threshold (in the following identified as E_{th}) was chosen according to the accepted

range of threshold required for hand motor activation. Secondly, the coil was moved 5.5 cm anteriorly to reach the prefrontal cortex, as shown in Fig. 1 for the model Glenn. With the purpose to describe the **E** distribution amplitude, the results in the following section will be presented in terms of descriptive statistics of the **E** amplitudes (median, 25th and 75th percentiles, minimum and maximum) in different brain regions. Moreover we also calculated the spread of the distribution in the PFC, DLPFC and MPFC by identifying the percentage of volume of these brain regions where the **E** amplitude was equal or greater than 50%, 70%, 80%, 90% and 100% (in the following of the paper named as V50, V70, V80, V90 and V100) of E_{th} [30].

With the specific intent of quantifying the **E** penetration depth reached in the frontal lobe of the two human models, we calculated the maximum depth of the point in the prefrontal lobe in which the induced **E** amplitude was equal or greater than the 70% and the 100% of E_{th}. Briefly, we assumed a brain centre located in the midpoint between the two nuclei accumbens, to identify a direction of depth in the prefrontal lobe. Then, we calculated the maximum depth from the scalp, the cortex and the white matter of the closest point to this centre with an **E** amplitude equal to or greater than 70 or 100% E_{th} along the depth direction (i.e., the one passing through the brain centre mentioned above and the identified point) For a schematic representation see the following Fig. 5 (a).
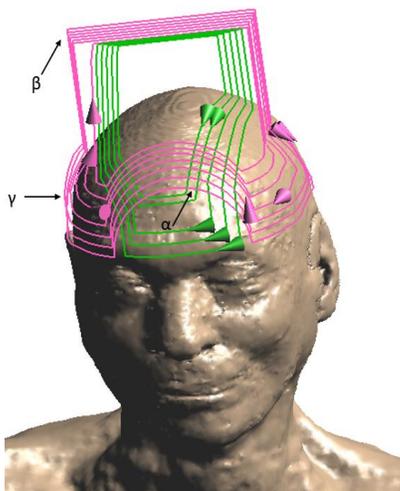
Fig. 1. Front view of H1 coil positioning on the head of model Glenn with the indication of the three portion described in the text: base portion (α), protruding return portion (β), and contacting portion (γ).

III. RESULTS

Figure 2 shows the descriptive statistic (25th, 50th, 75th percentile, minimum and maximum) of the **E** amplitude distributions induced in different brain

structures of the two human models. For both models, the maximum **E** was found in the DPFC and equal to 222.4 V/m and 186.3 V/m for Duke and Glenn, respectively. It is worth noting that, as expected, the maximum **E** amplitude has been found higher than the motor threshold E_{th} in various areas, e.g., over the cortex and the white matter and in all the regions of PFC.
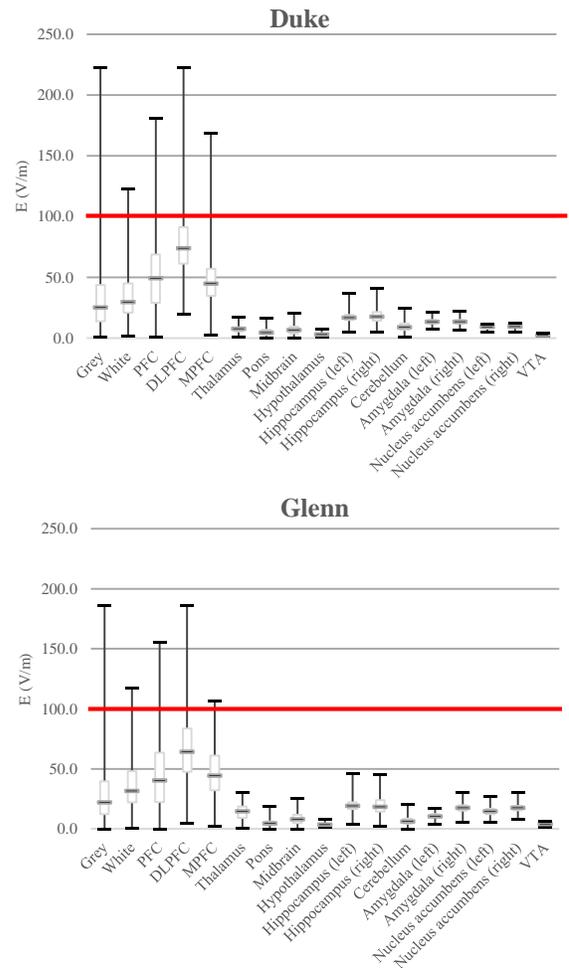
Fig. 2. Descriptive statistic of **E** amplitude in different brain regions for both models. Red line marks the level of the motor threshold E_{th}.

On the contrary, in the deeper regions, the maximum **E** amplitude remains always lower than the 50% of E_{th} (i.e., 50 V/m) in both models. The **E** amplitude values on the cortex, the white matter, the PFC and its specific regions (DLPFC and MPFC), are slightly higher in Duke than in Glenn both in terms of median and maximum values, with differences in percentage, across the tissues, ranging from 16.1% to 58.5 % in the maximum values and from 0.6% to 21.7% in the median values. On the contrary, the **E** amplitude levels in the deep regions are slightly higher in Glenn than in Duke, with a maximum

difference of 88.6% in the median values and up to 94% in the peak values, across the different deep brain structures.

Figure 3 shows an example of **E** amplitude distributions on two coronal slices of the brain (grey and white matter) of Duke (on the left) and of Glenn (on the right).
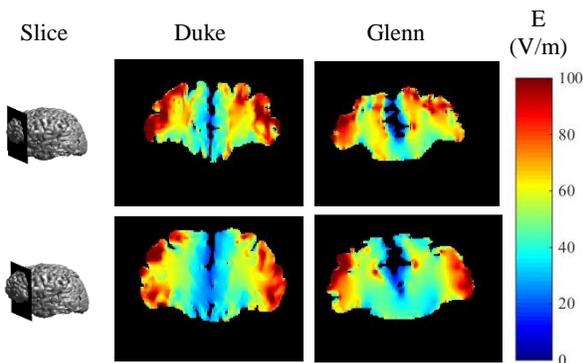
Fig. 3. Examples of **E** amplitude distributions on coronal slices of the brain of Duke (left) and of Glenn (right). The 1st column shows the coronal planes (taken 2 cm and 3 cm from the extremity of the PFC) where the sections were calculated. The colour bar is clamped to $E_{th}=100$ V/m.

The 1st column shows the coronal planes *(taken at 2 cm and 3 cm from the frontal extremity of the PFC)* where the sections were calculated. The colour bar is clamped at E_{th}. The panels clearly show that the H1 coil can induce an **E** amplitude value higher than E_{th} in a large part of the prefrontal cortex and in both hemispheres. Moreover, as one can note, it is also able to reach wider and deeper regions of the brain with E amplitude values greater than 50% of E_{th} in both human models. The different morphology of the brain, due to the different age, seems to affect both the focality and the amplitude of the distribution.

In order to better quantify the spread of the **E** amplitude distributions, Fig. 4 shows the percentages of volume (V50, V70, V80, V90 and V100) of PFC (left or right), DLPFC (left or right) and MPFC where the **E** amplitude is equal or greater than a certain percentage of E_{th} for both human models. The figure clearly shows that the H1 coil is able to induce **E** amplitude values above E_{th} in a not negligible percentage of volume of the DLPFC, where it can reach up to 21% of the volume in the left DLPFC of Duke. More broadly, comparing the two human models, these percentages are slightly higher in Duke's DLPFC (both left and right) and left PFC, the average percentage increasing across V50-V100 in Duke of the 7.0%, 16.3% and 7.8% in left PFC, left DLPFC and right DLPFC, respectively. On the contrary, in the right PFC and MPFC these percentages instead remain

quantitatively comparable between the two human models with an average increase of 1.4% and 1.3% in Duke right PFC and MPFC, respectively.
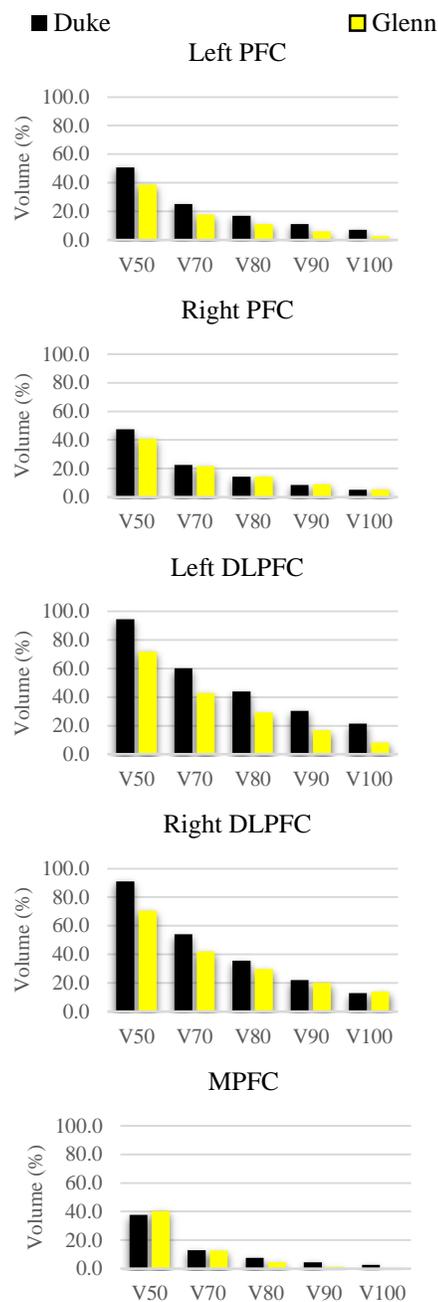
Fig 4. Percentages of volume of PFC, DLPFC, both divided in the two cerebral hemispheres, and MPFC with E amplitude equals or greater than 50% (V50), 70% (V70), 80% (V80), 90% (V90) and 100% (V100) of E_{th} for Duke (black) and Glenn (yellow).

Figure 5 summarizes the penetration depths calculated from the scalp, the cortex and the white matter

in the two models, with respect to the brain centre (in the figure a pictorial description of the brain centre identification is also shown). We can notice that in both models the H1 coil is able to penetrate the cortex to up to 3.9 cm with an **E** amplitude higher than the 70% of the neural threshold and up to 2.8 cm with an **E** amplitude above the neural threshold. Moreover, the H1 coil seems to be able to penetrate in the white matter with an **E** amplitude value above the neural threshold for approximately 2-2.5 cm. These penetration depths have been found always higher for Glenn.

(a)

(b)
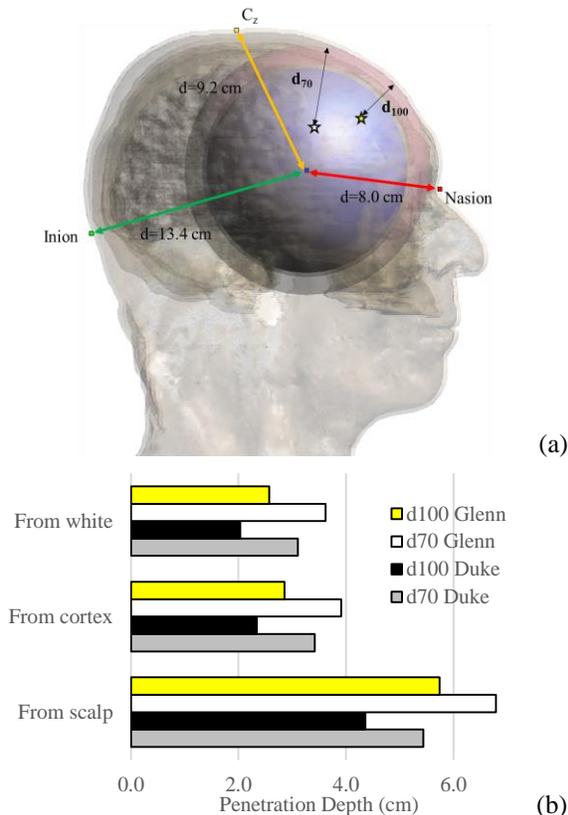
Fig. 5. (a) Pictorial representation of the penetration depth calculation from the surface of the scalp (taken as an example) over Glenn model. (b) Three-dimensional depth (cm) of the deepest point at 70% and at 100% of E_{th} (100 V/m) from the surface of the scalp, of the cortex and of the white matter of Duke and Glenn.

IV. DISCUSSION AND CONCLUSIONS

Although the recent application of dTMS for the treatment of neuropsychiatric disorders have attained significant outcomes, there is still a paucity of studies dedicated at a detailed description of the electric field distribution induced by coils specifically designed for dTMS. The very few studies that have recently addressed this topic [30]-[33], have used very simplified head models, such as spheres or have analysed just one

subject, mainly adult. In particular, no study has previously addressed the estimation of the **E** distributions in models of elderly people, for whom the presence of atrophy, due to the age, in the prefrontal area (one of the target of the stimulation for neuropsychiatric disorders), could modify the field distribution, and hence the treatment efficacy. In this study, we therefore have compared the **E** distributions in cerebral structures, typically target of dTMS by H-family coils, in two human models of 34 and 84 years old, respectively. The results of this study show that the maxima levels of the electric field are located mainly over the whole prefrontal cortex, the two dorsolateral prefrontal cortices and the medial prefrontal cortex, disregarding the age. These values can be noticeably higher than the motor threshold (see e.g., Fig. 2).

However, the anatomical variability affects directly both the levels of the fields in the PFC (Fig. 2), with a consistent decrease in the median and peak levels for the elderly model, and the field distribution (Fig. 3).

This could be due to the age related prefrontal atrophy that affects this latter model. Indeed, the distance between scalp and cortex equals to 20 mm in Duke against 29 mm in Glenn and the grey thickness in the prefrontal lobe is 3.1 mm in Duke, against 2.9 mm in Glenn. That age-effect is less evident if we compare the median levels over the entire cortex, it disappears in the white matter, and it reverses the trend in the subcortical regions, as a function of the reduction of the anatomical differences between the subjects.

The capability to reach deeper targets in the brain is higher for the elderly model, with an **E** amplitude below the 50% of the neural threshold (Fig. 2 and Fig. 5).

The maxima levels of **E** have been found in the two DLPFC, both in terms of field amplitude (Fig. 2) and spread of the distribution (Fig. 4), for both models. Indeed, almost the whole volume of DLPFC (90-94%, in the right and left DLPFC respectively) in the younger model and about the 70% in the older one, are above the 50% of E_{th} and a consistent volume across the models (10-20%) is above the neural threshold (see Fig. 4). These data could results of great interest in the clinical use of dTMS H1 coil, since those regions, as mentioned in the introductive section above, are strictly involved in the treatment of schizophrenia [14], dysthymia [15] and major depression [27]. The data about the spread (Fig. 4) show a slight effect of laterality in the stimulation of the DLPFC, with a prevalence for the left hemisphere (21% of the left DLPFC volume versus 13% of the right DLPFC volume above the neural threshold). This has been found in both models with a slight increase in the younger one. These results are in agreement with recent studies, which found the major depressive disorder associated with a decrease activity of the left DLPFC [39], [40].

As to the involvement of MPFC, Isseler and

colleagues [16] have indicated that cortical area as the target region for the treatment of post-traumatic stress disorder. Interestingly, our results show that the H1 coils is able to induce in about the 40% of the volume of this region an **E** amplitude above 50% of E_{th} in both models. Therefore, the use of H1 coil could be advisable for the stimulation of this target, disregarding the age.

Literature studies [16]-[18] have highlighted the possible involvement of some subcortical structures, such as amygdala, hippocampus, thalamus, nucleus accumbens and ventral tegmental area, in circuits related to the growth of depression disorders. Moreover, it is well known that the subthalamic area is strictly linked to the treatment of Parkinson disease and other dementias. Our results demonstrate that H1 coil can reach these structures with an amplitude field of about 25% E_{th}, with a slight prevalence on the older model. In line with this finding, we found a major capability to penetrate the cortex and the white matter with an amplitude field higher than the 70% and 100% of E_{th} in the old model (Fig. 5). This trend could be properly linked to the different anatomy between the two subjects (including the different scalp-grey distance and grey thickness mentioned above, as well as the head diameter and the cortical folding). In particular it could suggest that if on one side the prefrontal cortex atrophy of elderly people is responsible of lower E amplitude values on the cortex, on the other side it could facilitate the selectively reaching of brain regions below the grey and the white matter, improving the efficacy of this technique.

In conclusion, our study demonstrates that dTMS administered by H1 coil is capable to induced high levels of electric field **E** in typical target areas of neuropsychiatric disorders, disregarding the age of the subject. However, one should take into account that the levels of **E** slightly decrease in the elderly, although the depth of penetration of the induced filed increases. These results confirm that the description and the quantification in terms of amplitude, focality and penetration depth of the distribution of the **E** in different brain regions, as here presented, could be of great help in planning and optimizing the clinical protocols, and in evaluating the outcomes of therapeutic treatments of differently-aged patients.

REFERENCES

[1] P. M. Rossini, D. Burke, R. Chen, L. G. Cohen, Z. Daskalakis, R. Di Iorio, V. Di Lazzaro, F. Ferreri, P. B. Fitzgerald, et al., "Non invasive electrical and magnetic stimulation of the brain, spinal cord, roots and peripheral nerves: Basic principles and procedures for routine clinical and research application. An updated report from an I.F.C.N. Committee," *Clin. Neurophysiol.*, vol. 126, no. 6, pp. 1071-1107, 2015.

[2] A. V. Chervyakov, A. Y. Chernyavsky, D. O. Sinitsyn, and M. A. Piradov, "Possible mechanisms underlying the therapeutic effects of transcranial magnetic stimulation," *Front Hum. Neurosci.*, vol. 9, no. 303, (14 pp.), 2015.

[3] M. Hallett, "Transcranial magnetic stimulation: a primer," *Neuron.*, vol. 55, no. 2, pp 187-199, 2007.

[4] A. R. Brunoni, M. A. Nitsche, N. Bolognini, M. Bikson, T. Wagner, L. Merabet, et al., "Clinical research with transcranial direct current stimulation (tDCS): challenges and future directions," *Brain Stimul.*, vol. 5, no. 3, pp. 175-195, 2012.

[5] D. Meron, N. Hedger, M. Garner, and D. S. Baldwin, "Transcranial direct current stimulation (tDCS) in the treatment of depression: Systematic review and meta-analysis of efficacy and tolerability," *Neurosci. Biobehav. Rev.*, vol. 29, no. 57, pp. 46-62, 2015.

[6] M. Parazzini, S. Fiocchi, I. Liorni, E. Rossi, F. Cogiamanian, M. Vergari, A. Priori, and P. Ravazzani, "Modelling the current density generated by transcutaneous spinal direct current stimulation (tsDCS)," *Clinical Neurophysiology*, vol. 125, no. 11, pp. 2260-2270, 2014.

[7] J. Lüdemann-Podubecká, K. Bösl, S. Rothhardt, G. Verheyden, and D. A. Nowak, "Transcranial direct current stimulation for motor recovery of upper limb function after stroke," *Neurosci. Biobehav.*, vol. 47, pp. 245-259, 2014.

[8] C. Krishnan, L. Santos, M. D. Peterson, and M. Ehinger, "Safety of noninvasive brain stimulation in children and adolescents," *Brain Stimul.*, vol. 8, no. 1, pp. 76-87, 2015.

[9] P. O. Harvey, F. Van den Eynde, A. Zangen, and M. T. Berlim, "Neural correlates of clinical improvement after deep transcranial magnetic

stimulation (DTMS) for treatment-resistant depression: A case report using functional magnetic resonance imaging," *Neurocase.*, vol. 21, no. 1, pp. 16-22, 2015.

[10] E. J. Nestler, M. Barrot, R. J. Di Leone, A. J. Eisch, S. J. Gold, and L. M. Monteggia, "Neurobiology of depression," *Neuron.*, vol. 32, pp. 13-25, 2002.

[11] C. Rapinesi, M. Curto, G. D. Kotzalidis, A. Del Casale, D. Serata, V. R. Ferri, S. Di Pietro, et al., "Antidepressant effectiveness of deep transcranial magnetic stimulation (dTMS) in patients with major depressive disorder (MDD) with or without alcohol use disorders (AUDs): a 6-month, open label, follow-up study," *J. Affect Disord.*, vol. 174, pp. 57-63, 2015.

[12] T. Ye, J. Peng, B. Nie, J. Gao, J. Liu, Y. Li, G. Wang, X. Ma, K. Li, and B. Shan, "Altered functional connectivity of the dorsolateral prefrontal cortex in first-episode patients with major depressive disorder," *Eur. J. Radiol.*, vol. 81, pp. 4035-4040, 2012.

[13] L. Moreno-López, E. A. Stamatakis, M. J. Fernández-Serrano, M. Gómez-Río, A. Rodríguez-Fernández, M. Pérez-García, and A. Verdejo-García, "Neural correlates of the severity of cocaine, heroin, alcohol, MDMA and cannabis use in polysubstance abusers: A resting-PET brain metabolism study," *PLoS One*, vol. 7, no. 6, pp. e39830 (6 pp).

[14] Y. Levkovitz, L. Rabany, E. V. Harel, and A. Zangen, "Deep transcranial magnetic stimulation add-on for treatment of negative symptoms and cognitive deficits of schizophrenia: A feasibility study," *Int. J. Neuropsychopharmacol.*, vol. 14, no. 7, pp. 991-6, 2011.

[15] C. Rapinesi, G. D. Kotzalidis, D. Serata, A. Del Casale, F. S. Bersani, A. Solfanelli, P. Scatena, R. N. Raccah, R. Brugnoli, V. Digiacomantonio, P. Carbonetti, C. T. Fensore, R. Tatarelli, G. Angeletti, S. Ferracuti, and P. Girardi, "Efficacy of add-on deep transcranial magnetic stimulation in comorbid alcohol dependence and dysthymic disorder: Three case reports," *Prim Care Companion CNS Disord.*, vol. 15, no. 1, pp. 21, 2013.

[16] M. Isserles, A. Y. Shalev, Y. Roth, T. Peri, I. Kutz, E. Zlotnick, and A. Zangen, "Effectiveness of deep transcranial magnetic stimulation combined with a brief exposure procedure in post-traumatic stress disorder--a pilot study," *Brain Stimul.*, vol. 6, no. 3, pp. 377-383, 2013.

[17] P. Zwanzger, C. Steinberg, M. A. Rehbein, A. K. Bröckelmann, C. Dobel, M. Zavorotnyy, K. Domschke, and M. Junghöfer, "Inhibitory repetitive transcranial magnetic stimulation (rTMS) of the dorsolateral prefrontal cortex modulates early affective processing," *Neuroimage.*, vol. 101, pp. 193-203, 2014.

[18] M. Cantone, G. Di Pino, F. Capone, M. Piombo, D. Chiarello, B. Cheeran, G. Pennisi, and V. Di Lazzaro, "The contribution of transcranial magnetic stimulation in the diagnosis and in the management of dementia," *Clin. Neurophysiol.*, vol. 125, no. 8, pp. 1509-1532, 2014.

[19] Z. Nahas, X. Li, F. A. Kozel, D. Mirzki, M. Memon, K. Miller, K. Yamanaka, B. Anderson, J. H. Chae, D. E. Bohning, J. Mintzer, and M. S. George, "Safety and benefits of distance-adjusted prefrontal transcranial magnetic stimulation in depressed patients 55-75 years of age: A pilot study," *Depress Anxiety*, vol. 19, pp. 249-256, 2004.

[20] E. Onesti, M. Gabriele, C. Cambieri, M. Ceccanti, R. Raccah, G. Di Stefano, A. Biasiotta, A. Truini, A. Zangen, and M. Inghilleri, "H-coil repetitive transcranial magnetic stimulation for pain relief in patients with diabetic neuropathy," *Eur. J. Pain*, vol. 17, pp. 1347-1356, 2013.

[21] F. Spagnolo, M. A. Volonté, M. Fichera, R. Chieffo, E. Houdayer, M. Bianco, E. Coppi, A. Nuara, L. Straffi, G. Di Maggio, L. Ferrari, D. Dalla Libera, S. Velikova, G. Comi, A. Zangen, and L. Leocani, "Excitatory deep repetitive transcranial magnetic stimulation with H-coil as add-on treatment of motor symptoms in Parkinson's disease: An open label, pilot study," *Brain Stimul.*, vol. 72, pp. 297-300, 2014 .

[22] Y. Levkovitz, E. V Harel, Y. Roth, Y. Braw, D. Most, et al., "Deep transcranial magnetic stimulation over the prefrontal cortex: Evaluation of antidepressant and cognitive effects in depressive patients," *Brain Stimul.*, vol. 2, pp. 188-200, 2009.

[23] Y. Levkovitz , A. Sheer, E. V. Harel, L. N. Katz, D. Most, A. Zangen, and M. Isserles, "Differential effects of deep TMS of the prefrontal cortex on apathy and depression," *Brain Stimul.*, vol. 4, no. 4, pp. 266-74, Oct. 2011.

[24] M. Isserles, O. Rosenberg, P. Dannon, Y. Levkovitz, M. Kotler, F. Deutsch, B. Lerer, and A. Zangen, "Cognitive-emotional reactivation during deep transcranial magnetic stimulation over the prefrontal cortex of depressive patients affects antidepressant outcome," *J. Affect Disord.*, vol. 128, pp. 235-42, 2011.

[25] O. Rosenberg, N. Shoenfeld, A. Zangen, M. Kotler, and P. N. Dannon, "Deep TMS in a resistant major depressive disorder: a brief report," *Depress Anxiety.*, vol. 25, pp. 465-469, 2010.

[26] O. Rosenberg, Y. Roth, M. Kotler, A. Zangen, and P. Dannon, "Deep transcranial magnetic stimulation for the treatment of auditory hallucinations: A

preliminary open-label study," *Ann Gen Psychiatry*, vol. 10:3, 6 pp., 2011.

[27] E. V. Harel, L. Rabany, L. Deutsch, Y. Bloch, A. Zangen, and Y. Levkovitz, "H-coil repetitive transcranial magnetic stimulation for treatment resistant major depressive disorder: An 18-week continuation safety and feasibility study," *World J. Biol. Psychiatry*, vol. 15, pp. 298-306, 2014.

[28] F. S. Bersani, N. Girardi, L. Sanna, L. Mazzarini, et al., "Deep transcranial magnetic stimulation for treatment-resistant bipolar depression: A case report of acute and maintenance efficacy," *Neurocase*, vol. 19, pp. 451-457, 2013

[29] E. V. Harel, A. Zangen, Y. Roth, I. Reti, Y. Braw, et al., "H-coil repetitive transcranial magnetic stimulation for the treatment of bipolar depression: An add-on, safety and feasibility study," *World J. Biol. Psychiatry*, vol. 12, pp. 119-126, 2011.

[30] V. Guadagnin, M. Parazzini, S. Fiocchi, I. Liorni, and P. Ravazzani, "Deep transcranial magnetic stimulation: Modeling of different coil configurations," *IEEE Trans. Biomed. Eng.*, Epub ahead of print, Nov. 6, 2011.

[31] Y. Roth, A. Amir, Y. Levkovitz, and A. Zangen, "Three-dimensional distribution of the electric field induced in the brain by transcranial magnetic stimulation using figure-8 and deep H-coils," *Journal of Clinical Neurophysiology*, vol. 24, pp. 31-38, 2007.

[32] Z. D. Deng, S. H. Lisanby, and A. V. Peterchev, "Coil design considerations for deep transcranial magnetic stimulation," *Clin. Neurophysiol.*, vol. 125, pp. 1202-1212, 2014.

[33] Z. D. Deng, S. H. Lisanby, and A. V. Peterchev, "Electric field depth-focality tradeoff in transcranial magnetic stimulation: Simulation comparison of 50 coil design," *Brain Stimul.*, vol. 6, pp. 1-13, 2013.

[34] SEMCAD X, Version 14.8 by SPEAG, Schmid & Partner Engineering, AG, Zurich, Switzerland, www.speag.com

[35] A. Christ, W. Kainz, G. E. Hahn, K. Honegger, M. Zefferer, E. Neufeld, et al., "The virtual family-development of surface-based anatomical models of two adults and two children for dosimetric simulations," *Phys. Med. Biol.*, vol. 55, pp. N23-38, 2010.

[36] S. Gabriel, R. W. Lau, and C. Gabriel, "The dielectric properties of biological tissues: II. measurements in the frequency range 10 Hz to 20 GHz," *Phys. Med. Biol.*, vol. 41, pp. 2251-2269, 1996.

[37] C. Gabriel, A. Peyman, and E. H. Grant, "Electrical conductivity of tissue at frequencies below 1 MHz," *Phys. Med. Biol.*, vol. 54, pp. 4863-78, 2009.

[38] A. Zangen, Y. Roth, P. C. Miranda, D. Hazani, and M. Hallet, "Transcranial magnetic stimulation, systems and methods," U.S. Patent 0288365, Nov. 24, 2011.

[39] S. Grimm, J. Beck, D. Schuepbach, et al., "Imbalance between left and right dorsolateral prefrontal cortex in major depression is linked to negative emotional judgment: An fMRI study in severe major depressive disorder," *Biol. Psychiatry*, vol. 63, pp. 369-376, 2008.

[40] M. Garcia-Toro, J. M. Montes, and J. A. Talavera, "Functional cerebral asymmetry in affective disorders: new facts contributed by transcranial magnetic stimulation," *J. Affect Disord.*, vol. 66, pp. 103-109, 2001.

Stochastic Sensitivity in Homogeneous Electromagnetic-Thermal Dosimetry Model of Human Brain

Mario Cvetković [1], Sébastien Lalléchère [2], Khalil El Khamlichi Drissi [2], Pierre Bonnet [2], and Dragan Poljak [1]

[1] FESB, University of Split, Split, Croatia
(mcvetkov, dpoljak)@fesb.hr

[2] Institut Pascal, Université Blaise Pascal, Clermont-Ferrand, France
(sebastien.lallechere, drissi, pierre.bonnet)@lasmea.univ-bpclermont.fr

Abstract ─ In this work we examined how the variability in the brain morphology and the tissue properties affect the assessment of the homogeneous human brain exposed to high frequency electromagnetic (EM) field. Using the deterministic EM-thermal modeling and the stochastic theoretical basis we have studied the effects of these uncertainties on the maximum induced electric field, maximum local Specific Absorption Rate (SAR), average SAR, maximum temperature and the maximum temperature increase, respectively. The results show a good convergence of stochastic technique and an assessment of mean and variance of outputs for the incident plane wave of 900 MHz.

Index Terms ─ Bioelectromagnetism, electromagnetic-thermal model, sensitivity analysis, statistical dosimetry, stochastic collocation, surface integral equation approach.

I. INTRODUCTION

The exposure of a modern man to electromagnetic (EM) fields has raised some questions regarding the potentially harmful effects on the human health. This is, in particular, the case for the human head and brain exposed to high frequency (HF) radiation. The HF exposure assessment is based on the calculation of SAR distribution and the related temperature rise. As measurement of induced fields is not possible, human exposure assessment is carried out by using appropriate computational models. One difficulty of the modeling lies in the fact that values of the various model parameters can vary considerably due to, e.g., possible difference in individual size, but also due to different age (morphology) [1], or the general variability of electrical parameters such as permittivity and electrical conductivity [2], again, due to difference in age or sex. This uncertainty of the input parameters can result in the uncertainty of the dosimetric model outputs such as induced electric field and SAR. Thus, one of the key challenges that numerical dosimetry faces today is management of these uncertainties [3]. A novel approach to this problem, that is attracting more and more attention [4]-[7] is the so called stochastic dosimetry, combining deterministic electromagnetic techniques with the statistical methods.

The uncertainties that are discussed in this paper cover only a small subset of a huge variability apparent in the dosimetry literature due to variations in the exposure parameters and the anatomic variability of people [8], [9]. Review in [8] classified these differences due to the age dependent tissue dielectric properties, anatomically based models from children and adults of varying age and race, effects of pinna on SAR, distributions of SAR within the brain, and the effects of variability among models on SAR, respectively.

This paper presents the deterministic electromagnetic-thermal model coupled with the stochastic theoretical basis. The model is used to examine the effects of the variability in the brain morphology and the tissue properties on the dosimetric assessment in case of homogeneous human brain exposed to high frequency EM field. The sensitivity analysis of various parameters in this simplified model could thus aid in better formulation of a more realistic and computationally much more demanding models.

The paper is organized as follows. In the first part, description of the electromagnetic-thermal model proposed to compute SAR and temperature outputs is given. The following part gives details about the stochastic technique used jointly with previous model to propagate uncertainties. Finally, the numerical results for the case of brain exposed to radiation of vertically and horizontally polarized 900 MHz plane wave, respectively, are given with the corresponding statistical outputs.

II. DETERMINISTIC MODEL

A. Electromagnetic dosimetry model

The electromagnetic model is based on the surface integral equation (SIE) formulation [10], and, methodologically, represents a fresh perspective in the bioelectromagnetics area dominated mostly by the differential equation based methods such as FDTD (finite difference time domain). In addition to high accuracy, the advantages of the SIE formulation include: discretization of only boundary of the problem, hence reducing the dimensionality of the problem, it is suitable for open boundary problems (such as human head exposed to EM field), it gives exact solution to open boundary problem (no need to artificially limit the domain), does not suffer from staricasing errors related to FDTD, etc. Regardless of all these advantages, the integral equation approach has only recently begun its revival in the bioelectromagnetics community [11], [12].

It must be noted that the SIE formulation is only one way of transforming the original boundary value problem of Maxwell's equations into an integral equation form. The same problem could also be formulated using the volume integral equation (VIE), but then one loses the dimensionality reduction, in addition to having to deal with tensor-type integral equation and dyadic Green's functions. The choice of the particular integral technique will be primarily dependent on the domain problem type. Interested reader could find more details in [13], [14].

To set up the EM model, the human brain is considered as a lossy homogeneous dielectric material with complex permittivity and permeability (ε,μ), placed in a free space. The complex permittivity of the brain is given by:

$$\varepsilon = \varepsilon_0 \varepsilon_r - j\frac{\sigma}{\omega}, \quad (1)$$

while the value for the permeability of the brain is taken to be μ_0, i.e., the free space permeability, due to the fact that biological tissues do not posses magnetic properties. It is important to mention that human tissues have chiral characteristics, the property intrinsic to many biological molecules as well as human cells [15], meaning that the magnetic field will affect the electric flux and the electric field will affect the magnetic flux through material properties. But to the best of authors knowledge, there are no relevant study on this property for the human brain, hence, it was not taken into account.

The brain is exposed to a radiation of plane 900 MHz EM wave of power density of P=5 mW/cm². Using the equivalence theorem, two equivalent problems are formulated in terms of the equivalent electric and magnetic current densities placed on the surface of the brain. After the application of boundary condition at the surface S being interface of the two equivalent problems, the coupled set of integral equations is obtained:

$$j\omega\mu_i \int_S \vec{J}(\vec{r}')G_i dS' - \frac{j}{\omega\varepsilon_i}\nabla\int_S \nabla'_S \cdot \vec{J}(\vec{r}')G_i dS' + \nabla\times$$

$$\int_S \vec{M}(\vec{r}')G_i dS' = \begin{cases} \hat{n}\times\vec{E}^{inc}; & i=1 \\ 0 & ; i=2 \end{cases}, \quad (2)$$

where $\vec{E}^{inc}$ is the known incident field, $\vec{J}$ and $\vec{M}$ represent the unknown surface currents, while i is index of medium. The equivalent electric and magnetic currents $\vec{J}$ and $\vec{M}$ are expressed by the linear combination of RWG and $\hat{n}\times$RWG basis functions, respectively, defined on a pair of triangles.

The numerical solution of Eq. (2) is done via an efficient scheme of a method of moments (MoM) leading to a matrix type equation whose solution is a vector containing the unknown coefficients J_n and M_n. From these coefficients, the equivalent currents $\vec{J}$ and $\vec{M}$ can be determined from:

$$\vec{J}(\vec{r}) = \sum_{n=1}^N J_n\vec{f_n}(\vec{r}), \quad (3)$$

$$\vec{M}(\vec{r}) = \sum_{n=1}^N M_n\vec{g_n}(\vec{r}), \quad (4)$$

where $\vec{f_n}$ and $\vec{g_n}$ are known basis functions.

Subsequently, the electric field can be determined at an arbitrary point in brain using the following:

$$\vec{E}(\vec{r}) = -j\omega\mu\int_S \vec{J}(\vec{r}')G(\vec{r},\vec{r}')dS' - \frac{j}{\omega\varepsilon}\int_S \nabla'_S \cdot$$

$$\vec{J}(\vec{r}')G(\vec{r},\vec{r}')dS' - \int_S \vec{M}(\vec{r}')\times\nabla G(\vec{r},\vec{r}')dS'. \quad (5)$$

From the electric field distribution inside the brain, the specific absorption rate (SAR) is readily found using:

$$SAR = \frac{\sigma}{2\rho}\left|\vec{E}\right|^2, \quad (6)$$

where ρ is the brain tissue density given in kg/m³. SAR is latter used as input to the thermal part of the model.

B. Thermal dosimetry model

The experimental measurements of brain thermal response due to EM radiation is not possible in healthy humans. As indirect methods such as magnetic resonance imaging (MRI) lack sufficient resolution, and using animals as surrogate models raises the question of interspecies difference, the computational modeling seems to be the only alternative. It should be noted that the bioheat equation used for the kind of application presented here, has not been validated experimentally, and hence, presents forward only model.

The problem of determining the temperature distribution in the human brain is addressed using the finite element method (FEM). The steady-state temperature distribution in the brain, exposed to an incident time harmonic electromagnetic (EM) field, is governed by the stationary form of the Pennes' bioheat Equation [16]:

$$\nabla\cdot(\lambda\nabla T) + W_b c_b(T_a - T) + Q_m + Q_{ext} = 0, \quad (7)$$

where the heat generated due to metabolic processes is given by Q_m, W_b and c_b are the volumetric perfusion rate and the specific heat capacity of blood, respectively, λ is the thermal conductivity of the tissue, and T_a is the arterial

blood temperature. The last term in (7) represents the amount of heat generated due to absorption of EM energy in the tissue, and can be calculated from:

$$Q_{ext} = \rho \cdot SAR. \qquad (8)$$

The equation (7) is supplemented by the Robin boundary condition, while the heat loss due to radiation, and the forced convection are neglected. The finite element formulation of (7) is based on the weighted residual approach. The approximate solution of (7) is expanded in terms of the known basis functions and the unknown coefficients. After multiplying (7) by a set of weighting functions and integrating over the domain, after some work, we arrive to a suitable expression for the finite element method implementation:

$$\iiint_\Omega \lambda \nabla T \cdot \nabla N_j d\Omega + \iiint_\Omega W_b T N_j d\Omega +$$
$$\iint_{\partial\Omega} h_s T N_j dS = \iiint_\Omega (W_b T_a + Q_m + Q_{ext}) N_j d\Omega +$$
$$\iint_{\partial\Omega} h_s T_{amb} N_j dS. \qquad (9)$$

The processing part of the electromagnetic and the thermal dosimetry models was carried out using authors developed code.

C. The homogeneous human brain

Although the presented formulation could be used on a more detailed brain surface model built from an MRI, the source of the brain model was a freely available template from a Google Sketchup library. Assuming the dimensions of the average adult human brain are: width 131.8 mm, length 161.1 mm, height 139 mm, the frequency dependent parameters of the human brain are taken from [17]. The value for the relative permittivity and the electrical conductivity of the brain are given by ε_r=45.805 and σ=0.766 S/m, respectively, taken as the average values between white and gray matter at 900 MHz. Assuming each of the previous parameter may be impacted by random variations uniformly distributed, the following part will be dedicated to the propagation of uncertainties and discussion about numerical results.

III. STOCHASTIC MODELING

Complementary to solid deterministic modeling, stochastic techniques [1], [18] are helpful to precisely assess statistics of a given mapping and provide its sensitivity analysis.

A. Propagation of uncertainties

First, five random variables (RVs) are solely considered and devoted to the representation of parameters assumed as uncertain ones: brain's width (RV$_1$), length (RV$_2$), height (RV$_3$), relative dielectric permittivity ε_r (RV$_4$) and conductivity σ (RV$_5$). At this stage, and for the sake of simplicity, the RVs are loosely assumed to be independent and identically distributed (iid) following Uniform laws. Even though this point may be criticized, particularly related to morphing of

geometrical parameters, we may consider this as the first-order assumption. Indeed, there are solutions that easily integrate dependencies in stochastic collocation (SC) methods and the following methodology will still be valuable with iid-RVs. Assuming each RV$_k$ (k=1,...,5) is uniformly distributed around values from part II-C with common coefficient of variation (CV) equal to 5.77% [19], this first approach may offer a rapid estimation of potential importance of RVs. On the other hand, the study of a complete RV set is necessary, taking into account their interdependence, as is the case for morphological parameters [1].

B. Stochastic collocation theoretical basis

Among the different stochastic techniques available in the literature, the non-intrusive stochastic collocation (SC) method [18] was used in this dosimetric framework. The method is part of spectral approaches [20]. Similarly to strategies developed for Monte Carlo (MC) methods [21], the aim of these sampling techniques is to lead efficient experimental design (e.g., by decreasing the number of input samples needed). The basis of spectral techniques relies on a polynomial expansion of the considered output (e.g., u-th statistical moment of electric field, $[E]^u$) for given random parameters $(Z_1, Z_2, ..., Z_N)$ where each Z_k $(k = 1, ..., N)$ is defined from one given RV RV_k as:

$$Z_k = Z_k^0 + RV_k, \qquad (10)$$

where Z_k^0 is the initial (mean) value and RV_k is RV with assigned statistical distribution.

By assuming random parameter Z_k, the random output of interest $E(E \equiv [E]^u)$ is expanded over the stochastic space using the Lagrangian bases set [18]:

$$E(Z_k^0; t) = \sum_{i=0}^n E_i(Z_k^0) L_i(t), \qquad (11)$$

where $L_i(t)$ is Lagrange polynomial given by:

$$L_i(t) = \prod_{j=1, j\neq i}^n \frac{(t-t_j)}{(t_j-t_i)}. \qquad (12)$$

Utilizing the property of Lagrangian basis, yields:

$$E_i(Z_k^0) = E(Z_k^0; t_i). \qquad (13)$$

Applying the rules for the assessment of statistical moments on equation (10), the mean and the variance are easily derived, respectively:

$$[E(Z_k^0; t)]^1 = \sum_{i=0}^n \omega_i E_i(Z_k^0), \qquad (14)$$
$$[E(Z_k^0; t)]^2 = \sum_{i=0}^n \omega_i \{E_i(Z_k^0) - [E(Z_k^0); t]^1\}^2, \quad (15)$$

where ω_i is given by integral:

$$\omega_i = \int_D L_i(t) p(t) dt, \qquad (16)$$

where $p(t)$ denotes the probability density function of RV RV_k.

The order of approximation of the output E, i.e., the convergence, depends on number of collocation points t_i. The computation of integral (16) is carried out using Gaussian quadrature.

In a more general case, when extending the relations (14) and (15) to multi-RVs (e.g., case with N RVs), Lagrangian basis is used to approximate mapping $[E]^u$

as follows:

$$[E]^u(\mathbf{R}) = \sum_{v_1=0}^{n_1} \cdots \sum_{v_N=0}^{n_N} \eta_{v_1 \ldots v_N}^u \Phi^u(\mathbf{R}), \quad (17)$$

where $\mathbf{R} = (RV_1, RV_2, \ldots, RV_N)^T$ is called random vector (i.e., vector containing the N random parameters of the problem), $\Phi^u(\mathbf{R})$ is related to the chosen polynomial expansion, and $\eta_{v_1,\ldots,v_N}^u$ are the weights dedicated to SC points, respectively. Relation (17) implies $n_w + 1$ ($w = 1, \ldots, N$) SC points (SC n_w order expansion) to compute random component R_w in a straightforward manner.

For the interested reader, the developments and choice of Lagrangian polynomial basis are explained in [18], [22]. It is to be noticed that previous approach is proposed assuming the independence of random parameters. Similarly to alternative Unscented Transform (UT) sampling technique [23], taking into account correlation of RVs is possible throughout covariance matrix, and finally transform initial sigma points, keeping the same strategy as previously exposed. Computing statistical moments will be straightforward as depicted in relation (17).

C. Numerical results from 1-RV mean contributions

Using our deterministic EM model, the distribution of the electric field in our human brain model is determined, as shown in Fig. 1.
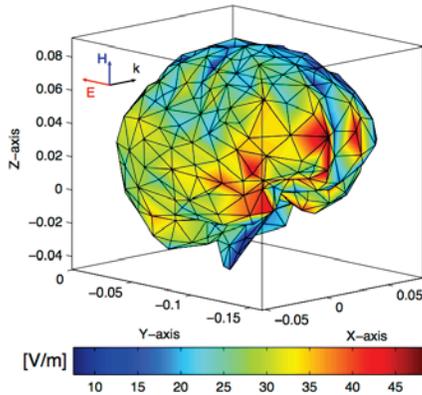
Fig. 1. Distribution of electric field on the brain surface. Horizontally polarized plane wave of frequency 900 MHz, power density P=5 mW/cm^2.

From the distribution of the electric field inside the brain, the SAR is determined next. The resulting SAR will cause a certain temperature increase, ΔT, determined using our thermal dosimetry model. As the incident wave's polarization presents an important role in the assessment of the electric field and the related SAR, all calculations were carried out for two polarizations of the incident plane wave: vertical and horizontal. Figures 2 and 3 show the results for the temperature rise in the human brain, due to horizontally and vertically polarized wave, respectively.
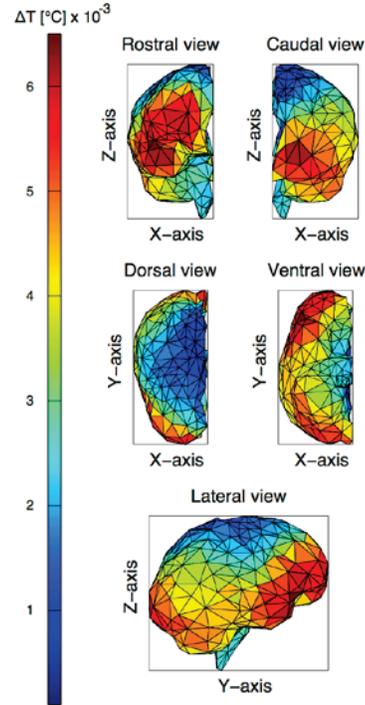
Fig. 2. Temperature rise in the human brain model due to incident 900 MHz horizontally polarized plane wave, power density P=5 mW/cm^2.
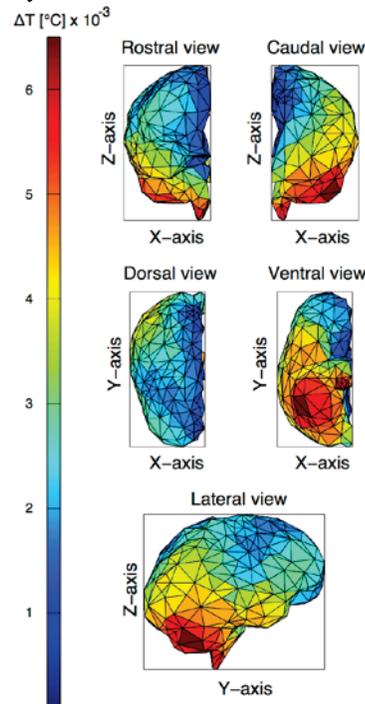
Fig. 3. Temperature rise in the human brain model due to incident 900 MHz vertically polarized plane wave, power density P=5 mW/cm^2.

Figure 4 shows the SC convergence of maximum electric field mean value for different RVs ($RV_k; k = 1, ...,5$) by taking into account the increasing number of points in SC experimental design (e.g., 3, 5, 7 points). Although the output (maximum SAR) is highly non linear, SC offers a precise assessment of its first statistical moment with 5 multi-physics simulations. It can be observed that the mean of the maximum E-field is between 48.8 and 49.8 V/m, indicating the importance of modeling RVs at the same time.
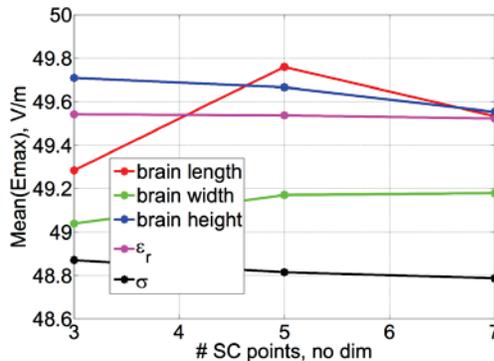
Fig. 4. Mean of maximum electric field in function of number of SC points (3, 5, 7) at frequency 900 MHz.

On the other hand, Fig. 5 shows the potential influence the individual random variables have on the variance of the maximum E-field. Similar to the case of mean assessment, the SC technique provides trustworthy results even with only 3 simulations.
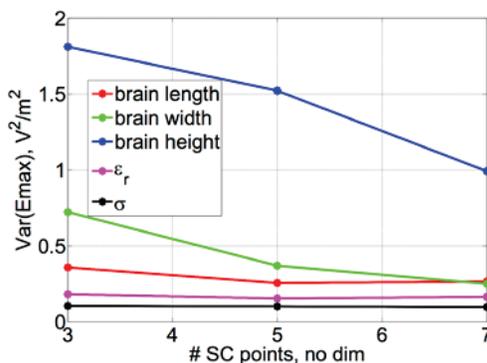
Fig. 5. Variance of maximum electric field in function of number of SC points (3, 5, 7) at frequency 900 MHz.

Similar to Figs. 4 and 5, the SC efficiency and convergence is assessed in Figs. 6 and 7 where mean and variance of a non-linear thermal parameter (temperature rise in brain) is given. A trustworthy result is obtained regarding independently each RV with only 3 full-wave

simulations.
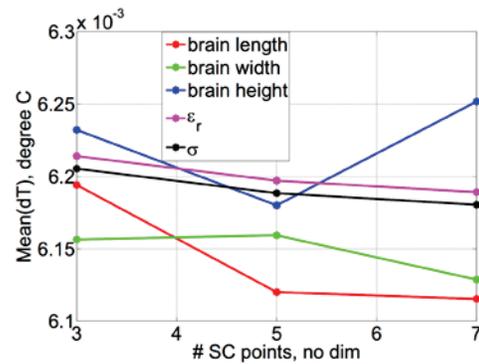
Fig. 6. Mean of temperature rise in function of number of SC points (3, 5, 7) at frequency 900 MHz.
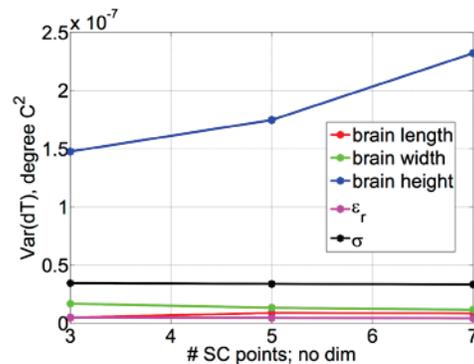
Fig. 7. Variance of temperature rise in function of number of SC points (3, 5, 7) at frequency 900 MHz.

In order to complement the preliminary results obtained with only 1-RV modeling, Tables 1 and 2 give an overview of the statistics obtained from a stochastic model including all RVs for both polarizations. Mean and variances obtained for each of the given outputs (maximum E-field, maximum SAR, averaged SAR, maximum temperature, temperature rise), considering a whole model including 5 RVs are presented. As expected, there are differences between the entire stochastic approach and 1-RV modeling. The experimental design chosen in this example is based upon 243 simulations (approaching each statistical moments using only 3 SC points for each RV, leading to 3^5=243 simulations). Of course, some alternative approaches are practicable but the crude tensor product (i.e. full-tensorized SC) given by relation (17) offers confidence related to the accuracy of the computed data. It should be noticed that the convergence of results has been checked (data not shown here) by using full-tensorized model with 5 SC points for each RV.

Table 1: SC results (mean/variance, var.) for given outputs (one may notice units are given for means; 1: maximum electric field in V/m, 2: maximum SAR in W/kg, 3: mean SAR in W/kg, 4: temperature in Celsius degrees, 5: temperature rise in Celsius degrees) for vertical (VV) polarization

Output	1	2	3	4	5
Output	49.9	0.9	0.16	37.1	6.1E-3
Var.($\times 10^4$)	37756	61.5	0.7	1.3	2.0E-3

Table 2: SC results (mean/variance, var.) for given outputs (one may notice units are given for means; 1: maximum electric field in V/m, 2: maximum SAR in W/kg, 3: mean SAR in W/kg, 4: temperature in Celsius degrees, 5: temperature rise in Celsius degrees) for horizontal (HH) polarization

Output	1	2	3	4	5
Output	48.7	0.9	0.17	37.0	7.3E-3
Var.($\times 10^4$)	23205	21.3	0.7	1.2	1.9E-3

D. Sensitivity analysis

A large diversity of techniques are available in [24] to assess the sensitivity analysis of various models. In the following, variance-based criteria are defined from SC data to assess the sensitivity of each random parameter (similarly to Sobol's first indices [24] but restricted to a qualitative evaluation). Indeed, for each given physical output j (where $j = 1, ..., 5$ stands respectively for maximum E-field, maximum SAR, mean SAR, maximum temperature, and temperature rise):

$$I_i^j = \frac{V_i^j}{V^j}, \qquad (18)$$

with i the RV indice (i.e., $i = 1, ..., 5$), V_i^j variance relative to RV i and output j, V^j represents variance of output j computed from 5-RVs stochastic model, and I_i^j is the aforementioned influence criterion. It should be noticed here that, assuming extension to dependent random variables (see Section III), the relation (18) is still valuable to assess RV "global" sensitivity.

Figures 8 and 9 show the influence of the different random parameters relative to the variance obtained from the entire (e.g., 5-RVs) stochastic model following relation (18), for both polarizations. Close to global sensitivity analysis [24], this offers a qualitative overview of the impact of different RVs over various outputs. As expected, the results are highly problem-dependent, implying the choice of the output may influence the SC experimental design needed for a complete stochastic modeling of the problem. In this

framework, Tables 3 and 4 provide a ranking of the most influential parameters depending on the output, for vertical and horizontal polarization, respectively.
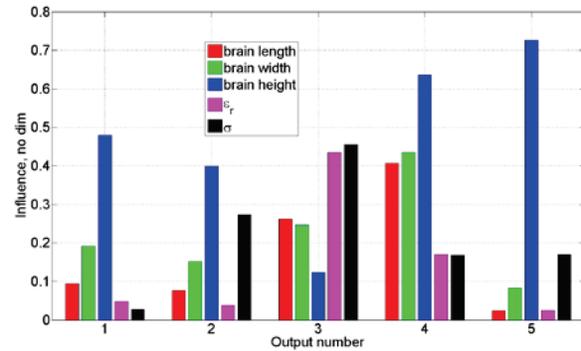
Fig. 8. Influence criterion I_i^j in function of outputs (1: E-field, 2: maximum SAR, 3: mean SAR, 4:max temperature, 5: temperature rise) and RV (brain's length, brain's width, brain's height, relative permittivity (ε_r) brain, conductivity (σ) brain) for vertical polarization.

Table 3: RV ranking from most (A) to least (E) influential parameters and given outputs (in relation with results in Fig. 8)

Output	1	2	3	4	5	Total
RV1: brain's length	C	D	C	C	E	D
RV2: brain's width	B	C	D	B	C	B
RV3: brain's height	A	A	E	A	A	A
RV4: ε_r brain	D	E	B	D	D	E
RV5: σ brain	E	B	A	E	B	C
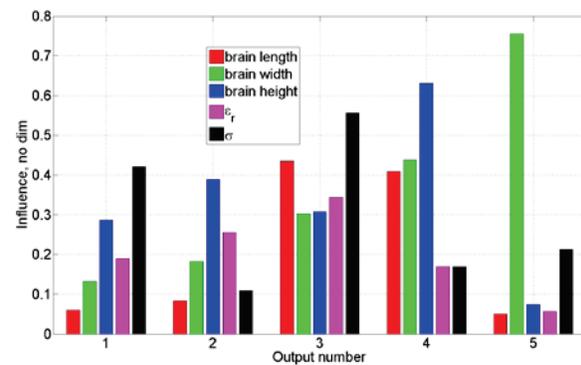
Fig. 9. Influence criterion I_i^j in function of outputs (1: E-field, 2: maximum SAR, 3: mean SAR, 4:max temperature, 5: temperature rise) and RV (brain's length, brain's width, brain's height, relative permittivity (ε_r) brain, conductivity (σ) brain) for horizontal polarization.

Table 4: RV ranking from most (A) to least (E) influential parameters and given outputs (in relation with results in Figure 9)

Output	1	2	3	4	5	Total
RV1: brain's length	E	E	B	C	E	E
RV2: brain's width	D	C	E	B	A	C
RV3: brain's height	B	A	D	A	C	A
RV4: ε_r brain	C	B	C	D	D	D
RV5: σ brain	A	D	A	E	B	B

E. Discussion

Due to the multi-physics of the problem (thermal and electromagnetic), the sensitivity of the statistical model is different from a given output to another.

As expected, conductivity σ seems to play a key role for SAR assessment (especially regarding mean value) (Tables 3 and 4). Contrary to σ, relative permittivity seems to produce weaker effects both considering EM and thermal outputs. Regarding geometrical parameters, brain's height seems to play a major role both considering thermal outputs and maximum electric ones (out of averaged SAR); this might be expected due to chosen EM sources (plane wave's orientation); brain's length and width are less influential in that case.

Similarly to thermal differences due to horizontal (Fig. 2) and vertical (Fig. 3) polarizations, EM sources involve various results when considering influence of each random parameter. Vertical polarization strengthens the importance of geometrical brain's parameters comparatively to geometrical ones except for averaged SAR since ε_r and σ are key parameters. The relative influence of materials is high for horizontal polarized wave regarding EM outputs. This validates the interest of the proposed methodology as a framework for sensitivity analysis combining deterministic and stochastic models.

From past discussions, an adaptation of the experimental design is possible. Thus, the least influential variables may be considered with a restricted number of points (e.g., changing some parameters to deterministic ones or withdrawing some inputs in the initial experimental design [25]), whereas the most effort may be put on the most influential ones.

Although the focus of presented paper was on the proposed methodology as a framework for sensitivity analysis combining deterministic and stochastic models, some limitations regarding the deterministic model should be addressed at this point. The homogeneous brain model insulated in free space does not represent a realistic scenario. As the actual brain is surrounded by various other tissues, such as e.g. cerebrospinal fluid, fat, skull and scalp, the overall electric field distribution and the related SAR will be affected due to these tissues. The work related to the inclusion of the surrounding tissues such as skull and scalp is currently under way. In order to take into account this type of scenario, it will be necessary to use a different integral equation formulation, such as a tensor-type volume integral equation approach.

Furthermore, the low number of triangular elements used to represent the surface of our model results in the less smooth appearance of the electric field. The brain surface model presented in this paper is smoothed out neglecting the detailed cortical structures, although the proposed integral equation formulation is applicable to an arbitrarily shaped biological tissue, including a more detailed brain model taking into account the cortex foldings. The downside of the detailed description of the brain is the total number of elements required to accurately represent the geometry. This would consequently lead to a very large matrix system whose solution would require the use of advanced techniques such as multilevel fast multipole algorithm and hence prevents our model at present stage in doing so.

Finally, the presented framework did not take into account the variability of thermal parameters such as the heat generated due to metabolic processes Q_m, the volumetric perfusion rate and the specific heat capacity of blood, W_b and c_b, respectively, the thermal conductivity of the tissue λ, and the arterial blood temperature T_a. The influence of these thermophysiological parameters on the induced SAR and the related temperature distribution related to the thermal dosimetry model is required due to their variability as well as general uncertainty [26], [27].

IV. CONCLUSION

One of the challenges the electromagnetic-thermal dosimetry models face is related to the uncertainty of the various input parameters. To overcome this, the stochastic dosimetry approach will be necessary, where both stochastic and deterministic models are used. Based upon a deterministic model coupling EM and thermal dosimetry, this contribution proposes to integrate uncertain variations around input parameters. The expansion of statistical outputs (e.g., mean and variance) over a polynomial basis (via SC) showed robustness and efficiency (limited size of experimental design) both for EM and temperature quantities.

The quantitative computing of statistical first and second order moments enables a qualitative sensitivity study in order to focus on the most influential parameters. From this analysis, a competitive and efficient model may be defined for instance in order to perform a more demanding computing (e.g., in order to provide probability density function, assess reliability analysis, and put the focus on extreme values). From an optimized statistical model, we may also achieve richer EM and thermal description of the brain's behavior by increasing the number of random variables and their complexity.

ACKNOWLEDGMENT

REFERENCES

[1] A. E. Habachi, et al., "Statistical analysis of whole-body absorption depending on anatomical human characteristics at a frequency of 2.1 GHz," *Phys. Med. Biol.*, vol. 55, no. 7, pp. 1875-1887, 2010.

[2] R. L. McIntosh and V. Anderson, "A comprehensive tissue properties database provided for the thermal assessment of a human at rest," *Biophysical Reviews and Letters*, vol. 5, no. 3, pp. 129-151, 2010.

[3] J. Wiart, et al., "Handle variability in numerical exposure assessment: The challenge of the stochastic dosimetry," in *Antennas and Propagation (EuCAP), 2013 7th European Conference on*, pp. 1979-1981, 2013.

[4] O. Aiouaz, et al., "Uncertainty analysis of the specific absorption rate induced in a phantom using a stochastic spectral collocation method," *Annals of Telecommunications*, vol. 66, no. 7-8, pp. 409-418, 2011.

[5] I. Liorni, et al., "Polynomial chaos decomposition applied to stochastic dosimetry: Study of the influence of the magnetic field orientation on the pregnant woman exposure at 50 Hz," in *Engineering in Medicine and Biology Society (EMBC), 2014 36th Annual International Conference of the IEEE*, pp. 342-344, 2014.

[6] D. Voyer, et al., "Probabilistic methods applied to 2D electromagnetic numerical dosimetry," *COMPEL*, vol. 27, no. 3, pp. 651-667, 2008.

[7] P. Kersaudy, et al., "A new surrogate modeling technique combining kriging and polynomial chaos expansions - application to uncertainty analysis in computational dosimetry," *J. Comput. Phys.*, vol. 286, no. 1, pp. 103-117, 2015.

[8] K. R. Foster and C.-K. Chou, "Are children more exposed to radio frequency energy from mobile phones than adults?," *Access, IEEE*, vol. 2, pp. 1497-1509, 2014.

[9] J. Wiart, et al., "Analysis of RF exposure in the head tissues of children and adults," *Phys. Med. Biol.*, vol. 53, no. 13, pp. 3681-3695, 2008.

[10] M. Cvetković and D. Poljak, "An efficient integral equation based dosimetry model of the human brain," in *Proceedings of 2014 International Symposium on Electromagnetic Compatibility (EMC EUROPE) 2014*, Gothenburg, Sweden, pp. 375-380, 1-4 September 2014.

[11] F. Wei and A. Yilmaz, "A more scalable and efficient parallelization of the adaptive integral method–part ii: Bioem application," *IEEE T. Antenn. Propag.*, vol. 62, no. 2, pp. 727-738, 2014.

[12] M. Cvetkovic, D. Poljak, and J. Haueisen, "Analysis of transcranial magnetic stimulation based on the surface integral equation formulation," *IEEE T. Bio-Med. Eng.*, vol. 62, no. 6, pp. 1535-1545, 2015.

[13] W. C. Chew, M. S. Tong, and B. Hu, Integral *Equation Methods for Electromagnetic and Elastic Waves*. Morgan & Claypol Publishers, 2009.

[14] J. Volakis and K. Sertel, *Integral Equation Methods for Electromagnetics*. IET, 2012.

[15] D. W. Green, et al., "Chiral biomaterials: From molecular design to regenerative medicine," *Advanced Materials Interfaces*, 2016.

[16] H. H. Pennes, "Analysis of tissue and arterial blood temperatures in the resting human forearm. 1948," *J. Appl. Physiol.*, vol. 85, no. 1, pp. 5-34, 1998.

[17] C. Gabriel, "Compilation of the dielectric properties of body tissues at RF and microwave frequencies," *Brooks Air Force Base*, TX, Report: AL/OE-TR-1996-0037, Tech. Rep., 1996.

[18] H. Dodig, et al., "Stochastic sensitivity of the electromagnetic distributions inside a human eye modeled with a 3D hybrid BEM/FEM edge element method," *Eng. Anal. Bound. Elem.*, vol. 49, pp. 48-62, 2014.

[19] K. R.Foster, et al., "Dielectric properties of brain tissue between 0.01 and 10 GHz," *Phys. Med. Biol.*, 1979.

[20] D. Xiu, "Fast numerical methods for stochastic computations: A review," *Communications in Computational Physics*, vol. 5, no. 2, pp. 242-272, 2009.

[21] D. Kroese, T. Taimre, and Z. Botev, *Handbook of Monte Carlo Methods*. John Wiley & Sons, New Jersey, USA: Wiley, 2011.

[22] S. Lalléchère, et al., "An electromagnetic compatibility problem via unscented transform and stochastic collocation methods," *ACES Journal*, vol. 27, no. 2, pp. 94-101, 2012.

[23] L. de Menezes, et al., "Efficient computation of stochastic electromagnetic problems using unscented transforms," *IET Sci. Meas. Technol.*, vol. 2, pp. 88-95, 2008.

[24] A. Saltelli, et al., *Global Sensitivity Analysis - The Primer*, John Wiley & Sons Inc., Hoboken, USA: Wiley, 2008.

[25] D. Thomas, O. Oke, and C. Smartt, "Statistical analysis in EMC using dimension reduction methods," *in Electromagnetic Compatibility (EMC), 2014 IEEE International Symposium on*, pp. 316-321, 2014.

[26] T. Samaras, E. Kalampaliki, and J. Sahalos,

"Influence of thermophysiological parameters on the calculations of temperature rise in the head of mobile phone users," *IEEE T. Electromagn. C.*, vol. 49, no. 4, pp. 936-939, 2007.

[27] M. Cvetkovic, D. Poljak, and A. Hirata, "The electromagnetic-thermal dosimetry for the homogeneous human brain model," *Eng. Anal. Bound. Elem.*, vol. 63, pp. 61-73, 2016.

Mario Cvetković received the B.S. degree in Electrical Engineering from the University of Split, Croatia in 2005, M.Phil degree from the Wessex Institute of Technology, University of Wales, UK, in 2009, and Ph.D. in 2013 from University of Split, Croatia, where he is currently working as a Postdoc. His research interests including numerical modeling including finite element and moment methods, computational bio-electromagnetics and heat transfer related phenomena.

Sébastien Lalléchère received the M.Sc. and Ph.D. degrees in Computational Modeling and Electronics/Electromagnetism from Polytech' Clermont and Blaise Pascal University, Clermont-Ferrand, France, in 2002 and 2006. He served as a Research Engineer in LASMEA, Clermont-Ferrand, France, in 2007 focusing on intensive computational methods for electromagnetics. He is currently an Associate Professor at Blaise Pascal University and Institut Pascal, Clermont-Ferrand, France. His research interests cover the fields of EMC including antennas and propagation, complex and reverberating electromagnetic environments, computational electromagnetics, stochastic modeling and sensitivity analysis in electrical engineering.

Khalil El Khamlichi Drissi received his M.Sc., and Ph.D. degrees in Electrical Engineering from Ecole Centrale de Lille and the University of Lille, in 1987 and 1990 respectively. He received the Habilitation in electronics, at the Doctoral School "Sciences Pour l'Ingénieur" of Blaise Pascal University, in 2001. Currently, he is Professor at the Department of Electrical Engineering where he was the Dean in the period from 2007 to 2011. He is also Senior Researcher at Institute Pascal Laboratory and his research interests include EMC in Power Electronics and Power Systems, in particular numerical modeling, EMI reduction and converter control.

Pierre Bonnet received the Ph.D. degree in Electromagnetism from Blaise Pascal University, Clermont-Ferrand, France. From 1999 to 2008 he was an Assistant Professor within the Department of Physics and Institut Pascal at Blaise Pascal University. He is currently a Full Professor in this University and the head of the EMC group of Institut Pascal. His research interests are in the area of numerical electromagnetics with an emphasis on EMC/EMI problems, time reversal, source identification and stochastic approaches.

Dragan Poljak received his B.Sc. in 1990, his M.Sc. in 1994 and Ph.D. in Electrical Engineering in 1996 from the University of Split, Croatia. He is the Full Professor at Department of Electronics, FESB at the University of Split, and he is also Adjunct Professor at Wessex Institute of Technology. His research interests include frequency and time domain computational methods in electromagnetics, particularly in the numerical modelling of wire antenna structures, and numerical modelling applied to environmental aspects of electromagnetic fields. From 2011 to 2015 Poljak was the Vice-Dean for research at FESB. In 2011, Poljak became a Member of WIT Board of Directors while in June 2013, he became a Member of the board of the Croatian Science Foundation.

Sensitivity Analysis and Tipping Calibration of A W-band Radiometer for Radiometric Measurements

Li Wu, Shusheng Peng, Zelong Xiao, and Jianzhong Xu

School of Electronic and Optical Engineering
Nanjing University of Science & Technology, Nanjing, 210094, China
li_wu@njust.edu.cn, pengshusheng@njust.edu.cn, zelongxiao@njust.edu.cn, xjz2018@yeah.net

Abstract ─ This paper deals with the sensitivity analysis and tipping calibration of a developed W-band radiometer system for radiometric measurements. Initially the equivalent integration time of the cascaded hardware and software integrators is derived and the radiometer sensitivity is then analyzed based on the established system measurement equation. Secondly, the applicable tipping calibration of the W-band radiometer is investigated and optimized to reduce calibration errors according to the system parameters. Sensitivity measurement and tipping calibration experiments of the developed W-band radiometer are conducted. The preliminary results show that the radiometer sensitivity is 0.51 K with an integration time of 1 s, and the tipping calibration has a better accuracy than the liquid nitrogen calibration, with a maximum difference of 2.5 K between both of the calibration methods.

Index Terms ─ Calibration, radiometric measurement, remote sensing, sensitivity.

I. INTRODUCTION

Due to the advantages of relatively simple design and high safety, radiometric sensors are increasingly being seen in non-invasive monitoring in harsh and or sensitive environments, such as the human body core where direct contact to the object under investigation is unachievable [1]. As lower microwave frequencies have penetration depths in tissues on the order of centimeters, microwave radiometric sensors have been employed to continuously monitor core body temperature which can provide a tool for monitoring drug delivery for cancer treatment [2], breast cancer detection [3], and hyperthermia temperature control [4,5]. While for the ingestible capsules which employs short-range wireless sensors to measure core body temperature [6], they measure the temperature somewhere in the digestive tract for a limited time and the device is still in the body.

At millimeter wave (MMW) frequencies, the penetration depth is limited to the top skin layer and can be used for surface temperature monitoring, such as in the case of surface burns [2]. Also, MMW radiometers are widely applied in security screening due to the advantage of clothes penetration. It is significant to accurately characterize the radiation of interested items like metal guns and knives, plastic explosives, ceramic knives to offer database for the detection, classification and identification [7].

A total power radiometer (TPR) for non-contact biomedical sensing is presented in [8] as a precursor to developing a health monitoring device. Unfortunately, the radiometer sensitivity, which is a critical issue in biomedical applications, is poor for the TPR due to system gain fluctuation. The Dicke radiometers are developed in [9,10] to stabilize the output for non-invasive temperature monitoring. However, any method that requires additional RF hardware will likely increase its system cost significantly [11]. Of all the approaches for radiometer sensitivity improvement, the noise-adding radiometer has the great potential to achieve this with minimal RF hardware added and has attracted a lot of attention [11-13]. Recently, a W-band radiometer which employs a receiver configuration based on the proposed radiometer in [13] was developed for radiometric characterization of interested items. It reduces the influences of unavoidable system gain fluctuations by injecting noise into the front end periodically. However, the sensitivity of the whole radiometer system was not presented in [13] which just analyzed the sensitivity of individual channels. And the both hardware and software integrators which contribute to the system integration time are employed for the flexibility in the receiver, so it is essential to derive the system sensitivity and the cascaded system integration time which determines the radiometer sensitivity directly.

Additionally, it is significant for an antenna to have a lower side-lobe level and a higher main-beam efficiency for radiometry. In this paper, an offset parabolic antenna is employed for the W-band radiometer to improve the measurement accuracy [14]. However, it is difficult to calibrate the developed radiometer with the offset parabolic antenna using the two point calibration method where a liquid nitrogen cooled absorber is

preferred in practical outdoor operations. Fortunately, the tipping calibration method which takes the atmosphere under clear weather conditions as a calibration reference is very convenient for the ground-based radiometer [15,16].

Aiming for the sensitivity analysis and the tipping calibration of the developed W-band radiometer with an offset parabolic antenna for radiometric measurements, this paper will be organized as follows. Section 2 introduces the developed radiometer receiver and establishes the corresponding system measurement model. The integration time of a cascaded integrator is derived and the sensitivity of the radiometer is analyzed in Section 3. The implementation of tipping calibration for the W-band radiometer and the primary calibration errors are described in Section 4. Experimental results and analysis are presented in Section 5. The last section is the conclusion.

II. THE DEVELOPED W-BAND RADIOMEER

Figure 1 shows the block diagram of an improved W-band radiometer receiver based on the noise adding type. While the radiometer working, the noise of antenna or matched load is added with the injected noise introduced by the noise source modulated with a periodic square wave. The coupled signal is converted to an IF signal via the mixer and goes through the IF amplifier, and the square law detector and is then divided into the direct current (DC) channel and the alternative current (AC) channel. Compared with the DC channel, the extra DC-block capacitor and the synchronous demodulator are needed for the AC channel. The output signals of the both channels are then acquired and processed by the data acquisition and processing unit to deduce the observed brightness temperature by applying the radiometer system measurement equations.
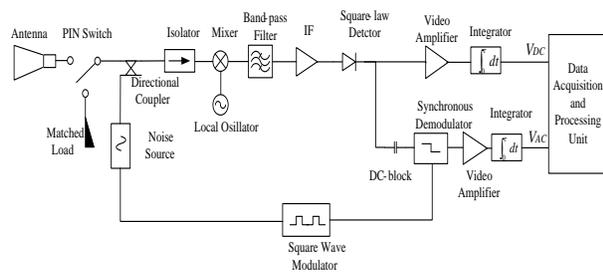
Fig. 1. Block diagram of the radiometer receiver.

The receiver front-end is housed in an insulated box with the stable temperature accomplished by a thermal controller. It is helpful to stabilize the receiver temperature due to the gain of the radiometer front-end is sensitive to the temperature variation. The W-band radiometer is placed on a two-dimensional scanner

driven by a servo controller when it works. A picture of the W-band radiometer is shown in Fig. 2.

Fig. 2. A picture of the developed W-band radiometer.

When the PIN switch is connected to the antenna, the radiometer observes the scene to be measured. Suppose T_a is the antenna temperature, T_R is the equivalent system input noise temperature of the radiometer receiver, T_H and T_L are the noise temperatures injected into the coupler when the noise source is on and off, respectively. Then the radiometer system noise temperature with the noise source switched on and off can be respectively written as:

$$T_{s\_on} = T_a + T_R + T_H ,\tag{1}$$

$$T_{s\_off} = T_a + T_R + T_L .\tag{2}$$

The difference between T_{s_on} and T_{s_off} is:

$$T_N = T_H - T_L = C_C \cdot T_o \cdot \mathrm{ENR} ,\tag{3}$$

where C_c is the coupling factor of the coupler, T_o=290 K is the standard temperature, ENR is the excess noise ratio of the noise source. So the mean voltage components of DC channel and AC channel outputs can be expressed respectively as:

$$V_{DC} = \gamma_d G_c g_{dc} kB (T_s + T_{NM}),\tag{4}$$

$$V_{AC} = \gamma_d G_c g_{ac} kBT_{NM} ,\tag{5}$$

where, V_{DC} and V_{AC} are the output voltages of DC channel and AC channel respectively, γ_d is the square-law detector sensitivity, G_c is the common receiver RF gain, g_{dc} and g_{ac} are the video amplifier gains of DC channel and AC channel respectively, k is the Boltzmann constant, B is the system bandwidth pre-detection, T_s is the receiver system noise temperature, and $T_{NM}=T_N/2$ is half of the injected noise temperature difference. Define a variable of K to be a ratio between the DC channel output voltage V_{DC} and the AC channel output voltage V_{AC}:

$$K = \frac{V_{DC}}{V_{AC}} = \frac{g_{dc}(T_s + T_{NM})}{g_{ac}T_{NM}} .\tag{6}$$

In order to reduce impact of the receiver system noise temperature drift to increase the measurement

accuracy, a periodic calibration technique is adopted [17], that is, the matched load and the scene are observed alternatively and the corresponding observation output voltage ratio values of K_c and K_x are obtained. Hence, the brightness temperature of observed scene can be determined by:

$$T_x = T_c - \frac{g_{ac} T_{NM}}{g_{dc}}(K_c - K_x) = T_c - C(K_c - K_x), \quad (7)$$

where, $C = \frac{g_{ac} T_{NM}}{g_{dc}}$ is the calibration coefficient and it can be determined by liquid nitrogen or tipping calibration. Once the value of C is solved, T_x could be obtained by the above expression.

III. SENSITIVITY ANALYSIS OF THE W-BAND RADIOMETER

As an important parameter for radiometer performance evaluation, the theoretical sensitivity ΔT_{min} which denotes the minimum detectable change in the antenna temperature can be given with the following expression:

$$\Delta T_{min} = C\sigma K_x, \quad (8)$$

where, σK_x is the standard deviation of K_x defined in Eq. (6). Using the standard propagation of error to obtain σK_x as follows:

$$\sigma K_x = \sqrt{\frac{\sigma V_{DC}^2}{V_{AC}^2} + \frac{V_{DC}^2 \sigma V_{AC}^2}{V_{AC}^4}}, \quad (9)$$

where, σV_{DC} is the standard deviation of DC channel output V_{DC}, and σV_{AC} is the standard deviation of AC channel output V_{AC}. Inserting Eq. (9) into Eq. (8),

$$\Delta T_{min} = C\sigma K_x = C\frac{V_{DC}}{V_{AC}}\sqrt{\frac{\sigma V_{DC}^2}{V_{DC}^2} + \frac{\sigma V_{AC}^2}{V_{AC}^2}}. \quad (10)$$

It is known from the radiometric principle [18] that the first and the second items in the above square root symbol can be respectively derived as follows:

$$\frac{\sigma V_{DC}^2}{V_{DC}^2} = \frac{[(\frac{T_s + 2T_{NM}}{\sqrt{B\tau_{dc}/2}})^2 + (\frac{T_s}{\sqrt{B\tau_{dc}/2}})^2]}{(T_s + T_{NM})^2} \approx \frac{4}{B\tau_{dc}}, \quad (11)$$

$$\frac{\sigma V_{AC}^2}{V_{AC}^2} = \frac{[(\frac{T_s + 2T_{NM}}{\sqrt{B\tau_{ac}/2}})^2 + (\frac{T_s}{\sqrt{B\tau_{ac}/2}})^2]}{T_{NM}^2} \approx \frac{4(T_s + T_{NM})^2}{B\tau_{ac}T_{NM}^2}, \quad (12)$$

where, τ_{dc} and τ_{ac} indicate the integration time of the DC and AC channel respectively, and have the same value of τ due to possessing the identical integrator parameters in this paper. So the obtained radiometer sensitivity is:

$$\Delta T_{min} = \frac{2(T_s + T_{NM})}{\sqrt{B\tau}}\sqrt{1 + (1 + \frac{T_s}{T_{NM}})^2}. \quad (13)$$

In the radiometer receiver a simple RC integrator circuit is commonly utilized to smooth the random fluctuation of output signal. However, the integration time of the hardware integrator is fixed and less flexible. So a software digital integrator is generally implemented by averaging digitized samples of the hardware integrator smoothed signal. For a RC integrator with a time constant of τ_{RC}, its pulse response function is:

$$h_{RC}(t) = \begin{cases} 0 & t < 0 \\ \frac{1}{\tau_{RC}}\exp\left(-\frac{t}{\tau_{RC}}\right) & t \geq 0 \end{cases}, \quad (14)$$

and the pulse response function of a digital integrator can be written as:

$$h_{num}(t) = \begin{cases} \frac{1}{\tau_{num}} & -\frac{\tau_{num}}{2} \leq t \leq \frac{\tau_{num}}{2} \\ 0 & else \end{cases}, \quad (15)$$

where, $\tau_{num} = Nt_s$ is the integration time of the digital integrator, N is the number of samples to average, t_s is the sampling interval. Subsequently, the equivalent integration time of the cascaded hardware and software integrators can be determined by combining the convolution computation, the Parseval theorem, and a relationship between the integration time and the power transfer function [19]:

$$\tau = \frac{\tau_{num}^2}{\tau_{num} - \tau_{RC}[1 - \exp(-\tau_{num}/\tau_{RC})]}. \quad (16)$$

Inserting Eq. (16) into Eq. (13), the ultimate expression for the W-band radiometer sensitivity can be rewritten as:

$$\Delta T_{min} = \frac{2(T_s + T_{NM})\sqrt{\tau_{num} - \tau_{RC}[1 - \exp(-\tau_{num}/\tau_{RC})]}}{\tau_{num}\sqrt{B}}\sqrt{1 + (1 + \frac{T_s}{T_{NM}})^2}. \quad (17)$$

IV. TIPPING CALIBRATION OF THE W-BAND RADIOMETER

Tipping calibration has been widely applied in the ground based radiometer to determine the calibration coefficient by iterations. For the ideal plane stratified atmosphere, atmospheric radiation transfer theory shows that [20]:

$$T_{sky}(\theta) = T_{bg}e^{-\tau(\theta)} + T_m(\theta)\left(1 - e^{-\tau(\theta)}\right), \quad (18)$$

where, θ is the zenith angle, $T_{sky}(\theta)$ is the sky brightness temperature at the direction of θ, $\tau(\theta)$ is the opacity of total slant path, $T_m(\theta)$ is the atmosphere mean radiative temperature. Define a ratio of opacity between an observation angle θ and the zenith as:

$$m_\theta = \tau(\theta)/\tau(0). \quad (19)$$

For the ideal plane stratified atmosphere, the opacity at the direction of θ is proportional to the opacity at the zenith as described as:

$$\tau(\theta) = \tau(0)\sec\theta. \quad (20)$$

It is seen from Eq. (19) and (20) that $m_\theta = \sec\theta$ for the case of plane stratified atmosphere, and the zenith opacity can be obtained with Eq. (21):

$$\tau(0) = \ln\left(\frac{T_{sky}(0) - T_m(\theta)}{T_{sky}(\theta) - T_m(\theta)}\right) \cdot \frac{1}{m_\theta - 1}, \qquad (21)$$

where, $T_{sky}(0)$ and $T_{sky}(\theta)$ are the measured sky brightness temperature values at the directions of 0 and θ. When the opacity is lower, $T_m(\theta)$ can be seen to be constant for different zenith angles, that is, $T_m(\theta) = T_m$. Based on Eq. (7), Eq. (21) can be rewritten as:

$$\tau(0) = \ln\left(\frac{K_{sky}(0) - K_m}{K_{sky}(\theta) - K_m}\right) \cdot \frac{1}{m_\theta - 1}, \qquad (22)$$

where, $K_{sky}(0)$ and $K_{sky}(\theta)$ means the acquired voltage ratio defined in Eq. (6) with the sky brightness temperature of $T_{sky}(0)$ and $T_{sky}(\theta)$ respectively. K_m is the voltage ratio associated with mean radiative temperature and can be deducted by K_b which is the voltage ratio of ambient absorber with temperature of T_b described by the following equation:

$$K_m = K_b - (T_b - T_m)/C, \qquad (23)$$

where, C is the estimated calibration coefficient. $T_{sky}(0)$ can be determined with the zenith opacity $\tau(0)$ which is calculated by substituting $K_{sky}(0)$、$K_{sky}(\theta)$、K_m and θ into Eq. (22), and hence the calibration coefficient can be rewritten as follows:

$$C = (T_b - T_{sky}(0))/(K_b - K_{sky}(0)). \qquad (24)$$

To improve the accuracy of calibration, the technique of tipping curve is adopted by implementing multiple measurements at different angles. Suppose there is a set of measurement data $\{(a_1, b_1)\cdots, (a_n, b_n)\}$,

$a_i = \ln\left(\frac{K_{sky}(0) - K_m}{K_{sky}(\theta_i) - K_m}\right)$, $b_i = m_{\theta_i} - 1$, so the zenith opacity can be calculated using linear regression:

$$y = \tau(0)x + b_\tau, \qquad (25)$$

where, $x = m_\theta - 1$, $y = \ln\left(\frac{K_{sky}(0) - K_m}{K_{sky}(\theta) - K_m}\right)$, $\tau(0)$ is the slope of the linear function, b_τ is the intercept which should be close to zero meaning that the fitted line crosses through the origin. The calibration measurement data are invalid unless the correlation coefficient of the regression is greater than a threshold required for accuracy. After renewing the calibration coefficient with $\tau(0)$, the zenith opacity $\tau(0)$ can be also updated and this process is repeated until the intercept converges to zero. It is important to note that the tipping calibration method is based on the ideal plane stratified atmosphere which is met by observations under clear weather conditions.

V. EXPERIMENTAL RESULTS AND ANALYSIS

A. Sensitivity measurement results

For the developed W-band radiometer system, T_R=1340 K, B=2 GHz, C_C=10.6 dB, ENR=15 dB, the integration time of RC integrator is τ_{RC}=50 ms, and the sampling interval is t_s=10 ms. The relationship between the system equivalent integration time and the number of samples to average is depicted in Fig. 3 according to the Eq. (16).
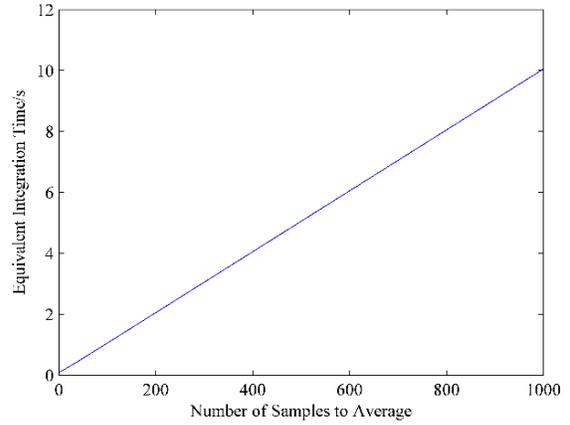
Fig. 3. The relationship between the equivalent integration time and the number of samples.

It can be found from the figure that the system equivalent integration time increases with the numbers of samples almost linearly. Therefore, the integration time of the radiometer can be adjusted by changing the number of samples to average which will lead to a subsequent adjustment of the sensitivity.

To estimate the practical radiometer sensitivity, an ambient absorber with the temperature of 298 K and a liquid nitrogen cooled absorber are observed as a hot and a cold load respectively in the experiment. And the offset parabolic antenna is replaced with a horn antenna for convenience. A group of data with a time length of 10 minutes are acquired for both the hot and cold load observations. And the practical radiometer sensitivity can be calculated as follows:

$$\Delta T_{\min} = \frac{298 - T_{LN2}}{\overline{K}_{Amb} - \overline{K}_{LN2}}\sigma K_x, \qquad (26)$$

where, $\overline{K}_{Amb}$ and $\overline{K}_{LN2}$ are the average output voltage ratios for the ambient and cooled absorbers respectively. T_{LN2} is the temperature of absorber soaked in the liquid nitrogen and it can be estimated as [21]:

$$T_{LN2} = 77.36 + 0.011(P - 760), \qquad (27)$$

where, P is the atmospheric pressure with the unit of

mmHg.

As presented in Fig. 4, the practical sensitivity is measured under different values of the integration time of 0.1 s, 1 s, and 10 s which are achieved by adjusting the number of samples to average. Also the theoretical sensitivity of the radiometer varied with the integration time is shown by inserting the corresponding parameters into Eq. (17).
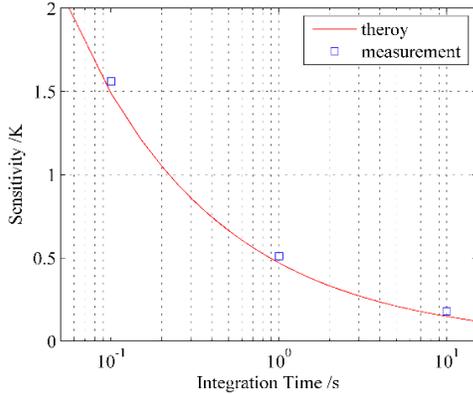
Fig. 4. The radiometer sensitivity with different integration time.

It can be seen that the a sensitivity of 1.56 K is obtained when the integration time is 0.1 s, and its value is reduced to 0.51 K and 0.18 K with a integration time of 1 s and 10 s respectively. Also, the measurement results are in good agreement with the theoretical values.

B. Tipping calibration results

To verify the presented calibration method, calibration experiments of the W-band radiometer were conducted under clear weather conditions in Nanjing, China. The W-band radiometer was placed on the two-dimensional scanner and the antenna pointing zenith angle is set as 0°, 48°, 60°, 66.5 ° and 70.5° respectively. The voltage ratios between the DC and AC signal output channels at different observation angles are calculated by the estimated calibration coefficient of C in the first iteration of data processing. Then the zenith opacity is obtained by fitting the calculated data using the least square method and the calibration coefficient of radiometer is renewed consequently. Repeat the above iterative process until the intercept converges to zero.

As the tipping calibration errors might be caused by the pointing angle offset, the mean radiative temperature, the antenna beam width, and the earth curvature, some measures are employed to reduce the calibration errors. For the angular measurement error of scanner is less than 0.05°, the influences of the antenna zenith pointing error on radiometer measurement accuracy could be neglected. To reduce the error caused by the mean

radiative temperature T_m, it is calculated by combining the ground temperature, the relative humidity and the meteorological statistics. While for the influence of antenna beam width on calibration error, it could be assessed with the following formula [15]:

$$\delta T_A = \frac{HPBW^2}{16\ln(2)}\left(T_{mr} - T_{bg}\right)e^{-\tau(\theta)}\left[2 + \left(2 - \tau(\theta)\right)\cot^{-2}(\theta)\right]\tau(\theta),$$

(28)

where, $HPBW$ is the antenna half-power beam width in radians. Since the half-power beam width of the radiometer offset parabolic antenna is 0.96°, the maximum of temperature correction within the range of observation angles is less than 0.03 K, and hence the error caused by the antenna beam width is negligible.

In order to reduce the radiometer calibration error caused by the earth curvature, an effective height as in [15] is calculated by utilizing the MMW atmospheric transport model in [22]. Then the ratio of opacity between an observation angle θ and the zenith should be corrected to be:

$$m'_\theta = m_\theta - Hm_\theta(m_\theta^2 - 1)/r_e,$$

(29)

where H is the effective height, r_e is the radius of the earth.

In the iterative process of calibration, the application of the above correction measures would contribute to a more accurate calibration coefficient. Also, it is essential that the correlation coefficient of the regression needs to meet the accuracy requirement (the minimum value is set to 0.998 in this paper). Two groups of measurement data in the specified angles and the fitted line after 4 iterations are shown in Fig. 5.
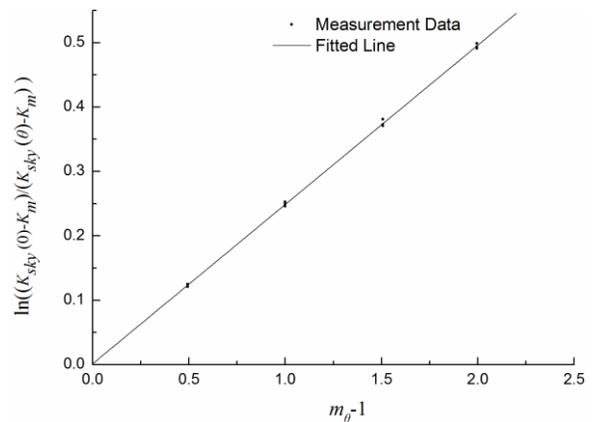
Fig. 5. The measurement data and fitted line of W band radiometer calibration.

The correlation coefficient of the regression is 0.9994, the intercept is 0.001, and the calculated zenith opacity is 0.248. The ultimate radiometer calibration coefficient is estimated to be 586.

C. Evaluation of calibration accuracy

Also to assess the accuracy of the W-band radiometer tipping calibration, a simple liquid nitrogen calibration device is designed. The calibration device is an incubator with wedge-shaped absorber covered inside, and its size is $70cm \times 60cm \times 40cm$. Initially, the radiometer observes the calibration device in the ambient temperature whose value is measured with a high precision thermometer. Then the device filled with liquid nitrogen is observed by the radiometer and the calibration coefficient can be deduced by processing the measurement data. After observations of clear sky at the different observation angles with radiometer, the measurement brightness temperatures are obtained using the calibration coefficient of tipping curve and liquid nitrogen respectively. Define a measurement brightness temperature error ΔT_B:

$$\Delta T_B = T_{B\_TP} - T_{B\_LN2}, \qquad (30)$$

where, T_{B_TP} is the measured brightness temperature with the tipping calibration method, T_{B_LN2} is the measured brightness temperature with the liquid nitrogen calibration method. The obtained mean brightness temperature errors at the different directions are shown in Table 1.

Table 1: The mean measurement brightness temperature error at different observation angles

Observation Angle(°)	ΔT_B (K)
0	2.48
30	2.34
45	2.16
60	1.85
70	1.40

As can be seen from the table, the brightness temperature deduced by liquid nitrogen calibration is smaller than that deduced by tipping calibration. And the brightness temperature error between the both reaches the maximum to 2.48 K. Also with the increase of observation angle, the mean measurement brightness temperature error decreases and reaches to about 1.4 K when the observation angle is 70°. The results of this phenomenon are thought to be that real temperature of absorber soaked in liquid nitrogen is higher than the theoretical calculated temperature for the sake of introduced ambient background temperature by radiometer antenna side-lobe and the produced reversed radiation by the liquid nitrogen surface. And then these items lead to a larger radiometer calibration coefficient C. However, it is seen from the W-band radiometer system measurement equation as shown in Eq. (7), a larger calibration coefficient will lead to that measured brightness temperature of sky is lower than the actual value. It is proved that the tipping calibration method has a higher accuracy than the liquid nitrogen.

In addition, the matched reference load with ambient temperature is regarded as a standard for the W-band radiometer. When the brightness temperature error between the standard load and the measured object is larger, the error of brightness temperature measurement caused by the calibration coefficient error will be larger due to a larger observation variable of $(K_c - K_x)$.

Also the calibrated W-band radiometer is placed on the two-dimensional scanner to image a tower with a field of view 30°×14°. The distance between the radiometer and the tower is about 105 m. A picture of the tower is presented in Fig. 6 (a) and the acquired MMW passive image is shown in Fig. 6 (b). The experiment was conducted in a cloudy day with the surface temperature about 310 K. It is shown from the figure that brightness temperature of the scenario varies from 160 K to 300 K where the coldest is the sky, whereas the middle part of tower has the highest temperature. The profile of the tower is clear due to a large contrast between it and the cold sky.
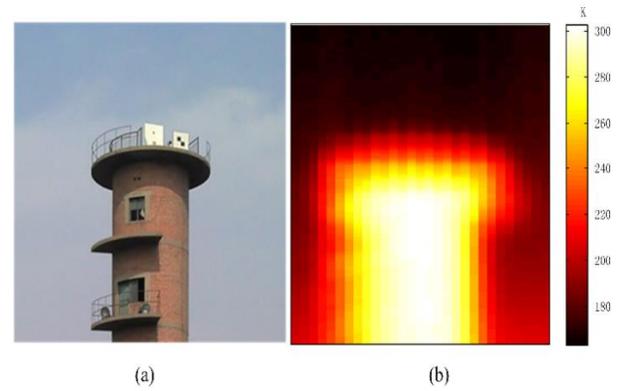
Fig. 6. (a) A picture and (b) a MMW passive image of the tower.

VI CONCLUSION

In this paper, the sensitivity analysis and tipping curve calibration of a developed radiometer for radiometric characterization are presented. The experimental results show that the radiometer sensitivity is 0.51 K with the integration time of 1 s, and the maximum mean measurement brightness temperature difference between tipping curve and liquid nitrogen calibration is 2.48 K for the clear sky and prove the accuracy of tipping calibration. Though the developed radiometer has a mediocre sensitivity due to a high noise figure, the sensitivity of this type of radiometer working at microwave frequencies will be heightened greatly for the noise figure improvements and it will have a great potential for non-contact biomedical sensing. In addition, the tipping calibration presented in this paper will also be promising for the calibration of radiometers in biomedical applications.

ACKNOWLEDGMENT

REFERENCES

[1] Q. Bonds, J. Gerig, T. M. Weller, and P. Herzig, "Towards core body temperature measurement via close proximity radiometric sensing," *IEEE Sensors J.*, vol. 12, no. 3, pp. 519-526, 2012.

[2] Z. Popovic, P. Momenroodaki, and R. Scheeler, "Toward wearable wireless thermometers for internal body temperature measurements," *IEEE Commun. Mag.*, vol. 52, no. 10, pp. 118-125, 2014.

[3] F. Bardati and S. Iudicello, "Modeling the visibility of breast malignancy by a microwave radiometer," *IEEE Trans. Biomed. Eng.*, vol. 55, no. 1, pp. 214-221, 2008.

[4] K. Arunachalam, P. R. Stauffer, P. F. Maccarini, S. Jacobsen, and F. Sterzer, "Characterization of a digital microwave radiometry system for noninvasive thermometry using a temperature controlled homogeneous test load," *Phys. Med. Biol.*, vol. 53, no. 14, 2008.

[5] R. Scheeler, E. F. Kuester, and Z. Popovic, "Sensing depth of microwave radiation for Internal body temperature measurement," *IEEE Trans. Antennas Propagat.*, vol. 62, no. 3, pp. 1293-1303, 2014.

[6] C. Liu, Y. X. Guo, and S. Xiao, "Circularly polarized helical antenna for ISM-band ingestible capsule endoscope systems," *IEEE Trans. Antennas Propagat.*, vol. 62, no. 12, pp. 6027-6039, 2014.

[7] S. Yeom, D. S. Lee, Y. S. Jang, M. K. Lee, and S. W. Jung, "Real-time concealed-object detection and recognition with passive millimeter wave imaging," *Opt. Express*, vol. 20, no. 9, pp. 9371-9381, 2012.

[8] B. Quenton, T. Weller, B. Roeder, and P. Herzig, "A total power radiometer (TPR) and measurement test bed for non-contact biomedical sensing applications," *IEEE 10th Annual Wireless and Microwave Technology Conference*, Clearwater, Florida, USA, pp. 1-5, April 2009.

[9] Ø. Klemetsen, Y. Birkelund, S. K. Jacobsen, P. F., Maccarini, and P. R. Stauffer, "Design of medical radiometer front-end for improved performance," *Prog. Electromagn. Res. B.*, vol. 27, pp. 289-306, 2011.

[10] T. Sugiura, H. Hirata, J. W. Hand, J. M. J. Van Leeuwen, and S. Mizushina, "Five-band microwave radiometer system for noninvasive brain temperature measurement in newborn babies: Phantom experiment and confidence interval," *Radio Sci.*, vol. 46, RS0F08, 2011.

[11] J. J. Lynch and R. G. Nagele, "Flicker noise effects in noise adding radiometers," *IEEE Trans. Microw. Theory Techn.*, vol. 59, no. 1, pp. 196-205, 2011.

[12] F. Alimenti, S. Bonafoni, and S. Leone, "A low-cost microwave radiometer for the detection of fire in forest environments," *IEEE Trans. Geosci. Remote Sens.*, vol. 46, no. 9, pp. 2632-2643, 2008.

[13] S. S. Peng, L. Wu, X. H. Ying, and Z. C. Xu, "A receiver in a millimeter wave radiometer for atmosphere remote sensing," *J. Infrared Millim. Terahertz Waves*, vol. 30, no. 3, pp. 259-269, 2009.

[14] S. S. Peng, L. Wu, and X. Q. Li, "Design of 300 mm W-band radiometer offset-feed reflector antenna," *J. Infrared Millim. Terahertz Waves*, vol. 32, no. 6, pp. 545-549, 2013.

[15] Y. Han and E. R. Westwater, "Analysis and improvement of tipping calibration for ground-based microwave radiometers," *IEEE Trans. Geosci. Remote Sens.*, vol. 38, no. 3, pp. 1260-1276, 2000.

[16] J. M. Li, L. X. Guo, L. K. Lin, Y. Y. Zhao, and X. H. Cheng, "A new method of tipping calibration for ground-based microwave radiometer in cloudy atmosphere," *IEEE Trans. Geosci. Remote Sens.*, vol. 52, no. 9, pp. 5506-5513, 2014.

[17] M. S. Hersman and A. P. Gene, "Sensitivity of the total power radiometer with periodic absolute calibration," *IEEE Trans. Microw. Theory Techn.*, vol. 29, no. 1, pp. 32-40, 1981.

[18] F. T. Ulaby, R. K. Moore, and A. K. Fung, *Microwave Remote Sensing-Active and Passive, vol. I: Microwave Remote Sensing Fundamentals and Radiometry*, Artech House, Norwood MA, 1981.

[19] L. Gui, K. Chen, L. Lang, and W. Guo, "The sensitivity analysis of full digital compensatory MMW radiometer," *Int. J. Infrared Millimeter Waves*, vol. 28, no. 7, pp. 579-585, 2007.

[20] C. Mätzler, "Ground-based observations of atmospheric radiation at 5, 10, 21, 35, and 94 GHz," *Radio Sci.*, vol. 27, no. 3, pp. 403-415, 1992.

[21] W. N Hardy, "Precision temperature reference for microwave radiometry," *IEEE Trans. Microw. Theory Techn.*, vol. 21, no. 3, pp. 149-150, 1973.

[22] H. J. Liebe, "MPM—An atmospheric millimeter-wave propagation model," *Int. J. Infrared Millimeter Waves*, vol. 10, no. 6, pp. 631-650, 1989.

Li Wu received the B.S., M.S. and Ph.D. degrees all in Electrical Engineering from Nanjing University of Science and Technology (NUST), Nanjing, China, in 2003, 2005 and 2009, respectively. Since 2009, he has been a Lecturer with the School of Electronic and Optical Engineering at NUST. His research interests involve passive imaging, remote sensing, millimeter wave radar system and application.

Shusheng Peng received his B.S. degree from Xiamen University in 1987, M.S. degree from Xi'an Institute of Space Radio Technology in 1990 and Ph.D. degree from Purple Mountain Observatory, Chinese Academy of Sciences in 1995. Since 1997, he has been an Associate Professor and then a Professor with the School

of Electronic and Optical Engineering at NUST. His current research interests include millimeter wave detection technology, microwave and millimeter wave radiation measurement technology, the application of embedded system and intelligent sensing and measurement technology.

Scalable GPU-Parallelized FDTD Method for Analysis of Large-Scale Electromagnetic Dosimetry Problems

Jerdvisanop Chakarothai, Kanako Wake, and Soichi Watanabe

Electromagnetic Compatibility Laboratory
National Institute of Information and Communications Technology, Tokyo, 184-8795, Japan
jerd@nict.go.jp, kana@nict.go.jp, wata@nict.go.jp

Abstract ─ A massively parallel finite-difference time-domain (FDTD) method using a GPU cluster of TSUBAME system has been developed for numerical exposure of a human body to electromagnetic fields. We have also developed and implemented a novel approach for tracing total energy absorbed into a human body in our parallel FDTD code. Our developed FDTD code has shown a strong scalability using 216 nodes and 648 GPUs in total with a high capability to calculate over ten billion cells per second. Whole-body specific absorption rate (SAR) at 200 MHz, as well as its distribution, of a human body with a 0.5 mm resolution with 40000 time steps was found in less than approximately three hours, showing the availability of the method for large-scale EM dosimetry problems.

Index Terms ─ Exposure assessment, GPU acceleration, parallel FDTD method, scalability, specific absorption rate.

I. INTRODUCTION

Numerical electromagnetic (EM) simulation using an anatomically realistic human model has recently been performed in many engineering fields including medical applications and investigation on EM biological effects [1]. The finite-difference time-domain (FDTD) method [2, 3] is useful for these studies with an application of realistic human model. Recently, many of finely-detailed realistic whole-body human voxel models have been developed by numerous academic groups and research institutes [4-7]. One of the examples is an anatomically realistic human voxel model of a Japanese adult male and female, and children, developed by National Institute of Information and Communications Technology, Japan [5, 6]. These models have a complex shape and structure of internal organs. Computation of the absorbed energy or the specific absorption rate (SAR) in such a detailed model actually requires the use of high-performance computation systems because a large scale of the models actually results in heavy burdens of computation. Specifically, dosimetry of induced electric field inside a human body, relating to stimulation effect by a trigger of

action potential in nervous cells at MHz-band frequencies, requires analyses of a finely-detailed human model with a resolution less than 1 mm [8]. Analysis of such a fine model will consume very large memory and could take prohibitively long calculation time by using a single workstation.

By virtue of the rapid development of computer industry, other types of processing units like Graphics Processing Unit (GPU) and Many Integrated Core (MIC) Architecture have been developed in order to improve the computation efficiency. Calculation algorithm of the FDTD method is seen suitable for such parallel computation since it requires only field information at the adjacent grid point for the communication between computing nodes. Nagaoka et al. [9] used multi-GPU system (3 GPUs/node) for FDTD simulations to cover a small memory size of a single GPU card, and achieved a speedup rate of 1.5 times compared to NEC SX-8R supercomputer. Kim and Park [10] used the overlap communication model in order to increase efficiency of parallelization. Xu et al. [11] used up to 80 NVIDIA Tesla K20 GPUs for FDTD simulations without a boundary and they found a linear scalability with parallel efficiency of higher than 95%.

In this paper, we implement a parallel FDTD algorithm for numerical EM exposure assessment of finely-detailed human model on the TSUBAME GPU cluster at Tokyo Institute of Technology, Japan. Different from previous implementation of parallel FDTD method on a GPU cluster [9], where it used only z-axis decomposition of the model to map the E and H data into each GPU's memory, our implementation apply a 3D/1D hybrid domain decomposition, in which the total analysis domain is divided into small regions along three axes (*x*, *y*, and *z*), and those regions for each node are further divided along one-dimensional axis into sub-regions to be mapped into each GPU in a node. By using this domain decomposition approach, the communication between nodes is kept as less as possible. An approach for tracing the whole-body SAR in time domain is also implemented in Section II. We first investigate performance of the parallel FDTD method on

TSUBAME systems, then discuss the validity of the method and parallel performance results in Section III. In Section IV, an application of the FDTD method to numerical EM exposure assessment of a realistic human model is demonstrated and the conclusion is eventually drawn in Section V.

II. IMPLEMENTATION OF PARALLEL FDTD METHOD ON GPU CLUSTER

GPU has a hierarchical memory structure and it consists of more than 2,000 computing cores (known as CUDA cores), depending on the generation and type of the GPU. In order for a GPU to reach its best performance, we have to consider GPU architecture in the implementation. Here we use an Integrated Development Environment of CUDA, provided by NVIDIA Corp. for GPU programming [12].

In this paper, we adopt the scattered-field formulation of the FDTD method so as to enable arbitrary incident field as a source. The update equations of the scattered-field FDTD method are derived by discretizing the Maxwell's equations, and for an interest reader, the detail of the FDTD formulation can be found in [4].

A. New approach for tracing whole-body SAR in time course

Here we use a new algorithm for determining whole-body average SAR or total absorption energy in a biological body for finding convergence of the FDTD solution. First, assume that we have two identical problem domains but their incident EM fields have a constant phase difference equal to a specific difference of $\Delta\theta$ at every grid point in the analysis domain as shown in Fig. 1, the field solutions for both problem domains will result in the same phase difference of $\Delta\theta$. The FDTD solutions obtained from each analysis domain, applying a single-frequency continuous sinusoidal waveform as incident EM fields, are also represented in the sinusoidal form as follows:

$$X_1(t) = A\sin(\omega t + \theta_1) \text{ for domain } D_1, \quad (1)$$
$$X_2(t) = A\sin(\omega t + \theta_2) \text{ for domain } D_2, \quad (2)$$

where $X_1(t)$ and $X_2(t)$ are the FDTD-calculated quantities; e.g., electric or magnetic fields, at the same location in the problem domain D_1 and D_2, respectively. A represents magnitude of the field solution which is equal in both analysis domains, θ_1 and θ_2 are the phase of the solutions in D_1 and D_2, respectively. The phase difference has a known constant value, i.e., $\Delta\theta = \theta_2 - \theta_1$. We can determine the cosine components of the solution by substituting $\Delta\theta$ into (2) and obtain:

$$X_2(t) = A\sin(\omega t + \theta_1 + \Delta\theta)$$
$$= AX_1(t)\cos(\Delta\theta) + A\cos(\omega t + \theta_1)\sin(\Delta\theta),$$
$$A\cos(\omega t + \theta_1) = \frac{X_2(t) - X_1(t)\cos(\Delta\theta)}{\sin(\Delta\theta)}. \quad (3)$$

Therefore, a square of the field magnitude A at arbitrary location in the problem domain is eventually found as:

$$A^2 = X_1^2(t) + \frac{[X_2(t) - X_1(t)\cos(\Delta\theta)]^2}{\sin^2(\Delta\theta)}$$
$$= \frac{X_1^2(t) + X_2^2(t) - 2X_1(t)X_2(t)\cos(\Delta\theta)}{\sin^2(\Delta\theta)}. \quad (4)$$

Meanwhile, the specific absorption rate (SAR) at arbitrary location in biological tissues is defined by the following equations:

$$\text{SAR} = \frac{\sigma}{2\rho}|\mathbf{E}|^2 = \frac{\sigma}{2\rho}\left(E_x^2 + E_y^2 + E_z^2\right), \quad (5)$$

where σ and ρ are the conductivity and density of the biological tissues. Therefore, Eq. (4) can be used for finding a square of electric field components in (5). The whole-body average SAR is then found by dividing total absorption energy with its weight W,

$$\text{WBSAR} = \frac{\sum \rho\text{SAR}}{W}. \quad (6)$$

In this way, we can determine whole-body SAR or total energy absorbed into a human body at any instant in time course and decide whether or not the solution reaches convergence in order to terminate the computation. This algorithm can be easily implemented into the conventional FDTD code by calculating an identical problem domain having an incident field of a constant phase difference in parallel.

$$\mathbf{E}_1^{inc} = \hat{p}K\sin(\omega t + \theta_1') \qquad \mathbf{E}_2^{inc} = \hat{p}K\sin(\omega t + \theta_2')$$
$$X_1 = A\sin(\omega t + \theta_1) \qquad X_2 = A\sin(\omega t + \theta_2)$$
$$\theta_2 - \theta_1 = \theta_2' - \theta_1' = \Delta\theta$$
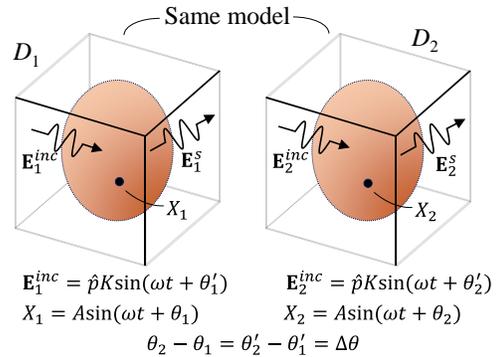
Fig. 1. Concept of an approach for determination of the whole-body average SAR in time course by defining two identical problem domain D_1 and D_2 with an incident field having a constant phase difference of $\Delta\theta = \theta_2' - \theta_1'$. K and A are the magnitude of the incident electric field $\mathbf{E}_{1,2}^{inc}$ and the FDTD-calculated field of the solution, respectively, $\hat{p}$ is the polarization vector.

B. Parallel FDTD implementation on GPU cluster

In order to employ multiple GPUs for the FDTD calculation, we adopt a hybrid 3D/1D domain decomposition as shown in Fig. 2. The whole FDTD analysis region is divided into several regions for each node in a three-dimensional way so as to reduce data size for the communications between nodes. Since each node

contains multiple GPUs, all divided regions are again decomposed into sub-regions in one-dimensional axis, and mapped to each GPU in a node. N_x, N_y, and N_z are number of voxels in x, y, and z axes, respectively. Total number of regions is equal to $M_x \times M_y \times M_z$, where M_x, M_y, and M_z are number of blocks in x, y, and z axes, respectively. Obviously, there are $(N_x/M_x) \times (N_y/M_y) \times (N_z/M_z)$ voxels for each region. Each region is then decomposed in one dimensional way in the z axis in order to be mapped in each GPU memory in an individual node. Size of the region associated to each GPU is equal to $(N_x/M_x) \times (N_y/M_y) \times (N_z/(N_{GPU}M_z))$ voxels, where N_{GPU} denotes number of GPUs in each node.
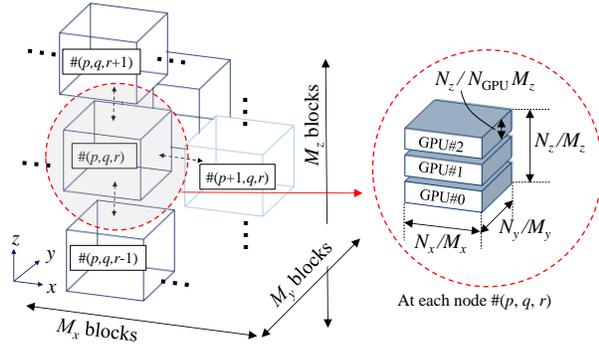
Fig. 2. Hybrid 3D/1D domain decomposition for multi-GPU computation. Total region is divided into M_x, M_y, and M_z blocks along the x, y, and z axes. Each block, corresponding to each computation node in the cluster, has a size of $(N_x/M_x) \times (N_y/M_y) \times (N_z/M_z)$ cells, where N_x, N_y, and N_z are number of voxels in x, y, and z directions. Each block is divided into many sub-regions along z axis and assigned to each GPU in computing nodes. p, q, and r indicate block index in x, y, and z axes, respectively.

Since the FDTD method is based on a finite difference scheme, electric and magnetic fields at a grid point are updated by referring information at the adjacent grid point. At the boundary, since the adjacent grid data resides in another GPU memory, we need to copy the data from one GPU memory to another GPU memory. The process of communications in the GPU cluster consists of three steps: (a) memory copy from GPU to host; (b) MPI send and receive communications; (c) memory copy from host to GPU. The communications between two nodes for electric field data in the GPU cluster are schematically shown in Fig. 3. Since the data in a node is mapped to multiple GPUs and the data in GPU memory does not locate in a consecutive order, so we need to rearrange the data to a consecutive temporary memory in each GPU in order to be copied once to the host memory and then we collect the data from each GPU and copy to the host memory for the boundary data at the left (-x) and front (-y) direction (see Fig. 3). The boundary data in the (-z) direction is arranged in a

consecutive way. Therefore, the consecutive data at the -z boundary can be directly copied from the GPU memory to the host node memory. Internode communications are done by using 'MPI_send' and 'MPI_receive' command of the MPI (Message Passing Interface). After the communications, the data must be copied back to the GPU memory and mapped to the original location in the memory for each GPU as shown in Fig. 3. The data flow for the magnetic field data and the internode communications are the same but in a reverse direction. It should be noted that the communications between the GPUs inside a node can be done effectively and directly by using the NIVIDIA GPUdirect function of 'cudaMemcpyPeer' [11].
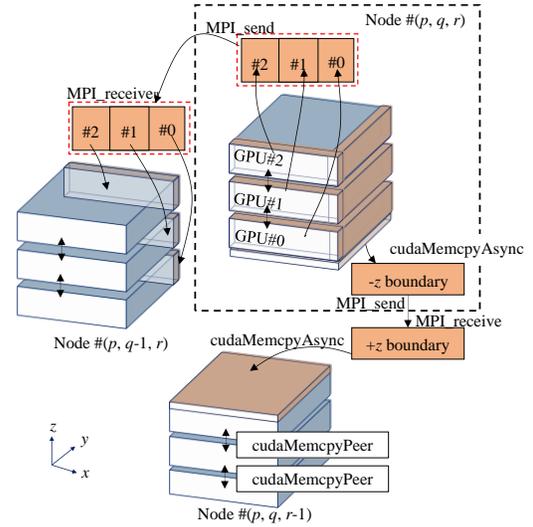
Fig. 3. Communications between nodes for electric field data. The electric field data at the front (-y) faces are gathered into one package before sending to another node by 'MPI_send' command while the data at the bottom (-z) face is retrieved only from the GPU index #0 and sent to the GPU index #2 of another node. Data communications between GPUs inside a node is directly done by the 'cudaMemcpyPeer' command. The data communications at the left (-x) face is done in the same manner with that of the front face. Data flow of the internode communications for magnetic field are performed in reverse way.

Figure 4 illustrates the program flowchart of the FDTD computation in the GPU cluster. First, in order to perform calculation on a GPU cluster, we need to transfer material data of a human model to GPU memory. The loop of the FDTD calculation is then started with update of the electric field data. It should be noted that some special treatment and calculation; e.g., separate memory allocation, for the field data at the PML boundaries is required. The SAR of each cell is also determined via (6) in this step. It is apparent that the SAR

calculation method proposed in this paper requires that analyses of two identical models with incident fields having phase different are simultaneously performed on the same GPU node. Consequently, memory usage and computation burden are also twice of the original FDTD method. After updating the electric field, the field data at the boundary between GPUs inside a node is directly transferred with the 'GPUdirect' function, whereas the boundary data must be packed into one bundle to reduce number and time of communications. The data bundle in the GPU memory is then transferred to the host memory and communicated through MPI functions. Before updating magnetic field, the boundary data is then copied back to the GPU memory and unpacked to the original grid points. After updating magnetic fields and those at the PML boundaries, the inter-GPU and internode communications are performed in the same way with those done for electric field data. The loop is repeated until the whole-body SAR or total absorbed energy reaches convergence and the calculated electric and magnetic fields are finally copied to the host memory.
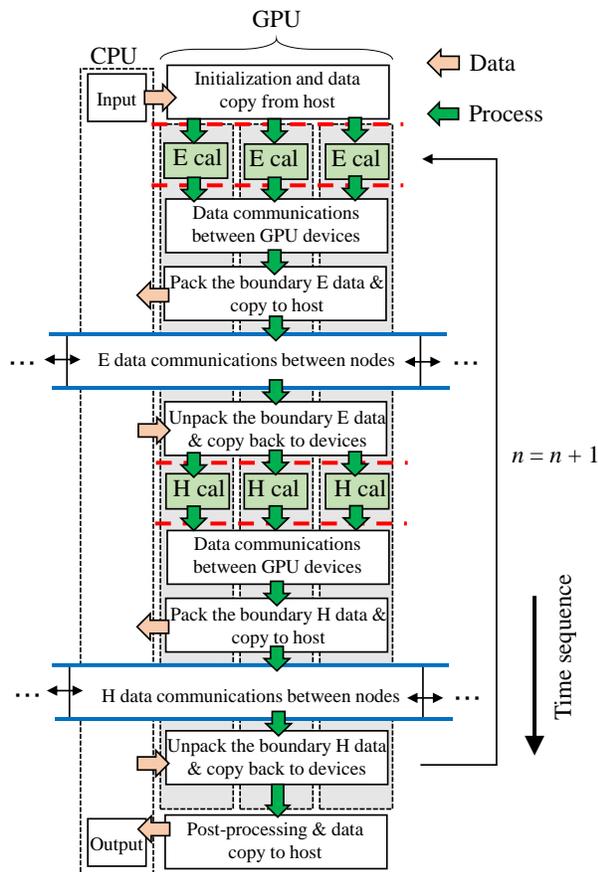
Fig. 4. Illustrative flowchart of the FDTD computation in a computing node. Dash line indicates synchronization between GPU devices (red dotted line) and MPI barrier between nodes (blue solid line).

In order to improve the GPU performance, all three-dimensional field data are allocated as one-dimensional array. Second, the communications between the GPUs inside a node are performed in an asynchronous mode. The asynchronous mode takes advantage of the GPU computational power and PCIe bandwidth. Third, the data for the front and left boundaries (x and y directions as shown in Fig. 3) is not continuous in the GPU memory so that the data packing is required, while the continuous data of the z boundary is directly transferred to the host memory and between nodes.

III. NUMERICAL RESULTS

A. Validity of parallel FDTD code

Most of our simulations are compiled and executed on a large-scale GPU cluster of TSUBAME2.5 system at Tokyo Institute of Technology, Japan. TSUBAME2.5 system has in total 1408 computing nodes. Each node in the GPU cluster is configured with two Intel Westmere-EP X5670 2.93 GHz (Turbo boost 3.2 GHz) of six cores per CPU, and equipped with three NVIDIA Tesla K20x GPUs in each node. There are 1367 computing nodes with 54 GB memory (DDR3-1333) and 41 nodes with 96 GB memory for each. All nodes are connected by two HP QDR InfiniBand. Peak performances of the total system for double- and single-precision floating points are 5.76 PFlops and 17.1 PFlops, respectively, ranking in the 22th fastest supercomputer in Top500 (List of June 2015) [13]. The FDTD code was written using C++ and CUDA using single-precision floating point for calculations which is considered to be sufficient for our dosimetry applications. Number of CUDA threads is fixed to 125 in all numerical experiments. Numerical results obtained from the GPU cluster are also compared to those obtained from an HP workstation equipped with two Intel Xeon CPU E5-2643v3 (3.4 GHz) of six cores (12 threads) per CPU. Main memory of the workstation is 96 GB. Phase difference of incident field of two identical analysis models was set to 90° or $\pi/2$ in all calculations.

Whole-body SAR of a dielectric sphere having a radius of 20 cm, and dielectric properties of $\varepsilon_r = 2$ and $\sigma = 0.1$ S/m, illuminated by a plane wave at 200 MHz, is shown in Fig. 5. Strength of incident electric field is 1 V/m. Total size of analysis region was 256×256×256 cells with a resolution of 2 mm in each axis. Number of calculation time steps was approximately 3000 steps. From Fig. 5, it can be seen that by using a new approach described in Section II, we can trace the whole-body SAR in time course. It is also observed that the whole-body SAR converged within two periods. Therefore, the calculation time can be kept as minimum as possible by using the proposed method. The calculation using GPUs was performed on TSUBAME system using only single node and three GPUs. The whole-body SARs obtained

by CPU (24 parallel threads) and GPU calculations were determined as 8.54 μW/kg and 8.52 μW/kg, respectively, showing good agreement of that obtained by analytic Mie's solution of 8.42 μW/kg. Errors between the Mie's result and the FDTD method were about 1.38% and 1.12% for the CPU and GPU computations, respectively, demonstrating the validity of the method. Figure 6 shows the SAR distribution obtained from each method. It is shown that the SAR distributions of the sphere obtained by the CPU and GPUs are in good agreement with the Mie's solution.
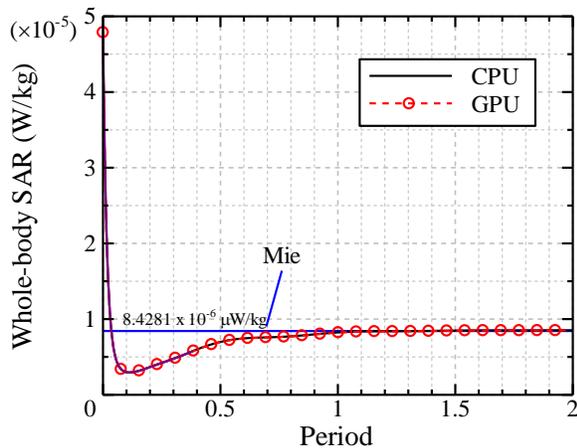
Fig. 5. Whole-body SAR of a dielectric sphere in time course, calculated by a workstation (24 parallel threads) and three GPUs (single node) on TSUBAME system.
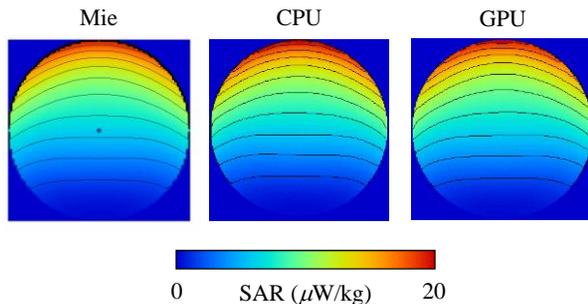
Fig. 6. SAR distribution of a dielectric sphere illuminated by a plane wave at 200 MHz, by the Mie's solution, and those obtained from the CPU and GPU computations.

B. Scalability and parallelization efficiency

We use a hybrid 3D/1D domain decomposition and the parallel FDTD method described in the previous section for an analysis of a dielectric sphere. In order to demonstrate a scalability of a large-scale EM simulation,

sizes of analysis model of 256^3, 512^3, and 1024^3 voxels with a resolution of 2 mm, 1 mm, and 0.5 mm, respectively, were used in the analyses. Number of time steps was 1000 steps in all simulations. Analysis model is a dielectric sphere illuminated with a plane wave at 200 MHz, same with that described in previous subsection.

Figure 7 shows scalability of the computation using multiple computing nodes of TSUBAME system. Vertical axis shows a number of cells divided by calculation time per a time step, indicating how much Yee's cells we can manipulate within a second. The ideal curve was calculated from the result of the 256^3 model calculated using three GPUs; i.e., the ideal number of cells/second N^{ideal} is determined as:

$$N^{\text{ideal}} = \frac{N_{\text{GPU}}}{3} \times N^{\text{3GPUs}}, \qquad (7)$$

where N^{3GPUs} is a number of cells calculated in a second when using three GPUs for the 256^3 model. Horizontal axis indicates a number of GPUs used in the simulations. The black dash line shows the ideal scalability. Our parallel FDTD method shows a strong scalability for a problem domain even when an analysis size grows up to 1024^3 cells. Highest performance using 648 GPUs in parallel was achieved at more than 12 billion cells per second. To the extent of the authors' knowledge, this result is the highest performance achieved by using a GPU cluster for the FDTD method. Table 1 shows the parallelization efficiency of the method varied by number of GPUs used in the simulation. The efficiency of parallelization is determined from a ratio of the real time used in the simulation and the expected time used for ideal parallelization. When number of GPUs is equal to three, there is no field data communications between nodes. The only existing communications is occurred between GPUs in a single computing node, which is performed by using fast GPUdirect technology provided by NVIDIA Corp [12]. The parallelization efficiency decreases as number of GPUs increases due to increase in data communications between nodes. Efficiency achieved by using 648 GPUs in parallel was about 57.1%. Speedup ratios using 180 GPUs and 648 GPUs in parallel were about 91 times and 290 times, respectively, compared to the calculation time used by the 24-cores-in-parallel workstation for the model size of 512^3 cells and 1024^3 cells. It should be noted that the FDTD method used in our simulations requires two identical models to be analyzed at the same time, and therefore computational burden is almost twice of the original FDTD method. Number of time steps can be, however, kept as minimum as possible and the calculation is terminated as soon as the whole-body SAR reaches its convergence in time domain.
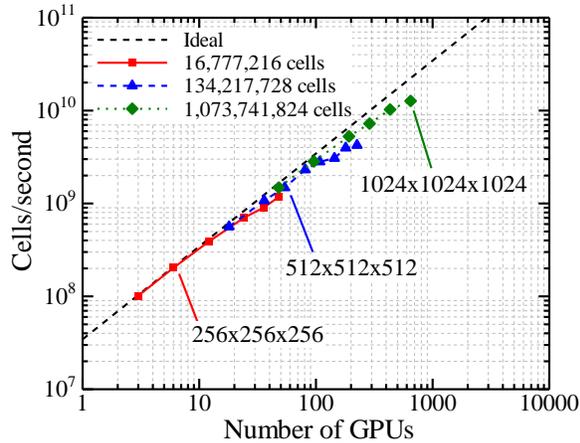
Fig. 7. Scalability for three problem sizes $N = 256^3$, 512^3, and 1024^3 on TSUBAME system at Tokyo Institute of Technology, Japan.

Table 1: Number of calculated cells per second and parallelization efficiency for various calculated conditions

Number of GPUs	Used Time Per Step (s)	Number of Cells Per Time Step	Efficiency
Model Size : 256×256×256			
3	0.1629	102,964,265	100.0%
6	0.0827	202,815,601	98.4%
12	0.0433	387,051,310	94.0%
24	0.0240	698,846,918	84.8%
48	0.0143	1,176,439,090	71.4%
Model Size : 512×512×512			
18	0.2389	561,866,603	91.0%
36	0.1250	1,074,102,769	86.9%
54	0.0905	1,483,221,863	80.0%
108	0.0477	2,813,593,720	75.9%
180	0.0338	3,965,555,632	64.2%
Model size : 1024×1024×1024			
48	0.7240	1,482,935,432	90.0%
96	0.3790	2,833,282,897	86.0%
192	0.2052	5,271,676,808	80.0%
432	0.1054	10,257,114,978	69.2%
648	0.0859	12,694,231,253	57.1%

IV. APPLICATION TO DOSIMETRY

Here we employ our parallel FDTD method to a practical problem of EM exposure assessment of a human body. We use a Japanese male model developed by National Institute of Information and Communications Technology, Japan [5]. The model is composed of 51 different tissues and organs with an original resolution of 2 mm. Height and weight of the model were 173 cm and 64 kg, respectively. The permittivity and conductivity of biological tissues are extracted from the Gabriel's data [14]. Figure 8 shows analysis model of a realistic human model, irradiated to an EM plane wave at 200 MHz. The propagation direction of the z-polarized incident plane wave was along $+x$ direction. Total sizes of analysis domain are 190×350×896, 350×670×1767, and 670×1310×3498 cells for a model resolution of 2 mm, 1 mm, and 0.5 mm respectively. Maximum number of time step was 10000, 20000, and 40000 steps for the 2 mm, 1 mm, and 0.5 mm models, respectively.

Figure 9 indicates the whole-body average SAR of human body in time course, excited by a plane wave at 200 MHz. It is obvious that the WBSAR converges to a constant value within five periods. The WBSAR of the human with 2 mm, 1 mm, and 0.5 mm resolutions was calculated as 13.6 μW/kg, 13.9 μW/kg, and 14.0 μW/kg, respectively, for an incident electric field strength of 1 V/m. Calculation time in finding the whole-body SAR for 2 mm resolution was approximately 227 minutes using a 24-core (3.5 GHz) workstation with OpenMP, while it was only 13 minutes when using 24 GPUs which is about 17 times faster. The dosimetry analysis of the whole human model with a 1 mm resolution takes about 85 minutes by using 54 GPUs in parallel, which was approximately 47 times faster than computation by our 24-core workstation. The calculation time for the 0.5 mm model with 40000 time steps was less than 3 hours (175 minutes). Figure 10 illustrates the SAR distribution calculated by using the GPU cluster with 24, 54, and 432 GPUs. The SAR distributions obtained by either the workstation or the GPU cluster of TSUBAME are in good agreement each other, showing availability and efficiency of our parallel FDTD code in use with the GPU cluster. From our results, speedup ratio can be achieved at a rate of more than a thousand times faster than using a single-core workstation, depending on number of GPUs used in analysis.
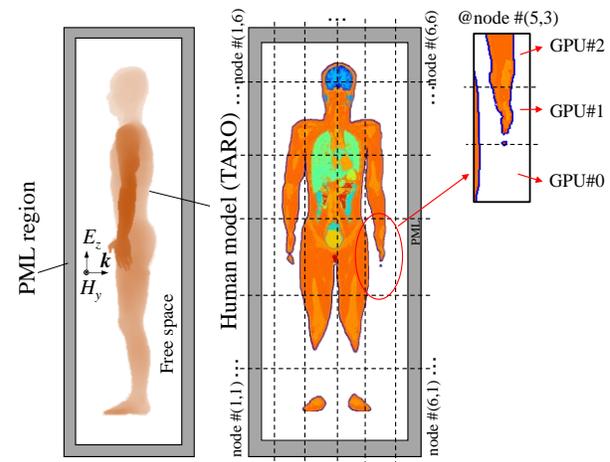
Fig. 8. Analysis model of EM exposure assessment of a realistic human model and the model decomposition into 6×6 blocks in yz-plane. Each block corresponds to a computation node with three GPUs inside.
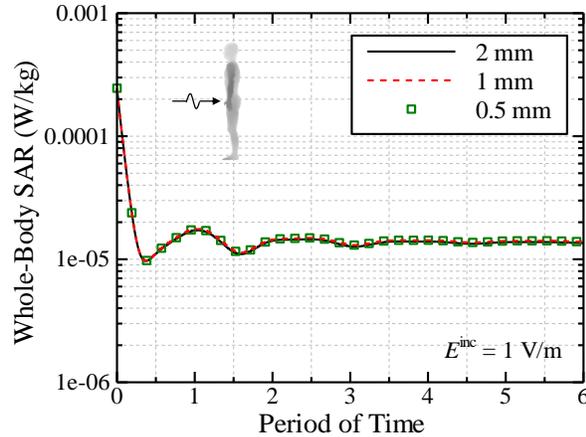
Fig. 9. Whole-body SAR with respect to period of actual time for 2 mm, 1 mm, and 0.5 mm human models.
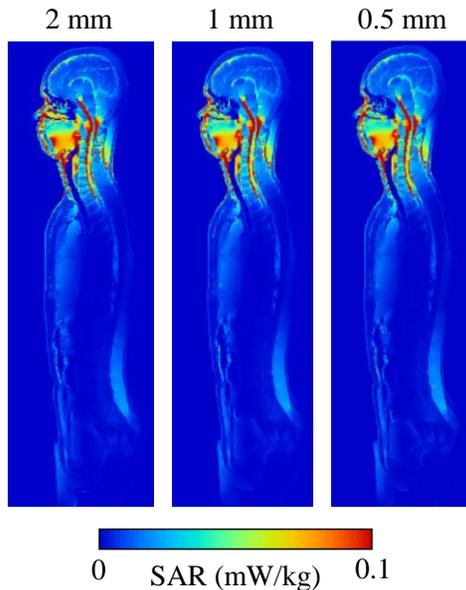
Fig. 10. SAR distribution in the human models.

V. CONCLUSION

A scalable and parallel finite-difference time-domain method for a large-scale electromagnetic simulation of human exposures using the GPU cluster of TSUBAME system has been developed. A novel approach for tracing the convergence of the whole-body SAR in a time course has also been adapted in our FDTD-GPU code. Validity of the method was demonstrated by comparing with the analytical Mie's results of the dielectric sphere. Strong scalability with parallelization efficiency of 57% has been found for an analysis model size up to 1024^3 grid cells using 216 nodes and 648 GPUs in total. High performance of the FDTD calculation with more than 12 billion cells per second can be achieved using in total 648 GPUs in parallel. Finally, the numerical exposure of

a human body having a resolution of 0.5 mm and a model size of 670×1310×3498 cells, irradiated by EM plane wave at 200 MHz, has been performed and the simulation was terminated in about 175 minutes for 40000 time steps using 144 nodes with 432 GPUs of TSUBAME system. A high computation performance of our parallel FDTD method for large-scale EM dosimetry has been demonstrated and achieved by using the GPU cluster of TSUBAME system.

The analysis of a signal triggered in human nervous system due to EM exposures at MHz-band frequencies will be done by using the TSUBAME GPU cluster in the future.

REFERENCES

[1] D. M. Sullivan, D. T. Borup, and O. P. Gandhi, "Use of the finite-difference time-domain method in calculating EM absorption in human tissues," *IEEE Trans. Biomedical Engineering*, vol. BME-34, no. 2, pp. 148-157, Feb. 1987.

[2] K. S. Yee, "Numerical solution of initial boundary value problems involving Maxwell's equations in isotropic media," *IEEE Trans. Antennas Propag.*, vol. 14, no. 4, pp. 302-307, 1966.

[3] K. S. Kunz and R. J. Luebbers, *The Finite Difference Time Domain Method for Electromagnetics*, CRC Press, May 3, 1993.

[4] P. J. Dimbylow, "FDTD calculations of the whole-body averaged SAR in an anatomically realistic voxel model of the human body from 1 MHz to 1 GHz," *Phys. Med. Biol.*, vol. 42, pp. 479-490, 1997.

[5] T. Nagaoka, S. Watanabe, K. Sakurai, E. Kunieda, S. Watanabe, M. Taki, and Y. Yamanaka, "Development of realistic high-resolution whole-body voxel models of Japanese adult and females of average height and weight, and application of models to radio-frequency electromagnetic field dosimetry," *Phys. Med. Biol.*, vol. 49, pp. 1-15, 2004.

[6] T. Nagaoka, E. Kunieda, and S. Watanabe, "Proportion corrected scaled voxel models for Japanese children and their application to the numerical dosimetry of specific absorption rate for frequencies from 30 MHz to 3 GHz," *Phys. Med. Biol.*, vol. 53, pp. 6695-6711, 2008.

[7] A. Christ, W. Kainz, E. G. Hahn, K. Honegger, M. Zefferer, E. Neufeld, W. Rascher, R. Janka, W. Bautz, J. Chen, B. Kiefer, P. Schmitt, H.-P.

Hollenbach, J. Shen, M. Oberle, D. Szczerba, A. Kam, J. W. Guag, and N. Kuster, "The virtual family – development of surface-based anatomical models of two adults and two children for dosimetric simulations," *Phys. Med. Biol.*, vol. 55, pp. N23-N38, 2010.

[8]   I. Laakso, H. Matsumoto, A. Hirata, Y. Terao, R. Hanajima, and Y. Ugawa, "Multi-scale simulations predict responses to non-invasive nerve root stimulation," *J. Neural Eng.*, vol. 11, pp. 1-9, 2014.

[9]   T. Nagaoka and S. Watanabe, "Accelerating three-dimensional FDTD calculations on GPU clusters for electromagnetic field simulation," in *Proceedings of the Annual International Conference of the IEEE Engineering in Medicine and Biology Society* (EMBC'12), pp. 5691-5694, 2012.

[10] K. H. Kim and Q. H. Park, "Overlapping computation and communication of three-dimensional FDTD on a GPU cluster," *Computer Physics Communications*, vol. 183, pp. 2364-2369, 2012.

[11] L. Xu, Y. Xu, R. Jiang, and D. Zhang, "Implementation and optimization of three-dimensional UPML-FDTD algorithm on GPU cluster," *Computer Engineering & Science*, vol. 35, p. 160, 2013.

[12] NVIDIA, NVIDIA CUDA programming guide version 4.0, NVIDIA Corporation, 2011.

[13] TOP500 supercomputer, http://www.top500.org

[14] C. Gabriel, "Compilation of the dielectric properties of body tissues at RF and microwave frequencies," *Brooks AFB, San Antonio, TX, Brooks Air Force Tech. Rep.*, AL/OE-TR-1996-0037, 1996.

Jerdvisanop Chakarothai receives his B.E. degree in Electrical and Electronic Engineering from Akita University, Akita, Japan, in 2003 and his M.E. and D.E. degrees from Tohoku University, Sendai, Japan, in 2005 and 2010, respectively, both in Electrical and Communication Engineering.

He was a Research Associate at Tohoku University from 2010, prior to joining the Nagoya Institute of Technology, Nagoya, Japan, in 2011. He was a Research Associate at Tokyo Metropolitan University in 2013. He is currently with the National Institute of Information and Communications Technology, Tokyo, Japan. His research interests include computational bio-electro-magnetics and electromagnetic compatibility. He received the 2014 Young Scientist Award from the International Scientific Radio Union.

Kanako Wake received her B.E., M.E. and D.E. degrees in Electrical Engineering from Tokyo Metropolitan University, Tokyo, Japan, in 1995, 1997, and 2000, respectively.

She is currently with the National Institute of Information and Communications Technology, Tokyo, Japan, where she is involved in research on biomedical electromagnetic compatibility.

Soichi Watanabe received the B.E., M.E. and D.E. degrees in Electrical Engineering from Tokyo Metropolitan University, Tokyo, Japan, in 1991, 1993, and 1996, respectively.

He is currently with the National Institute of Information and Communications Technology, Tokyo. His main research interest includes biomedical electromagnetic compatibility.

Watanabe is a Member of IEEE and the Bio-electromagnetics Society. From 2004 to 2012, he is a Member of the Main Commission of ICNIRP from 2012. He received the 1996 Young Scientist Award from the International Scientific Radio Union, the 1997 Best Paper Award from IEICE, and the 2004 Best Paper Award (The Roberts Prize) of Physics in Medicine and Biology.

Suppression of Surface Currents at Microwave Frequency Using Graphene-Application to Microwave Cancer Treatment

Hulusi Acikgoz [1] and Raj Mittra [2,3]

[1] Material Science and Nanotechnology Engineering Department
KTO Karatay University, Konya, Turkey
hulusi.acikgoz@karatay.edu.tr

[2] University of Central Florida, Orlando, USA
[3] King Abdulaziz University (KAU), Saudi Arabia
rajmittra@ieee.org

Abstract ─ In this work we consider the problem of surface currents suppression using graphene in the context of microwave cancer treatment. Most of the research on graphene has been focused on its applications at terahertz frequencies, and not at microwave frequencies. The use of microwave cancer ablation technique using a coaxial slot antenna is being limited because of the existence of surface currents which lead to the heating of the healthy tissues along its outer surface. In this work we propose to use graphene which is a single-atom sheet of carbon, as a solution to prevent the propagation of surface currents on the outer conductor of the coaxial antenna. We show that by properly designing and tuning the conductivity of the graphene layer, we can not only suppress the surface currents, but also control the amount of energy deposited in the surrounding tissue.

I. INTRODUCTION

Currently surgery, chemotherapy and radiotherapy are the most widely methods for cancer treatment. We note however, that only 25% of the patients are candidates for surgery, and radiotherapy can treat only 1-2 cm of the targeted area [1]. As for chemotherapy, it has numerous physical and non-physical side effects which affect the life of the patients [2].

The microwave ablation technique has attracted increased attention in recent years, owing to its ability to heat much larger lesion size but with a shorter treatment time. Microwave ablation treatment is performed by using a small interstitial antenna, which radiates electromagnetic energy into the tissue through an aperture positioned at its end. The most common applicator is of coaxial type classified as dipole, monopole or slot antenna [3]. Although these antennas have several important advantages, such as increased power deposition near the aperture within a shorter treatment time, they have drawbacks that prevent them to be considered as alternatives to the RF ablation devices [4], which has witnessed extensive use in recent years. This is because with these antennas, electromagnetic power is not only deposited near the aperture (or slot), but also all the way along the interstitial antenna, towards the feed point. This phenomenon can be primarily associated with the surface currents that travel along the outer conductor of the coaxial antenna and cause an overheating of the healthy tissues in the vicinity of the coaxial line. As can be seen from the discussion presented in the subsequent sections, considerable research has been carried out in attempts to reduce the backward-heating problem, and thereby increase the radiation properties of the antenna. For example, in [5] and [6] the authors have proposed to use cap-chokes or sleeves to impede the propagation of the surface currents. Although the results obtained were somewhat promising, it was found that the surface currents were not completely suppressed and the overheating problem was not eliminated entirely.

In this work, we propose a new approach based on the use of graphene, to reduce the surface currents along the antenna and to maximize the SAR in the region where the cancerous tissue is present. The use of graphene at microwaves is novel, since it has primarily been a potential candidate at terahertz and other applications [7].

The paper is organized as follows: Section II reviews the basics of microwave cancer ablation and proposed techniques to reduce the backward heating problem. Section III presents a review of the properties of the graphene, and its recent electromagnetic applications. The use of a graphene materials as a high impedance surfaces is also discussed in Section III. Numerical results showing the performance of a graphene layer as a wrapper for the coaxial slot antenna

are presented in Section IV.

II. MICROWAVE CANCER ABLATION

Cancer therapy using microwaves energy is based on the interaction between electromagnetic waves and biological tissues. Cell destruction is induced by transferring high microwave energy into the tissue via a thin applicator that we call hereafter "antenna". The heat generated at the targeted cancerous cells increases the tissue temperature locally and leads to a shrinkage of the tumor. Generally, this type of treatment is referred as hyperthermia or thermal therapy. Temperatures ranging between 50-60 °C are needed to have coagulation and necrosis of cells [8]. The physical phenomena behind the hyperthermia is the ability of the high frequency waves to induce oscillation of the polar water molecules contained in the tissue, which in turn causes frictional heating. Hence, microwave heating strongly depends on the water content of the tissue. The more the percentage of water is high the more microwave energy is absorbed into the tissue such as liver, kidney, etc.

Ablation with microwaves have several advantages over the RF ablation methods. For the RF ablation technique, a closed electrical circuit must be created by the use of a ground pad which is the main cause of the skin burn [9]. The electrical conduction of the tissue plays an important role for the tissue heating. As the temperature in the tissue increases during the RF ablation, its impedance increases and the electrical current conduction becomes more difficult. This leads to a restricted area of ablation. Microwaves does not need a high conductivity tissue in order to propagate through it. Thus, the increase in the impedance with the temperature is not a limitation. Therefore, the treatment is faster and larger volume around the antenna can be reached and coagulated [4], [10], [11]. Also, microwaves does not require a ground pad.

A. Microwave antennas as applicators

Microwave energy is transferred to the tissue via an antenna. There has been intensive theoretical, experimental and clinical research to study which type of antenna to use and how to solve problems that occur while performing ablation. The microwave antenna should be minimally invasive, i.e., the organ being ablated must not be damaged by the insertion or contact of the antenna. Also it should be bio-compatible. Generally, in the beginning of its development tumor is localized in a small zone in the tissue. Hence, the aim of the microwave ablation should be highly localizing the microwave energy to this area. Otherwise, an ablation zone larger than that of the tumor can lead to the death of healthy tissues. Moreover, the localized power must be as large as the tumor so that it is completely eradicated. The microwave antenna must be designed so that maximum power is radiated into the tissue. At the operating frequency the return loss, i.e., the reflection coefficient should be as low as possible.

Several antenna types that have followed the design criteria cited above have been proposed in the literature. Monopoles [12], dipoles [13], tri-axials antennas [14], coaxial slot antennas [15], etc., are among the most widely used linear element antennas. Only a few examples of applications using loops [16] and helical [17] antennas exist in the literature. Among the linear element antenna cited above, coaxial slot antenna is one the most widely investigated. It consists of a coaxial line covered by a catheter usually made of Polytetrafluoroethylene (PTFE). The catheter avoid adhesion of the antenna to the ablated tissue. The electromagnetic energy is radiated through a small annular aperture (slot) positioned close to the end of the antenna. The coaxial slot antenna has a relatively low return loss and it concentrates the radiation around the slot. However, in common with other coaxial type antennas, it suffers from unwanted backward heating along the antenna, especially near the region of the feed. This phenomenon can lead to the overheating of the healthy tissues – one of main drawbacks which limits the use of microwaves as an alternative treatment technique in clinics. Some of the works published on this topic are briefly reviewed in the following.

B. Backward heating

Backward heating is attributed to the propagation of surface currents, generated at the slot, between the outer conductor of the coaxial cable and the catheter. Numerous attempts to limit this problem have been made. One of them is to use a cooling system along with the antenna, and either gas or water is used for this purpose [18]. Choked antenna design is a common technique to limit the propagation of surface currents appearing on coaxial antennas [19]. The choke is a metallic ring connected to the outer conductor of the coaxial antenna. Usually a choke length of $\lambda/4$ (λ is the wavelength) is necessary to achieve a good performance with lowest backward heating. In addition to the choke, the use of a cap at the distal end of the antenna has been also proposed [5] to increase the power radiated in the tissue. Sleeve antennas [6] and floating sleeve antennas [20], are some of the designs that are commonly used for the same purpose. In a previous work, the authors have shown that, a double choke element can improve the radiation pattern and further decrease the backward heating, if properly oriented and spaced. Readers interested in learning more about this new design and others on the backward heating reducing techniques are referred to [21]. It appears that the introduction of a choke can substantially increase the radial size of the antenna [22]. This is conflicting with the nature of an interstitial antenna which must be non-invasive. In [22], the authors have proposed to use a miniaturized choke which could lead to a minimally invasive interstitial

heating.

In the present work, we propose a novel approach which is based on the use of a very thin graphene layer (1-atom thick) as a high impedance surface. The low profile is important for microwave cancer ablation because, in contrast to the other techniques, the use of 1-atom thick graphene does not increase the radial size of the antenna. As it will be shown later, at microwave frequencies, the graphene layer could be made to behave as a poor conductor. We take advantage of this highly important characteristic to stop the propagation of surface currents and thereby mitigating the backward heating problem.

III. GRAPHENE

Although the graphene has been known for many decades, it is only in 2014 that a group of researchers isolated it from graphite by means of a simple method using mechanical exfoliation [23]. Since, this novel material which has engendered considerable research activities in fundamental sciences as well as in engineering. Electromagnetics is one these area in which the researchers are attempting to improve devices such as antennas, filters, transistor etc., to achieve improved performances with smaller element sizes. The conductivity of graphene is a tunable parameter, which makes it attractive and useful for many applications. For instance, tunable low pass THz filters [24], graphene-based nano-antennas [25], reconfigurable absorbers [26] are few examples.

The conductivity of the graphene can be expressed following the Kubo's formalism which shows a frequency dependency [27]. It is approximated as the sum of a Drude-like intraband contribution and an interband contribution. At microwaves frequencies, the total conductivity is mostly dominated by the intraband contribution; hence, the interband contribution can be neglected at the frequency region of interest. In a local form, the Drude-like intraband contribution can be expressed as follows [28]:

$$\sigma(\omega) = \frac{2e^2}{\pi\hbar}\frac{k_B T}{\hbar}ln\left[2cosh\left[\frac{\mu_c}{2k_B T}\right]\right]\frac{j}{\omega+j\tau^{-1}}, \qquad (1)$$

where $\tau=10^{-13}$s is the relaxation time, μ_c is the chemical potential, k_B is the Boltzmann's constant, $\hbar$ is the reduced Planck's constant, T is the room temperature in Kelvin, ω is the radian frequency and e is the charge of an electron.

The tunability of the conductivity is due to the presence of the chemical potential μ_c. Indeed, the chemical potential depends on the carrier density which can either be controlled by an electrostatic bias (gate voltage) or a chemical doping. The evolution of the graphene conductivity, from microwaves to terahertz frequencies, calculated by means of the above expression (1) is depicted in Fig. 1.
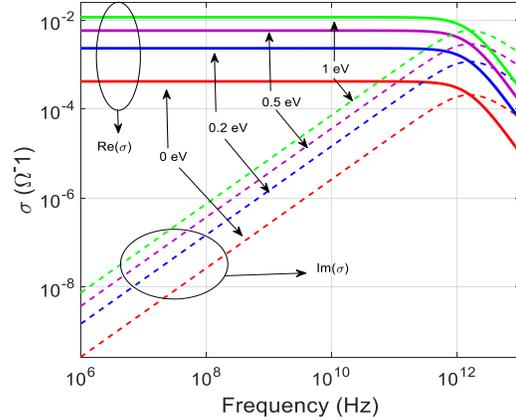
Fig. 1. Real and imaginary parts of the electrical conductivity of the graphene sheet as a function of the frequency for different values of the chemical potential.

The graphene sheet can be modeled either by considering a finite thickness material with corresponding dielectric/electrical properties, or by approximating it as an equivalent infinitesimal thin surface represented by its surface impedance. It is obvious that the first method involves a time consuming task because the geometrical size ratio of the sheet is very high. In this work, we model the graphene by using its surface impedance, given by:

$$Z(\omega) = \frac{1}{\sigma(\omega)}. \qquad (2)$$

The corresponding surface impedance of the graphene sheet (at 2.45 GHz) as a function of the chemical potential is plotted in Fig. 2. It is evident that at the frequency of interest (frequency at which we perform the microwave ablation), the graphene has a very high resistance which depends on the chemical potential, which makes it a relatively poor conductor. The impedance can be lowered or increased either by using a chemical doping or by applying a gate voltage.
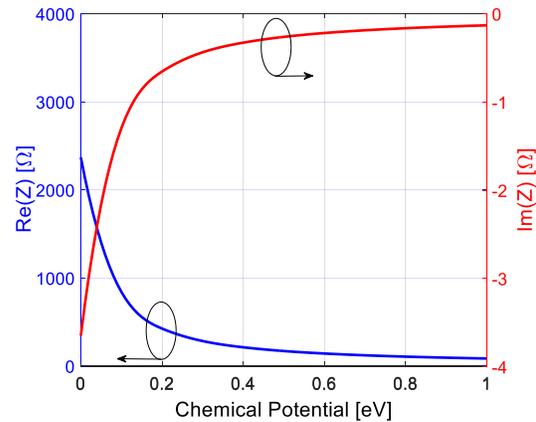
Fig. 2. Resistance and the reactance of the surface impedance of a graphene sheet as functions of the chemical potential.

IV. DESIGN OF THE MICROWAVE CANCER ABLATION ANTENNA AND NUMERICAL RESULTS

The proposed design consists of the coaxial slot antenna which has a sheet of graphene wrapped around. The overall antenna operating in a biological tissue environment is modeled by using the full-wave simulation software HFSS. In this work, we use the liver as a host medium for our antenna. A sketch of the coaxial slot antenna in the biological tissue is shown in Fig. 3.
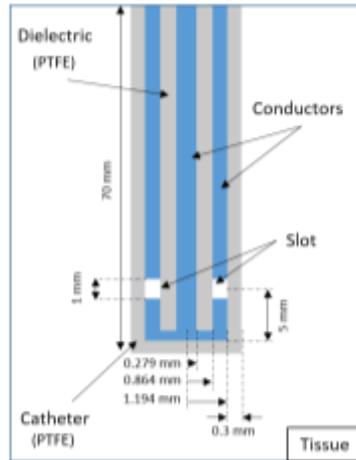
Fig. 3. Schematic 2D view of the microwave coaxial antenna in the biological tissue (not drawn to scale).

Figure 4 shows three different configurations studied in this work. Only the coaxial slot antenna and the graphene are represented. The catheter which enclose the entire antenna is not shown.
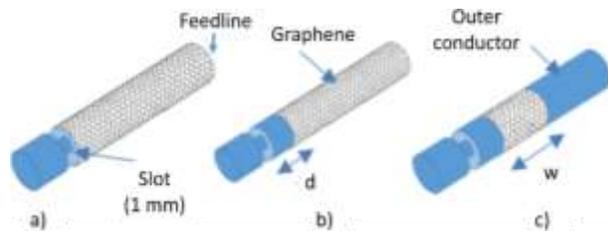
Fig. 4. Microwave coaxial antenna with the graphene sheet: (a) antenna fully covered by the graphene sheet from the slot all the way to the feedline; (b) graphene shifted from the slot and covering all the way to the feedline; (c) graphene strip shifted from the slot.

As mentioned earlier, the catheter and the coaxial antenna dielectric are considered to be PTFE. An annular slot located in the outer conductor is modeled as an air gap. Table 1 shows the values for the dielectric constant and the electrical conductivity of the liver and the antenna along with the catheter values at 2.45 GHz. For

all configurations, the antenna is modeled as a perfect electric conductor (PEC). The tip of the coaxial antenna is short-circuited. The slot width is 1 mm and it is positioned at 5 mm from the distal tip. The total insertion depth of the antenna is 70 mm.

First, the configuration where the graphene sheet covers the entire antenna from the slot position to the feedline is considered (Fig. 4 (a), and the effect of the graphene sheet on the antenna performance is investigated.

Table 1: Physical constant for the liver and the antenna

Parameter	Value
Dielectric constant of the liver	43.03
Electrical conductivity of the liver	1.68 S/m
Dielectric constant of the catheter	2.2
Dielectric constant of the coaxial antenna dielectric	2.2

One can see from Fig. 5 that the presence of the graphene shifts considerably the resonance to higher frequencies. The resonance is an important characteristic of an antenna that occurs when the antenna input impedance matches the impedance of the source. For a well matched antenna, most of the energy is transferred to the medium. However, for our antenna wrapped with the graphene sheet, most of the energy is reflected back from the slot to the coaxial cable and only a small portion is transferred to the tissue at 2.45 GHz. The antenna becomes poorly matched at this frequency. Obviously, for the sake of the ablation, this is not desirable. Otherwise, the returned energy would heat up the coaxial cable and damage the equipment especially if high power radiation is used.
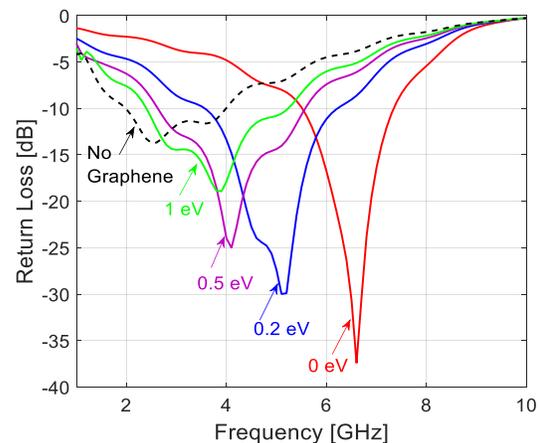
Fig. 5. Return loss obtained with and without graphene sheet for different chemical potential level.

The Specific Absorption Rates (SARs) calculated at a distance of 1.5 mm from the outer conductor of the

antenna, for different values of the chemical potential, are presented in Fig. 6. We note that although the SAR level along the longitudinal direction of the antenna is lower away from the slot, the maximum SAR which should be high around the slot, is also reduced. One can thus deduce that surface currents created on the outer conductor enhance the efficiency of the antenna and increase the amount of energy deposited in the cancerous tissue. The simulation result with the surface currents are presented in Figs. 5 and 6 with the label "No Graphene". Since graphene conductivity (accordingly the surface impedance) can be dynamically tuned, the resonance frequency (with the lowest return loss) and therefore the SAR absorbed in the tissue can be controlled in a simple and efficient manner. The more we augment the chemical potential the more we increase the carrier (electrons and/or holes) density. Thus, the electrical conductivity (resp. the surface impedance) is higher (resp. lower). Figure 6 clearly shows that the SAR along the antenna as well as around the slot is highly dependent on the chemical potential.

Since the surface currents contribute to the efficiency of the antenna, the next step in our work is naturally to use a graphene sheet partially enclosing the antenna. This 2nd configuration is depicted in Fig. 4 (b). Surface currents contributing the most to the radiation into the tissue are those very nearby the slot. As a remainder, we want to reduce the SAR far away from the slot, outside the cancerous tissue region. For this reason, we have deliberately left some distance between the graphene and the slot. By doing this, the current generated at the slot and propagating towards the feedline radiates into the tissue and takes part in the efficiency of the antenna before getting stopped by the graphene.
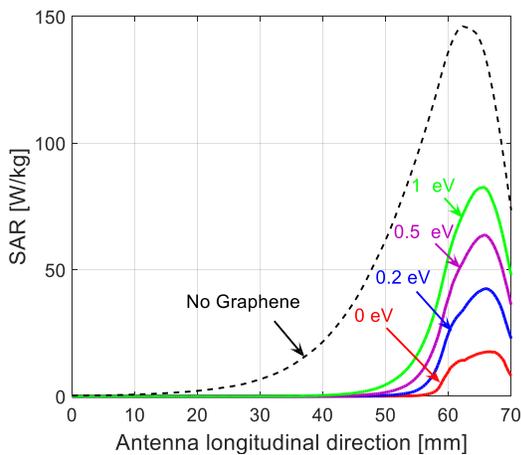
Fig. 6. Specific Absorption Rate (SAR) along the antenna at 1.5 mm from the outer conductor for the 1st configuration where the graphene cover all the way from

the slot to the feedline. The feedline is at 0 mm and the slot is located at 65 mm.

The return loss in the case of the 2nd configuration is shown in Fig. 7. The return loss (Fig. 7) and the SAR (Fig. 8) characteristics are plotted for different spacings between the slot and the graphene sheet, as listed in Table 2.
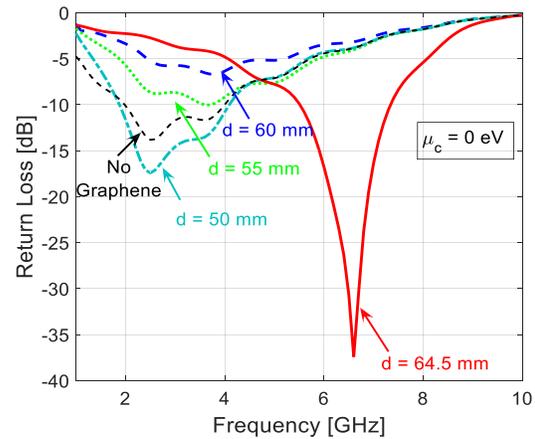
Fig. 7. Return loss obtained with the second configuration for different distances between the graphene and the slot.
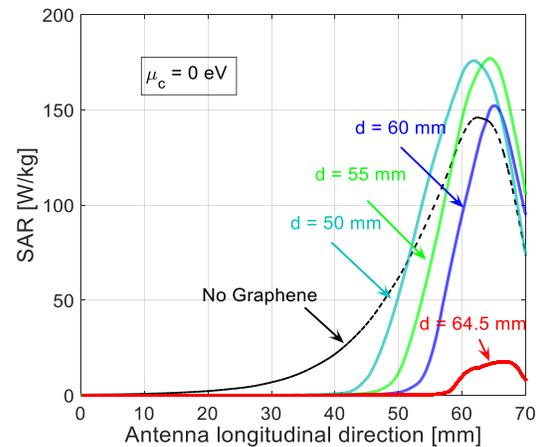
Fig. 8. Specific Absorption Rate (SAR) along the antenna at 1.5 mm from the outer conductor for the 2nd configuration for different distances between graphene and the slot. The feedline is at 0 mm and the slot is located at 65 mm.

Table 2: Spacing between the slot and the graphene sheet

Distance d	Value (mm)
d0	0
d1	4.5
d2	14.5

For this configuration, the chemical potential is taken as 0 eV. It is worthwhile to note that, introducing a spacing between the slot and the graphene causes the minimum return loss frequency to shift back to lower frequencies, eventually attaining the desired 2.45 GHz, the operating frequency for the cancer ablation. The return loss at 2.45 GHz is even better with a gap of d2 = 14.5 mm between the graphene and the slot, than it is for the reference antenna without graphene.

The corresponding SAR distribution along the longitudinal direction of the antenna is presented in Fig. 8. Although the SAR peak is shifted toward the feedline because the graphene is displaced, its level along the longitudinal direction remains largely acceptable compared to the case where there is no graphene. The results also confirm the fact that surface currents are participating in the radiation in the tissue through the slot. In fact, the maximum SAR becomes higher when there is a gap between the slot and the graphene.

Although with the current nano-engineering technologies one can grow a large size of graphene sheet, it should be interesting to consider only a narrow strip of graphene and to study the effect of its width when it is wrapped-up on a small portion of the outer conductor of the coaxial antenna.

This third configuration is shown in Fig. 3 (c). The graphene is placed at a distance d1 from the slot. The effect of its width on the SAR at 30 mm from the feedline and 1.5 mm away from the outer conductor is depicted in Fig. 9, for different values of the chemical potential (i.e, for different surface impedances). It is useful to note that, the SAR is computed at a position between the feedline and the graphene strip.

The effect of the width is clearly seen in Fig. 9. The SAR values decrease as the graphene width is increased. For a very narrow strip, the SAR level is closed to the reference case where there is no graphene. On the other hand, as the graphene becomes wider, the SAR characteristics tend to behave as those for the case of the second configuration when the graphene is extended all the way to the feedline. For instance, for a graphene width of 2 mm, it is possible to have seven times lower SAR level at this position.

Finally, Fig. 10 shows the SAR distribution on a plane parallel to the axis of the microwave coaxial antenna for the two different configurations (2 and 3). For the sake of comparison, the result for the reference antenna where the graphene is not present, is also displayed. The distance d between the slot and the graphene is 4.5 mm and the μ_c = 0 eV. For the 3rd configuration, the width of the graphene strip is 3 mm. The plots show considerable improvement of the antenna performance, and we note that the "tail" present in the case of the reference antenna no longer exists.
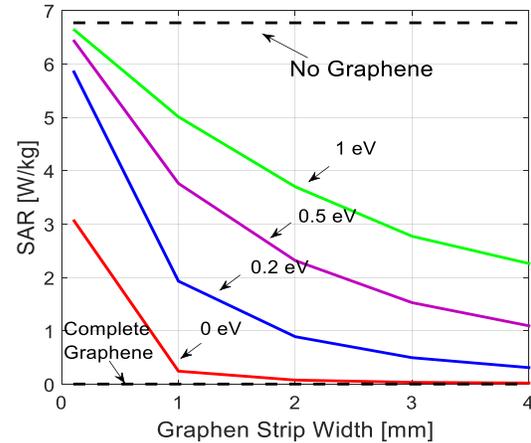
Fig. 9. SAR at 30 mm from the feedline vs. the width w of the graphene strip, for different level of chemical potential.
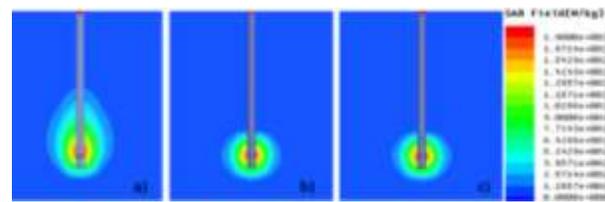
Fig. 10. SAR on a plane parallel to the axis of the antenna: (a) the reference antenna, (b) 2nd configuration (Fig. 4 (b)), 3rd configuration (Fig. 4(c)).

V. CONCLUSION

The backward heating is an important problem which must be addressed in order to increase the performance of a microwave coaxial antenna used as an ablation device. In this contribution we have proposed an alternative to reduce or even eliminate the surface currents that are responsible for that unwanted radiation along the antenna. The graphene is used as a high impedance surface to block the surface currents propagating along the antenna. Results show that, the graphene sheet can significantly reduce the SAR level while improving the efficiency of the antenna. Since graphene is extremely thin (only 1-atom thickness), it satisfies the criterion that the antenna must be minimally invasive.

ACKNOWLEDGMENT

REFERENCES

[1]   D. Yang, "Measurements, antenna design and

advanced computer modeling for microwave tissue ablation" *Ph.D. Dissertation*, Dept. Elect. Eng, University of Wısconsin-Madison, WI, 2005.

[2] A. Coates, S. Abraham, B. Kaye, T. Sowerbitts, C. Frewin, R. M. Fox, and M. H. N. Tattersall, "On the receiving end- patient perception of the side-effects of cancer chemotherapy," *Eur. J. Cancer Clin. Oncol.*, vol. 19, pp. 203-208, 1983.

[3] J. M. Bertram, D. Yang, M. C. Converse, J. G. Webster, and D. M. Mahvi, "A review of coaxial-based interstitial antennas for hepatic microwave ablation," *Critical Reviews in Biomedical Engineering*, vol. 34, no. 3, pp. 187-213, 2006.

[4] C. L. Brace, "Radiofrequency and microwave ablation of the liver, lung, kidney and bone: what are the differences: 'organ-specific thermal ablation," *Current Problems in Diagnostic Radiology*, vol. 38, no. 3, pp. 135-143, 2009.

[5] J. C. Lin and Y. J. Wang, "The cap-choke catheter antenna for microwave ablation treatment," *IEEE Transactions on Biomedical Engineering*, vol. 43, no. 6, pp. 657-660, 1996.

[6] K. Ito, M. Hyodo, M. Shimura, and H. Kasai, "Thin applicator having coaxial ring slots for interstitial microwave hyperthermia," *Antennas and Propagation Society International Symposium, 1990. AP-S. Merging Technologies for the 90's*, vol. 3, pp. 1233-1236, 7-11 May 1990.

[7] K. S. Novoselov, V. I. Fal'ko, L. Colombo, P. R. Gellert, M. G. Schwab, and K. Kim, "A roadmap for graphene," *Nature*, vol. 490, pp. 192-200, 2012.

[8] C. L. Brace, "Radiofrequency and microwave ablation of the liver, lung, kidney and bone: what are the differences," *Curr. Probl. Diagn. Radiol.*, vol. 38, no. 3, pp. 135-143, 2009.

[9] S. D. Huffman, N. P. Huffman, R. J. Lewandowski, and D. B. Brown, "Radiofrequency ablation complicated by skin burn," *Semin. Intervent. Radiol.*, vol. 28, no. 2, pp. 179-182, June 2011.

[10] C. L. Brace, Microwave ablation technology: what every use should know, *Curr. Probl. Diagn. Radiol.*, vol. 38, no. 3, pp. 61-67, 2009.

[11] A. S. Wright, L. A. Sampson, T. F. Warner, D. M. Mahvi, and F. T. Lee, "Radiofrequency versus microwave ablation in a hepatic porcine model," *Radiology*, vol. 236, no. 1, pp. 132-139, 2005.

[12] S. Labonte, A. Blais, S. R. Legault, H. O. Ali, and L. Roy, "Monopole antennas for microwave catheter ablation," *IEEE Trans. Microwave Theory Tech.*, vol. 44, pp. 1832-1840, 1996.

[13] W. Hurter, F. Reinbold, and W. J. Lorenz, "A dipole antenna for interstitial microwave hyperthermia," *IEEE Trans. Microwave Theory Tech.*, vol. 39, pp. 1048-1054, 1991.

[14] C. L. Brace, et al., "Analysis and experimental validation of a triaxial antenna for microwave tumor ablation," *IEEE MTTS Int. Microw. Symp.*, vol. 3, pp. 1437-1440, 2004.

[15] H. Acikgoz and I. Turer, "A novel microwave coaxial slot antenna for liver tumor ablation," *Advanced Electromagnetics*, vol. 3, no. 1, Apr. 2014.

[16] S. A. Shock, et al., "Microwave ablation with loop antenna: in vivo porcine liver model," *Radiology*, vol. 231, pp. 143-149, 2004.

[17] F. Rossetto, M. N. Prakash, and J. Masangcay, "Cooled helical antenna for microwave ablation," *U.S. Patent US 7998139 B2*, 2011.

[18] M. Kuang, et al., "Liver cancer: increased microwave delivery to ablation zone with cooled-shaft antenna--experimental and clinical studies," *Radiology*, vol. 242, vol. 3, pp. 914-924, 2007.

[19] C. L. Brace, "Microwave tissue ablation: biophysics, technology and applications," *Crit. Rev. Biomed. Eng.*, vol. 38, no. 1, pp. 65-78, 2010.

[20] D. Yang, et al., "A floating sleeve antenna yields localized hepatic microwave ablation," *IEEE Trans. Biomed. Eng.*, vol. 53, pp. 533-537, 2006.

[21] H. Acikgoz and R. Mittra, "Microwave coaxial antenna for cancer treatment: reducing the backward heating using a double choke," *International Symposium on Antenna and Propagation (ISAP)*, Australia, 9-12 Nov. 2015.

[22] I. Longo, G. B. Gentili, M. Cerretelli, and N. Tosoratti, "A coaxial antenna with miniaturized choke for minimally invasive interstitial heating," *IEEE Transactions On Biomedical Engineering*, vol. 50, no. 1, pp. 82-88, 2003.

[23] K. S. Novoselov, A. K. Geim, S. V. Morozov, D. Jiang, Y. Zhang, S. V. Dubonos, I. V. Grigorieva, and A. A. Firsov, "Electric field effect in atomically thin carbon films," *Science*, 2004.

[24] D. Correas-Serrano, J. S. Gomez-Diaz, J. Perruisseau-Carrier, and A. Alvarez-Melcon, "Graphene based plasmonic tunable low pass filters in the THz band," *IEEE Transactions on Nanotechnology*, 2014.

[25] I. Llatser, C. Kremers, A. Cabellos- Aparicio, J. M. Jornet, E. Alarco´n, and D. N. Chigrin, "Graphene-based nano-patch antenna for terahertz radiation," *Photonics and Nanostructures – Fundamentals and Applications*, vol. 10, pp. 353-358, 2012.

[26] J. Perruisseau-Carrier, "Graphene for antenna applications: opportunities and challenges from microwaves to THz," *Loughborough Antennas & Propagation Conference*, UK, 2012.

[27] D. L. Sounas, C. Caloz, *Novel Electromagnetic Phenomena in Graphene and Subsequent Microwave Devices Enabled by Multi-Scale Metamaterials, Metamaterial*, Dr. X.-Y. Jiang (Ed.), ISBN: 978-953-51-0591-6, InTech, 2012.

[28] I. Llatser, C. Kremers, A. Cabellos-Aparicio, J. M.

Jornet, E. Alarco´n, and D. N. Chigrin, "Graphene-based nano-patch antenna for terahertz radiation," *Photonics and Nanostructures – Fundamentals and Applications*, vol. 10, no. 4, Oct. 2012.

Hulusi Acikgoz received the B.S. and Master degrees in Applied Physics from the Paris-Est Marne-La-Valée University, France, and the Ph.D. degree from the Pierre and Marie Curie University (UPMC-Paris IV), Paris, France, in 2008 in Electrical Engineering. He has been a Teaching Assistant at UPMC-Paris IV in 2009-2010. After a year of post-doctoral research at the L2E (Laboratoire d'Electronique et d'Electromagnétisme) in computational electromagnetic dosimetry, he joined the KTO Karatay University, Konya, Turkey, in 2011, as an Assistant Professor. He spent a year as Visiting Scholar with Dr. Raj Mittra's research group at Pennsylvania State and Central Florida Universities, USA. His research interests include, microwave characterization of dielectric materials, electromagnetic dosimetry, homogenization, antennas for microwave cancer ablation, high impedance surfaces, graphene applications in EM and statistical analysis of EM structures.

Raj Mittra is a Professor in the Department of Electrical & Computer Science of the University of Central Florida in Orlando, FL., where he is the Director of the Electromagnetic Communication Laboratory. Prior to joining the University of Central Florida, he worked at Penn State as a Professor in the Electrical and Computer Engineering from 1996 through June, 2015. He also worked as a Professor in the Electrical and Computer Engineering at the University of Illinois in Urbana Champaign from 1957 through 1996, when he moved to the Penn State University. Currently, he also holds the position of Hi-Ci Professor at King Abdulaziz University in Saudi Arabia,

He is a Life Fellow of the IEEE, a Past-President of AP-S, and he has served as the Editor of the Transactions of the Antennas and Propagation Society. He won the Guggenheim Fellowship Award in 1965, the IEEE Centennial Medal in 1984, and the IEEE Millennium medal in 2000. Other honors include the IEEE/AP-S Distinguished Achievement Award in 2002, the Chen-To Tai Education Award in 2004 and the IEEE Electromagnetics Award in 2006, and the IEEE James H. Mulligan Award in 2011.

Mittra is a Principal Scientist and President of RM Associates, a consulting company founded in 1980, which provides services to industrial and governmental organizations, both in the U.S. and abroad.

Joint L^1 and Total Variation Regularization for Magnetic Detection Electrical Impedance Tomography

Liling Hao and Lisheng Xu

Department of SINO-DUTCH Biomedical and Information Engineering
Northeastern University, Shenyang, 110169, China
haoll@bmie.neu.edu.cn, xuls@bmie.neu.edu.cn

Abstract ─ Magnetic detection electrical impedance tomography (MDEIT) is an imaging modality that aims to compute the cross-sectional distribution of the conductivity of a volume from the magnetic flux density surrounding the object. Owing to the Biot-Savart law, the MDEIT inverse problem is inherently ill-conditioned making image reconstruction highly susceptible to the effects of noise and numerical errors. Appropriate priors or penalties are needed to facilitate reconstruction and to restrict the search space to a specific solution set. The images have the sparsity property and sharp variations. Consequently, this paper presents an approach involving a combination of the L^1 and total variation norm penalties, the former to suppress spurious background signals and enforce sparsity and the latter to preserve local smoothness and piecewise constancy in the MDEIT reconstructed images. The primal dual-interior point method (PD-IPM) for minimizing the joint L^1–TV penalty was used in the paper. The method was validated by using MDEIT simulated data and experimental data in comparison with the performances of the L^2, L^1 and total variation norm penalty-based approaches. The results show that the joint L^1–TV regularized algorithm preserves sparsity property, local smoothness and piecewise constancy, leading to improvements in the localization of the reconstructed images in MDEIT.

Index Terms ─ Inverse problem, joint regularization, L^1 norm, magnetic detection electrical impedance tomography, total variation.

I. INTRODUCTION

Magnetic detection electrical impedance tomography (MDEIT) is an experimental imaging modality that aims to reconstruct electrical conductivity images from the magnetic flux density surrounding the object induced by an injected current. Since measurements of the magnetic flux density surrounding the object don't require surface contact, MDEIT can record a greater number of measurements with precise detector positions. While electrical impedance tomography (EIT) records the surface voltage by electrodes on the surface, leading to

the more errors in the measurement and less number of measurements. As a different type of EIT, MDEIT overcomes the shortcomings of the standard EIT and retains its merits. MDEIT also has some comparative advantages over other similar imaging techniques in some respects. Magnetic resonance impedance tomography (MREIT) eliminates some of the principle advantages of EIT, such as low cost and the potential for long-time monitoring. Magnetic induction tomography (MIT) has limitation in the biomedical application due to the smaller signal produced by the eddy current compared to the signal produced by the injected current.

The concept of MDEIT was introduced in 1992 by Ahlfors and Ilmoniemi. They proposed a method that determines the conductivity distribution within an object using magnetic field measurements, which called magnetic impedance tomography (MIT) [1]. The feasibility of using magnetic field measurements to produce current density images was demonstrated with four examples in two dimensions, and made the first step towards developing MIT as a new medical imaging technique [2]. Then, this technique was called as MDEIT, because original name was easily confused with magnetic induction tomography [3]. They applied the Tikhonov regularization and truncated singular value method (TSVD) to MDEIT current density reconstruction. Ireland described a method of iterative grid refinement, improving the ill-posed nature of the MDEIT inverse problem by limiting the number of unknowns to be solved [4]. But they just constructed the current density image, the conductivity distribution reconstruction leaved to be solved. In this work we construct the conductivity image using simulated data.

The inverse problem of MDEIT is ill-posed. Consequently regularization techniques have been adopted to stabilize the solution [2-4]. However, these L^2 norm regularization methods limit the capability of describing sharp variations in the conductivity and tend to smooth out edges in images. The human images have well defined organ boundaries that present sharp transitions in conductivity. The ability of reconstructing sharp changes should lead to a better estimation of the

boundaries and a better accuracy in the estimated values. Sharp images could better identify the boundaries between the regions. The L^2 norm algorithms blur such contrasts and make more difficult to estimate the size and the contrast value. These inspire us to investigate a regularization method that preserves the edge information of the reconstructed conductivity image.

The total variation (TV) minimizing function regularization preserves discontinuities in the reconstructed profiles [5]. The TV is defined as the L^1 norm of the differences between neighbouring pixels. This particular form of the TV penalty enforces sparsity on pixel differences and consequently tends to generate images with piecewise constant regions and sharp boundaries. As a result, we studied TV regularization strategy and showed its superiority over the conventional L^2 regularization in our previous work [6]. However, in some cases, the images tend to be very sparse with some locally smooth high value regions. For example, the cancer is the localized high impedance tissue. Another application is the difference imaging, where the goal of the reconstruction is to recover the conductivity difference that commonly exhibits the sparsity. The L^1 norm is often used to enforce sparsity in images and is particularly popular in the field of compressed sensing [7-8]. But it tends to shrink the support of large or non-sparse sources. The TV regularization can preserve the boundary of large object well while removing small features and sparse sources. This inspires us to joint L^1 norm penalty and TV penalty, enforcing sparsity and smoothness in the reconstructed images. The similar methods have recently been applied to microwave imaging [9] and fluorescence molecular tomography [10-11]. This paper firstly uses the joint L^1 and total variation regularization to solve the inverse problem of magnetic detection electrical impedance tomography. In this work, the primal dual-interior point method (PD-IPM) was applied to minimize the joint L^1–TV penalty.

II. METHODS

MDEIT is technically based on generating a current distribution inside of the object by injecting an alternating current, at one of a range of frequencies, into a conducting object with surface electrodes. A large number of magnetic flux density measurements recorded with magnetic field sensors at fixed positions around the object are used to reconstruct the conductivity distributions on tomographic planes.

A. Inverse problem of MDEIT

A straightforward approach for solving the inverse problem of MDEIT is seeking the optimal solution by minimizing the cost function which is the residual norm between the calculated data and the measured data. The resulting optimization problem is as follows:

$$\hat{\boldsymbol{\sigma}} = \arg\min_{\boldsymbol{\sigma}} \frac{1}{2} \left\| F(\boldsymbol{\sigma}) - \mathbf{B} \right\|_2^2, \tag{1}$$

where $F(\boldsymbol{\sigma})$ is the forward operator calculated at the conductivity $\boldsymbol{\sigma}$, and $\mathbf{B}$ is the measured magnetic field. The reconstruction algorithm is capable of finding relative conductivity distribution only. Yet, the inverse problem of MDEIT is ill-posed, making the image reconstruction highly sensitive to the noise of the measurement data and numerical errors, and necessitating the use of regularization. The forward operator $F(\boldsymbol{\sigma})$ can be stated as [12]:

$$F(\boldsymbol{\sigma}) = \frac{\mu_0}{4\pi} \cdot \int_{\Omega} -\boldsymbol{\sigma}\nabla\varphi \times \frac{(\mathbf{r}-\mathbf{r}')}{\left|\mathbf{r}-\mathbf{r}'\right|^3} d\mathbf{r}'. \tag{2}$$

The Jacobian matrix $\mathbf{A}$ is defined as:

$$\mathbf{A} = \frac{\partial F(\boldsymbol{\sigma})}{\partial \boldsymbol{\sigma}} = \frac{\partial F(\boldsymbol{\sigma})}{\partial \mathbf{J}} \cdot \frac{\partial \mathbf{J}}{\partial \boldsymbol{\sigma}}, \tag{3}$$

with

$$\frac{\partial \mathbf{J}}{\partial \sigma_j} = \frac{\partial(-\boldsymbol{\sigma}\nabla\varphi)}{\partial \sigma_j} = -(\nabla\varphi)_j - \boldsymbol{\sigma}\frac{\partial(\nabla\varphi)}{\partial \sigma_j}. \tag{4}$$

Alternate the index of partial derivative in $\partial\nabla\varphi/\partial\sigma$, and obtain the following equation:

$$\frac{\partial \mathbf{J}}{\partial \sigma_j} = -(\nabla\varphi)_j - \boldsymbol{\sigma}\nabla\frac{\partial\varphi}{\partial \sigma_j}. \tag{5}$$

The partial derivative of electrical potential to conductivity $\partial\varphi/\partial\sigma$ can be calculated through the linear equation system of the forward problem. Calculate the partial derivative to the conductivity σ, and obtain the following equation:

$$\frac{\partial \varphi}{\partial \sigma_j} = -\mathbf{S}^{-1} \cdot \frac{\partial \mathbf{S}}{\partial \sigma_j} \cdot \varphi, \tag{6}$$

where $\mathbf{S}$ is the coefficient matrix between the excitation matrix and the nodal voltage matrix based on the finite element method.

B. Joint L^1 and total variation regularization

The cost function we seek to minimize contains three parts—a data-fitting term, a sparsifying penalty term and a smoothing penalty term. The sparsifying penalty under consideration is the L^1 norm of the conductivity image $\boldsymbol{\sigma}$. The cost function is:

$$\hat{\boldsymbol{\sigma}} = \arg\min_{\boldsymbol{\sigma}} f(\boldsymbol{\sigma}) =$$

$$\arg\min_{\boldsymbol{\sigma}} \frac{1}{2} \left\| F(\boldsymbol{\sigma}) - \mathbf{B} \right\|_2^2 + \lambda_{L^1} \left\| \boldsymbol{\sigma} \right\|_1 + \lambda_{TV} \sum_i \sqrt{\left|\mathbf{L}_i\boldsymbol{\sigma}\right|^2 + \delta}, \tag{7}$$

where δ is a constant with a small positive value, which enforces the differentiability of the TV penalty. $\mathbf{L}$ is a regularization matrix. λ_{L^1} and λ_{TV} are the regularization parameter for L^1 regularization and TV regularization,

respectively.

Primal Dual-Interior Point Method (PD-IPM) was utilized for minimizing the joint L^1–TV penalty [13-14]. The joint L^1–TV regularized inverse problem can be formulated as:

$$(\text{P}) \arg \min_{\boldsymbol{\sigma}} \frac{1}{2} \left\| F(\boldsymbol{\sigma}) - \mathbf{B} \right\|_2^2 + \lambda_{L^1} \left\| \boldsymbol{\sigma} \right\|_1 + \lambda_{TV} \sum_i \left| \mathbf{L}_i \boldsymbol{\sigma} \right| \quad (8)$$

We call Equation (8) primal problem and label it (P), where $\boldsymbol{\sigma}$ is the primal variable. An equivalent problem to (P) is called dual problem which is a maximization problem:

$$(\text{D}) \max_{\mathbf{x}: |x_i| \le 1} \min_{\boldsymbol{\sigma}} \frac{1}{2} \left\| F(\boldsymbol{\sigma}) - \mathbf{B} \right\|_2^2 + \lambda_{L^1} \left\| \boldsymbol{\sigma} \right\|_1 + \lambda_{TV} \sum_i x_i \mathbf{L}_i \boldsymbol{\sigma}, \quad (9)$$

where $\mathbf{x}$ is the dual variable. The complementarity condition is:

$$\left| \mathbf{L}_i \boldsymbol{\sigma} \right| - x_i \sqrt{\left| \mathbf{L}_i \boldsymbol{\sigma} \right|^2 + \delta} = 0 \quad i = 1, \cdots, n, \quad (10)$$

with the feasibility conditions,

$$\left| x_i \right| \le 1 \quad i = 1, \cdots, n$$
$$\mathbf{A}^T \left(F(\boldsymbol{\sigma}) - \mathbf{B} \right) + \lambda_{L^1} \mathbf{1} + \lambda_{TV} \mathbf{L} \mathbf{x} = 0 \quad (11)$$

Apply the Gauss Newton method and obtain the updates of the primal and dual variables:

$$\Delta \boldsymbol{\sigma}_k = -\left(\mathbf{A}_k^T \mathbf{A}_k + \lambda_{TV} \mathbf{L}^T \mathbf{P}_k^{-1} \mathbf{Q}_k \mathbf{L} \right)^{-1}$$
$$\cdot \left[\mathbf{A}_k^T \left(F(\boldsymbol{\sigma}_k) - \mathbf{B} \right) + \lambda_{L^1} \mathbf{1} + \lambda_{TV} \mathbf{L}^T \mathbf{P}_k^{-1} \mathbf{L} \boldsymbol{\sigma}_k \right],$$
$$\Delta \mathbf{x}_k = -\mathbf{x}_k + \mathbf{P}_k^{-1} \mathbf{L} \boldsymbol{\sigma}_k + \mathbf{P}_k^{-1} \mathbf{Q}_k \mathbf{L} \Delta \boldsymbol{\sigma}_k$$
$$(12)$$

with

$$\eta_i^k = \sqrt{\left| \mathbf{L}_i \boldsymbol{\sigma}_k \right|^2 + \delta}$$
$$\mathbf{P}_k = diag\left(\eta_i^k \right)$$
$$\mathbf{Q}_k = diag\left(1 - \frac{x_i^k \mathbf{L}_i \boldsymbol{\sigma}_k}{\eta_i^k} \right) \quad (13)$$

Moreover, for maintaining dual feasibility, we calculate the exact value of step length according to the step rule:

$$\mathbf{x}_{k+1} = \mathbf{x}_k + \min\left(1, \phi^* \right) \Delta \mathbf{x}_k, \quad (14)$$

where ϕ^* is a scalar value such that,

$$\phi^* = \sup\left\{ \phi : \left| x_{ki} + \phi \Delta x_{ki} \right| \le 1, i = 1, \cdots, n \right\}. \quad (15)$$

With joint L^1 and TV penalties, there are two regularization parameters to be selected. These parameters were empirically determined by sweeping them over a range of values. The sparsifying and smoothing effects increase as we increase the weights on the L^1 and TV penalties, respectively.

III. EXPERIMENTS AND RESULTS

We tested the joint L^1–TV regularization approach and compared it with the L^1, TV and L^2 penalties using simulated and experimental data.

A. Simulation results

In the section, we evaluated the performance of the joint L^1–TV regularization algorithm and compared its performance with the L^1, TV and L^2 penalties. The evaluation was conducted on the simulated data. The simulated phantom is shown in Fig. 1 (a). Suppose a 10 mA current was injected by one pair of opposite electrodes and the size of the electrode is just the same as the area of an element. The total element number is 2160 for simulating the magnetic flux density data (forward model) and 540 for the image reconstruction (inverse model). The positions of the magnetic flux density measurement coils at 120 equally spaced angles along 3 equally spaced circles surrounding the circular imaging object, which results 360 measurements in all, are displayed in Fig. 1 (b). In this paper, the numerical treatment was applied to the singular values of the sensitivity matrix in the presence of noisy measurements, subsequently suggesting the optimal detector configurations [15]. For the simulated phantom, only magnetic flux density B_z can be recorded by coil at these positions. So the orientations of coils are displayed as Fig. 1 (b).

(a) (b)
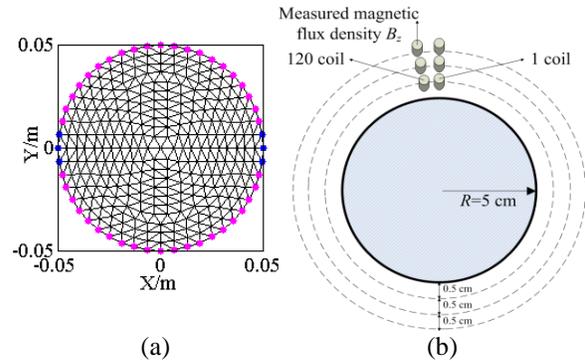
Fig. 1. The simulated phantom used for generating the simulated data. (a) The opposite electrodes covering 2 elements located in the horizontal direction, (b) the diagram displaying the positions of the magnetic flux density measurement coils at 120 equally spaced angles along 3 equally spaced circles surrounding the circular imaging object, and orientations for the measured magnetic flux density B_z.

The hypersensitivity near the boundary results in the better resolution of inhomogeneity near the boundary,

while the insensitivity in the centre leads to a worse resolution of inhomogeneity in the centre. For the different regularizations, the differences among the reconstructed conductivity distributions may be smaller for the inhomogeneity in the centre, and be bigger for the inhomogeneity near the boundary. In order to better test the performance of the joint L^1–TV regularization, we selected three simulation models with the conductivity distributions as shown in Fig. 2 (a), Fig. 3 (a) and Fig. 4 (a). We set the background conductivity for 0.1 S/m, the small inclusions present the same value of 0.2 S/m. In actually measurements, there will be some necessary noise. White Gaussian noise with a signal-to-noise (SNR) of 60 dB was added to the simulated magnetic flux density data to make the simulations realistic.

For the model 1 with inhomogeneity near the boundary, the reconstruction results for L^2, L^1, TV and joint L^1–TV penalties are show in Fig. 2 (b)–(e), respectively. This figure clearly indicates the L^2 penalty generates the most blurred solution and the most mean background signal level. The L^1 penalty suppresses spurious background and enforces sparsity. The TV penalty preserves the edge. The joint L^1–TV penalty simultaneously encourages properties of sparsity and smoothness in the reconstructed image. The L^1, TV and the joint L^1–TV schemes lead to significantly stronger mean signal levels over the region of interest (ROI) than the L^2 penalty. The result obtained using the joint L^1–TV penalty is most similar to the conductivity image displayed in Fig. 2 (a).
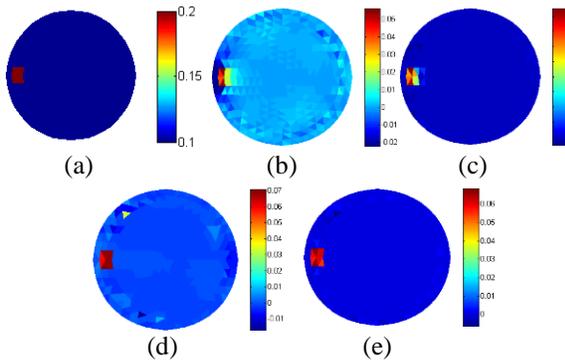
Fig. 2. The reconstructed results of model 1 with inhomogeneity near the boundary. (a) Conductivity map, (b) the reconstructed image using L^2 norm penalty, (c) the reconstructed image using the L^1 norm penalty, (d) the reconstructed image using TV penalty, and (e) the reconstructed image using both L^1 and TV penalties.

For the model 2 with inhomogeneity in the centre, the reconstructed results are shown in Fig. 3. The L^2 and the TV schemes led to the worse resolution of inhomogeneity than the model 1. The L^1 and the joint L^1–TV approaches generated the least mean background

signal level, while the joint L^1–TV approach yielded a lower background standard deviation than the L^1 and TV penalties individually.

The reconstructed results of the model 3 with two small inclusions are presented in Fig. 4, where the reconstructed images are shown for different regularizations. The joint L^1–TV penalty was observed to yield the best result, which preserves local smoothness and piecewise constancy with TV penalty and simultaneously encourages properties of sparsity and eliminates the artifacts between the two small inclusions with L^1 norm approach.
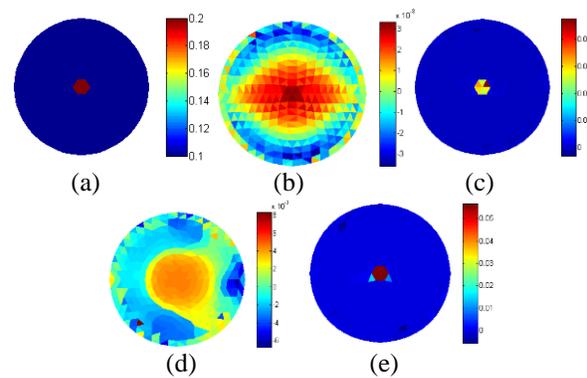
Fig. 3. The reconstructed results of model 2 with inhomogeneity in the centre. (a) Conductivity map, (b) the reconstructed image using L^2 norm penalty, (c) the reconstructed image using the L^1 norm penalty, (d) the reconstructed image using TV penalty, and (e) the reconstructed image using both L^1 and TV penalties.
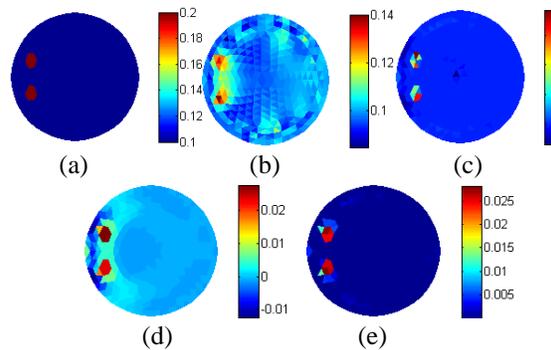
Fig. 4. The reconstructed results of model 3 with two small inclusions. (a) Conductivity map, (b) the reconstructed image using L^2 norm penalty, (c) the reconstructed image using the L^1 norm penalty, (d) the reconstructed image using TV penalty, and (e) the reconstructed image using both L^1 and TV penalties.

B. Current density image reconstruction experiment

In order to test the performance of joint regularized algorithm for the realistic magnetic field data, a discrete

phantom consisting of one conducting rod of length 1.2 m in free space was used (Fig. 5 (a)). The coil was used to record the magnetic field measurements made with an injected current of 10 mA at 31.25 kHz. Fig. 5 (b) presents the axial current density distribution of the imaging area with a 5 cm radius. The magnetic field data was measured on a perpendicular plane surrounding the object in the middle height of the object. The position of the measurement point on the perpendicular plane at 36 equally spaced angles along 3 equally spaced circles surrounding the circular imaging object, which results 108 measurements in all, is shown in the Fig. 5 (c). The orientation of coil at each angle was tangent to the circle region of interest at every point. The data recorded by the coil was amplified by a low-noise amplifier, and then fed to the data acquisition board NI-PCI6281 produced by National Instruments. The SNR of voltage acquired by the data acquisition board was 42-57 dB. The digital voltage data was processed by the digital lock-in amplifier to filter the noise and produce the amplitude of the voltage. Fig. 6 presents the vector graphics of the simulated and measured magnetic flux density. The mean difference between the measured and simulated data is 4.08%, with values ranging from 0.55% to 8.74%.

The region of the imaging object was meshed into 316 elements. We reconstructed the current density image at the 316 positions from the 108 external magnetic field measurements. For the current density image presented in the paper (Fig. 5 (b)), it has sparsity and sharp edges. The joint L^1–TV penalty was used to reconstruct the current density image for this ill-posed inverse problem, enforcing sparsity and preserving local smoothness and piecewise constancy in the reconstructed images.
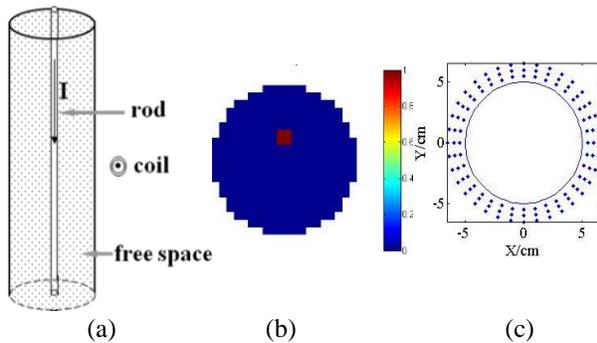
Fig. 6. The vector graphics of the simulated and measured magnetic field, which display the magnetic flux density as arrows at the measurement points. The length of arrows represents the magnitude of magnetic field, while the direction of arrow corresponds to the direction of the magnetic field. (a) The vector graphic displaying the simulated magnetic field, and (b) the vector graphic displaying the measured magnetic field.

Figure 7 shows the reconstructed current density images for L^2, L^1, TV and joint L^1–TV penalties, using the simulated magnetic field data with 50 dB white Gaussian noise. The commonly used L^2 penalty generates the most blurred solution. The L^1 penalty suppresses spurious background and enforces sparsity, but reduces the object region. The TV penalty preserves the edge, but enlarges the object region. The joint L^1–TV penalty simultaneously encourages properties of sparsity and smoothness in the reconstructed image. The result obtained using the joint L^1–TV penalty is most similar to the current density image displayed in Fig. 5 (b).
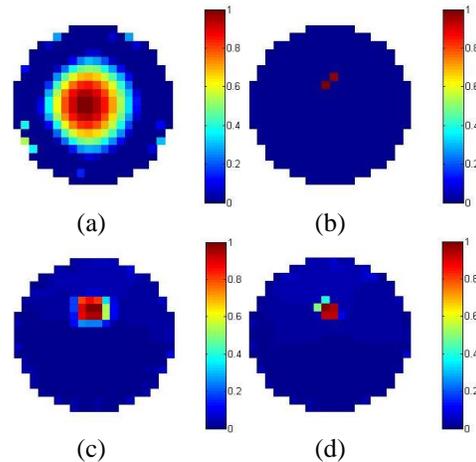
Fig. 7. The reconstructed current density images from the simulated magnetic field data with 50 dB white Gaussian noise. (a) The reconstructed image using L^2 norm penalty, (b) the reconstructed image using the L^1 norm penalty, (c) the reconstructed image using TV penalty, and (d) the reconstructed image using both L^1 and TV penalties.

Fig. 5. The magnetic field measurement configuration. (a) The discrete phantom consisting of one conducting rod with an injected current, (b) the original current density distribution of the imaging object, and (c) the positions of the magnetic flux density measurement points on a perpendicular plane surrounding the object in the middle height of the object.

Based on the experimental data, we employed the L^2, L^1, TV and joint L^1–TV penalties to reconstruct the current density images shown in Fig. 8. Using L^1 or TV regularization, in combination or separately, clearly leads to improvements in localizing the inhomogeneity in MDEIT. There is less difference between the L^1, TV and joint L^1–TV images than between any of these and L^2 image. The joint L^1–TV images have the most natural appearance in the simulated and experimental results.

(a)   (b)

(c)   (d)
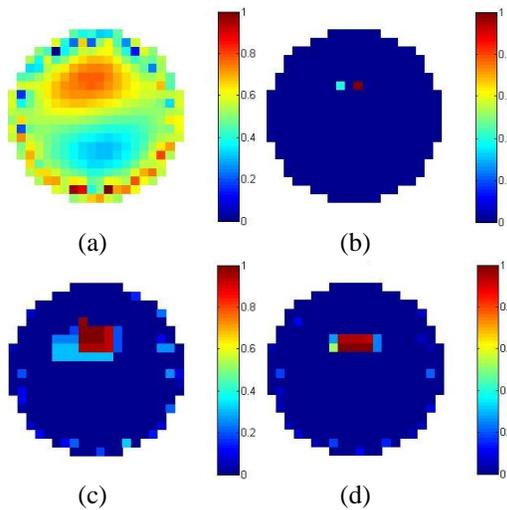
Fig. 8. The reconstructed current density images from the experimental magnetic field data. (a) The reconstructed image using L^2 norm penalty, (b) the reconstructed image using the L^1 norm penalty, (c) the reconstructed image using TV penalty, and (d) the reconstructed image using both L^1 and TV penalties.

VI. CONCLUSION

In this work, the joint L^1–TV regularization was applied to the inverse problem of magnetic detection electrical impedance tomography. We used the primal dual-interior point method for efficiently minimizing joint L^1–TV penalty, and compared its performance with the L^2 norm, L^1 norm and TV regularizations. Through the simulations of differential conductivity image reconstructions, it showed that the joint L^1–TV regularization preserved sparsity, discontinuities and piecewise constancy in the reconstructed image.

For the experiment of current density image reconstruction, the joint L^1–TV penalty reconstructed the more accurate current density image than either L^1 penalty or TV penalty. Moreover, all of these performed better than the conventional L^2 penalty. The simulated and experimental results of the current density image reconstruction appeared similar, but the simulation result was little better than the experimental result. The possible reason of the difference in results is as follow. The sources of inaccuracy in simulation result are noise

and numerical errors. In comparison, the experimental results are also subject to some other nonidealities. These include geometric error and position error of the coil. Additionally, the measured magnetic field is an average measurement over the area of the coil, which is not identical to the magnetic field in the centre point of the coil. As the coil area decreases, it gives an accurate point measurement of magnetic field. However, the signal induced in the coil is small, leading to the degradation in the quality of data. Therefore, the coil should provide a suitable compromise between accuracy and signal amplitude.

The joint L^1–TV regularization leads to the improvement in localizing the inhomogeneities for MDEIT. Furthermore, the sharp edges and piecewise constancy of the TV regularization and the sparsity of L^1 penalty may encourage the enhancement in clinical applications. For example, MDEIT may be useful in the detection of cancer which is the localized high impedance tissue. And the sharp impedance contrast between the lung and the surrounding tissues might be better reconstructed by MDEIT. Further simulation studies could be considered and techniques developed to reconstruct images from more complex phantoms. Another application of MDEIT might provide enhancements over current imaging techniques is the dynamic continuous real-time monitoring of the imaging object such as the brain. But MDEIT still struggles to produce images with good resolution that are routine in CT and MRI because of the inherent ill-posedness of MDEIT inverse problem and the measurement system. At the present time, there are two above-mentioned restrictions on the quality of images from the measurements taken on the human subjects. Therefore, the objective of the next phase in the development of MDEIT will be to improve both data collection system and reconstruction methods to enable accurate imaging.

With the present measurement system, we only reconstructed the current density image from the experimental data. Further conductivity image reconstruction of more complex phantoms should be considered. Therefore, the next work is to improve the MDEIT data measurement system, obtaining more accurate magnetic field data.

REFERENCES

[1] S. Ahlfors and R. Ilmoniemi, "Magnetic imaging

of conductivity," *Proc. 14th Ann. Int. Conf. IEEE Eng. Med. Biol. Soc.*, Paris, pp. 1717-1718, 1992.

[2] J. C. Tozer, R. H. Ireland, D. C. Barber, and A. T. Barker, "Magnetic impedance tomography," *Ann. N. Y. Acad. Sci.*, vol. 873, pp. 353-359, Apr. 1999.

[3] R. H. Ireland, J. C. Tozer, A. T. Barker, and D. C. Barber, "Towards magnetic detection electrical impedance tomography: data acquisition and image reconstruction of current density in phantoms and in vivo," *Physiol. Meas.*, vol. 25, no. 3, pp. 775-796, Jun. 2004.

[4] R. H. Ireland and D. C. Barber, "Constrained image reconstruction for magnetic detection electrical impedance tomography," *Int. J. Imag. Syst. Technol.*, vol. 17, no. 6, pp. 379-382, Dec. 2007.

[5] D. Strong and T. Chan, "Edge-preserving and scale-dependent properties of total variation regularization," *Inverse Problems*, vol. 19, no. 6, pp. 165-187, 2003.

[6] L. Hao, G. Li, and L. Xu, "Magnetic detection electrical impedance tomography with total variation regularization," *Biomed. Mater. Eng.*, vol. 24, no. 6, pp. 2857-2864, 2014.

[7] D. Donoho, "Compresse sensing," *IEEE Trans. Inf. Theory*, vol. 52, no. 4, pp. 1289-1306, 2006.

[8] E. J. Candes and T. Tao, "Near optimal signal recovery from random projections: universal encoding strategies," *IEEE Trans. Inf. Theory*, vol. 52, no. 12, pp. 5406-5425, 2006.

[9] G. Oliveri, N. Anselmi, and A. Massa, "Compressive sensing imaging of non-sparse 2d scatterers by a total-variation approach within the born approximation," *IEEE Transactions on Antennas & Propagation*, vol. 62, no. 10, pp. 5157-5170, 2014.

[10] D. Joyita, A. Sangtae, L. Changqing, R. C. Simon, and M. L. Richard, "Joint L1 and total variation regularization for fluorescence molecular tomography," *Physics in Medicine & Biology*, vol. 57, no. 6, pp. 1459-1476, 2012.

[11] G. Hao and Z. Hongkai, "Multilevel bioluminescence tomography based on radiative transfer equation part 2: total variation and l1 data fidelity," *Optics Express*, vol. 18, no. 3, pp. 2894-2912, 2010.

[12] G. Li, L. Hao, R. Chen, and L. Lin, "A new electrode mode for magnetic detection electrical impedance tomography: Computer simulation study," *IEEE Transactions on Magnetics*, vol. 48, no. 10, pp. 2543-2550, 2010.

[13] K. D. Andersen, E. Christiansen, A. Conn, and M. L. Overton, "An efficient primal-dual interior-point method for minimizing a sum of Euclidean norms," *SIAM J. on Scientific Computing*, vol. 22, no. 1, pp. 243-262, 2000.

[14] A. Borsic, B. M. Graham, A. Alder, and W. R. B. Lionheart, "In vivo impedance imaging with total variation regularization," *IEEE Transactions on Medical Imaging*, vol. 29, no. 1, pp. 44-54, 2010.

[15] L. Hao, G. Li, and L. Lin, "Optimization of measurement arrangements for magnetic detection electrical impedance tomography," *IEEE Transactions on Bio-medical Engineering*, vol. 61, no. 2, pp. 444-452, 2014.

Membrane Conductance Analysis on Single-cell Electroporation with Electrolyte-filled Capillary

J. Anselmo [1], L. C. Ramos [1], J. L. B. Marques [1], F. R. M. B. Silva [2], and D. O. H. Suzuki [1]

[1] Institute of Biomedical Engineering, Department of Electrical Engineering
Federal University of Santa Catarina, Florianópolis, SC 88040-900, Brazil
suzuki@eel.ufsc.br

[2] Department of Biochemistry
Federal University of Santa Catarina, Florianópolis, SC 88040-900, Brazil

Abstract ─ Single-cell electroporation with electrolyte-filled capillary is a selective technique that affects the target cell without any consequences for the neighbouring cells. Inhomogeneous electric field caused by interaction of capillary, cell and environment in the experiment make the optimization setup difficult for DNA transfection efficiency. A electroporation model of membrane conductivity with experimental parameters was used to analyze the influence of cell-to-tip distance, cell-capillary dimensions relation, electrolyte and cytoplasm conductivity, and strength of the pulses on electroporation. Simulation results demonstrate that the nonlinear electric field distribution on cell membrane depends on tip-to-cell distance and may be the cause of cell survival. The electroporation with capillary are affected by the external medium, relation between the cell and capillary radius, tip-to-cell distance, and strength of the applied potential.

Index Terms ─ Electrolyte-filled capillary, electroporation, electroporation model, membrane conductivity, single cell.

I. INTRODUCTION

Electroporation or electropermeabilization is a phenomenon that occurs when high electric field is applied to increase the cell membrane permeability [1, 2].

The main applications of electroporation are electrochemotherapy [3], [4] and genetic manipulation [5]. The electroporation traditional methods to genetic transference use large, planar electrodes to produce a uniform electric field. However, some experimental cases investigate the response of a single cell, such as brain tissue and primary cultures [6], [7]. These cells present problems to DNA transfection. They tend to be very sensitive to physical stress alteration in temperature, ph shifts and changes in osmolarity. The strengths of single cell electroporations are surviving cells are completely functional; subsequent transfection of the same neuron with more than one construct at different time points; neurons up to 1 mm deep into a tissue can be transfected [8]; no need for vector or cytotoxic carriers [9]. The great disadvantages of single cell electroporation is the difficult of optimization [8], demands experimenter skill, laborious procedure [9].

The efficiency of this technique depends of interaction of environment (cell size and geometry, internal and external conductivity), capillary (cell-to-tip distance, capillary diameter) and electric field (strength and duration electric pulse). Some works proposed relations among parameters to improve the electroporation efficiency [2], [10]. These studies provide understanding about mechanical and electrical aspects of electroporation in cell membrane. It increases the gene transfer efficiency and viability of cells.

The inhomogeneous electric field caused by capillary and complex geometries in the experiment make the optimization setup difficult for the electroporation efficiency. The cell-to-tip distance and cell size affect the electroporation success rate and cell viability [6-8]. Each cell needs electroporation protocols in specific micropipette according to their characteristics.

In this study, a membrane conductivity model based on Glaser *et al.* [11] with electroporation parameters from cell suspension experiments [12] is implemented. This electroporation model was applied to study the effect of cell-to-tip distance, cell-capillary dimensions relation, electrolyte and cytoplasm conductivity, and strength of the pulses. The consequences of electric field distribution on membrane conductivity and current density through the membrane cell are analyzed. We start the elucidation of the physical and electrical influences of single cell electroporation to improve the efficiency of DNA transfection.

II. MATERIALS AND METHODS

A. Numerical and geometry modeling

The simulations in this study were performed using the COMSOL Multiphysics® software package (COMSOL Inc., Burlington, MA) based on the finite-element method.

The electric field distribution models were calculated using the steady current module. If the electric current density J in tissue is divergence-free, the solved equation is Poisson's equation:

$$-\nabla \cdot (\sigma \nabla V) = 0, \tag{1}$$

where σ is the conductivity (S/m) and V is the electric potential (V).

The processing was performed on a PC equipped with AMD Athlon™ II X2 250 3.0 GHz processor and 4.0 GB RAM. The computer was operating on a Microsoft® Windows 8 de 64 bits platform.

The geometrical model was simulated with a capillary perpendicular to the dish surface (Fig. 1). The full capillary length L_{cap} is 1.5×10^{-2} m, and extremely thin membranes (5×10^{-9} m) are problematic in meshing and solving the problem.
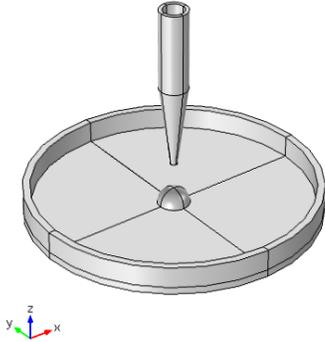
Fig. 1. Schematic representation of single-cell electroporation geometry. Components are not drawn to scale.

The solution was simulated by only 2×10^{-3} m of the pulled capillary. The cell and capillary are placed in the centred axis of simulation region for axial symmetry. The potential drop in the unpulled capillary is given by [13]:

$$V_a = V_{cap} + \frac{\partial V}{\partial z}(L_{cap} - l), \tag{2}$$

where $(\partial V/\partial z)$ is the electric field normal to the boundary where V_a exists, V_{cap} is the potential applied across L_{cap}, and l is the pulled tip length.

The boundary conditions and geometry simulated a represented in Fig. 2 and Table 1. A grid independence study was performed to establish an optimized mesh. Extremely fine mesh was set on the cell membrane and fine mesh in other geometries. The total mesh was 61,730 tetrahedral elements.
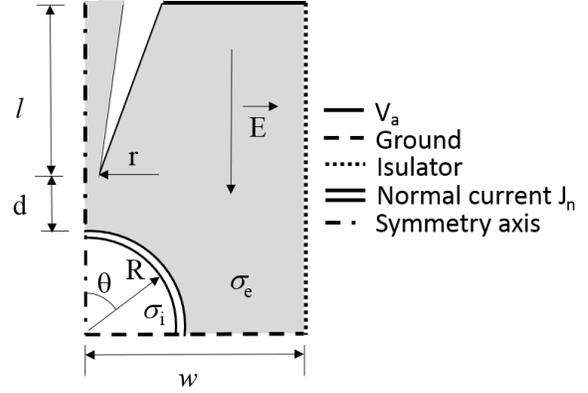
Fig. 2. Isolated single-cell model under nonlinear electric field. The capillary is positioned perpendicular to the Petri dish. The axisymmetry is used to reduce the computational resources.

Table 1: Units and corresponding symbols

Parameter	Symbol	Value
External conductivity [13]	σ_e	$0.60 \; S/m$
Internal conductivity [13]	σ_i	$0.13 \; S/m$
Cell radius	R	$10 \times 10^{-6} \; m$
Membrane thickness [12]	h	$5 \times 10^{-9} \; m$
Length of pulled tip	l	$2 \times 10^{-3} \; m$
Internal diameter unpulled capillary	D_i	$100 \times 10^{-6} \; m$
Internal diameter pulled capillary	r	$2.5 \times 10^{-6} \; m$

B. Electroporation model

The ionic transport across the pores formed on the electroporated membrane increase membrane conductivity. Assuming that the intact lipid matrix has a negligible ionic mobility, all ionic transports should happen through the pores. Glaser's experiments [11] suggest that the ionic mobility in an electroporated membrane increases with the rate depending on the transmembrane voltage. The electroporated membrane conductivity can be calculated by:

$$\frac{d\sigma_m}{dt} = K e^{\left(\frac{V_m}{V_{pp}}\right)^2}, \tag{3}$$

where K is a electroporation constant and V_{pp} sets the critical transmembrane potential at which the membrane breaks down. This expression agrees with Glaser's model and experimental results.

The electroporation is a threshold phenomenon: when the induced transmembrane potential exceeds a critical value V_{pp}, there is pores formation on the membrane. The critical transmembrane potential is 0.2 V [14]. The K parameter was obtained by comparing the point at 100 μs of experimental and numerical suspension conductivity

during electroporation pulse [12] and simulation of single cell in a uniform electric field.

In this simulation, an increase in the suspension concentration is incorporated as a reduction in the correction factor on the local electric field around the cells [15]:

$$E_f = \frac{1+p/2}{1+(3p/4N\pi)^{1/3}} E, \qquad (4)$$

where N is the arrangement type of cells and p is the volume fraction occupied by the cell.

The simulation took into account Equation (4) on the electric properties of cell membrane. Electric field distribution models were calculated using the steady current module as in Equation (1). The boundary conditions, electric and geometric parameters for these simulations are in Fig. 3 and Table 2.
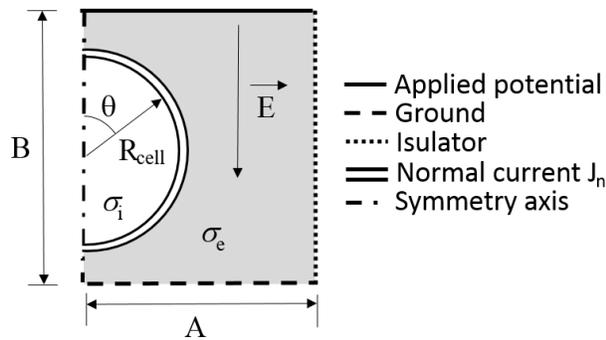
Fig. 3. Schematic of a spherical cell of radius R_{cell} in a uniform electric field. Arrow indicates the direction of the electric field E, polar angle θ measures the position along the cell circumference. The axial-symmetry geometry and boundary conditions are presented.

Table 2: Units and corresponding symbols

Definition	Symbol	Value
Electroporation constant	K	$3\times10^{-2}\ S/m.s$
Critical transmembrane potential [14]	V_{pp}	$0.20\ V$
Cell radius[12]	R_{cell}	$4.87\times10^{-6}\ m$
External conductivity [12]	σ_e	$0.55\ S/m$
Internal conductivity [12]	σ_i	$1.0\ S/m$
Arrangement type of cells [12]	N	4
volume fraction of cells [12]	p	0.28
Simulation width	B	1×10^{-3}m
Simulation height	A	0.5×10^{-3}m

III. RESULTS

Comparing the experimental and theoretical results of cell suspension conductivity, the parameter $K = 3.10^{-2}$S/m. s is obtained for $V_m(\sigma_m = 0)$ between 1.8 V

and 3.3 V. The errors between the theoretical and experimental curves account for less than 15% as shown in Table 3.

The transmembrane potential increases according to Equation (1): when V_m exceeds a critical value (V_{pp}), there are the creations of pores and σ_m increases. The angular distributions of membrane conductivity and transmembrane potential are strongly dependent on the distance between cell membrane and capillary (d) as shown in Fig. 4, electric potential applied are 500 V and 1000 V. The maximum values of σ_m were near the pole. The simulation was performed with parameters from Table 1, the electroporation phenomena was modeled by Equation (3) with $K = 3.10^{-2}$ S/s and $V_{pp} = 0.20\ V$.

Table 3: Comparing of Ramos *et al.* [12] experiments and electroporation model of Equation (3)

$V_m(\sigma_m=0)$ (V)	Ref. [10]* (S/m)	Model (S/m)	Error %
1.8	6.5×10^{-6}	5.9×10^{-6}	9.8
2.2	9.0×10^{-6}	7.7×10^{-6}	14.2
2.6	1.2×10^{-5}	1.1×10^{-5}	10.3
2.9	1.3×10^{-5}	1.5×10^{-5}	11.1
3.3	2.0×10^{-5}	2.1×10^{-5}	6.0

*$\sigma_m=h.G_m$ [29].

Figure 5 presents the electric field distribution between capillary and cell membrane, d = 0.5 μm, and applied potential of 500 V and 1000 V. The lines represent the current density during the electroporation.

Dynamics of transmembrane potential induced and membrane conductance for different applied potentials through the capillary are shown in Fig. 6.

Figure 7 shows the influence of cell geometry on the electroporation with capillary near the cell. The transmembrane potential did not differ significantly when the cell radius is over 20 μm. The effects of internal and external conductivity are analyzed in Figs. 8 and 9. The conductivities values and cell radii of the simulations are limited to biological parameters [16].

IV. DISCUSSION

Based on Glaser's experiments [11], we propose that the membrane conductivity increases with the rate depending on the transmembrane voltage, Equation (3). The critical membrane potential proposed by Glaser is 0.46 V. However this potential was obtained with experiments with lipid bilayer. The experiments with different cells conclude that $V_{pp} = 0.2$ V [14]. These results are suitable for our experiments, because the K value was obtained from experiments with cell suspensions [12]. This parameter has different values when compared with the literature [2, 11, 15]. The difficulty in comparing the K value is caused by different

parameters measured between experiments. Glaser *et al.* [11] fit the current results with the electroporation model of Equation (3). Suzuki *et al.* [2] investigated the conductivity of cell suspensions when compared with two electroporation models. Although a variation was

expected in these values, the dynamics of the model is consistent with different experiments. The results obtained with our findings and literature experiments support the model at the beginning of the electroporation processes.
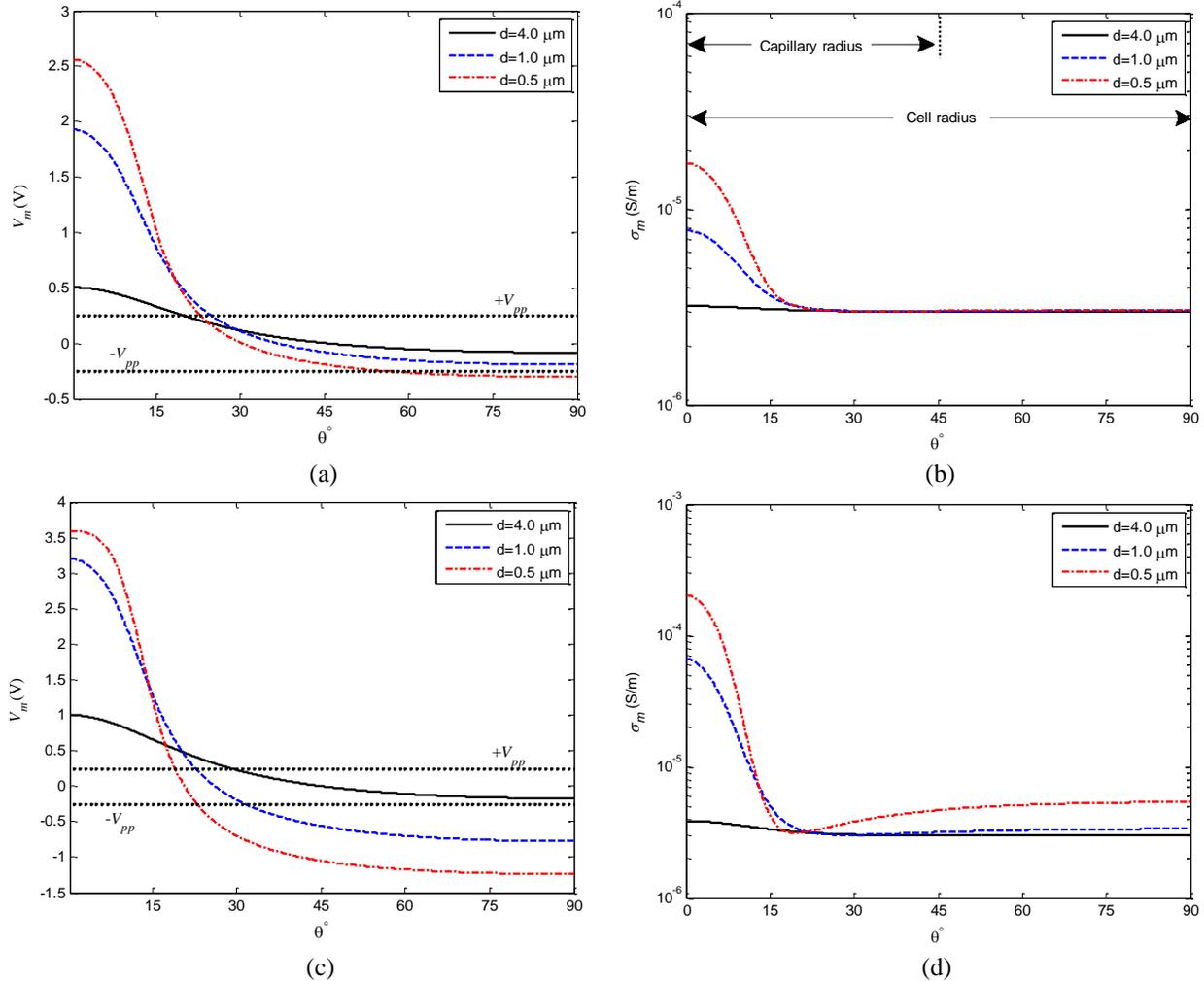
Fig. 4. Angular distribution of transmembrane potential and electroporated membrane conductivity, respectively, for applied electric potential (a) and (c) 500V, (b) and (d) 1000V. (d) Is the distance between capillary and cell membrane (tip-to-cell). Dashed parallel lines mark threshold electroporation potential V_{pp}=0.2 V [14]. Cell radius of 10 μm, electroporation model on the Equation (3) at steady state, σ_o=0.60 S/m and σ_i=0.13 S/m.

Our findings are consistent with the previous reports of membrane conductance indicating that the electroporation model and the geometric implementation of the model are consistent for these studies [16-20]. In this work, the intact membrane conductance is neglected. The σ_m with 500 V and d=4×10^{-6} m is about 3×10^{-6} S/m as shown in Fig. 4 (b). This value can be considered insignificant because it does not cause reduction of transmembrane potential. The comparison between V_m curve in Fig. 4 (a), d=4×10^{-6} m, and Zudans *et al.* (Fig. 9 from [13]) present less than 2% error. Some experimental

and theoretical work estimated the electroporated membrane conductivity (σ_m= $h.G_m$ [17]) at about 10^{-4} S/m [2], [18]. However, Hibino *et al.* [19] presented estimated values in the range from 10^{-4} S/m to 5×10^{-4} S/m. Pavlin *et al.* [20], [21] showed theoretical studies of effective conductivity of a suspension of cells, using σ_m=4×10^{-4} S/m. Kinosita and Tsong [22], [23] presented values on erythrocytes between σ_m=5×10^{-4} and 5×10^{-3} S/m. The results in Figs. 4 (b) and 4 (c) confirm the previous results.

The σ_m and V_m variation is higher on polar angle as

shown in Figs. 4 and 6. The reduction of distance between the capillary and the membrane increases the transmembrane potential and, consequently, σ_m.

The applied potential of 500 V produces opened pores on the membrane between 0° and 20° (Fig. 4 (b)). It happens because the outer to inner face of the cell membrane is over threshold potential. This area is smaller than the capillary radius. For 1000 V, σ_m increases until 20°. However, over 20°, the pores are created because there is a $V_m > V_{pp}$ from inner to outer face of the cell membrane as shown in Fig. 4 (d). It is of interest to note that most ionic current flows from the capillary to the cytoplasm through the electropores (solid lines in Fig. 5). However, over 20° there is a small current that flow out from the cell. It is insignificant when compared with the current on the pole cell.

The temporal dynamic of electroporation are presented in Fig. 6 with different electric fields. After the applied potential, V_m increases. When the threshold potential is over 200 mV, there is a quick increase in σ_m, the pores are created and the ions flow across the cell membrane. These ionic fluxes through the membrane reduce the V_m and stabilize σ_m, as shown in Fig. 6 (b). After the initial electroporation process, there is equilibrium between V_m and ion diffusion through the electropores.

The relation between the cell and capillary radius (R/r) is associated with the electroporated membrane conductivity and pore opened as shown in Figs. 7 and 8. The electroporation effect is not effective when cell radius is smaller than the capillary radius (*e.g.*, bacteria). However, the electroporation with capillary presents optimization results if cell dimensions are twice the capillary diameter. The transport of molecules and DNA using this technique is adequate for adherent cells and tissues (*in vivo*) as CHO and WSS Cells [24] and brain tissue [25], because the cell dimensions are bigger than those of the capillary. Agarwal *et al.* [26] presented experimental and numerical evidences of the cell size dependence on electroporation effect with the capillary as shown in Fig. 7.

The proximity of cell and capillarity is 0.5×10^{-6} m when R/r is over 4 and it produces localized high transmembrane potential ($\theta < 15°$). This effect happens because the cell membrane is almost plane in relation to the capillary.

An important factor for efficiency on electroporation is the cell survival. This parameter is associated with a fraction of the electroporated area [26]. In cell suspension, the cell survival is related with pulse amplitude [1]. The pulse amplitude is not suitable for the available cell survival with capillary. The applied electric field is not uniform and the transmembrane potential without electroporation is not available from Equation (1), Figs. 4 (a) and 4 (c). The cell survival on

electroporation is related to the ions efflux into cell. This ionic imbalance and swelling can provide the death of the cell [27]. Figure 4 (d), $d = 0.5 \times 10^{-6}$ m, presents an extensive electroporated area in relation to total membrane area. The simulation provides information that the applied electric pulses of 1000 V, $d = 0.5 \times 10^{-6}$ m, and cell radius of 10×10^{-6} m can kill the cells.

Figures 8 and 9 show that the membrane conductivity is higher when the external medium increases. Some experiments with electroporation present low conductivity medium ($\sigma_o < 0.2$ S/m) [21], [26]. Our model prediction provides results that these media can decrease the membrane conductivity. However, there is no consensus about any direct relation between membrane conductivity and molecular uptake to cells. Sadik *et al.* [28] describe a decrease of molecule diffusion with increase in medium conductivity. The physical mechanism underlying diffusion through the electropores is not completely understood.

(a)

(b)
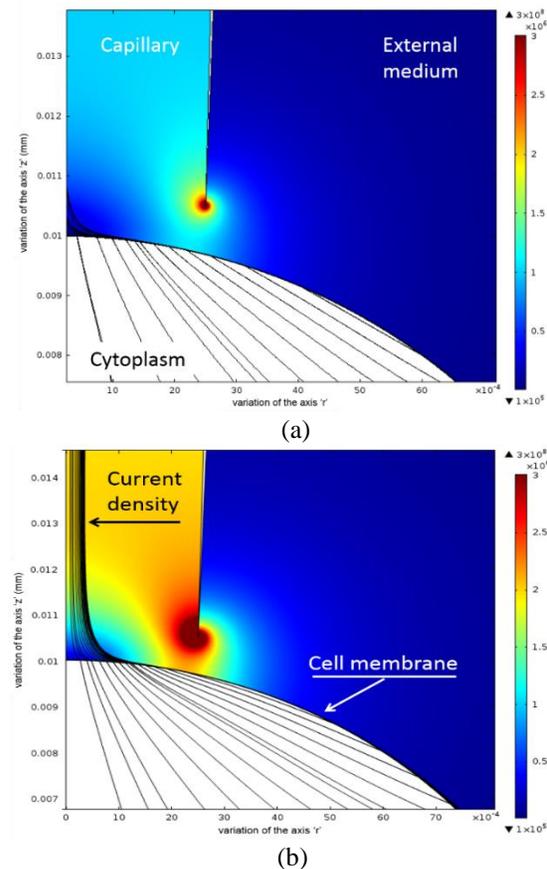
Fig. 5. Electric field distribution with distance between capillary and membrane cell of 0.5 μm. The lines represent current density components. (a) 500 V and (b) 1000 V. The color bar unit is V/m. The electropores are concentrated on the pole cell where the current lines are intense.

(a)

(b)
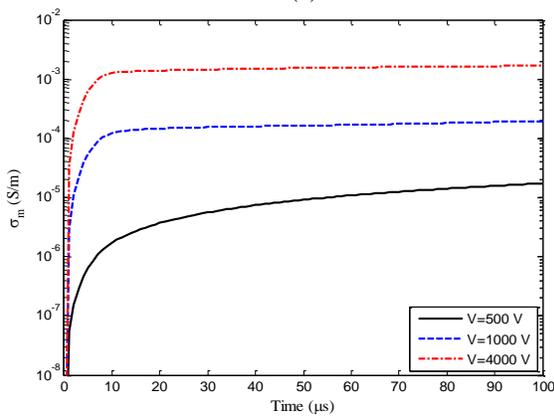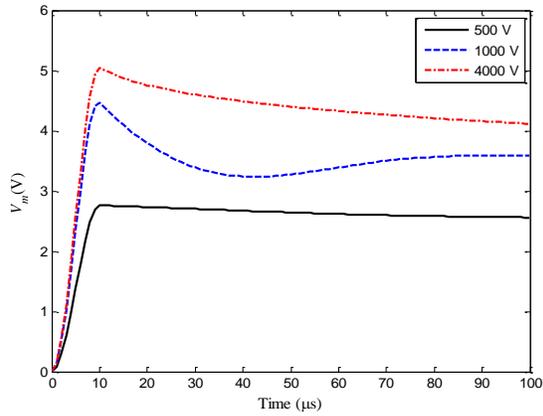
Fig. 6. Simulation of different applied potentials through the capillary on cell membrane with d=0.5 µm. (a) Transmembrane potential and (b) membrane conductance on the cell pole for different applied potentials. The cell radius is 10 µm.

(a)

(b)

Fig. 7. Effect of relation between cell and capillary radius (R/r) on (a) transmembrane potential and (b) membrane conductivity at steady state. Distance between capillary and cell membrane is d=0.5×10^{-6} m, applied potential is 500V, σ_o=0.60 S/m and σ_i=0.13 S/m. The capillary radius is 5×10^{-6} m.

Fig. 8. Relation of membrane conductivity and internal conductivity for three external conductivity. Applied potential is 500V and d= 0.5µm. The capillary radius is 5×10^{-6} m.
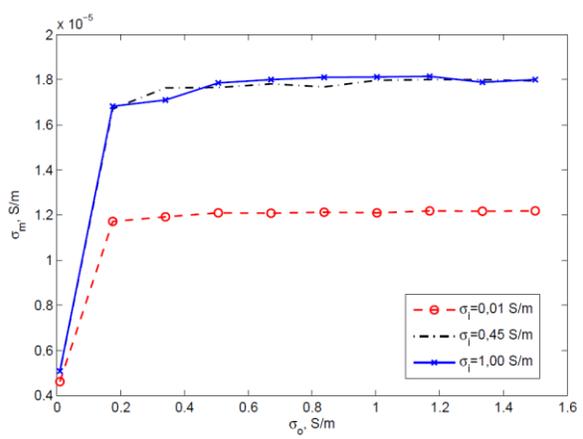
Fig. 9. Effect of external conductivity on membrane conductance for three internal conductivity. Applied potential is 500V and d= 0.5µm. The capillary radius is 5×10^{-6} m.

V. CONCLUSION

This study proposed an electroporation model based on Glaser *et al.* theories and Ramos *et al.* experiments. The membrane conductivity results are similar to previous works.

The high electric potential applied through capillary presented non linear electric field distribution on cell membrane (Figs. 4 (a), 4 (c) and 5). This effect may be reduced the cell survival.

The important factors that affect the electroporation with capillary are: external medium; relation between cell and capillary radius; distance between capillary; and membrane and strength applied potential.

ACKNOWLEDGMENT

REFERENCES

[1] T. Kotnik, P. Gorazd, and D. Miklavcic, *The Cell in the Electric Field*, in Clinical Aspects of Electroporation, J. G. Stephen, T. Kee, and E. W. Lee, Ed. New York, NY: Springer Science+Business Media, pp. 19-29, 2011.

[2] D. O. H. Suzuki, A. Ramos, M. C. M. Ribeiro, L. H. Cazarolli, F. R. M. B. Silva, L. D. Leite, and J. L. B. Marques, "Theoretical and experimental analysis of electroporated membrane conductance in cell suspension," *IEEE Trans. Biomed. Eng.*, vol. 58, no. 12, pp. 3310-8, Dec. 2011.

[3] D. O. H. Suzuki, J. Anselmo, K. D. de Oliveira, J. O. Freytag, M. M. M. Rangel, J. L. B. Marques, and A. Ramos, "Numerical model of dog mast cell tumor treated by electrochemotherapy," *Artif. Organs*, vol. in press, Jul. 2015.

[4] L. M. Mir, L. F. Glass, G. Sersa, J. Teissie, C. Domenge, D. Miklavcic, M. J. Jaroszeski, S. Orlowski, D. S. Reintgen, and Z. Rudolf, "Effective treatment of cutaneous and subcutaneous malignant tumours by electrochemotherapy," *Br. J. Cancer*, vol. 77, no. 12, p. 2336, 1998.

[5] P. A. Beare, K. M. Sandoz, A. Omsland, D. D. Rockey, and R. A. Heinzen, "Advances in genetic manipulation of obligate intracellular bacterial pathogens," *Front. Microbiol.*, vol. 2, no. May, p. 97, Jan. 2011.

[6] M. Wang, O. Orwar, J. Olofsson, and S. G. Weber, "Single-cell electroporation," *Anal. Bioanal. Chem.*, vol. 397, no. 8, pp. 3235-3248, 2010.

[7] K. Baek, C. Tu, J. Zoldan, and L. J. Suggs, "Gene transfection for stem cell therapy," *Curr. Stem Cell Reports*, pp. 52-61, 2016.

[8] D. Karra and R. Dahm, "Transfection techniques for neuronal cells," *J. Neurosci.*, vol. 30, no. 18, pp. 6171-6177, 2010.

[9] T. K. Kim and J. H. Eberwine, "Mammalian cell transfection: The present and the future," *Anal. Bioanal. Chem.*, vol. 397, no. 8, pp. 3173-3178, 2010.

[10] J. Li, W. Tan, M. Yu, and H. Lin, "The effect of extracellular conductivity on electroporation-mediated molecular delivery," *Biochim. Biophys. Acta - Biomembr.*, vol. 1828, no. 2, pp. 461-470, 2013.

[11] R. W. Glaser, S. L. Leikin, L. V Chernomordik, V. F. Pastushenko, and A. I. Sokirko, "Reversible electrical breakdown of lipid bilayers: formation and evolution of pores," *Biochim. Biophys. Acta (BBA)-Biomembranes*, vol. 940, no. 2, pp. 275-287, 1988.

[12] A. Ramos, A. L. S. Schneider, D. O. H. Suzuki, and J. L. B. Marques, "Sinusoidal signal analysis of electroporation in biological cells," *IEEE Trans. Biomed. Eng.*, vol. 59, no. 10, pp. 2965-73, Oct. 2012.

[13] I. Zudans, A. Agarwal, O. Orwar, and S. G. Weber, "Numerical calculations of single-cell electroporation with an electrolyte-filled capillary," *Biophys. J.*, vol. 92, no. 10, pp. 3696-705, May 2007.

[14] J. Teissié and M. P. Rols, "An experimental evaluation of the critical potential difference inducing cell membrane electropermeabilization," *Biophys. J.*, vol. 65, no. 1, pp. 409-413, 1993.

[15] Y. Qin, S. Lai, Y. Jiang, T. Yang, and J. Wang, "Transmembrane voltage induced on a cell membrane in suspensions exposed to an alternating field: A theoretical analysis," *Bioelectrochemistry*, vol. 67, no. 1, pp. 57-65, 2005.

[16] "Sensitivity of transmembrane voltage induced by applied electric fields – A theoretical analysis.pdf."

[17] W. M. Arnold, R. K. Schmutzler, A. G. Schmutzler, H. van der Ven, S. Al-Hasani, D. Krebs, and U. Zimmermann, "Electro-rotation of mouse oocytes: single-cell measurements of zona-intact and zona-free cells and of the isolated zona pellucida," *Biochim. Biophys. Acta (BBA)-Biomembranes*, vol. 905, no. 2, pp. 454-464, 1987.

[18] M. Schmeer, T. Seipp, U. Pliquett, S. Kakorin, and E. Neumann, "Mechanism for the conductivity changes caused by membrane electroporation of CHO cell-pellets," *Phys. Chem. Chem. Phys.*, vol. 6, no. 24, pp. 5564-5574, 2004.

[19] M. Hibino, H. Itoh, and K. Kinosita Jr., "Time courses of cell electroporation as revealed by submicrosecond imaging of transmembrane potential," *Biophys. J.*, vol. 64, no. 6, pp. 1789-1800, 1993.

[20] M. Pavlin and D. Miklavčič, "Effective conductivity of a suspension of permeabilized cells: a theoretical analysis," *Biophys. J.*, vol. 85, no. 2, pp. 719-729, 2003.

[21] M. Pavlin, M. Kandušer, M. Reberšek, G. Pucihar, F. X. Hart, D. Miklavčič, et al., "Effect of cell electroporation on the conductivity of a cell suspension," *Biophys. J.*, vol. 88, no. 6, pp. 4378-4390, 2005.

[22] K. Kinosita Jr. and T. Y. Tsong, "Voltage-induced pore formation and hemolysis of human erythrocytes," *Biochim. Biophys. Acta (BBA)-Biomembranes*, vol. 471, no. 2, pp. 227-242, 1977.

[23] K. Kinosita Jr. and T. Y. Tsong, "Voltage-induced conductance in human erythrocyte membranes," *Biochim. Biophys. Acta (BBA)-Biomembranes*, vol. 554, no. 2, pp. 479-497, 1979.

[24] J. Olofsson, M. Levin, A. Strömberg, S. G. Weber, F. Ryttsén, and O. Orwar, "Scanning electroporation of selected areas of adherent cell cultures," *Anal. Chem.*, vol. 79, no. 12, pp. 4410-4418, 2007.

[25] K. Nolkrantz, C. Farre, A. Brederlau, R. I. D. Karlsson, C. Brennan, P. S. Eriksson, S. G. Weber, M. Sandberg, and O. Orwar, "Electroporation of single cells and tissues with an electrolyte-filled capillary," *Anal. Chem.*, vol. 73, no. 18, pp. 4469-4477, 2001.

[26] A. Agarwal, I. Zudans, E. A. Weber, J. Olofsson, O. Orwar, and S. G. Weber, "Effect of cell size and shape on single-cell electroporation," *Anal. Chem.*, vol. 79, no. 10, pp. 3589-3596, 2007.

[27] S. Haberl, D. Miklavcic, G. Sersa, W. Frey, and B. Rubinsky, "Cell membrane electroporation-Part 2: the applications," *IEEE Electr. Insul. Mag.*, vol. 29, no. 1, pp. 29-37, Jan. 2013.

[28] M. M. Sadik, J. Li, J. W. Shan, D. I. Shreiber, and H. Lin, "Quantification of propidium iodide delivery using millisecond electric pulses: Experiments," *Biochim. Biophys. Acta (BBA)-Biomembranes*, vol. 1828, no. 4, pp. 1322-1328, 2013.

[29] W. M. Arnold, R. K. Schmutzler, A. G. Schmutzler, H. van der Ven, S. Al-Hasani, D. Krebs, and U. Zimmermann, "Electro-rotation of mouse oocytes: Single-cell measurements of zona-intact and zona-free cells and of the isolated zona pellucida," *Biochim. Biophys. Acta*, vol. 905, pp. 454-464, 1987.

Jânio Anselmo received a graduate degree in Electrical Engineering in 2011 from the University of Southern Santa Catarina (UNISUL), Florianópolis-SC, Brazil. He is currently an M.Sc. Student in Biomedical Engineering program at the Graduate in Electrical Engineering from the Federal University of Santa Catarina (UFSC-PGEEL). His research interests include modeling of biological processes through the phenomenon of electroporation.

Luciana Costa Ramos received a graduate degree in Electrical Engineering in 1996 from the Federal Technological University of Paraná (UTFPR), Curitiba-PR, Brazil. She is currently a M.Sc. Student in Biomedical Engineering program at the Graduate in Electrical Engineering from the Federal University of Santa Catarina (UFSC-PGEEL). Her research interests include modeling of biological processes through the phenomenon of electroporation.

Fátima R.M. B. Silva received the graduate degree in Chemistry from the Catholic University of Pelotas, Pelotas-RS, Brazil, in 1984, and the Ph.D. degree in Biochemistry from the Federal University of Rio Grande do Sul, Porto Alegre, SC, Brazil, in 1995. Since 1994, she has been researching and teaching as an Associate Professor at the Federal University of Santa Catarina. Her current interests include endocrine, physiology, and biochemical alterations in cells.

Jefferson L. B. Marques (M'02) received a graduate degree in Electrical Engineering in 1985 from the Federal University of Santa Maria, Santa Maria-RS, Brazil, and a Ph.D. degree in Medical Physics and Clinical Engineering in 1994 from the University of Sheffield, Sheffield, UK. He is currently an Associate Professor at the Federal University of Santa Catarina. His research interests include modeling of physiological phenomena.

Daniela O. H. Suzuki (M'09) received a graduate degree in Electrical Engineering in 1996 and a Ph.D. degree in Electrical Engineering in 2009 from the Federal University of Santa Catarina (UFSC), Florianópolis-SC, Brazil. She is currently an Assistant Professor at the Federal University of Santa Catarina. Her current interests include modeling biological processes, experimental and numerical investigation of membrane electropermeabilization.

A Practical UWB Microwave Imaging System Using Time-Domain DORT for Tumor Detection

S. Sadeghi and R. Faraji-Dana

School of Electrical and Computer Engineering, College of Engineering
University of Tehran, Tehran, Iran
sajjadsadeqi@ut.ac.ir, reza@ut.ac.ir

Abstract ─ In this paper Time Reversal (TR) and Decomposition of Time Reversal operator (DORT) methods are employed in an Ultra-WideBand (UWB) microwave imaging system. The possibility of multiple tumor detection in using selective focusing DORT is investigated and a number of improvements are proposed in DORT algorithm. A practical UWB imaging system for tumor-like object detection consisting of just two revolving UWB antennas is then introduced. The proposed system does not need costly switches or network analyzers as it just uses a UWB transceiver to acquire the required time domain signals. Challenging problems of this system are addressed and their solutions are proposed and vindicated through both simulations and measurements carried out on a simple model by using an experimental setup. The proposed system is suitable for different applications such as breast cancer and tumor detection where high accuracy and resolution is necessary.

Index Terms ─ DORT and tumor detection, microwave imaging, time-reversal.

I. INTRODUCTION

In recent years, microwave imaging has gained diverse applications in different domains such as radar imaging [1,2], detection of buried objects [3], detection of fault in networks [4], medical imaging [4–8], and so on. Among these applications, early detection and localization of breast cancer tumors has obtained considerable attention. Several algorithms have already been introduced for the improvement of accuracy and obtaining a better resolution of the detection [7–12]. This growing attention is especially motivated by the significant contrast in the dielectric properties of malignant breast tissues and the background medium at microwave frequencies.

Microwave imaging methods for tumor detection is mainly divided in two different categories: tomography imaging and ultra-wideband (UWB) radar imaging. In tomography imaging, dielectric properties of tissue are obtained by solving an inverse scattering problem. In contrast, in UWB radar imaging the goal is to identify and localize significant scatterers in the tissues. As a result, a much simpler problem has to be solved compared to the former category.

Among different methods proposed in UWB imaging, the time-reversal (TR) methods which were first developed and implemented in acoustics [13], show a better performance in high clutter and noisy environments like breast tissues [14].

Conventional TR methods can only detect the dominant scatterer; thus, no information about other scatterers would be achieved. In order to overcome this shortcoming, eigenvalue decomposition (EVD) of the time-reversal operator (TRO) is employed [14]. The eigenvalues and related eigenvectors of the TRO provide the required information about all well-resolved point-like scatterers. Using these eigenvectors and transmitting them by the detecting antenna array makes selective focusing of each scatterer possible. This strategy is the basis of the decomposition of the time-reversal operator (DORT) method [15].

In most of the previous work, DORT method is used in single or multiple frequency schemes while some major challenges would occur when employing DORT in UWB imaging systems. In UWB DORT, first the EVD is applied on several discrete frequencies in the desired frequency range, next discrete time domain signal is obtained by using inverse discrete Fourier transform (IDFT) [14]. In this process the main challenge is how to relate different eigenvalues to distinct scatterers in the frequency range. To the best of our knowledge this problem which results in the loss of information of some scatterers has not been properly addressed in the literature. In this paper, we propose a new method to overcome this problem through sorting the eigenvalues at each frequency.

Another challenge arises from the lack of knowledge about the frequency dependence of the phases of eigenvectors. In fact, no information exists on the phases of the frequency domain signals. Therefore, after performing the IDFT the time domain results become incoherent. This is particularly important in

inhomogeneous background media with multiple scatterers, where multiple reflections has to be coherently combined over the entire bandwidth at the target(s) location(s) [16]. Such preprocessing can be done by using a power singular value decomposition (SVD) or by projecting the incoherent eigenvectors onto columns of the MDM [16, 17]. In [16], space-frequency TR is used for UWB imaging. In this paper however we introduce a new modification in the phase of eigenvectors to achieve coherent time-domain signals.

By addressing the above-mentioned challenges in employing DORT in a practical UWB imaging system, we built and employed an imaging system for breast cancer detection at the UWB frequency band of 3.1-10.6 GHz. This system uses two moving antennas for transmitting and receiving signals. This arrangement is much simpler and less-expensive compared with the previously introduced complicated systems [18-22] and will be shown to enjoy comparable performance.

This paper is organized as follows. In Section II the conventional TR method along with some improving modifications are introduced. The proposed microwave imaging system is presented in Section III. Validating system performance through simulations and measurements will be given in Sections IV and V, respectively. Section VI concludes the paper.

II. TIME REVERSAL METHOD

Time reversing is the retransmission of the received electromagnetic waves in the receivers back to the propagation medium in the reverse form relative to time. In this method the received signals in the receivers are first reversed and then transmitted back into the medium. It can be shown that these transmitted signals will propagate back in the same paths as in the forward propagation and focus on near to the primary source in practical situation [23]. This behavior of the reversed waves remains true in a situation where the medium contains unknown scatterers imposing reflection, refraction or diffraction on the propagating waves.

In media with multiple discrete scatterers, back-propagation of the time reversed scattered fields, causes the focal spots to be created on all scatterers at the same time, naturally with more intensity expected on the dominant scatterer. As a result, the information of dominated scatterers may be lost. In DORT, this problem is overcome by isolating and sorting different scatterers by using eigenvalue decomposition.

In DORT method, N transceiver antennas, called time-reversal array (TRA), generate an N×N symmetric matrix denoted by $K(t)$. This symmetry is due to the reciprocity property of the electromagnetic fields. In the frequency domain this matrix is represented by $K(\omega)$ and is referred to as the Multi Data Matrix (MDM), where ω is the angular frequency [14]. TR operation in the time domain corresponds to the phase conjugation in the frequency domain denoted by the Hermitian conjugate $K^{\dagger}(\omega)$. In [14], TRO is defined as the self-adjoint matrix of $T(\omega) = K^{\dagger}(\omega)K(\omega)$. By applying singular value decomposition (SVD) to $K(\omega)$, it is given by $K(\omega) = U(\omega)\Lambda(\omega)V^{\dagger}(\omega)$, where is the diagonal matrix of singular values and $U(\omega)$ and $V(\omega)$ are unitary matrices. In this way the EVD of the TRO can be written as $T(\omega) = V(\omega)S(\omega)V^{\dagger}(\omega)$, where $S(\omega) = \Lambda^{\dagger}(\omega)\Lambda(\omega)$ is the diagonal matrix of eigenvalues [14]. It is obvious that the eigenvalues of the TRO and the squared singular values of the MDM are equal; hence, both expressions are used interchangeably in references.

Normalized eigenvectors of the TRO form the columns of the unitary matrix $V(\omega)$ [24]. In the case of recognizable point-like scatterers in homogeneous media, each significant eigenvalue of the TRO means a single scatterer generating isotropic scattered fields. Since in reality no scatterer generates isotropic EM waves multiple eigenvalues will be referring to a single scatterer [25, 26]. In this case, the associated eigenvector $v_p(\omega_c)$, where ω_c is the central operation frequency, produces the back-propagated fields radiated from the TRA for focusing on the pth scatterer. The normalized vector $v_p(\omega_c)$ is the pth column of $V(\omega_c)$. However, a similar decomposition should be applied to the entire bandwidth at each frequency point to make a frequency dependent amplitude distribution of eigenvectors for UWB signals.

The main difficulty of this algorithm lies in the fact that locating and tracking of singular values in the frequency domain is a challenge due to the change of their orders. In Fig. 1 singular values of a sample configuration consisting of two PEC spheres with two different radii r1=1.5 cm and r2=0.5 cm are shown. As it is clear in the figure, due to the comparable sizes of the scatterers with the wavelengths of the frequency components of a UWB signal, there exist multiple singular values with considerable magnitudes in the entire frequency band. Also, changes in the order of singular values at different frequencies are evident as marked by arrows in the figure.

In our implementation of the DORT in a UWB system, we solved this problem by using the orthogonality of eigenvectors. It is obvious that at a single frequency, eigenvectors of a specific scatterer are parallel and eigenvectors of two well-resolved scatterer are orthogonal. By tracking the inner product of dominant eigenvectors in adjacent frequencies, eigenvectors of each scatterer in the entire frequency band will be identified. In Fig. 2 inner product of the two first eigenvectors in the imaging problem of Fig. 1 is

shown. As it is seen the inner product of the 1st and 2nd eigenvectors are almost zero while and self-inner product of the 1st eigenvectors are almost equal to 1. Also, for the eigenvalues whose orders have been changed inner products of the 1st and 2nd eigenvectors are greater than self-inner product. It is evident that by using this technique eigenvalues and eigenvectors which have changed their order can be identified.
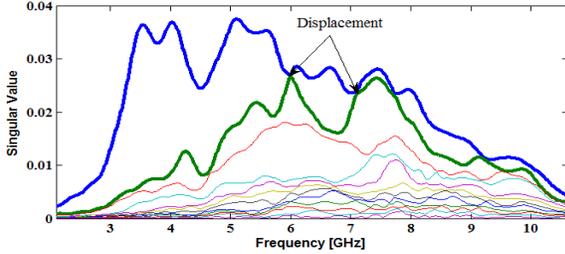
Fig. 1. Variations of singular values of two PEC spheres with different radii over the entire UWB frequency band.
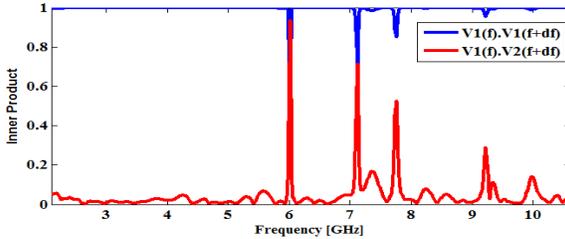
Fig. 2. Inner product of the 1st eigenvector by itself (blue), and the 1st and 2nd eigenvectors (green), in two adjacent frequencies.

The second challenging problem in using the frequency domain eigenvectors in image reconstruction process is the lack of knowledge about the true relative phases of eigenvectors. In [16], left singular vectors of TRO is obtained by using:

$$u_p(\omega) = e^{j\Phi_{SVD}(\omega)} \frac{g(\overline{X_p},\omega)}{\left\| g^*(\overline{X_p},\omega) \right\|},$$ (1)

where u_p is the pth left singular vector, $\Phi_{SVD}(\omega)$ is the frequency-dependent phase of SVD, g is Green's function vectors which relates the scatterer location to TRA and finally $\overline{X_p}$ is the location of the pth scatterer in medium.

One may find other methods like space frequency TR [16], [27] or phase smoothing [14] to overcome this problem. In this paper we propose a simple solution to this problem. Since in computing the eigenvectors with MATLAB the first element of each vector has a random phase and the phases of all other elements are determined relative to the first element, we have set the phase of first element to zero while preserving the relative phases of

other elements. With this modification a coherent signal could be obtained. Also, since the eigenvectors are normalized to 1, these vectors need to renormalize to their corresponding eigenvalues. In the TR process these vectors have to be conjugated as well. These operations can be written as $(\lambda_p u_p)^* = \lambda_p u_p^* = \lambda_p v_p$, and the time-domain signals are calculated by using the inverse Fourier transform $e_p(t) = F^{-1}\{\lambda_p(\omega)v_p(\omega)\}$.

After reconstructing the required time domain signals for back-propagation by following the above-mentioned procedure, the last step is the retransmitting of the signals by TRA to the medium. For retransmitting of the signals, solving a forward problem by using the excitation signal $e_p(t)$ at the transmitters is required. In solving this forward problem, electric field at each time step at all positions should be computed and saved. Then by assigning a color map to the field strength at each position, the image at that time will be constructed.

The last issue arises in the construction of final images by the TR method is the selection of optimum time when the waves converge to the scatterers. The images in this time have an intense peak at the object locations and lower intensity at other locations. Since these images have a small entropy, minimum entropy can be used as a criterion for selecting optimum time images. In [28] the inverse of varimax norm is used for the computation of entropy. This criterion has also been used for breast cancer detection in [28, 30]. It reads as:

$$R(E_{tot}^{n\,2}) = \frac{\left[\sum_{j,k}\sum E_{tot}^{n\,2}(j,k) \right]^2}{\sum_{j,k}\sum E_{tot}^{n\,4}(j,k)},$$ (2)

where E_{tot} represents the total electric field, n is the time step of solving the forward problem, (j,k) are the grid cell coordinates, and summation is taken over the portion of the grid that represents the tissue.

III. PROPOSED MICROWAVE IMAGING SYSTEM

To examine performance of the proposed algorithm in an example, a new simple measurement setup for potential application in breast cancer detection is introduced. In most of the previous researches a multi-antenna configuration along with a multiport RF switch is used for acquiring the required data [1, 20, 31]. Here, to reduce the cost and complexity of the measurement setup we use a two antenna scanning system to replace a 12-antenna configuration. This method also reduces the undesired mutual couplings between the antennas.

For acquiring the same data as in a multi-antenna configuration, first, the transmitter is fixed and the receiver antenna scans the defined space at the specified steps. Next, the transmitter moves one step forward and

the receiver scans the remaining locations. This process is continued until the transmitter antenna completes scanning of the specified path. Because of the hemisphere shape a circular scanning path is assumed around the tissue under investigation. Selected angular step is 30º and in each scan 12 signals are recorded. It is worth mentioning that the returned signal to the transmitting antenna is also measured, that is a total of 144 measurements will be recorded. The received signals are recorded and saved for preprocessing as explained below, but before that let us consider the practical challenges encountered in this imaging system.

The main challenge is the unwanted signals which are received by the receiver antenna in addition to the signal that comes from the tumor. These signals can be categorized into three main groups. First are the unwanted signals due to the line of sight path between the transmitter and the receiver. Second is the reflected signals from the breast skin, and the last unwanted signal is due to the multipath reflections from clutter sources in tissue media.

The line of sight unwanted signals dominate the possible tumor signals, causing the failure of the imaging process. To eliminate these signals, a calibration process is employed. In this process, first in the absence of the object (here the breast tissue) all received signals are measured and saved. This calibration data is subtracted from the signals measured in the presences of the object.

For removing the effect of reflected signals from the breast skin, we first take the average of the signals received by those receivers which have the same distance and angle to the transmitter. Assuming that the skin is symmetric, by subtracting the average signal corresponding to the same distance and angle between the transmitter and receiver- from the received signal, we are able to elicit the main signal.

It is shown that the last unwanted signals due to multipath reflections in tissue media are useful for resolution improvement in TR [32].

To achieve a better resolution enabling the detection of small tumors, high frequency components should be applied. On the other hand for increasing the penetration depth to detect deep tumors in a tissue, low frequency components are required.

For these reasons UWB imaging is a good choice. Excitation signal is a Gaussian modulated signal with the standard UWB frequency band of 3.1-10.6 GHz in which acceptable contrast between malignant and normal tissues is observed [33].

Vivaldi antenna of Fig. 3 which was designed and fabricated for the experimental setup of the system explained in Section V was also used in simulations for transmitting waves to the medium and receiving signals from the tissue. Figure 4 shows the variations of the antenna VSWR and gain over the working frequency band computed by using CST Microwave Studio [34].
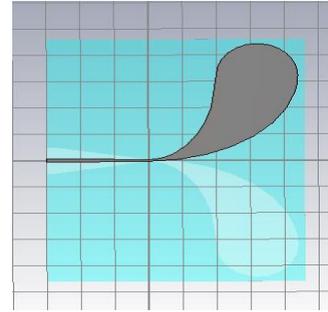
Fig. 3. Vivaldi antenna used in the proposed UWB imaging, each side of the square divisions is 1 cm.

(a)

(b)
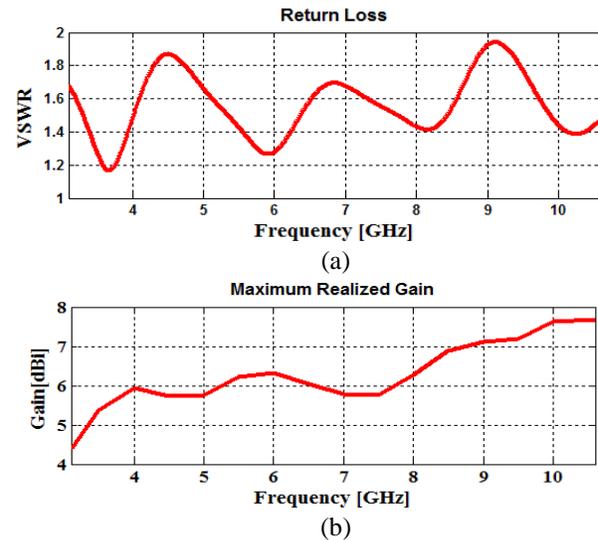
Fig. 4. Simulated (a) VSWR and (b) maximum gain of the UWB antenna.

IV. IMAGE RECONSTRUCTION SIMULATION

In this section, simulation process and simulated models for verification of the proposed algorithms are introduced. To obtain the simulated signals in time-domain, the forward problem is solved by using CST Microwave Studio software and its transient solver. Figure 5 shows the simulation environment for the two antenna configuration in the presence of the breast tissue and a typical tumor.

Discrete ports for excitation of transmitter antenna and capturing the backscattered signals in receiver are used. To simulate the breast tissue, a homogenous hemisphere with relative permittivity of 10 and radius of 10 cm is used as the simplest model. Tumor is modeled by a dielectric sphere with relative permittivity of 25 and the radius of 0.1 cm located at the coordinates (1 cm, 1 cm). Also, for modeling the skin a symmetric thin layer with thickness of 0.2 cm and relative permittivity of 35 is considered. This simple configuration permits fast and

easy data acquisitions for the 144 signals required in the data acquisition step of the proposed imaging system.

After acquiring the time domain signals, the TR signals are constructed by following the algorithm discussed before. Then these signals are fed back to the 12 antennas shown in the reconstruction configuration of Fig. 6. Again the CST Microwave Studio package is employed to solve the new forward problem at hand.
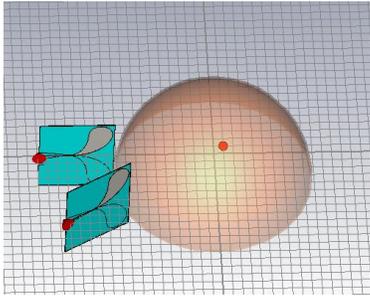
Fig. 5. A simple model for the breast tissue with one tumor used in the data acquisition process.
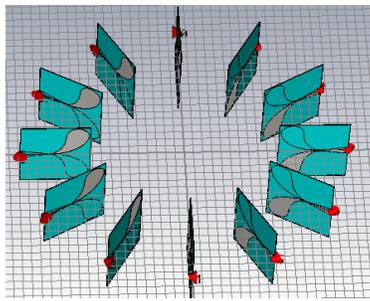
Fig. 6. Configuration of the image reconstruction process.

Since there is just one scatterer in the tissue, the conventional TR method can produce an accurate image of the tumor as shown in Fig. 7. We have used the calibration techniques introduced in Section II for removing the line of sight and skin reflections. As can be seen the tumor is well diagnosed and peak of the intensity is located exactly at the center of the tumor.

To validate the proposed modified DORT method a clutter is added to the tissue in the previous model. First two equi-radius spheres are considered at the (2 cm, 4 cm) and (-2 cm, -5 cm) locations. Dielectric properties for the tissue, skin and tumor is the same as before and clutter is considered to be caused by a relative permittivity similar to the tumor. In this situation skin reflections and the line of sight signals are omitted by using the calibration method introduced in Section II. Fig. 8 shows that the proposed modified DORT can selectively reconstruct the images of the spheres.

To examine the capability of the proposed algorithm to detect non-dominant scatterers, two spheres with

the same dielectric constants but different radii are considered. One scatterer has the radius of 1.5cm and is located at (2cm, 4cm), and the other scatterer has the radius of 0.5m and is located at (-2 cm, -5 cm). As can be seen in Fig. 9, despite of having dominant scatterer, both scatterers are detected and localized with small errors.
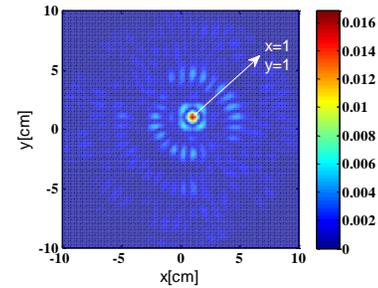
Fig. 7. The reconstructed image of the tumor by using the conventional TR method.

(a)

(b)
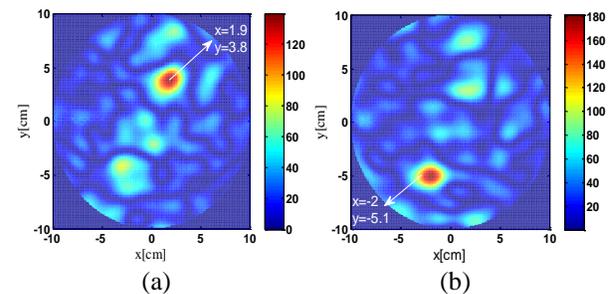
Fig. 8. The reconstructed images of two equi-radius spheres located at: (a) (2, 4), and (b) (-2,-5) coordinates.

(a)

(b)
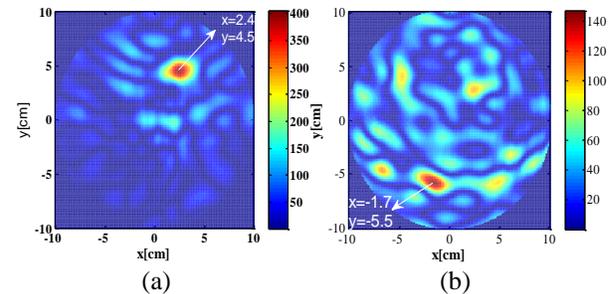
Fig. 9. Reconstructed images of two spheres with different radii of 1.5 cm and 5 mm located respectively at: (a) (2, 4) and (b) (-2, -5) coordinates.

V. EXPERIMENTAL VALIDATION

In this section, the data collected by an experimental setup of the proposed two-antenna system is used to reconstruct an object by employing the proposed algorithm. Figure 10 shows the experimental setup that has been used for this purpose. In order to demonstrate the ability of the proposed setup for detection of

scatterers, two test tubes filled with pure liquid propanol are used as detection targets. These two tubes are placed at (-2,4) and (3.5,-4) coordinates with different heights of 22 cm and 16 cm and different radii of 0.5 and 0.75 cm, respectively. The two Vivaldi antennas shown in the

Fig. 10 (a) have been used to take 64 signals at 8 locations 45° apart as explained in Section III. Here we have seven angular separations between the transmitting and the receiving antennas, at each separation the two antennas are fixed and the objects are rotated in 45° intervals by using a positioning platform, and this process is repeated for each angular separation. The angular accuracy of the positioner which is controlled by a computer is ±1° which is considered to be very coarse compared to the modern positioning systems.

First, we used a commercial UWB transceiver, i.e., TIME DOMAIN®PulsON 220, which generates and captures UWB pulses in the 3.1-6.3 GHz frequency range. In other words, this instrument has a UWB bandwidth of 3.2 GHz instead of the standard 7.5 GHz bandwidth (from 3.1 to 10.6 GHz) used in the previous section. Figure 10 (b) and Fig. 10 (c) show the reconstructed images by using the proposed method. It is clear that the two rods could be detected with reasonable accuracy.

To show the full capacity of the proposed UWB imaging system when the whole 3.1-10.6 GHz frequency band is harvested, since we could not find a commercial instrument with this specifications we designed a frequency domain measurement setup to take the required time domain data. In this experiment we employed a vector network analyzer to measure the S21 parameters of the two antennas in each location for the 1024 frequency points in the desired frequency band.

The spectrum of the desired time domain signal is then calculated by taking the product of S21 values with the spectrum of the input Gaussian excitation signal. Finally the desired UWB output signals are obtained by using IFFT. Figure 10 (d) and 10 (e) show the reconstructed images by using this setup. It is clear that more accurate images are obtained by harvesting the whole UWB frequency band; therefore it is expected that the same quality of images achieved by employing a simple UWB transceiver provided that it can use the whole 3.1-10.6 GHz UWB band.
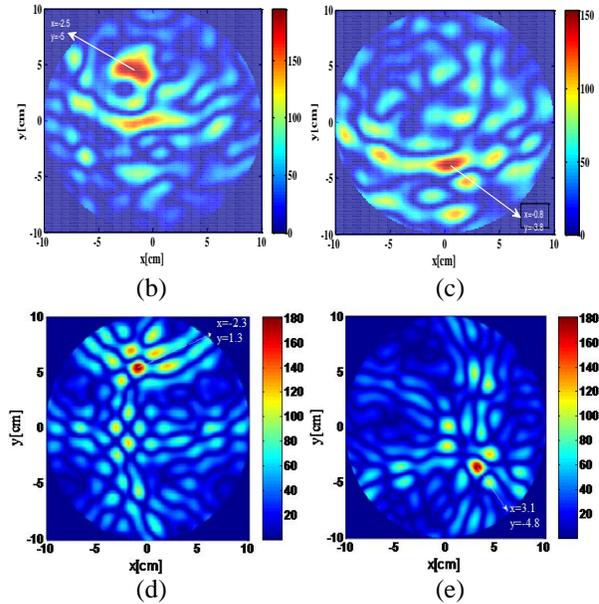
Fig. 10. (a) Experimental setup used to validate the proposed imaging system and the reconstructed images of the two tubes located at (b), (d) (-2,4) and (c), (e) (3.5, -4) coordinates first by a UWB transceiver (3.1-6.3 GHz frequency band), and then by using a Vector Network Analyzer (3.1-10.6 GHz frequency band).

VI. CONCLUSION

In this paper a TR approach for microwave imaging using UWB signals is introduced. In this approach DORT has been applied for selective focusing on multiple scatterers. A simple and cost effective imaging system has been proposed for detecting tumor-like objects using just two UWB scanning antennas and a UWB transceiver. By improving the TR algorithm, simulation results illustrates that a 1mm diameter object in a homogenous media can be detected.

The DORT algorithm is then modified to enhance itseffectiveness in detecting a non-dominant scatterer in presence of a dominant one. To implement the imaging system, two experimental setups performing in time and frequency domains, respectively, are designed. The performance of these setups to resolve two dielectric rods with different dimensions placed in a homogeneous medium are compared. It is shown that using wider frequency bands results in higher resolution as well as lower ambiguity in detecting targets. Due to the generality of the proposed imaging system, it can be used in a wide range of applications such as breast cancer recognition as well as tumor detection.

Although we considered a simple static configuration to show the effectiveness of our proposed imaging system, comprehensive clinical studies should be carried out on any medical imaging system to study its behavior in a practical dynamic situation. It is however our

expectation that the ease and speed of the data acquisition process in our proposed system can contribute to its success in the real clinical tests.

REFERENCES

[1] G. L. Charvat, L. C. Kempel, E. J. Rothwell, C. M. Coleman, and E. L. Mokole, "A through-dielectric radar imaging system," *IEEE Transactions on Antennas and Propagation*, vol. 58, no. 8, pp. 2594-2603, Aug. 2010.

[2] J. T. Case, M. T. Ghasr, and R. Zoughi, "Nonuniform manual scanning for rapid microwave nondestructive evaluation imaging," *IEEE Transactions on Instrumentation and Measurement*, vol. 62, no. 5, pp. 1250-1258, May 2013.

[3] G. S. Smith and L. E. R. Petersson, "On the use of evanescent electromagnetic waves in the detection and identification of objects buried in lossy soil," *IEEE Transactions on Antennas and Propagation*, vol. 48, no. 9, pp. 1295-1300, 2000.

[4] L. Abboud, A. Cozza, and L. Pichon, "A noniterative method for locating soft faults in complex wire networks," *IEEE Transactions on Vehicular Technology*, vol. 62, no. 3, pp. 1010-1019, Mar. 2013.

[5] J. D. Shea, B. D. Van Veen, and S. C. Hagness, "A TSVD analysis of microwave inverse scattering for breast imaging," *IEEE Transactions on Bio-medical Engineering*, vol. 59, no. 4, pp. 936-45, Apr. 2012.

[6] Y. Chen and P. Kosmas, "Detection and localization of tissue malignancy using contrast-enhanced microwave imaging: Exploring information theoretic criteria," *IEEE Transactions on Bio-medical Engineering*, vol. 59, no. 3, pp. 766-76, Mar. 2012.

[7] S. M. Aguilar, M. A. Al-Joumayly, M. J. Burfeindt, N. Behdad, and S. C. Hagness, "Multi-band miniaturized patch antennas for a compact, shielded microwave breast imaging array," *IEEE Transactions on Antennas and Propagation*, vol. 62, no. 3, pp. 1221-1231, Dec. 2013.

[8] E. J. Bond, S. C. Hagness, and B. D. Van Veen, "Microwave imaging via space-time beamforming for early detection of breast cancer," *IEEE Transactions on Antennas and Propagation*, vol. 51, no. 8, pp. 1690-1705, Aug. 2003.

[9] E. J. Bond, B. D. Van Veen, and S. C. Hagness, "An overview of ultra-wideband microwave imaging via space-time beamforming for early-stage breast-cancer detection," *IEEE Antennas and Propagation Magazine*, vol. 47, no. 1, pp. 19-34, Feb. 2005.

[10] X. Li, S. K. Davis, S. Member, S. C. Hagness, D. W. Van Der Weide, and B. D. Van Veen, "Microwave imaging via space−time beamforming: Experimental investigation of tumor detection in

multilayer breast phantoms," vol. 52, no. 8, pp. 1856-1865, 2004.

[11] Y. Xie, B. Guo, L. Xu, J. Li, and P. Stoica, "Multistatic adaptive microwave imaging for early breast cancer detection," *IEEE Transactions on Bio-medical Engineering*, vol. 53, no. 8, pp. 1647-57, Aug. 2006.

[12] F.-C. Chen and W. C. Chew, "Time-domain ultra-wideband microwave imaging radar system," *Journal of Electromagnetic Waves and Applications*, vol. 17, no. 2, pp. 313-331, 2003.

[13] M. Fink, D. Cassereau, A. Derode, C. Prada, P. Roux, and M. Tanter, "Time-reversed acoustics," *Rep. Prog. Phys.*, vol. 63, pp. 1933-1955, 2000.

[14] M. E. Yavuz and F. L. Teixeira, "Full time-domain DORT for ultrawideband electromagnetic fields in dispersive, random inhomogeneous media," *IEEE Transactions on Antennas and Propagation*, vol. 54, no. 8, pp. 2305-2315, Aug. 2006.

[15] C. Prada and M. Fink, "Eigenmodes of the time reversal operator: A solution to selective focusing in multiple-target media," *Wave Motion*, vol. 20, no. 2, pp. 151-163, Sep. 1994.

[16] M. E. Yavuz and F. L. Teixeira, "Space−frequency ultrawideband time-reversal imaging," *IEEE Transactions on Geoscience and Remote Sensing*, vol. 46, no. 4, pp. 1115-1124, Apr. 2008.

[17] J. G. Berryman, L. Borcea, G. C. Papanicolaou, and C. Tsogka, "Statistically stable ultrasonic imaging in random media," *The Journal of the Acoustical Society of America*, vol. 112, no. 4, pp. 1509, 2002.

[18] X.-M. Zhong, C. Liao, W.-B. Lin, H.-Y. Li, and H.-J. Zhou, "Time-reversal imaging based on the space-frequency MDM and cancellation operator," *Journal of Electromagnetic Waves and Applications*, vol. 28, no. 3, pp. 265-274, 2014.

[19] G. L. Charvat, L. C. Kempel, E. J. Rothwell, C. M. Coleman, and E. L. Mokole, "A through-dielectric ultrawideband (UWB) switched-antenna-array radar imaging system," *IEEE Transactions on Antennas and Propagation*, vol. 60, no. 11, pp. 5495-5500, Nov. 2012.

[20] N. Ghavami, G. Tiberi, D. J. Edwards, and A. Monorchio, "UWB microwave imaging of objects with canonical shape," *IEEE Transactions on Antennas and Propagation*, vol. 60, no. 1, pp. 231-239, Jan. 2012.

[21] L. Bellomo, M. Saillard, S. Pioch, K. Belkebir, and P. Chaumet, "An ultrawideband time reversal-based RADAR for microwave-range imaging in cluttered media," in *Proceedings of the XIII Internarional Conference on Ground Penetrating Radar*, pp. 1-5, 2010.

[22] M. Zhou, X. Chen, L. Li, and C. Parini, "The UWB imaging system with rotating antenna array for

concealed metallic object," in *EUCAP*, no. EuCAP, pp. 117-119, 2014.

[23] M. E. Yavuz and F. L. Teixeira, "Effects of array restriction on time-reversal methods," in *2007 IEEE Antennas and Propagation International Symposium*, pp. 405-408, 2007.

[24] M. E. Yavuz and F. L. Teixeira, "On the sensitivity of time-reversal imaging techniques to model perturbations," *IEEE Transactions on Antennas and Propagation*, vol. 56, no. 3, pp. 834-843, Mar. 2008.

[25] D. H. Chambers and J. G. Berryman, "Analysis of the time-reversal operator for a small spherical scatterer in an electromagnetic field," *IEEE Transactions on Antennas and Propagation*, vol. 52, no. 7, pp. 1729-1738, Jul. 2004.

[26] G. Micolau, M. Saillard, and P. Borderies, "DORT method as applied to ultrawideband signals for detection of buried objects," *IEEE Transactions on Geoscience and Remote Sensing*, vol. 41, no. 8, pp. 1813-1820, Aug. 2003.

[27] M. E. Yavuz and F. L. Teixeira, "Space-frequency ultrawideband time-reversal Imaging method as applied to subsurface objects," in *IGARSS 2008 - 2008 IEEE International Geoscience and Remote Sensing Symposium*, no. 1, pp. III – 12– III – 15, 2008.

[28] X. Xu, S. Member, E. L. Miller, C. M. Rappaport, and S. Member, "Minimum entropy regularization in frequency-wavenumber migration to localize subsurface objects," vol. 41, no. 8, pp. 1804-1812, 2003.

[29] P. Kosmas and C. M. Rappaport, "Time reversal with the FDTD method for microwave breast cancer detection," *IEEE Transactions on Microwave Theory and Techniques*, vol. 53, no. 7, pp. 2317-2323, Jul. 2005.

[30] P. Kosmas and C. M. Rappaport, "A matched-filter FDTD-based time reversal approach for microwave breast cancer detection," *IEEE Transactions on Antennas and Propagation*, vol. 54, no. 4, pp. 1257-1264, Apr. 2006.

[31] B. J. Mohammed, D. Ireland, and A. M. Abbosh, "Experimental investigations into detection of breast tumour using microwave system with planar array," *IET Microwaves, Antennas & Propagation*, vol. 6, no. 12, pp. 1311, 2012.

[32] M. E. Yavuz, "Time Reversal Based Signal Processing Techniques for Ultrawideband Electro-magnetic Sensnig in Random Media," Ohio State University, 2008.

[33] S. S. Chaudhury, R. K. Mishra, A. Swarup, and J. M. Thomas, "Dielectric properties of normal and malignant human breast tissues at radiowave and microwave frequencies," *Ind. J. Biochem. Biophys*, vol. 21, pp. 76-79, 1984.

[34] A. Mehdipour, "Antenna for ultra wideband applications," PIER, vol. 77, pp. 85-96, 2007.

Image Reconstruction Based on the Anatomical Information for Magnetic Resonance Electrical Impedance Tomography

Liling Hao [1], Lisheng Xu [1,2], Benqiang Yang [3], and Gang Li [4]

[1] Department of Sino-Dutch Biomedical and Information Engineering
Northeastern University, Shenyang, 110169, China
haoll@bmie.neu.edu.cn, xuls@bmie.neu.edu.cn

[2] Key Laboratory of Medical Image Computing (Northeastern University), Ministry of Education, China
xuls@bmie.neu.edu.cn

[3] General Hospital of Shenyang Military, Shenyang, 110016, China
bqyang888@sina.com

[4] College of Precision Instrument and Opto-Electronics Engineering, Tianjin University, 300072, Tianjin, China
ligang59@tju.edu.cn

Abstract ─ Magnetic resonance electrical impedance tomography (MREIT) is a noninvasive modality to visualize the internal electrical conductivity distribution of an electrically conductive object using a magnetic resonance imaging (MRI) scanner. The impedance tomography step may provide valuable additional information that cannot be recovered from the MR reconstruction. Previous research has been mostly performed on the reconstruction algorithms and the measurement system. However, the anatomical information provided by the MR images is not in full use. This paper proposes an image reconstruction method based on anatomical information which provides the prior knowledge. The sensitivity algorithm with generalized minimum residual (GMRES) is proposed to reconstruct conductivity image. Simulations of a realistic geometry leg model are performed to show that our approach is not only capable of achieving high accuracy, but also able to improve the speed of the image reconstruction. At the end, a preliminary phantom experiment is presented, illustrating the feasibility of this proposed method.

Index Terms ─ Anatomical information, image reconstruction, magnetic resonance electrical impedance tomography, prior knowledge.

I. INTRODUCTION

Magnetic resonance electrical impedance tomography (MREIT) is a promising imaging technique that aims to reconstruct the cross-sectional conductivity image with the high spatial resolution by measuring the internal magnetic flux density of injection currents with the magnetic resonance imaging (MRI) scanner [1-4]. As a noninvasive imaging technique, it has potential of becoming a new clinical device for the detection of diagnostically valuable information about the status of human tissue [5]. When current is injected into an object through a pair of surface electrodes, the component of the induced magnetic flux density which parallels the direction of the main magnetic field of a MRI scanner can be obtained by scaling the phase shift in the MR complex images. According to the relationship between the conductivity and the induced magnetic flux density, the conductivity distribution of the imaging object can be reconstructed from the measured magnetic flux density data.

Early MREIT researches attempted to reconstruct the conductivity image based on the current density such as **J**-substitution algorithm [6], CCVSR algorithm [7], and equipotential line method [8]. These current density based algorithms need all three components of the magnetic flux density, where each component of magnetic flux density can be obtained by a single measurement. Thus, for the current density based algorithms, the subject must be rotated twice after its original placement to acquire all three components of the induced magnetic flux density. Recently, some simple and efficient methods were reported [9-16] to reconstruct the conductivity image using the component of a magnetic flux density directly which parallels to the main magnetic field of a MRI scanner, such as sensitivity-based algorithm [9-11], the algebraic reconstruction technique [12], harmonic B_z algorithm [13-14], gradient B_z decomposition algorithm [15], response surface methodology algorithm [16]. Among

these methods, the sensitivity algorithm has received a good evaluation in terms of accuracy and efficiency [17]. Moreover, it is necessary to make the most use of the anatomical information generated from segmented MR images benefit MREIT image reconstruction. The impedance tomography combined with the existing imaging parameter of MRI may provide much more pathological information for the diagnosis of human diseases.

This paper proposes an improved image reconstruction technique based on the anatomical information generated from segmented MR images. The sensitivity algorithm with generalized minimum residual (GMRES) method is utilized to solve the inverse problem of MREIT. The simulation results with a realistic geometry leg model are analyzed for the feasibility of the proposed method. The result of a phantom experiment performed on an Open 0.36T MRI scanner is also presented in this work.

II. METHODS

A. Forward problem of MREIT

The electrical current I is injected into a conductive object Ω through a pair of electrodes fixed to the object's boundary $\partial\Omega$. The relation between conductivity and electric potential satisfies the Laplace equation with the Neumann boundary condition:

$$\begin{cases} \nabla \cdot \sigma \nabla \varphi = 0 & \text{in } \Omega \\ -\sigma \dfrac{\partial \varphi}{\partial \mathbf{n}} = J_I & \text{on } \partial\Omega \end{cases}, \qquad (1)$$

where σ is the conductivity distribution, and φ is the electric potential in Ω, $\mathbf{n}$ denotes the unit outward unit normal vector on $\partial\Omega$, J_I is the current density at the boundary $\partial\Omega$. The Neumann boundary condition can be written as :

$$\frac{\partial \varphi}{\partial \boldsymbol{n}} = \begin{cases} I/A_{+} \, \sigma & \text{on current entrance electrode} \\ -I/A_{-} \, \sigma & \text{on current exit electrode} \\ 0 & \text{elsewhere} \end{cases}, \quad (2)$$

where A_{+} and A_{-} are the areas of two electrodes.

The most popular numerical solution method—finite element method (FEM) is used to obtain the approximate solution of the partial differential equation (PDE) as in Equation (1). After electric potential distribution φ is found, the computations of electrical field intensity and current density can be expressed as:

$$\begin{aligned} \mathbf{E} &= -\nabla \varphi \\ \mathbf{J} &= \sigma \mathbf{E} \end{aligned}. \qquad (3)$$

Once the current density $\mathbf{J}$ is obtained, denoting r as the field point and r' as the source point, the magnetic flux density distribution can be computed according to the Biot-Savart law:

$$\mathbf{B}(r) = \frac{\mu_0}{4\pi} \int_{\Omega} \mathbf{J}(\mathbf{r}') \times \frac{\mathbf{r} - \mathbf{r}'}{\left| \mathbf{r} - \mathbf{r}' \right|^3} d\mathbf{r}'. \qquad (4)$$

B. Sensitivity reconstruction algorithm based on the anatomical information

A sensitivity based reconstruction algorithm [9-11] is mainly based on linearization of the variation of magnetic flux density due to conductivity perturbations. It initially assumes a uniform conductivity distribution, and calculates a current density distribution with the FEM method the same with the forward problem of conventional electrical impedance tomography (EIT) [18, 19]. Next, the magnetic flux density $\mathbf{B_0}$ can be described according to the Biot-Savart law. Then, suppose there is a conductivity perturbation $\Delta\sigma$ in the imaging region around the uniform values, the electrical potential is changed by $\Delta\varphi$, and the current density changes correspondingly cause an increment of magnetic flux density as $\Delta\mathbf{B}$. According to the sensitivity reconstruction algorithm, the total matrix equation can be represented as:

$$\Delta\mathbf{B} = \mathbf{S}\Delta\boldsymbol{\sigma}, \qquad (5)$$

where $\mathbf{S}$ is the sensitivity matrix. Once $\mathbf{S}$ is obtained, the conductivity perturbation $\Delta\sigma$ causing variation of the magnetic flux density $\Delta\mathbf{B}$ can be solved by equation (5). The element of $\mathbf{S}$ at the ith row and j^{th} column which denotes the increment of magnetic flux density at the ith measurement point due to the conductivity perturbation of the jth element can be calculated by:

$$\begin{aligned} S_{ij} &= -\frac{\mu_0}{4\pi} \int_{\Omega_j} \left(\nabla \varphi + \sigma_0 \frac{\partial \nabla \varphi}{\partial \sigma} \right) \times \frac{\mathbf{r} - \mathbf{r}'}{\left| \mathbf{r} - \mathbf{r}' \right|^3} d\mathbf{r}' \\ &= -\frac{\mu_0 v_j}{4\pi} \left(-E_j + \sigma_0 \nabla \frac{\partial \varphi}{\partial \sigma} \right) \times \frac{\mathbf{r} - \mathbf{r}'}{\left| \mathbf{r} - \mathbf{r}' \right|^3} \end{aligned}. \qquad (6)$$

Then the conductivity is calculated with the perturbation $\Delta\boldsymbol{\sigma}$ as:

$$\boldsymbol{\sigma} = \boldsymbol{\sigma}_0 + \Delta\boldsymbol{\sigma}. \qquad (7)$$

The sensitivity reconstruction algorithm initially assumes a uniform conductivity distribution. However, the conductivities of biological tissues vary with different tissues, physiological and pathological states. The tremendous changes of conductivity distributions may lead to the big error of the reconstructed result and the long iteration time. The MREIT system can get the MR image while measuring the internal magnetic flux density of injection currents using a MRI scanner. Therefore, the MR image is segmented to generate the anatomical information. Then the different conductivities of different anatomical structures are set as the initial conductivity distribution according to prior knowledge, the known conductivities of the tissues reported by the researchers.

In the first iteration, the method tries to reconstruct only a single slice of an object from $\mathbf{B}_z$ for only its slices which is the middle slice. Before starting to the second iteration, assign the blurred versions of the middle slice for upper and lower slices. In the result, for second iteration we can calculate current density and also

magnetic flux density more accurately unless the upper or lower slices include very high or low conductivity regions.

Considering that the initial conductivity distribution is similar to the true one, the reconstruction algorithm may take advantage of good stability, fast convergence rate and high accuracy. The algorithm which reconstructs the conductivity distribution with anatomical information is described in detail as Fig. 1.

```
            ( start )
               │
  ┌────────────────────────────┐
  │  Construct the FEM model   │
  └────────────────────────────┘
               │
  ┌────────────────────────────┐
  │ Set the initial conductivity σ₀ │
  │ Based on the prior knowledge │
  └────────────────────────────┘
               │
  ┌────────────────────────────┐◄──────┐
  │ Calculate ∂φ/∂ σ ,∂ ▽φ/∂ σ │       │
  └────────────────────────────┘       │
               │                        │
  ┌────────────────────────────┐       │
  │ Calculate the sensitivity matrix S │
  └────────────────────────────┘       │
               │                        │
  ┌────────────────────────────┐       │
  │ Calculate Δσ from S×Δσ = ΔB │      │
  └────────────────────────────┘       │
               │                        │
  ┌────────────────────────────┐       │
  │  Update the conductivity   │       │
  └────────────────────────────┘       │
               │                        │
        ◇ Satisfy terminal condition ◇ ──NO──┘
               │
              YES
               │
             ( end )
```
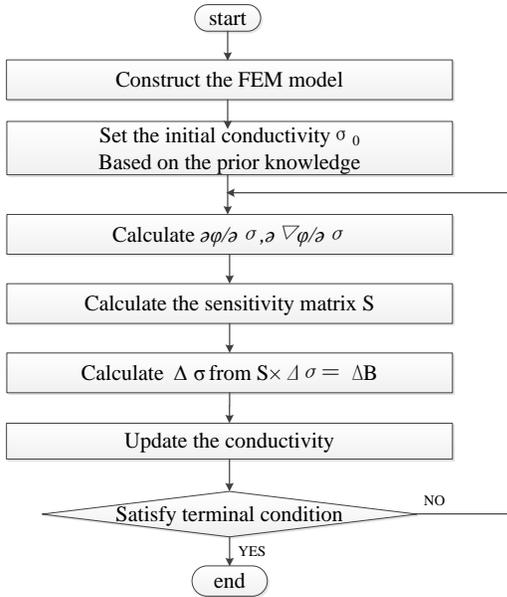
Fig. 1. The flow chart of sensitivity reconstruction algorithm based on the anatomical information.

III. EXPERIMENTS AND RESULTS

A. Simulation results

A realistic geometry model of human leg was constructed for simulation experiment, which was extracted from the realistic MRI magnitude images. The transverse section of the first layer MR magnitude image and the calculation model are shown in Fig. 2 (a) and Fig. 2 (b), respectively. There are four media in the calculation model: fat, muscle, tibia and fibula. And the conductivities of different tissues labelled in Table 1 were set according to the researches published in [20, 21]. The number of slices in MRI scanning is 8, and the size of each voxel is 2 mm × 2 mm × 2 mm. A pair of annular electrodes is located at the first and last slices of the leg model with the electrodes 2 mm width around both ends of the leg model, injecting 10 mA current into the leg model. The model was meshed into hexahedron elements with the size of voxel in MRI. For FEM solution, a mesh structure constructed with tetrahedrons is needed. Therefore, every hexahedron of mesh was subdivided into six tetrahedrons. And each element was assumed to have a uniform conductivity. The FEM mesh

for the realistic geometry human leg model is shown in Fig. 2 (c) and Fig. 2 (d). To avoid the inverse crime, the forward problem was calculated on the finer mesh with tetrahedrons elements, while the conductivity images were reconstructed on the coarse mesh with hexahedron elements.

Table 1: Conductivity of different tissues in the model

Tissue	Fat	Skeletal Muscle	Tibia	Fibula
Conductivity (S/m)	0.026	0.5848	0.0057	0.0057
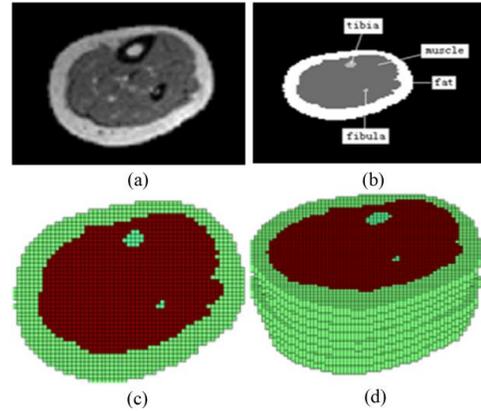
Fig. 2. The calculation model of realistic geometry human leg. (a) The realistic MR image, (b) the calculation model of human leg, (c) top view of the finite element mesh for the model, and (d) three dimensional view of the finite element mesh.

The white Gaussian noise with standard deviation s_B was added to a simulated magnetic flux density data. s_B is given in Equation (8):

$$s_B = 1/(2\gamma \times T_c \times SNR_{MR}),\qquad(8)$$

where $\gamma = 26.75\times10^7$ radT^{-1}s^{-1} is the gyromagnetic ratio of hydrogen and T_c is the current pulse width in seconds. T_c was set as 50 ms in the simulation experiments. As shown in Equation (8), the standard deviation is inversely proportional to the SNR of the MR magnitude image [22]. In this paper, Gaussian white noise with s_B=0.83405 nT for SNR=70 dB of MR magnitude images was added to the simulated magnetic data.

Figure 3 shows the results of noise added reconstruction for the 3rd-6th slice under the annular electrode mode by sensitivity reconstruction algorithm with the anatomical information and without the anatomical information. The sensitivity reconstruction algorithm based on the anatomical information is observed to yield the better result, which approaches the true conductivity distribution. Moreover, the improved algorithm took 4 iterations and 561.4 s for the reconstruction process, compared to 10 iterations and

2085.8 s for the algorithm based on the uniform conductivity distribution.

(a)

(b)

(c)
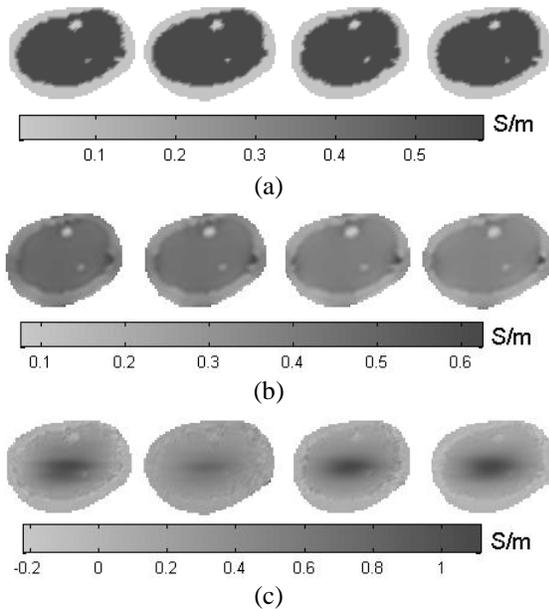
Fig. 3. The results of noise added reconstruction for the 3rd-6th slice under the annular electrode mode. (a) The conductivity image, (b) the reconstructed conductivity image with sensitivity reconstruction algorithm based on the anatomical information, and (c) the reconstructed conductivity image with sensitivity reconstruction algorithm based on the uniform conductivity distribution.

B. Phantom experiment

For a realistic experiment, the current was injected into an imaging object through a pair of annular electrodes attached on a cylindrical phantom shown in Fig. 4. In MREIT imaging, current was injected into an imaging object at the time between a slice select gradient pulse and a read out gradient pulse. An injected current induces a magnetic flux density perturbing the main magnetic field. The perturbation can be calculated from phase differences of MR complex images between one with current injection and another without it.

A cylindrical phantom with 64 mm diameter and 120 mm height was used with a pair of annular carbon electrodes whose widths are 7 mm at the two ends of the phantom as Fig. 3 shows. The phantom was filled with an agar gel (30 g/L NaCl, 1 g/L $CuSO_4$ and 30 g/L agar) to control the T1 and T2 decay of spin density. A piece of pork was immersed in the agar gelatin to create a contrast in both conductivity and spin density. After positioning the phantom inside an Open 0.36 T MRI scanner, the K-space MR data could be collected using the spin pulse sequence. The current injected into the imaging object is 20 mA, and the total current injection time in a TR cycle is 20 ms. The slice thickness is 7 mm

with no slice gap, the number of axial slices is 10 at the center of the phantom and TR/TE = 700/59.2 ms. The FOV is 256×256 mm^2 with the matrix size 128×128 and the NEX (number of excitation / acquisition) is 2.

(a)   (b)
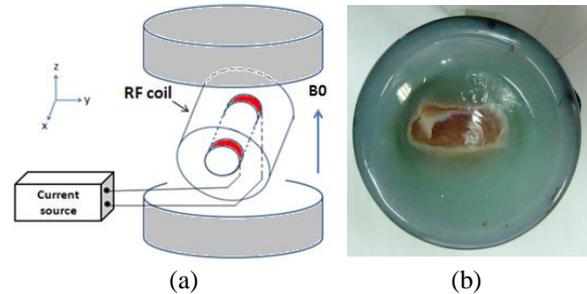
Fig. 4. The phantom experiment for MREIT in an Open MRI scanner. (a) The measurement system, and (b) the phantom with pork.

Using the sensitivity reconstruction algorithm based on the anatomical information, the internal conductivity distribution σ was reconstructed to prove the proposed algorithm. The reconstructed conductivity distribution image is shown in Fig. 5. The pork is shown in Fig. 5 (a) as the darker region in the magnetic resonance magnitude image, which also has a similar contour in Fig. 5 (b). The reconstructed conductivity images with sensitivity reconstruction algorithm based on the uniform conductivity distribution are shown in Fig. 5 (c). The algorithm based on the prior knowledge indeed gives better results than that with the uniform conductivity distribution. In Fig. 5, regarding the reconstruction with experimental data, the improved method is still able to separate the agar and pork, and roughly preserve image boundaries with acceptable background noise. While, one can hardly see anything through the sensitivity reconstruction algorithm based on the uniform conductivity distribution.

The primary experiment result shows the validity of the sensitivity algorithm based on the anatomical information with single current injection under annular electrode mode. Unfortunately, the true conductivity values were not measured, so the reconstructed error will not be discussed.

(a)

(b)

(c)
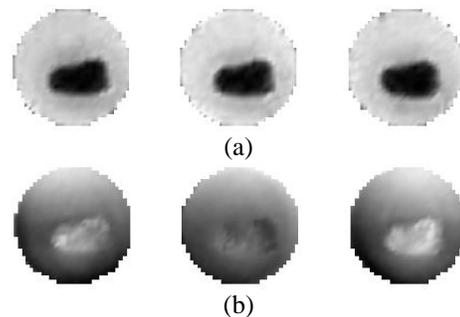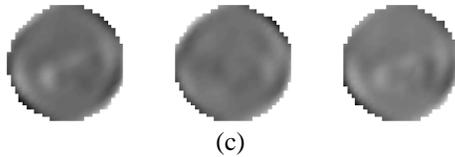
Fig. 5. The MRI images and reconstructed results of the 3rd-5th slice under the annular electrode mode. (a) Magnetic resonance magnitude image of the phantom, (b) the reconstructed conductivity image sensitivity reconstruction algorithm based on the prior knowledge, and (c) the reconstructed conductivity image with sensitivity reconstruction algorithm based on the uniform conductivity distribution.

IV. CONCLUSION

In this paper, the anatomical information was applied to the inverse problem of magnetic resonance electrical impedance tomography. The sensitivity reconstruction algorithm was used to solve the inverse problem. In the proposed algorithm, the different conductivities of different anatomical structures generated from the segmented MR image are set as the initial conductivity distribution according to the conductivities of the tissues reported by the researchers. Its performance was compared with the sensitivity reconstruction algorithm based on the uniform conductivity distribution. The results of conductivity image reconstructions show that the improved algorithm takes advantage of good stability, fast convergence rate and high accuracy.

This paper utilized the annular electrode mode for an Open MRI scanner whose main magnetic field is perpendicular to the horizontal plane have been widely used in clinical applications for the advantages of its low cost, patient comfort and convenience for interventional treatment. In the annular electrode mode, the distribution of current density component parallels to the main direction of current reflects the distribution of the electrical conductivity. Conductivity images were reconstructed accurately using only one current injection and one component of the magnetic flux density without rotating an image object.

In the modern society, MRI has been one of the most powerful medical imaging modalities currently used. However, the existing MRI parameters are still not enough to diagnose all the diseases accurately. For example, it cannot detect early cancers effectively. And, it can't differentiate calcified tissue. MREIT which aims to image the conductivity distribution is a promising imaging technique to make up for these shortcomings. Moreover, it may provide much more pathological information for the diagnosis of human diseases by combining with the existed imaging parameters. Yet in MREIT, the anatomical information provided by the MR images is not in full use. A sensitivity reconstruction algorithm based on the anatomical information is put forward to improve the quality and speed of image reconstruction. As a new way to improve the conductivity images, the improved algorithm may provide a promising clinical application for MREIT.

REFERENCES

[1] E. J. Woo and J. K. Seo, "Magnetic resonance electrical impedance tomography (MREIT) for high-resolution conductivity imaging," *Physiol. Meas.*, vol. 29, pp. R1-R26, 2008.

[2] H. J. Kim, T. I. Oh, Y. T. Kim, B. I. Lee, E. J. Woo, J. K. Seo, S. Y. Lee, O. Kwon, C. Park, B. T. Kang, and H. M. Park, "In vivo electrical conductivity imaging of a canine brain using a 3 T MREIT system," *Physiol. Meas.*, vol. 29, pp. 1145-1155, 2008.

[3] J. K. Seo, S. W. Kim, S. Kim, J. J. Liu, E. J. Woo, K. Jeon, and C. O. Lee, "Local harmonic Bz algorithm with domain decomposition in MREIT: computer simulation study," *IEEE Trans. Med. Imaging.*, vol. 27, pp. 1754-1761, 2008.

[4] A. Nachman, A. Tamasan, and A. Timonov, "Conductivity imaging with a single measurement of boundary and interior data," *Inverse Problems*, vol. 23, pp. 2551-2563, 2007.

[5] H. M. Park, H. S. Nam, and O. I. Kwon, "Magnetic flux density reconstruction using interleaved partial Fourier acquisitions in MREIT," *Phys. Med. Biol.*, vol. 56, pp. 2059-2073, 2011.

[6] O. Kwon, E. J. Woo, J. R. Yoon, and J. K. Seo, "Magnetic resonance electrical impedance tomography (MREIT): Simulation study of J-substitution algorithm," *IEEE Trans. Biomed. Eng.*, vol. 49, no. 2, 2002.

[7] O. Birgul, B. M. Eyuboglu, and Y. Z. Ider, "Current constrained voltage scaled reconstruction (CCVSR) algorithm for MR-EIT and its performance with different probing current patterns," *Phys. Med. Biol.*, vol. 48, pp. 653-671, 2003.

[8] O. Kwon, J. Y. Lee, and J. R. Yoon, "Equipotential line method for magnetic resonance electrical impedance tomography," *Inverse Problems*, vol. 18, pp. 1089-1100, 2002.

[9] Y. Z. Ider and O. Birgul, "Use of the magnetic field generated by the internal distribution of injected currents for electrical impedance tomography

(MR-EIT)," *Elektrik*, vol. 6, pp. 215-225, 1998.

[10] O. Birgul, B. M. Eyuboglu, and Y. Z. Ider, "Experimental results for 2D magnetic resonance electrical impedance tomography (MR-EIT) using magnetic flux density in one direction," *Phys. Med. Biol.*, vol. 48, pp. 3485-3504, 2003.

[11] O. Birgul, M. Hamamura, L. Muftuler, and O. Nalcioglu, "Contrast and spatial resolution in MREIT using low amplitude current," *Phys. Med. Biol.*, vol. 51, pp. 5035-5049, 2006.

[12] Y. Z. Ider and S. Onart, "Algebraic reconstruction for 3D magnetic resonance-electrical impedance tomography (MREIT) using one component of magnetic flux density," *Physiol. Meas.*, vol. 25, pp. 281-294, 2004.

[13] S. H. Oh, B. I. Lee, E. J. Woo, S. Y. Lee, M. H. Cho, O. Kwon, and J. K. Seo, "Conductivity and current density image reconstruction using harmonic Bz algorithm in magnetic resonance electrical impedance tomography," *Phys. Med. Biol.*, vol. 48, pp. 3101-3116, 2003.

[14] H. J. Kim, Y. T. Kim, A. S. Minhas, W. C. Jeong, E. J. Woo, J. K. Seo, and O. J. Kwon, "In vivo high-resolution conductivity imaging of the human leg using MREIT: The first human experiment," *IEEE Trans. Med. Imaging.*, vol. 28, pp. 1681-1687, 2009.

[15] C. Park, O. Kwon, E. J. Woo, and J. K. Seo, "Electrical conductivity imaging using gradient Bz decomposition algorithm in magnetic resonance electrical impedance tomography (MREIT)," *IEEE Trans. Med. Imaging.*, vol. 23, pp. 388-394, 2004.

[16] N. Gao, S. A. Zhu, and B. He, "A new magnetic resonance electrical impedance tomography (MREIT) algorithm: the RSM-MREIT algorithm with applications to estimation of human head

conductivity," *Phys. Med. Biol.*, vol. 51, pp. 3067-3083, 2006.

[17] B. M. Eyuboglu, V. E. Arpinar, and R. Boyacioglu, "Comparison of magnetic resonance electrical impedance tomography (MR-EIT) reconstruction algorithms," *7th IEEE International Symposium on Biomedical Imaging: From Nano to Macro*, Rotterdam, pp. 700-703, 2010.

[18] B. I. Lee, S. H. Oh, E. J. Woo, S. Y. Lee, M. H. Cho, O. Kwon, J. K. Seo, J. Y. Lee, and W. S. Baek, "Three-dimensional forward solver and its performance analysis for magnetic resonance electrical impedance tomography (MREIT) using recessed electrodes," *Phys. Med. Biol.*, vol. 48, pp. 1971-1986, 2003.

[19] G. Z. Xu, H. L. Wu, S. Yang, S. Liu, Y. Li, Q. X. Yang, W. L. Yan, and M. S. Wang, "3-D electrical impedance tomography forward problem with finite element method," *IEEE T. Magn.*, vol. 41, pp. 1832-1835, 2005.

[20] S. Gabriel, R. W. Lau, and C. Gabriel, "The dielectric properties of biological tissues: III. Parametric models for the dielectric spectrum of tissues," *Phys. Med. Biol.*, vol. 41, pp. 2271-2293, 1996.

[21] T. J. C. Faes, H. A. Meij, J. C. Munck, and R. M. Heethaar, "The electric resistivity of human tissues (100 Hz-10 MHz): A meta-analysis of review studies," *Physiol. Meas.*, vol. 20, no. 4, pp. R1-R10, Nov. 1999.

[22] R. Sadleir, S. Grant, S. U. Zhang, B. I. Lee, H. C. Pyo, S. H. Oh, C. Park, E. J. Woo, S. Y. Lee, O. Kwonand, and J. K. Seo, "Noise analysis in MREIT at 3 and 11 Tesla field strength," *Physiol. Meas.*, vol. 26, pp. 875-884, 2005.

Internal Homogenization of Biological Tissues for Electromagnetic Dosimetry

Hulusi Acikgoz

Material Science and Nanotechnology Engineering Department
KTO Karatay University, Konya, Turkey
hulusi.acikgoz@karatay.edu.tr

Abstract ─ In this paper, the internal homogenization method is introduced to determine the effective physical properties (permittivity and conductivity) of biological tissues. This method is performed on a 2D child head model obtained from MRI data. An original procedure where the complex 2D head model is represented as a multilayered circular structure is employed to retrieve the effective medium parameters. Results obtained with the proposed internal homogenization concept are compared with those obtained from the original heterogeneous model (with 4 tissues) and effective medium theories such as Maxwell-Garnett and Polder van Santen.

I. INTRODUCTION

Nowadays, mobile phones and wireless handy computers are widely used and there have been public concerns about their possible hazardous effects due to the emitted electromagnetic radiation. To quantify these effects, the most widely used quantity is the specific absorption rate (SAR) [1]. Dosimetry based on computer simulations is usually preferred because the SAR measurement on a living human body is difficult to perform [2]. In numerical dosimetry, the finite difference – time domain (FDTD) method is a well-known method to solve Maxwell's equations, but its cubic meshing scheme reduces the accuracy when complex geometries with curvature are simulated [3].

In this paper, the finite element method (FEM) is used. However, the FEM is a time consuming technique. Furthermore, human head is a complex structure composed of several biological tissues with different thicknesses and physical properties. This complex and fine structure is very difficult to simulate even with high computing systems. Therefore, homogenization plays an important role to simplify the structure and then reducing the time required for the simulation. Homogenization consists of replacing the entire complex structure with a simplified model having effective physical properties. In literature, different approaches were proposed to homogenize composite materials such as metamaterials, periodic structures, etc. [4]. In [5], to homogenize a multilayered structure, authors proposed to use FDTD grid with a coarser mesh which allows to reduce the computation. In [6], authors developed the adjoint method combined with the FDTD method for the homogenization of human body's models. The retrieval method based on S parameters is a classical method to determine the effective medium constitutive parameters [7]. This method has been successfully applied to metamaterials in [8] and [9]. The field averaging technique has been applied to homogenize periodic structures with unit cells having inclusions much smaller than the electromagnetic wavelength [10, 11]. In the present work, the "internal homogenization" method, introduced by [12], is used and the obtained results are compared with those of the heterogeneous medium and results given from Maxwell-Garnett and Polder van Santen theories. Moreover, a new effective parameters extracting procedure based on the representation of the complex heterogeneous head as a simplified circular model is also presented.

II. HOMOGENIZATION

Homogenization is a term given to the treatment of inhomogeneous medium where physical properties are dependent of the space coordinates. Its aim is to find an effective medium model where physical properties do not vary within the model. In case of an external excitation, such a medium should exhibit similar behavior to the equivalent inhomogeneous medium. To calculate the effective material parameters of a heterogeneous medium, effective medium theories (EMT) are often used. In subsequent sections, the internal homogenization based on a layered circular structure and some of widely used EMT such as Maxwell-Garnett and Polder van Santen mixing theories will be presented.

A. Internal homogenization procedure

Although, the concept of "internal homogenization" was introduced to assign an effective permittivity for a single inclusion contained in a bulk material, we applied it to attribute an effective medium parameter to a simplified child head. As opposed to the internal homogenization, the external homogenization consists

of assigning an effective permittivity to a distribution of inclusions in a matrix.

For simplicity, the child head model is considered to have subwavelength structure so that the quasi-static approximation can be applied. The simplified model is assumed to have multi-layered circular geometry that is composed of 4 different tissues: skin, muscle, skull and brain.

The internal homogenization procedure is as follows: the 2D heterogeneous model is replaced by an equivalent multi-layered circular structure (Fig. 1). The radius of each tissue is calculated in accordance to its total area given by MRI data (Table 1). The homogenization is then applied to the multi-layered circular structure. Thereafter, in order to calculate its response to an external electromagnetic excitation, the calculated effective medium parameters are presented to the 2D model of the head.
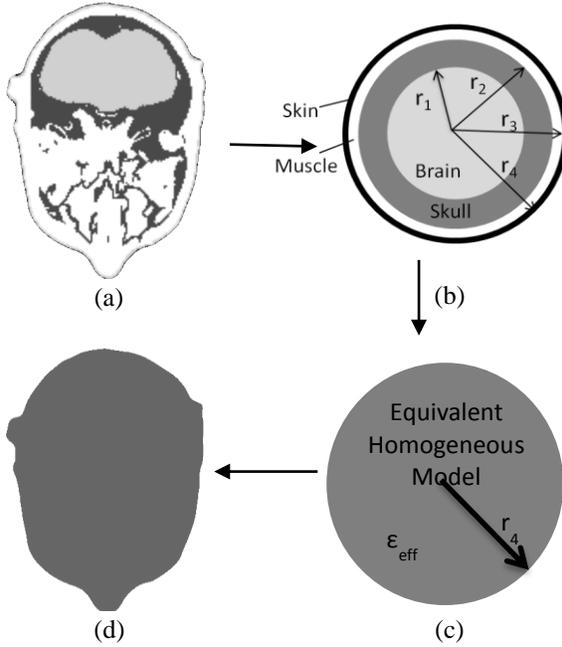
Fig. 1. Effective parameters extracting scheme: (a) heterogeneous head model, (b) simplified circular multi-layered model, (c) equivalent homogeneous model with effective permittivity ε_{eff} and radius r_4, and (d) homogeneous head model.

Table 1: Approximated thickness for each tissue

Tissues	Skin	Muscle	Skull	Brain
Radius	0.1286	0.1139	0.0686	0.0324
(meter)	(r_4)	(r_3)	(r_2)	(r_1)

The internal homogenization method is based on the equivalence of the polarizability of the multi-layered model and the equivalent homogeneous model. The derivations of the polarizability expressions are long and out of the scope of this paper. The interested readers are invited to refer to [13], [14] and [15]. The homogenization procedure begins with the first two inner layers, i.e., the brain and the skull tissues. The polarizability is expressed as α_1 and α_2 for the two layered sphere (brain + skull) (1) and the equivalent homogeneous sphere (2), respectively:

$$\alpha_1 = -4\pi\varepsilon_0 \left(\frac{r_2^3(\varepsilon_1 + 2\varepsilon_2)(\varepsilon_2 - \varepsilon_0) + r_1^3(\varepsilon_1 - \varepsilon_2)(2\varepsilon_2 + \varepsilon_0)}{2r_1^3(\varepsilon_1 - \varepsilon_2)(\varepsilon_2 - \varepsilon_0) + r_2^3(\varepsilon_1 + 2\varepsilon_2)(\varepsilon_2 + 2\varepsilon_0)} \right) r_2^3,$$

(1)

$$\alpha_2 = 4\pi\varepsilon_0 \left(\frac{\varepsilon_{12} - \varepsilon_0}{\varepsilon_{12} + 2\varepsilon_0} \right) r_2^3,$$

(2)

where ε_1 and ε_2 are the permittivities of the brain and the skull respectively, and r_1, r_2 are the approximated radius of each tissue. By equating these two polarizabilities, the effective permittivity ε_{12} (for the brain and the skull) of the equivalent sphere is given by (3):

$$\varepsilon_{12} = \varepsilon_2 \frac{r_2^3(\varepsilon_1 + 2\varepsilon_2) + 2r_1^3(\varepsilon_1 - \varepsilon_2)}{r_2^3(\varepsilon_1 + 2\varepsilon_2) - r_1^3(\varepsilon_1 - \varepsilon_2)}.$$

(3)

This calculation is repeated in an iterative manner until the effective permittivity ε_{eff} of the whole model (4 layers structure) is determined.

B. Maxwell-Garnett EMT

One of the most popular and widely used effective medium theories is the so called Maxwell-Garnett EMT [16]. It dates from the beginning of the last century. It is expressed as (4):

$$\varepsilon_{eff} = \varepsilon_e + 3f\varepsilon_e \frac{\varepsilon_i - \varepsilon_e}{\varepsilon_i + 2\varepsilon_e - f(\varepsilon_i - \varepsilon_e)}.$$

(4)

The Maxwell-Garnett formula is based on the fact that the heterogeneous medium is composed of isotropic spherical inclusion with ε_i diluted in isotropic host material of permittivity ε_e. The volume fraction occupied by the inclusion is f. The formula is valid for very low concentration inclusions ($f \ll 1$). As for the internal homogenization described above, this theory implies the quasi-static approximation. It has been applied for several material types including microwave absorbing material containing conducting particles [17], composite dielectric medium [18], conducting polymers [19], etc.

C. Polder van Santen EMT

A derivation of the Maxwell-Garnett mixing expression is Polder van Santen formula (also called Böttcher formula) that can treat a variety of mixtures [16], [20]. Especially, it is valid for ellipsoid inclusion and for all volume fractions. For spherical inclusion the formula takes the form given below (5):

$$\frac{\varepsilon_{eff} - \varepsilon_e}{3\varepsilon_{eff}} = f \frac{\varepsilon_i - \varepsilon_e}{\varepsilon_i + 2\varepsilon_e}.$$

(5)

For dilute materials, Maxwell-Garnett and Polder van Santen formulas should give similar effective medium parameters [16].

III. RESULTS

The homogenization procedures described above is applied to a 2D child head model obtained from MRI data. The physical properties of the head tissues from 10 MHz to 3 GHz are given below (Fig. 2 and Fig. 3) [21].
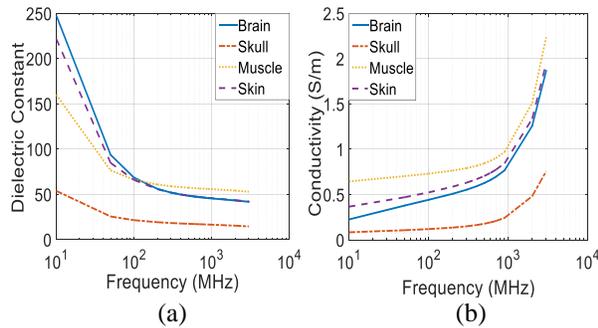
Fig. 2. Tissues parameters (10 MHz to 3 GHz): (a) dielectric constant, and (b) conductivity [11].
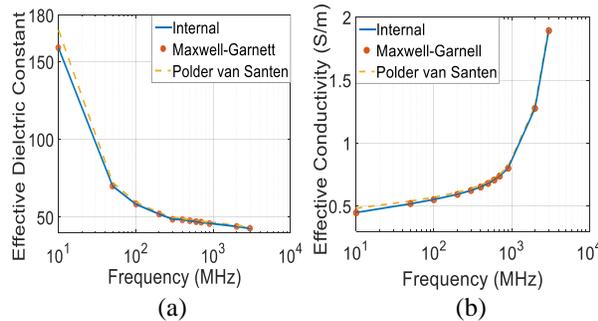
Fig. 3. Effective parameters of the homogeneous head model obtained with the three EMTs (10 MHz to 3 GHz): (a) effective dielectric constant, and (b) effective conductivity.

The same procedure described in 2.1 (Fig. 1) is used to obtain the effective parameters with the three different EMTs. These are given in Fig. 3. As the multilayered structure is composed of the core materials embedded in a medium of the shell material, and the same process is applied for both methods, the internal homogenization and Maxwell-Garnett EMT are expected to give the same effective parameters independently of the frequency of the excitation [12], [16]. This is confirmed by the Fig. 3. However, as the filling fraction for each tissue layer is not negligible, especially for the skin, the muscle and the skull (Table 2), Polder van Santen EMT give slightly different results compared to the two other methods.

Table 2: Filling fraction for each layer

r_1^3/r_2^3	0.1052
r_2^3/r_3^3	0.2184
r_3^3/r_4^3	0.6948

These effective properties are then used in the 2D head model where only the external boundary exists and all internal boundaries are suppressed. Thus, due to a lower cell number, the computation time will be reduced consequently. In fact, the number of cells when the heterogeneous model is considered is 85490, whereas after the homogenization only 6146 cells remain due to the removal of all internal boundaries. The FEM computation is about ten times faster after the homogenization.

Validation of the internal homogenization method is carried out by computing the electric field distribution inside the original heterogeneous and the homogeneous models using a commercial FEM software. The computational resource used for this work is a computer equipped with Intel® Core™ Quad CPU Q8400 @ 2.66 GHz processor with 4 GB of memory. The source of radiation is an infinitesimal dipole placed at 1 cm from the boundary of the skin. Figure 4 and Fig. 5 show the electric field distribution at two frequencies, 100 MHz and 900 MHz, for heterogeneous and homogeneous models, respectively.
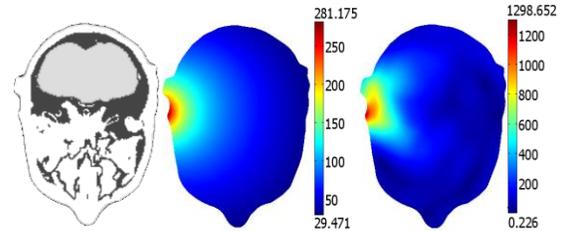
Fig. 4. Heterogeneous model (left), the electric field distribution at 100 MHz (center) and 900 MHz (right).
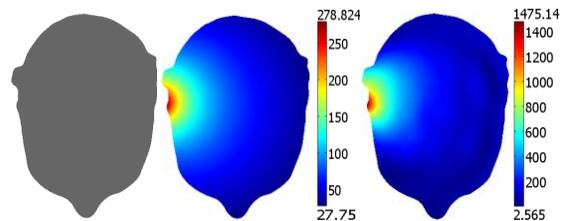
Fig. 5. Homogeneous model (left), the electric field distribution at 100 MHz (center) and 900 MHz (right).

It is clearly shown that at low frequency (100 MHz) the electric field distribution is similar for both models. However, at higher frequency (900 MHz), there is a net difference between them. To quantify this difference, the

relative error induced by each EMTs, i.e., internal homogenization, Maxwell-Garnett and Polder van Santen are computed. This is achieved by plotting the induced electric field magnitude along a horizontal line crossing the head at the level of the source point (Fig. 6).
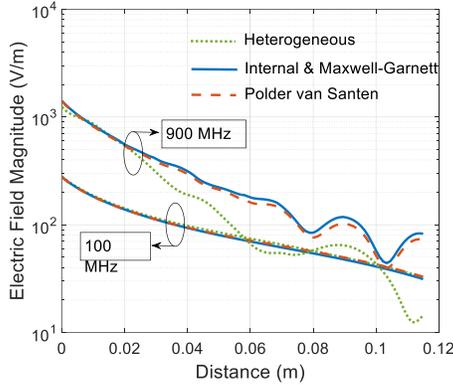
Fig. 6: Electric field magnitude along a line in the the head at 100 MHz and 900 MHz.

The plots in Fig. 7 are based on the data presented in Fig. 6, where the relative errors are calculated between the electric field distribution in the heterogeneous model and each presented EMTs.

(a)

(b)
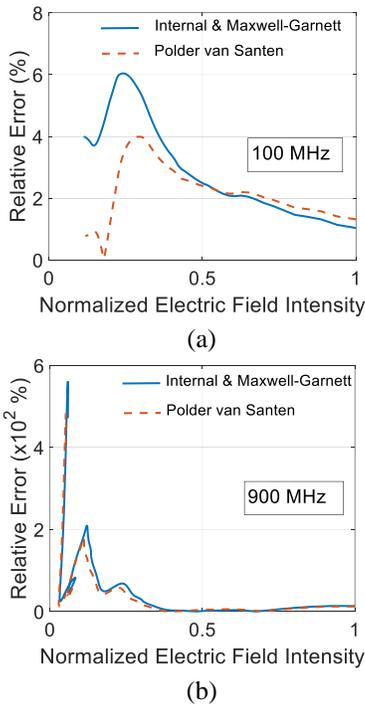
Fig. 7. Relative error vs. normalized electric field at: (a) 100 MHz and (b) 900 MHz.

Figure 7 shows that the overall error is more important at 900 MHz than at 100 MHz. Especially in

the vicinity of the excitation (higher electric field magnitude), where the EM radiation is much likely to have damage on biological tissue, the error induced by the homogenization techniques are very low.

Furthermore, to confirm the validity of the employed internal homogenization method, the average relative error is plotted versus the frequency (Fig. 8). It is obtained by summing up the relative errors calculated at each point along the line and dividing it by the number of points. The average error remains acceptable up to 400 MHz (about 10%). Beyond this frequency, the homogenization gives inaccurate results. This important error is due on one hand to the fact that the quasi-static approximation is no more valid beyond this frequency. On the other hand, the circular multilayered structure is not fully representative of the complex 2D head structure. Furthermore, at high frequencies, the EM response is more dependent on fine details of the structure.
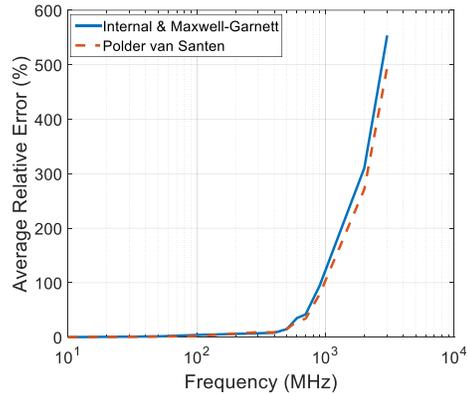
Fig. 8. Average relative error vs. frequency.

IV. SENSITIVITY ANALYSIS

In this part, the influence of the head model parameters to the electric field distribution is studied. These parameters are the approximated thickness (radius) obtained for each tissue and the physical properties such as the dielectric constant and the electrical conductivity. The Monte Carlo (MC) method is used for this purpose.

First, the influence of both physical constants and the radius of each tissue is considered. The model parameters are considered to have 10% of uncertainty with a uniform distribution over the range of variation centered at the nominal values presented in the previous section. 100000-sample MC simulation based on the internal homogenization formula (3) presented in Section II is used to analyze the dispersion of the effective medium parameters, i.e., the average values and the standard deviation of the dielectric constant and the conductivity. For instance, results at 100 MHz are presented in Table 3. It is shown that 10% of uncertainty

of the model parameters induces about 5% of dispersion of the effective dielectric constant and about 7% of the effective conductivity when all model parameters are considered, i.e., physical constants (Δp, dielectric constants and conductivities) of each tissue and corresponding radius (Δr). The first two columns show the results corresponding to this case. In Table 3, the first row corresponds to the values obtained with the nominal values of the model parameters, without any uncertainties, and are given as a comparison.

Second, if one supposes that the physical constants of each tissue are fixed and only the radii of the tissues have uncertainties (Δr), the results presented in Table 3 (right two columns) are obtained. The uncertainties due to the approximated radii is about 62% (for the dielectric constant) and 78% (for the conductivity) of the previous results when all model parameters are considered. Thus, the radius has more effect on the effective medium parameters. However, the uncertainty induced remains reasonably low.

Table 3: Uncertainty on the effective dielectric constant at 100 MHz

	Δp and Δr		Δr Only	
	ε	σ	ε	σ
Effective parameters for nominal values	58.40	0.5528	58.40	0.5528
Average effective parameters	58.18	0.5540	58.20	0.5542
Standard deviation	3.12	0.0403	1.96	0.0318
Variation (%)	5.37%	7.28%	3.36%	5.74%

Finally, the variability of the electric field magnitude in a horizontal line due to the uncertainty of the effective dielectric constants and conductivities has been studied. For both frequencies, 100 MHz and 900 MHz, the average electric field magnitude and the standard deviation versus the horizontal distance from the feed point side of the head are estimated and plotted (dotted lines) in Fig. 9.

For this study, the first case where both physical constants and radii have uncertainties is considered (columns 1 and 2 in Table 3). It can be seen in Fig. 9 that, the variation in the effective parameters induces small changes in the electric field magnitude at 100 MHz. Depending on the distance, the uncertainty of the electric field varies between 2% and 7%. As expected, at 900 MHz the uncertainties of the effective parameters and radii have more effect on the electric field. The uncertainty can be as high as 17%.

The electric fields obtained when the homogeneous head model is made entirely out of the constituent tissues parameters are also shown in Fig. 9. One can observe that, there is a discrepancy between the results given by our method (dotted lines in Fig. 9) and those obtained if one were using one of the tissues parameters as effective

medium parameter. The model made out of the skin seems to give the closest results because at those particular frequencies the effective parameters obtained are close to those of the skin.
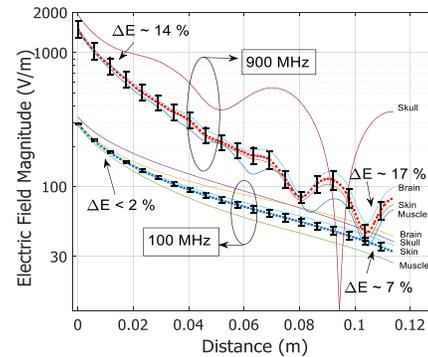
Fig. 9. The electric field magnitude variation in a horizontal line with the corresponding uncertainties due to the effective medium physical constants variations.

V. CONCLUSIONS

In this paper, the concept of internal homogenization is presented and the results are compared with the heterogeneous model and Maxwell-Garnett and Polder van Santen effective medium theories. It has been shown that, up to a certain frequency where the quasi-static approximation is valid, the complex multi-layered structure can be replaced by its counterpart effective medium. The internal homogenization method gives similar results to those obtained from Maxwell-Garnett but slightly different results compared to Polder van Santen EMT. The use of a multilayered circular model to extract the effective parameters is also presented. This procedure highly simplifies the modeling of the complex head structure by removing boundaries between tissues and by replacing the space-depending physical parameters by a homogeneous effective parameter. For this 2D case, the simulation with the homogeneous model is about 10 times faster than for the heterogeneous one. The difference in terms of computation time will be even higher if a 3D model is considered.

Although, the employed method is limited in frequency, it is worth to note that, most of the error is far away from the excitation and is located where the electric field intensity is weak. Thus, one can propose to use the homogenization only in the vicinity of the radiation source, inside the head, a few centimeters from the skin. Homogenization allows to diminish the number of cells required to represent thin shells and consequently the simulation time is reduced considerably.

Finally, the sensitivity analysis showed that the possible uncertainty in the head model parameters might have impacts on the electric field magnitude. The level of the induced uncertainty depends on the distance to the source point and the frequency. Histerically

REFERENCES

[1] IEEE, *Recommended Practice for Determining the Peak Spatial-Average Specific Absorption Rate (SAR) in the Human Head from Wireless Communications Devices: Measurement Techniques*, IEEE Standard 1528, 2003.

[2] V. Monebhurrun, M.-F. Wong, and J. Wiart, "Numerical and experimental investigations of a commercial mobile handset for SAR calculations," *The 2nd International Conference on Bioinformatics and Biomedical Engineering*, May 16-18, 2008.

[3] U. S. Inan and R. A. Marshall, *Numerical Electromagnetics, The FDTD Method*, Cambridge University Press, 2011.

[4] X. Chen, T. M. Grzegorczyk, B. Wu, J. Pacheco, and J. A. Kong, "Robust method to retrieve the constitutive effective parameters of metamaterials," *Phys. Rev. E*, vol. 70, pp. 016608-1–016608-7, 2004.

[5] A. Pradier, F. Lacroux, D. Lautru, M.-F. Wong, V. Fouad Hanna, and J. Wiart, "Influence of the homogenization of tissues on the electric field calculation in numerical dosimetry for wireless application," *Proceedings of the 9th European Conference on Wireless Technology*, Manchester, UK, Sep. 2006.

[6] J. Silly-Carette, D. Lautru, A. Gati, M.-F. Wong, J. Wiart, and V. Fouad Hanna, "Optimisation of the homogenization of tissues using the adjoint method and the FDTD," *International Microwave Symposium Digest, IEEE MTT-S*, June 15-20, 2008.

[7] J. Qi, H. Kettunen, H. Wallén, and A. Sihvola, "Different retrieval methods based on S-parameters for the permittivity of composites," *URSI International Symposium on Electromagnetic Theory*, 2010.

[8] D. R. Smith, S. Schultz, P. Markoš, and C. M. Soukoulis, "Determination of effective permittivity and permeability of metamaterials from reflection and transmission coefficients," *Physical Review B*, vol. 65, pp. 195104, 2002.

[9] X. Chen, T. M. Grzegorczyk, B.-I. Wu, J. Pacheco, and J. A. Kong, "Robust method to retrieve the constitutive effective parameters of metamaterials," *Physical Review E*, vol. 70, pp. 016608, 2004.

[10] D. R. Smith and J. Pendry, "Homogenization of metamaterials by field averaging," *J. Opt. Soc. Am. B*, vol. 23, no. 3, Mar. 2006.

[11] I. Bardi, J. Tharp, and R. Petersson, "Homogenization of periodic structures using the FEM," *IEEE Transactions on Magnetics*, vol. 50, no. 2, Feb. 2014.

[12] U. K. Chettiar and N. Engheta, "Internal homogenization: effective permittivity of a coated sphere," *Optics Express*, vol. 20, no. 21, Oct. 8, 2012.

[13] C. F. Bohren and D. R. Huffman, *Absorption and Scattering of Light by Small Particles*, John Wiley & Sons, New York, 1983.

[14] H. C. van de Hulst, *Light Scattering by Small Particles*, John Wiley & Sons, New York, 1957.

[15] M. E. Ermutlu and A. H. Sihvola, "Polarizability of matrix of layered chiral sphere," *Progress In Electromagetic Research*, vol. 9, pp. 87-101, 1994.

[16] A. Sihvola, *Electromagnetic Mixing Formulas and Applications*, IEE Publishing, London, 2008.

[17] M. Y. Koledintseva, P. C. Ravva, R. E. DuBroff, J. L. Drewniak, K. N. Rozanov, and B. Archambeault, "Engineering of composite media for shields at microwave frequencies," *Proc. IEEE EMC Symposium*, vol. 1, pp. 169-174, Chicago, Aug. 2005.

[18] P. Mallet, C. A. Guérin, and A. Sentenac, "Maxwell-Garnett mixing rule in the presence of multiple scattering: derivation and accuracy," *Phys. Rev. B*, vol. 72, 014205, July 25, 2005.

[19] O. Levy, "Maxwell Garnett theory for mixtures of anisotropic inclusions: application to conducting polymers," *Physical Review B*, vol. 56, no. 13, Oct. 1, 1997.

[20] M. Scheller, C. Jansen, and M. Koch, *Applications of Effective Medium Theories in the Terahertz Regime*, Recent Optical and Photonic Technologies, Book edited by: Ki Young Kim, 2010.

[21] Federal Communication Commission, *Body Tissue Dielectric Parameters*, http://transition.fcc.gov/oet/rfsafety/dielectric.html

Hulusi Acikgoz received the B.S. and Master degrees in Applied Physics from the Paris-Est Marne-La-Valée University, France, and the Ph.D. degree from the Pierre and Marie Curie University (UPMCParis IV), Paris, France, in 2008 in Electrical Engineering. He has been a Teaching Assistant at UPMC-Paris IV in 2009-2010. After a year of Post-Doctoral Research at the L2E (Laboratoire d'Electronique et d'Electromagnétisme) in Computational Electromagnetic Dosimetry, he joined the KTO Karatay University, Konya, Turkey, in 2011, as an Assistant Professor. Currently, he is a Visiting Scholar working with Dr. Raj Mittra's research group at the University of Central Florida, USA. His research interests include, microwave characterization of dielectric materials, electromagnetic dosimetry, homogenization, antennas for microwave cancer ablation, high impedance surfaces, graphene applications in electromagnetics and statistical analysis of electromagnetic devices.

Compact Implantable Rectenna with Light-Emitting Diode for Implantable Wireless Optogenetics

Yuehang Xu, Yu Lan, Yijie Qiu, and Ruimin Xu

School of Electronic Engineering
University of Electronic Science and Technology of China, Chengdu 611731, China
yuehangxu@uestc.edu.cn

Abstract ─ In this paper, a compact rectenna which is capable to operate at 2.45 GHz for wireless implanted optogenetic stimulation is proposed. The rectenna consists of a monopole antenna and a rectifier circuit which drives the on-board blue light-emitting diode (LED). The presented rectenna is fabricated on 50 μm liquid crystalline polymer (LCP) substrate and has a dimension of 7 mm × 7.2 mm. The measured results of the rectenna embedded in the pork shows that the integrated LED can be lit wirelessly under the maximum permissible human exposure limit in controlled environments.

Index Terms─ Flexible application, implantable antenna, LCP, rectenna, wireless optogenetic.

I. INTRODUCTION

With the rapid advances in flexible devices and biomedical telemetry [1-3], the battery-free wireless devices and optogenetics devices such as diagnostic measurement, stimulation and intervention devices [4-7] have been developed dramatically because they can be utilized to make incessant and non-invasive stimulating or monitoring. Wireless energy harvesting technology [8-10] also has been developed in last decade, which is essential for biomedical implanted device due to the fact that recharging or replacing the batteries of the tiny devices is inconvenient.

Various kinds of rectennas have been developed since the first experimental study of rectenna carried out in 1963 [11-13]. Several implantable rectennas have also been reported to provide electrical power to implanted device [14-15]. Recently an integrated injectable neural probe using microscale light-emitting diode (μLED) for optogenetic stimulation was developed [16]. Optogenetic stimulation has the advantage of using light to activate or silence the neurons which have been genetically sensitized to light with extreme precision. However, the rectenna used to drive the μLED in the wireless optoelectronic system in [16] was not implantable, which is very useful for the freely moving animal or

human experiments. Up to now, few studies have investigated the rectenna which is both implantable and able to drive the LED.

In this letter, a compact implantable rectenna including a blue on-board LED for nerve stimulation application is presented. The rectenna embedded in the pork successfully lit the on-board LED at 2.45 GHz. Measured results of the rectenna showed that it could be used in optogenetic applications.

II. DESIGN AND FABRICATION

The presented implantable rectenna operating at 2.45 GHz is composed of a compact monopole antenna and a rectifier. Figure 1 displays the geometry of the proposed implantable rectenna along with its photo and dimensions. The rectenna has an overall size of 7 mm × 7.2 mm and is manufactured on double sided 18 μm copper clad Rogers ULTRALAM 3850 laminate which utilizes 50 μm liquid crystalline polymer (LCP) as the dielectric film. The dielectric constant and loss tangent of the substrate is 2.9 and 0.0025, respectively.

The antenna and rectifier were separately analysed by Ansys HFSS and Agilent Advanced Design System (ADS) software. The antenna consists of a simple folded radiating strip with the width of 2.2 mm and a short section of the line with the width the same as the width of the 50 Ohms feeding microstrip.

The implantable antenna needs to be put into test tissue to confirm its effectiveness. Recently the minced pork was confirmed that it is suitable to mimic the human skin and muscle between 100 MHz and 3 GHz [4]. Therefore the design of the implantable rectenna will be verified by embedding the rectenna into the pork as shown in Fig. 2 (a). The dimensions of the test pork were 85 mm × 80 mm × 45 mm.

The rectifying diode is essential in determining the RF-to-DC conversion efficiency of the rectifier. Basically, increasing the rectification stages can gradually improve the output voltage. However, the efficiency will decrease with the increase of the number of stages. Considering the voltage required to light a blue

LED is approximately 2.4 V, the surface mount Schottky barrier diode pair HSMS-282C from Avago Technologies were chosen for the rectifier design.
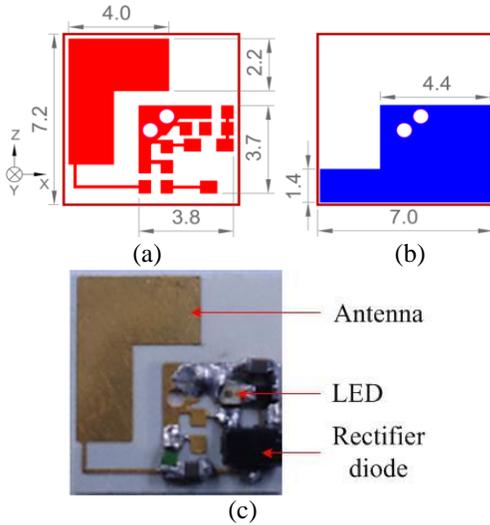
Fig. 1. Geometry of the proposed rectenna (dimensions in millimeters): (a) front view, (b) back view, and (c) photograph.
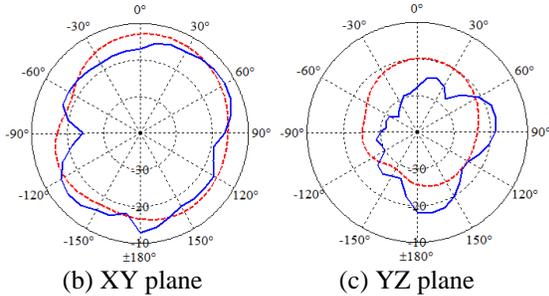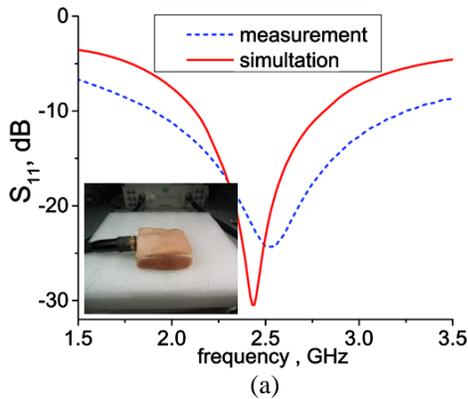
Fig. 2. Measured and simulated S11 and radiation gain patterns of the antenna embedded in the pork. (a) Measured and simulated S11 of the embedded antenna, (b) measured (blue line) and simulated (red line) gain patterns of the embedded antenna at XY plane, and (c) measured (blue line) and simulated (red line) gain patterns of the embedded antenna at YZ plane.

The schematic and photograph of the proposed rectifier circuit are presented in Fig. 3 (a). The dimensions of the rectifier circuit are 3.7 mm × 3.8 mm. The inductor L1 (= 1.6 nH) is used to improve the input matching of the rectifier. The capacitor C1 (= 39 pF) is a DC block capacitor. The diode D1 and D2 are the Schottky diode pair HSMS-282C. The capacitor C2 (= 1 μF) in a shunt configuration with respect to the load acts as a low pass filter, which isolates the load from unwanted RF signals. The surface mount diode D3 is a blue LED in series with the current limiting resistor R1 (= 2 KΩ).
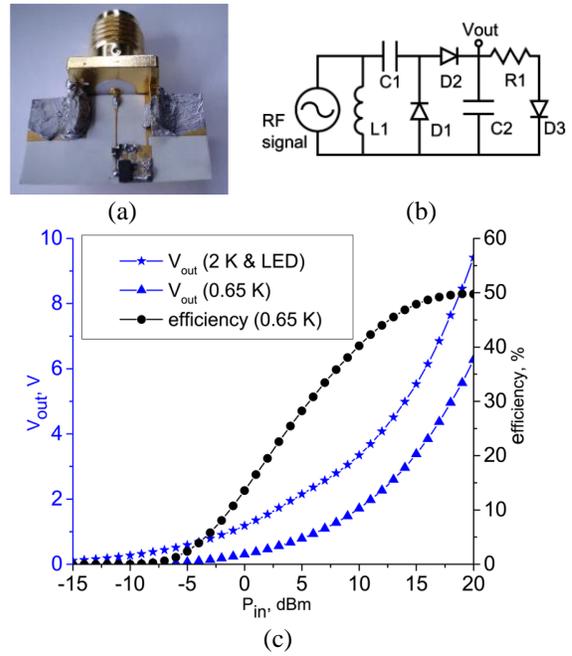
Fig. 3. Schematic and measured performance of the rectifier: (a) schematic, (b) photograph of the rectifier, and (c) performance of the rectifier.

III. RESULTS AND DISSCUSION

The fabricated rectenna, antenna and rectifier are coated with thin protective film of CRC Plasticote 70 for insulating them from the pork. The performances of the antenna were measured in an anechoic chamber. Figure 2 (a) shows the simulated and measured return loss of the antenna embedded into the pork. The simulation result of S11 agrees well with the measured S11 of the antenna. Figure 2 shows the measured radiation patterns of the antenna embedded in the pork at XY and YZ plane, respectively. The 2.45 GHz associated measured maximum radiation front gain of the embedded antenna is -12.9 dBi.

To measure the best efficiency of the rectifier, the LED was removed and the resistor R1 was chosen to be 0.65 KΩ. Figure 3 (b) shows the conversion efficiency of the rectifier as the function of RF input power when

R1 is 0.65 KΩ. The measured output voltages on the node Vout presented in Fig. 3 (a) were also shown in Fig. 3 (b). As can be seen in Fig. 3 (b), the output voltage Vout when both R1 (= 2 KΩ) and LED are loaded is higher than the output voltage when only R1 (= 0.65 KΩ) is loaded.

Figure 4 shows the photographs of the blue LED light-up demonstration when the rectenna was put on the surface of the pork and powered wirelessly. Figure 5 shows the power transmission efficiency (PTE) measurement setup for the proposed implantable rectenna. A blue lead LED and 2 KΩ lead resistor were used instead in order to facilitate finding out whether the LED is lit wirelessly. A power amplifier (power output from 0.02 W to 8.7 W) has been connected between the RF signal generator Agilent N9310A (power output from -20 dBm to 13 dBm) and a transmitting horn antenna with the gain of 5.1 dBi. The output power of the power amplifier was calibrated by the power meter Agilent N1912A. The rectenna was placed into the pork and the transmitting horn antenna was positioned at a distance of 10 cm in front of the rectenna. The PTE of the rectenna is defined as:

$$PTE(\%) = \frac{P_{DC}}{P_T} \times 100\% = \frac{V_{out} \cdot I_{out}}{P_T} \times 100\% , \qquad (1)$$

where PDC is the DC output power, PT is the transmitting power of the power amplifier, Vout is the output voltage of the rectifier [4].

(a)   (b)
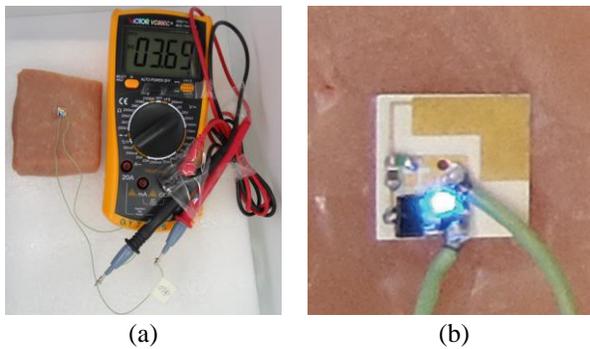
Fig. 4. Photograph of the LED light-up demonstration for the rectenna: (a) photograph of the LED light-up demonstration, and (b) enlarged photograph of the wirelessly lit LED in the rectenna.
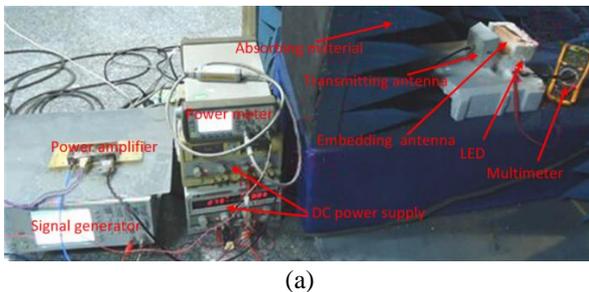
(a)
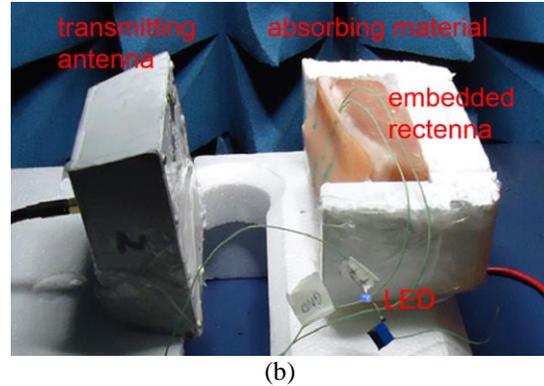
(b)

Fig. 5. Efficiency measurement system of the rectenna: (a) experiment setup of the efficiency measurement system, and (b) enlarged photograph of the transmitting antenna and the embedded rectenna with the lit LED.

The measured results shown in Fig. 6 are the measured output DC voltage and power transmission efficiency of the embedded rectenna as a function of the power density on the surface of the pork. The power transmission efficiency is low due to the free space loss, the biological tissue loss, the low antenna gain and the relatively low conversion efficiency of the detector. However, the blue LED begin to shine when the power density reaches 1.8 mW/cm^2, which is substantially lower than the maximum permissible human exposure limits (5 mW/cm^2) in controlled environments at 2.45 GHz based on the corresponding Federal Communications Commission (FCC) standard [6].
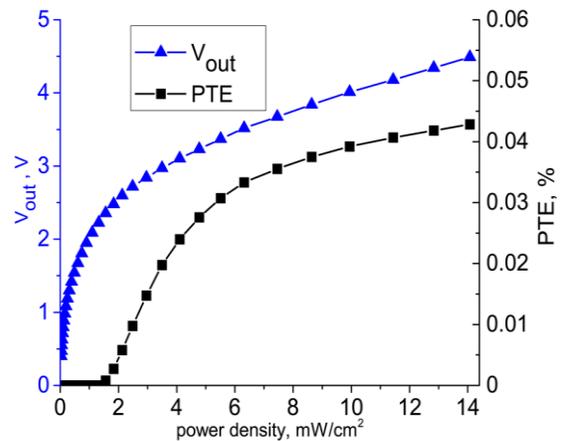
Fig. 6. Measured output DC voltage and power transmission efficiency of the embedded rectenna.

VI. CONCLUSION

In this paper, a compact implantable rectenna with a blue LED has been designed for optogenetics applications. The compact rectenna with the dimension of 7 mm × 7.2 mm operates at 2.45 GHz. The measured

maximum gain of the antenna is –12.9 dBi. The design of the flexible rectenna was verified in the biomedical implantable environment through measuring the PTE of the rectenna. The measured results showed that the LED in the rectenna was successfully lit and the rectenna can be used in applications such as wireless optogentics. Due to the thin thickness and good flexibility property of the substrate of the rectenna, the proposed rectenna will be more flexible by implementing the rectenna using on-chip components instead of the surface mount components. We will fabricate the on-chip flexible rectenna for implantable electronics in the future work.

ACKNOWLEDGMENT

REFERENCES

[1] Y. J. Qiu, Y. H. Jung, S. Lee, T. Y. Shih, J. H. Lee, Y. H. Xu, W. G. Lin, N. Behdad, and Z. Q. Ma, "Compact parylene-c-coated flexible antenna for WLAN and upper-band UWB applications," *Electronic Letters*, vol. 50, no. 24, pp. 1782-1784, Nov. 2014.

[2] Y. Lan, Y. H. Xu, C. S. Wang, Z. Wen, Y. J. Qiu, T. D. Mei, Y. Q. Wu, and R. M. Xu, "Flexible microwave filters on ultra thin liquid crystal polymer substrate," *IEEE MTT-S International Microwave Symposium*, Phoenix, AZ, USA, pp. 1-4, May 2015.

[3] S. Park, J. H. Ahn, X. Feng, S. D. Wang, Y. G. Huang, and J. A. Rogers, "Theoretical and experimental studies of bending of inorganic electronic materials on plastic substrates," *Advanced Functional Materials*, vol. 18, no. 18, pp. 2673-2684, Sep. 2008.

[4] C. H. Lee, S. K. Kang, G. A. Salvatore, Y. Ma, B. H. Kim, Y. Jiang, J. S. Kim, L. Yan, D. S. Wie, A. Banks, S. J. Oh, X. Feng, Y. Huang, G. Troester, and J. A. Rogers, "Wireless microfluidic systems for programmed, functional transformation of transient electronic devices," *Advanced Functional Materials 25*, pp. 5100-5106, Aug. 2015.

[5] E. R. Siuda, J. G. MaCall, R. AI-Hasani, G. Shin, S. I. Park, M. J. Schmidt, S. L. Anderson, W. J. Planer, J. A. Rogers, and M. R. Bruchas, "Optodynamic simulation of b-adrenergic receptor signaling," *Nature Communications*, 6:8480, Sep. 2015. DOI: 10.1038/ncomms9480.

[6] J. W. Jeong, J. G. McCall, G. Shin, Y. Zhang, R. AI-Hasani, M. Kim, S. Li, J. Y. Sim, K-I. Jang, Y. Shi, D. Y. Hong, Y. Liu, G. P. Schmiz, L. Xia, Z.

He, P. Gamble, W. Z. Ray, Y. Huang, M. R. Bruchas, and J. A. Rogers, "Wireless optofludic system for programmable in vivo pharmacology and optogenetics," *Cell 162, 2015*, pp. 1-13, 2015.

[7] C. Dagdeviren, Y. W. Su, P. Joe, R. Yona, Y. H. Liu, Y. S. Kim, Y. A. Huang, A. R. Damadoran, J. Xia, L. W. Martin, Y. G. Huang, and J. A. Rogers, "Conformable amplified lead zirconate titanate sensors with ehanced piezoelectric response for cutaneous pressure monitoring," *Nature Communications*, article no. 4496, Aug. 2014. DOI: 10.1038/ncomms5496.

[8] R. G. C. Fuentes, A. C. Aparicio, E. Alarcon, "Energy buffer dimensioning through energy-erlangs in spatio-temporal-correlated energy-harvesting-enabled wiressless sensor network," *Emerging and Slected Topics in Circuits and Systems*, 4, pp. 301-312, 2014.

[9] Y. Wu and W. B. Liu, "Routing protocol based on genetic algorithm for energy harvesting-wireless sensor networks," *Wireless Sensor Systems*, vol. 3, pp. 112-118, 2013.

[10] C. Y. Song, Y. Huang, J. W. Zhang, S. Yuan, and P. Carter, "A high-efficiency broadband rectenna for ambient wireless energy harvesting," *IEEE Transactions on Antenna and Propagation*, vol. 63, pp. 3486-349, 2015.

[11] J. I. Moon, I. K. Cho, S. M. Kim, and Y. B. Jung, "Design of efficient rectenna with vertical ground-walls for RF energy harvesting," *Electronics Letters*, vol. 49, no. 17, pp. 1050-1052, 2013.

[12] A. Takacs, H. Aubert, L. Despoisse, and S. Fredon, "Microwave energy harvesting for satellite applications," *Electronics Letters*, vol. 49, no. 11, pp. 722-724, 2013.

[13] S. Ladan, A. B. Guntupalli, and W. Ke, "A high-efficiency 24 GHz rectenna development towards millimeter-wave energy harvesting and wireless power transmission," *IEEE Transactions Circuits and Systems I: Regular Papers*, vol. 61, no. 12, pp. 3358-3366, 2014.

[14] H. Fu-Jhuan, et al., "Rectenna application of miniaturized implantable antenna design for triple-band biotelemetry communication," *IEEE Transactions on Antennas and Propagation*, vol. 59, no. 7, pp. 2646-2653, 2011.

[15] Y.-L. Yang, C.-L. Tsai, and C.-L. Yang, "Enhancement of output voltage for novel dental rectennas," *2012 42nd European Microwave Conference (EuMC)*, pp. 321-324, 2012.

[16] T. I. Kim, et al., "Injectable, cellular-scale optoelectronics with applications for wireless optogenetics," *Science*, vol. 340, (6129), pp. 211-216, 2013.

Yuehang Xu was born in Zhejiang Province, China, in 1981. He received the B.S. and M.S. degrees in Electromagnetic Field and Microwave Techniques from the University of Electronic Science and Technology of China (UESTC), Chengdu, in 2004 and 2007, respectively, and the Ph.D. from the UESTC jointed with Columbia University in the City of New York in 2010.

He joined the department of Electronic Engineering, UESTC, in Dec. 2010 and was promoted to Associate Professor in Aug. 2012, exceptionally. His current research interests are on modeling and characterization of micro/nano-scale electronic devices for RF applications, especially on GaN HEMTs and graphene electronics. He is an author or a co-author of more than 30 scientific papers in international journals and conference proceedings.

YijieQiu received the B.S. degree from the University of Electronic Science and Technology of China (UESTC), Chengdu, China, in 1992 and the M.S. degree from Southeast University, Nanjing, China, in 1995. He is currently pursuing the Ph.D. degree at the University of Electronic Science and Technology of China (UESTC), Chengdu, China.

From 1995 to 2009, he was a Senior Engineer with Southwest China Research Institute of Electronic Equipment, Chengdu, China. His research interests include microwave antennas, amplifiers, oscillators and subassemblies.

Yu Lan was born in Sichuan Province, China, in 1991. He received the B.S. degrees in Physical Electronic Technology from the University of Electronic Science and Technology of China (UESTC), Chengdu, in 2013, and is pursuing his Ph.D. degree in Electromagnetic Filed and Microwave Technology from the UESTC, Chengdu, China. His current research interest is on flexible electronic devices for RF applications.

Ruimin Xu received the B.S., M.S. and Ph.D. degrees from the University of Electronic Science and Technology of China (UESTC), Chengdu, China, in 1982, 1987, and 2008, respectively.

From November 1993 to May 1996, he was appointed to attend advanced study and work with the Agilis Communication Corporation of the Singapore Science and Technology Group by UESTC, during which time he mainly took charge of research in high frequency front-ends of the satellite ground VSAT system. In May 1996, he returned to UESTC. In 2000, he became a Full Professor with the School of Electrical Engineering, UESTC, and became the Director of the Microwave Engineering Department. His current research interests include microwave and millimeter-wave circuits and systems.

Multimodal Medical Image Fusion Using Dual-Tree Complex Wavelet Transform (DTCWT) with Modified Lion Optimization Technique (mLOT) and Intensity Co-Variance Verification (ICV)

C. G. Ravichandran [1] and Rubesh Selvakumar [2*]

[1] Department of Electronic and Communication Engineering
SCAD Institute of Technology, Trippur-641664, TamilNadu, India
cg_ravi@yahoo.com

[2] Department of Computer Science and Engineering
Madurai Institute of Engg. & Tech., Madurai, TamilNadu-630611, India
Seshind2014@gmail.com

Abstract ─ Image fusion is place as a key role in medical image investigation and preparation of treatments for bio-medical research and clinical diagnosis. The most incentive is fuse to capture a large amount of vital information from the input images to have its output image. In this paper, a well-organized multimodal medical image fusion approach is obtainable to fuse computer tomography (CT) and magnetic resonance image (MRI). The significant co-efficient of source images are line up through the dual-tree complex wavelet transform (DTCWT), followed by unit of low and high frequency components. Two completely different proposed fusion rules based on weighted fusion rule, the weights are optimized by modified lion optimization technique (mLOT) and intensity co-variance verification (ICV) are used to fuse the low and high frequency co-efficient. The fused image is reconstructed by inverse DTCWT with all amalgamate co-efficient. To prove the potency of the new approach is greater than the well-known standard algorithm, experiments are conducted. Based on experimental comparison and proposed approach, the better results are fused image quality are obtained. The studies of qualitative and quantitative metrics are clearly demonstrated that the new approach is to display the high superior than the present.

Index Terms ─ CT, DTCWT, ICV, low and high frequency, medical image fusion, mLOT, MRI.

I. INTRODUCTION

Multimodal medical image fusion refers to the identical and fusion between two or more images of the identical sight from single or different medical imaging modalities. The resultant image is acquired complementary information and makes it precise, further the ideal information is to help for the clinical diagnosis and treatment planning [1]. The aspiration of medical image fusion may be a single modality of medical image which cannot give the comprehensive and accurate information. And also, the physical process of integrating several modalities of medical images are rigorous, time overwhelming, human error and needs a lot of experiences. Therefore, different modality of medical images by automatic combining through the image fusion technique will acquire the complementary information employed in biomedical research and treatment planning of clinical diagnosis for doctors [2]. There are variety of medical images with individual application boundaries are together with the CT, MRI, PET and SPECT etc. Fusion of CT and MRI images will preserve far more edge and component information and produce a high quality fused image for doctors to obtain for accurate diagnosis. In worldwide, the multimodal medical image fusion grabs attention of specialists and scholars [3].

In dual approach for image fusion offered spatial domain and transform domain. The spatial domain oriented approach leads the pixel level to contrast reduction. Based on the subsequent approaches, Intensity-Hue-Saturation (IHS), Principal Component Analysis (PCA) and Brovey method supply higher results, however it suffers from the spectral degradation. In transform domain conjointly referred as multi-resolution, supported on pyramidal image fusion schemes fail to introduce any spatial orientation selectivity in the decomposition process and therefore usually cause blocking effects. Most of the above mentioned schemes with its own limitations [4-6].

In MRA technique of the discrete wavelet transform (DWT) will preserve spectral information powerfully; however, the spatial characteristics are not expressed in fine [7]. A huge vary of signal processing tasks will

apply effectively by the DWT. But its performance is inadequate of owing to the subsequent issues like, oscillations of the coefficients at a singularity, shift variance once tiny changes within the input cause giant changes within the output, aliasing is due to down sampling and non-ideal filtering throughout the analysis and a lack of directional selectivity in higher dimensions, i.e., distinguish between $+45^0$ and -45^0 edge orientations. An extensively best known methodology is to provide the shift invariance of the use of un-decimated quite, the dyadic filter tree that's required are most expeditiously with a tros algorithmic. On the conflicting furnish, the fully decimated DWT is smaller computational requirements than traditional and also conjointly exhibits high redundancy inside the yield information [8].

In the last decade, many software and systems are developed to employment the image fusion drawback. Those methods are based on multi-resolution transform fusion methods, have fascinated a significant quantity of research thought. An amount of accepted transforms embody the principal component analysis (PCA) [9], discrete wavelet (DWT) [10], stationary wavelet (SWT) [11], dual-tree complex wavelet [12], curvelet (CVT) [13], non sub-sampled contourlet transform (NSCT) [14], dual-tree complex wavelet with PSO (DTCWT-PSO) [15], non sub-sampled contourlet transform with SF_PCNN (NSCT_SF-PCNN) [5].

In this paper, a novel fusion skeleton is proposed for multimodal medical image fusions are supported on DTCWT fusion scheme. The core plan is to decompose the DTCWT on the source images followed by the fusion of low- and high-frequency coefficients. By incorporating the features of modified lion optimization technique (mLOT) and intensity co-variance verification (ICV) with the fusion rules for low- and high-frequency coefficients, in low frequency coefficients fusion that holds a number of significant information, can have an effect on the natural look of the fused results by using this fusion rule algorithm. It often used the weighted average fusion rule for the average low-frequency coefficients; it completely expected to diminish the contrast of the fused image in some extent. This paper is to conserve the region features and emphasize the different parts adaptively, exploitation the region based weighted average fusion rule is to fuse the low frequency coefficients. The weights are optimized with mLOA. In this technique, it is anticipated that the optimum fused results are adaptively intensity. The co-variance verification expeditiously verifies the frequency components from the high frequency coefficients. Grouping of these two will preserve the additional details of source images and improves the standard for fused images. The potency of the proposed framework is dispensed by the in-depth fusion experiments is totally different from multimodal CT/MRI and PET/SPECT/MRI dataset. Further, visual and quantitative analysis shows the proposed framework which provides a more robust fusion of outcome when the traditional image fusion technique applies.

The rest of this paper is organized as follows. Section II describes in the materials and methods, which includes summary of the DTCWT-PSO, primarily based image fusion theme is given and provides the procedure of the proposed technique. Section III provides the results and discussion followed by some experiments and conclusions in Section IV.

II. MATERIALS AND METHODS

This section covers the description of theory on which the future framework is based. These concepts include DTCWT which described as follows.

A. Dual-tree complex wavelet transform

Because of down-sampling a small change occurs within the input by DWT, it might cause aliasing immense within the wavelet coefficients. Inverse DWT revoke this aliasing offer, if the wavelet and scaling coefficients aren't changed [12]. And also, with shortcoming of DWT gives a deprived directional selectivity. These evils of real DWT are resolved using complex wavelets algorithm. However, complex wavelet decomposition of level 1 in perfect reconstruction creates a trouble. To conquer this, Kingsbury proposed the DT-CWT, which permit the perfect reconstruction, whereas it still provides the other benefits of complex wavelets [8].

The DT CWT makes use of two real DWT in its structure. The earliest DWT gives the real part of the transform and subsequent part gives the imaginary part. Filter banks of the analysis and synthesis are utilized in DT CWT are shown in Figs. 1 (a) and 1 (b) respectively. Two real wavelets transform use two completely different set of filters that satisfying the perfect reconstruction condition. It filters h_o (n), h_1 (n), g_0 (n) and g_1 (n) denote the low pass/high pass filter pairs for the upper and lower filter banks respectively. Both filters are real but their mixture produces a complex wavelet. For fulfilling a perfect reconstruction condition the filters are intended to make a complex wavelet $\varphi(t) = \varphi_h(t) + j\varphi_g(t)$ approximately analytic by two real wavelet transforms $\varphi_h(t)$ and $\varphi_g(t)$. Consistently they are intended so that the lower wavelet $\varphi_g(t)$ is the Hilbert transform of upper wavelets $\varphi_g(t); \approx H\{\varphi_h(t)\}$.

In the inverse of DTCWT, the real part and imaginary part are all inverted and therefore, the inverse of the two real DWTs furnish a two real signal and to end with the average of two real signals gives a final output. We will acquire an inventive signal from either real part or imaginary part alone.

(a)

(b)
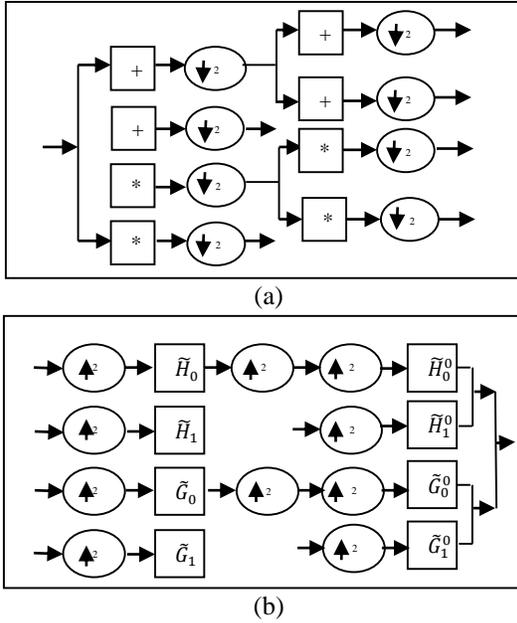
Fig. 1. (a) Analysis filter bank of DTCWT at two levels. (b) Synthesis filter bank of DTCWT at two levels.

B. Proposed fusion framework

In this section, the design and the approach of multimodal medical image fusion will be discussed. The proposed structure recognizes the modified lion optimization technique (mLOT) and intensity co-variance verification (ICV) in DTCWT domain, which acquires a couple of source image and to produce a combined image. The fundamental state in the proposed framework is that all the source images must be registered in order to align the matching pixels.

i. Modified lion optimization technique in DTCWT domain:

In general, finding the most optimal solution for problems in nature by humans under the guidance of several optimization techniques like genetic algorithm, ant colony optimization, honey bee optimization, bacterial foraging algorithm, teaching learning algorithm, particle swarm optimization, etc., to apply in different areas. However, none of the have proposed a technique to increase good number of optimal solution for all optimization problems. A few algorithms offer to improve the solutions for a little specific problem which compare with others. Therefore, the modified lion optimization pechnique [16] is based on a behavior of lion and social organization for applying in medical image fusion process for the purpose of the selection of optimal fusion weight of an image and the summarization of the process given below.

Step1: Initialization

To generate the populations (Lions) over the solution space in randomly,

$$Let\ f(L) = (x_1, x_2 \ldots x_n)\ for\ x_i, b_i,$$

where $a_i\ and\ b_i$ are lower and upper bound between 0 and 1, set and define in the all required parameters.

Step2: Hunting

a. Calculate the p based on the given formula of standard deviation and set in the p in center of the n(FH), where n(FH) is the number of female hunters:

$$\sigma = \sqrt{\frac{1}{N}\sum_{i=1}^{N}(x_i - \mu)^2}. \qquad (1)$$

b. Set the female pride in some percentage for hunting and calculate the fitness value (β) [17,18], choose the best fitness to place on the center on the p and remaining are left and right of the center.

c. Select one after another female hunters randomly for attack the p. During this time D is added where, D is the disturbances of the hunters.

d. Once again estimate the fitness value of n(FH) and p then check and compare the previous and present and choose to best and discard the D.

e. Finally, move the p and n (FH) before that estimating the value of λ, where, λ is the variance of the p and H:

$$p' = p + R(0,1) \times \lambda \times (p - FH), \qquad (2)$$

$$H' = \begin{cases} R(FH, p), if\ FH < p \\ R(p, FH), \quad FH > p \end{cases}. \qquad (3)$$

Step3: Move to safe place

To move the safe place in the remaining female hunter and estimate the current and new position fitness value:

$$FH' = FH + C\big(R(0,1)\big) \times FH. \qquad (4)$$

$$FH' = \begin{cases} \beta' \quad, if\ \beta < \beta' \\ \beta, otherwise \end{cases}. \qquad (5)$$

where, C is the constant value between the 0 and 1.

Step4: Roaming

Select the male lion in the roaming and check if it is mad lion (ML) or nomad lion (NML). If it is ML, estimate the β current and new selected position in randomly:

$$ML' = \begin{cases} current\ \beta\ , if\ current\ \beta > new\ \beta \\ new\ \beta, \qquad\qquad otherwise \end{cases}. \qquad (6)$$

If the NML, estimate the probability of all using the given below equation:

$$Pr_i = 0.1 + \min\left(0.5, \frac{NML_i - best_{NML}}{best_{NML}}\right), i = 1,2 \ldots, \qquad (7)$$

$$NML_{ij} = \begin{cases} NML_j, if\ R_j > Pr_i \\ R_j, otherwise \end{cases}. \qquad (8)$$

Step5: Mating

Set the female lion (FL) with all pride for mating to all male in the all pride and produce the two's c:

$$c_j, 1 = N \times FL_j + \sum \frac{(1-N)}{\sum_{i=1}^{NR} S_i} \times ML_j^i \times S_i, \qquad (9)$$

$$c_j, 2 = 1 - N \times FL_j + \sum \frac{(N)}{\sum_{i=1}^{NR} S_i} \times ML_j^i \times S_i, \qquad (10)$$

where, j is the dimension, $S_i = \begin{cases} 1, if\ male = i \\ 0, otherwise \end{cases}$ and N is the randomly generated numbers with a normal distribution with μ and σ, i.e., N(0,1).

Step6: Defense

To evaluate the β of mad and nomad of the male lion and choose the best using the given below Equation (11):

$$ML = \begin{cases} NML, if\ NML > ML \\ ML, otherwise \end{cases}. \qquad (11)$$

Step7: Migration

Select in some of the mad female lion in equal for all pride to become a nomad and sort in the new and old nomad female using a sorting technique according to their β, then choose the best female among them randomly one after another to fill the empty place of the migrated female.

Step8: Equilibrium

Remove the worst β of the nomad with respect of the maximum permitted in the number of each gender in nomad.

Step9: Stopping criteria

Evaluate the best results and then stop the process based on the number of iterations.

ii.   Intensity co-variance verification in DTCWT domain:

In general, fusion for high frequency coefficients which applies only the maximum selection rule for getting the absolute value, by applying this it doesn't consider the encircling pixels of image [Chandana *et al.*, 2011]. So, we propose a new unique fusion rule of intensity co-variance verification based on the local variance with the neighbors. The summarized process of this rule is as follows.

Step1:

After the decomposition process using DTCWT to get the high pass sub-bands $H_{l,d}^A(i,j)$ and $H_{l,d}^B(i,j)$ from images, they are split into 3x3 windows.

Step2:

Each window (both images) estimates the local mean value using the Equation (12):

$$\mu = \frac{1}{N}\sum_1^N (i,j). \qquad (12)$$

Step3:

And then compute the local variance using the below Equation (13):

$$\sigma^2(X_{i,j}) = \frac{\sum_1^N (H_d^{A,B}(i,j) - \mu)^2}{N-1}, \qquad (13)$$

where, N is no. of neighbor's data.

Step4:

Estimate the sum of variance is defined as:

$$sv = \sigma^2\left(H_d^A(i,j)\right) + \sigma^2\left(H_d^B(i,j)\right). \qquad (14)$$

Step5:

Compute the percentage (p) of variances in both images using the Equation (15):

$$p = \sigma^2(H_d^{A,B}(i,j))/s. \qquad (15)$$

Step6:

Finally, choose the best values between the 0 and 1 to the fused image.

iii.   Fusion framework:

In this subsection the detailed enlightenment of the proposed fusion structure is considered by two absolute registered source images A and B. We proposed image fusion methods with two different modalities consisting of the subsequent steps:

Step1: Decomposition process

Perform the DTCWT decomposition process up to level n, to get two low frequency sub-bands and six high frequency sub-bands in each level. These sub-bands are defined as:

$$\{(L_t^A(i,j), H_{l,d}^A(i,j) : l = n, t = 1,2, d = 1 \dots 6\},$$
$$\{(L_t^B(i,j), H_{l,d}^B(i,j) : l = n, t = 1,2, d = 1 \dots 6\},$$

where $L_t^A(i,j), L_t^B(i,j)$ the low frequency sub-bands in the t orientation are, $H_{l,d}^A(i,j) H_{l,d}^B(i,j)$ represent the high frequency sub-bands *l* level in the *d* orientation and show the DWT coefficients of CT and MRI in Figs. 2 (a) and 2 (b).

(a)

(b)
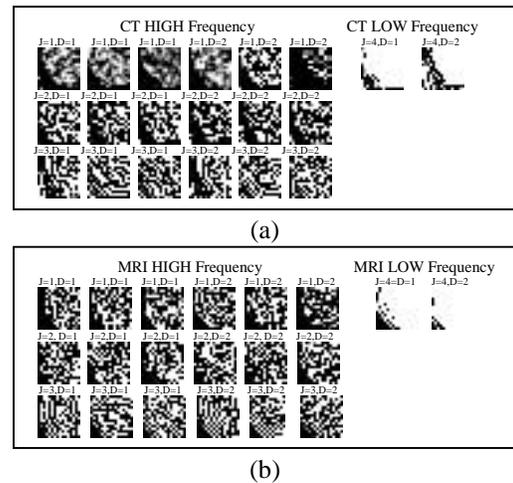
Fig. 2. (a) DTCWT coefficients for low and high in the first image at 3 levels. (b) DTCWT coefficients for low and high in the second image at 3 levels.

Step2: Segmentation process

A number of segmentation algorithms are obtainable in the literature [19] for thresholding and clustering. This algorithm usually generates undesired segmented regions, throughout the existing paper, the low pass sub-bands are segmented by the normalized cut [20, 21] image segmentation and it shows the segmented process in Fig. 3.
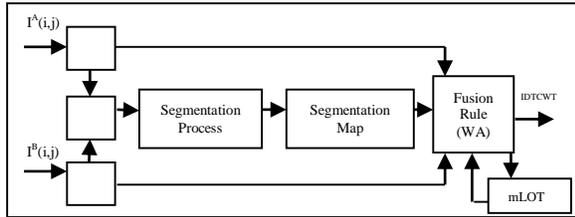
Fig. 3. Segmentation process in low frequency coefficients.

Based on segmentation approach, the low frequency coefficients of both source images are segmented by the region and to get a better segmentation.

Step3: Fusion of low frequency sub images

The low-frequency sub images of the coefficients will be a character of the approximation component of the source images. The traditional averaging methods are used to construct the composite bands. However, it cannot provide the fused low-frequency component of high quality for medical image. As a result, it leads to the economical contrast within the fused images. So, one simplest way is to use the pixel based weighted average fusion rule to present the fused coefficients, the weights are taken as a value between 0 and 1. In general, the weights value will be 0.5. However, this process is suitable only for the same modality and it won't fuse multi-modal images as various dynamic ranges; PBAVE

can considerably alter the intensity range of the images and it reduces the contrast within the fused image. Therefore, a contemporary principle is proposed on region-based fusion rules employed by manipulating the measures of the significance of a region as a priority and choosing with the higher priority in the analogous region. The source images features of the regions are preserved, but the optimal results couldn't be obtained by merely selecting coefficients from one input. So, the weights are optimized by mLOA and the process will be described as Section III.A;

$$L_{F,R_k}(i,j) = w_k \times L_{t,R_k}^A(i,j) + (1 - w_k) \times L_{t,R_k}^B(i,j), \quad (16)$$

where $L_{F,R_k}(i,j)$ denotes the fused coefficients of R_k corresponding to $L_{t,R_k}^A(i,j)$ and $L_{t,R_k}^B(i,j)$.

Step4: Fusion of high frequency sub images

Generally, the high-frequency sub-image coefficients takes up fine detail components with the source image. Because the fusion process will have an effect on the fusion performance as a result of its notable, that the noise is additionally involved in high frequency and will cause fault of sharpness.

Therefore, a brand new criterion is proposed here, based on intensity co-variance verification. In general, the most choice of maximum selection rule accustomed construct the composite bands; however, this rule doesn't take any thought of the surrounding pixels. Therefore, a completely unique approach is proposed by intensity verification. This rule is employed to elaborate $I^A(i, j)$ $I^B(i, j)$.

Step5:

Perform inverse DTCWT on the composite low- and high-frequency sub-bands up to n levels to obtain the fused image F and the information flow, the diagram of proposed image fusion algorithm is shown in Fig. 4.
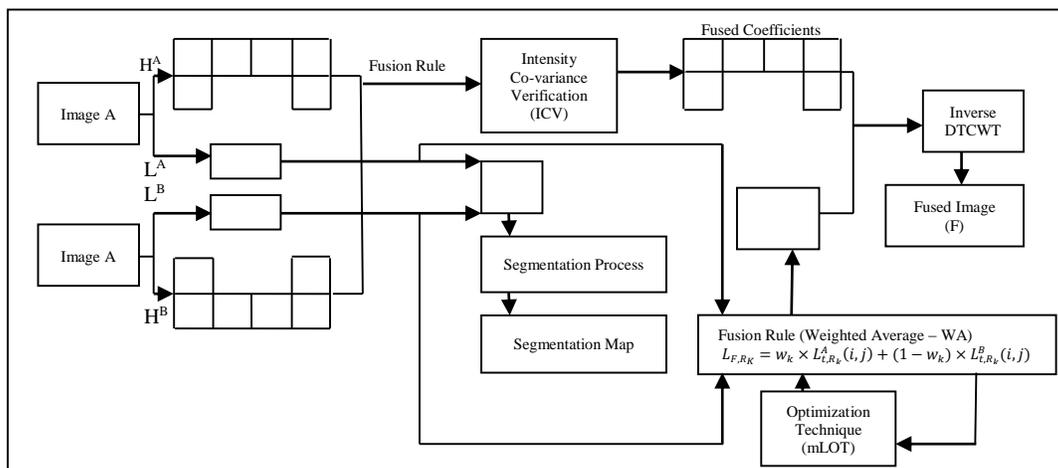
Fig. 4. Block diagram of information flow of proposed multimodal medical image fusion framework.

III. RESULTS AND DISCUSSIONS

It has been developed with MATLAB 15a for simulation of image fusion algorithms, many versions obtainable, however a new version of Math work 15a is an additional feature for the present work such as sub-version supply management integration, advanced new graphic systems etc. In general, MATLAB is an interactive program for numerical computations and information image, used extensively by management engineers for analysis and it support to completely different operational systems like UNIX, Windows etc. Here, are a few reasons to choosing the MATLAB 15a during this analysis work as provides several functions, enable one to make sure top numerical preciseness, commanding mathematical and geometric support for the implementing of superior algorithms over ever, helpful to loosen the matter with matrix and vectors formulation of the present work.

In general, the CT image will offer bone dense structures and implants with a smaller amount of falsity, but it cannot discover physiological changes. The MRI image will present customary and pathological soft tissue data; however, it cannot read the position of bones information and CT-MRI images to be fused can yield a combined image with the contents and MRI fusion of proton density and weighted images of T2 place in harmonizing image details to the results of fusion. During this case, one image may not be capable to offer precise clinical requirements for the physicians. Therefore, needed for the multimodal medical image fusion and it has secured. The simulation results can exhibit fusion of these multimodal images, get a composite fused image consisting of complementary information from varied image modalities. The earlier depends on human visual characteristics and additionally the expert knowledge of the viewer, hence fuzzy, time-consuming and poor-repeatable. However these are typically correct if performed properly. The alternative one is comparatively formal and simply accomplished by the computer algorithms that typically valuate the similarity between the fused and source images. However, choosing a proper consistent criterion with the subjective assessment of the image quality is rigorous. Hence, there is a desire to form an evaluation system. Therefore, primary an evaluation index system is recognized to gauge the proposed fusion algorithm. These indices are determined consistent with the statistical parameters.

A. Performance of proposed system using the quality metrics

i. *Standard Deviation (SD)*:

This metric is additionally efficient in the lack of noise. It deals with the contrast in the fused image. An image with high contrast would have a high standard deviation [22]. The statistical moment $_{MF}$ is the fused image histogram *(f)* is defined as:

$$M_F = \sum_{i=0}^{n-1}(f_i - m)^2 p(f_i), \qquad (17)$$

where *m* is the average intensity, *n* is the maximum possible intensity levels and $P(f_i)$ is the probability of specific level *i* occurs in fused image. Average *m* intensity is defined as:

$$M = \sum_{i=0}^{n-1} f_i p(f_i^{''}). \qquad (18)$$

Standard deviation σ can be defined as the second moment about mean [12]:

$$\sigma = \sqrt{M_2(f)}. \qquad (19)$$

The metric based on standard deviation (σ) can be successfully implemented in noise free situation. Average contrast in fused image is represented by standard deviation. There is direct variation between the standard deviation and the amount of contrast in the given image.

ii. *Structural Similarity Index Metric (SSIM)*:

Structural similarity is intended by modeling some image deformation as the combination of loss of correlation, radiometric and contrast distortion. Mathematically, SSIM between two variables U and V is defined as [23]:

$$SSIM(U,V) = \frac{\sigma_{UV}}{\sigma_U \sigma_V} \frac{2\mu_U \mu_V}{\mu_U^2 \mu_V^2} \frac{2\sigma_U \sigma_V}{\sigma_U^2 \sigma_V^2}, \qquad (20)$$

where μ_U, μ_V mean intensity, $\sigma_U, \sigma_V \text{ and } \sigma_{UV}$ are the variances and covariance respectively. Based on the definition of SSIM, a new way to use SSIM for the image fusion assessment is proposed in [23] and is defined as:

$$Q_S = \begin{cases} \lambda(w)SSIM(A,F/w + \left(1 - \lambda(w)\right)SSIM(B,F/w), \\ \qquad if \ SSIM(A,B/w) > 0.75 \\ \max\left[SSIM\left(A,\frac{F}{w}\right), \ SSIM\left(B,\frac{F}{w}\right)\right] \\ \qquad if \ SSIM\left(B,\frac{F}{w}\right) < 0.75 \ , \end{cases} \qquad (21)$$

where w is a sliding window of size, which moves pixel by pixel from the top-left to the bottom-right corner and λ (w) is the local weight obtained from the local image salience.

iii. *Normalized Mutual Information (NMI)*:

It is a quantitative appraise of the mutual dependence of two variables [24]. It typically illustrates measurement of the information shared by two images. Mathematically, MI between two discrete random variables U and V is defined as:

$$MI(U,V) = \sum_{u \in U} \sum_{v \in V} p(u,v) \log_2 \frac{p(u,v)}{p(u)P(v)}, \qquad (22)$$

where $p(u,v)$, the joint probability distribution function of U and V, whereas $p(u) \text{ and } p(v)$ are the marginal probability distribution functions of U and V respectively. Based on the above definition, the quality

of the fused image with respect to input images A and B can be expressed as:

$$Q_{MI} = 2\left[\frac{MI(A,F)}{H(A)+H(F)} + \frac{MI(B,F)}{H(B)+H(F)}\right], \quad (23)$$

where H(A), H(B) and H(F) is the marginal entropy of images A,B and F respectively.

iv. Edge Similarity Index Measure (ESIM):

It provides the similarity between the edges transferred in the fusion process. Mathematically, $Q^{AB/F}$ is defined as [23]:

$$Q^{AB/F} = \left(\sum_{i=1}^{M}\sum_{j=1}^{N}\left[Q_{i,j}^{AF}w_{i,j}^{x} + Q_{i,j}^{BF}w_{i,j}^{x}\right]\right) /$$
$$\left(\sum_{i=1}^{M}\sum_{j=1}^{N}\left[w_{i,j}^{x} + w_{i,j}^{x}\right]\right), \quad (24)$$

where A, B and F represents the input and fused images respectively. The definition of Q^{AF} and Q^{BF} are same and given as:

$$Q_{i,j}^{AF} = Q_{g,i,j}^{AF}Q_{\alpha,i,j}^{AF} \qquad Q_{i,j}^{BF} = Q_{g,i,j}^{BF}Q_{\alpha,i,j}^{BF}, \quad (25)$$

where Q_{gj}^{F} and Q_{α}^{F} are the edge strength and orientation preservation values at location (i,j) respectively for images. The dynamic range for $Q^{AB/F}$ is [0, 1] and it should be close to 1 as possible for better fusion.

B. Experiments on CT/MRI image fusion

Evaluation and the performance of the image fusion are proposed in these rules with six sets. And is perfectly registered in CT-MRI images and the MR-T1-MR-T2 images are experimented with few collection of fusion algorithms. All the images shown in Fig. 5 is in the size of 256×256 pixel and then applied to the given datasets by numerous existing and proposed algorithms are delivered from the complete brain image database, which furnish the free access of images for educational and research purpose [25]. After this validation, we demonstrated the potential of our fusion rule to fuse other modalities. In addition, it is consulted with the radiologist, this proposed approach gives enhanced information and also it will be useful for medical applications like medical diagnosis etc. for doctors.

With high opinion to several imaging state and principles, the source images with different modalities have complementary information. Based on these, all the image groups are proposed fusion results are good to compared with the some acceptable existing and present approaches. The assessment of statistical parameters for the fused images is totally varied from the fusion algorithms and it is shown in the Table 1, visually in Fig. 6 and graphically in Figs. 7 (a), 7 (b), 7 (c) and 7 (d) separately because of clear variation of the parameters representation. Based on the graph, figure and the table, the proposed algorithm is obvious, preserves spectral information and also improves the spatial detail information to the overall existing algorithm, which can be easily observed to obtain the maximum values of evaluation indices of SD, NMI, SSIM and ESIM. The values of the all techniques based on the above performance indices with respect to fusion for existing and the proposed, the proposed value of all are higher and occurs it gives a better quality fused image compared with the others.
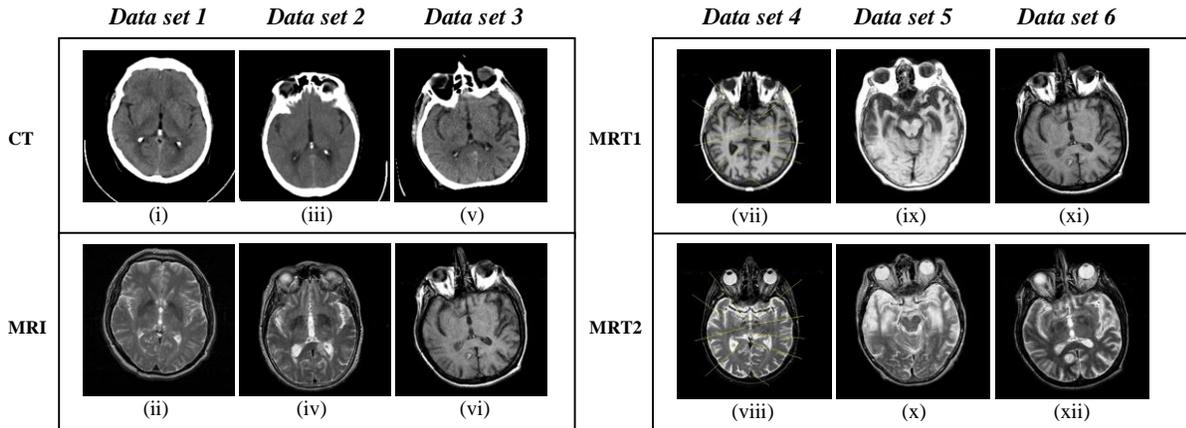
Fig. 5. Multimodal medical image data sets: (i), (iii) and (v) CT image; (ii), (iv) and (vi) MRI image; (vii), (ix) and (xi) MR-T1 image; (viii), (x) and (xii) MR-T2 image.
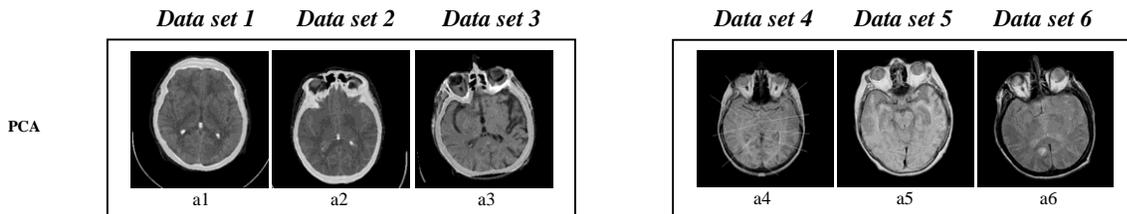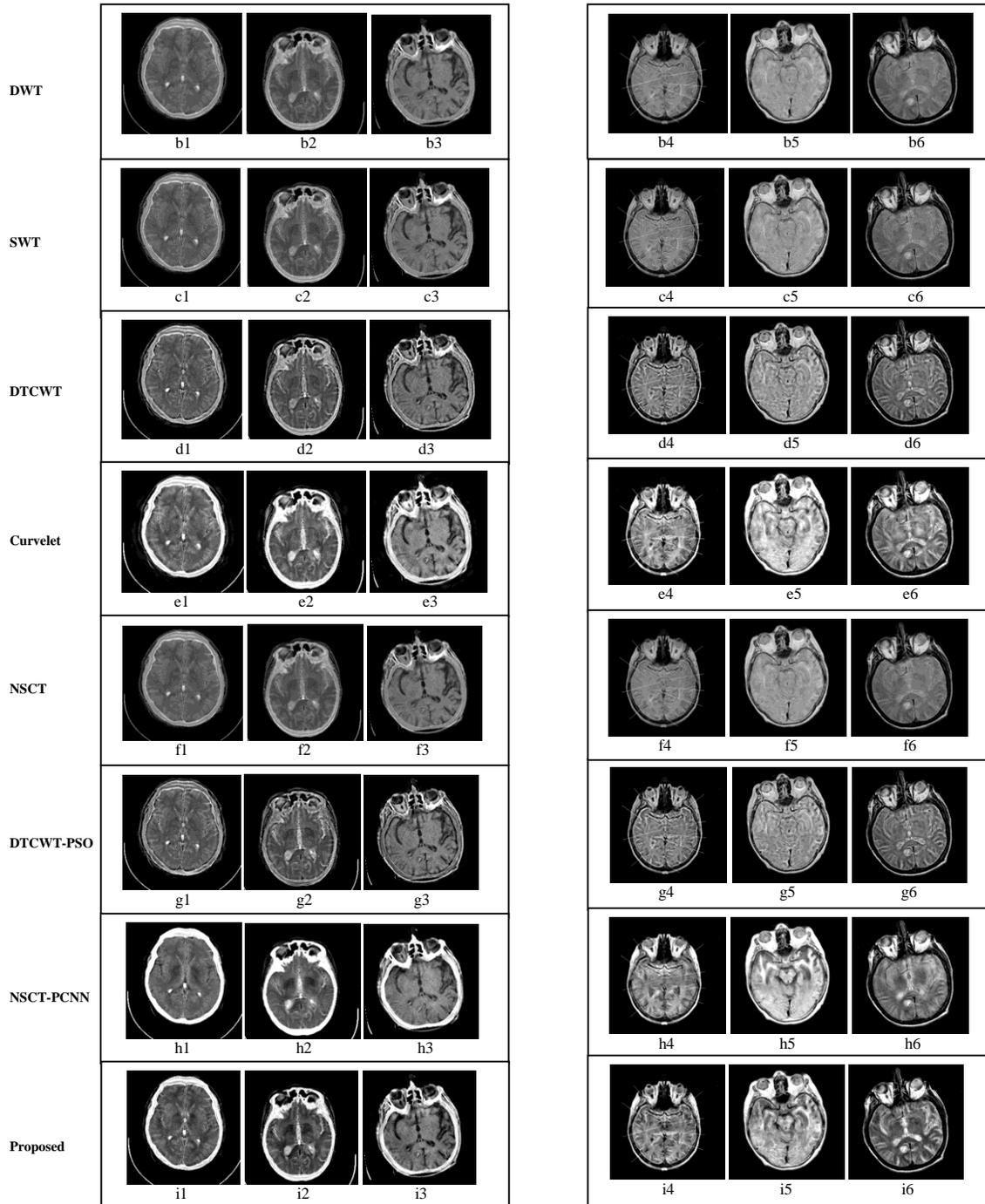
Fig. 6. The multimodal medical image fusion results of different fusion algorithms: fused images from (a1-a6) PCA based technique; (b1-b6) DWT based technique; (c1-c6) SWT based technique; (d1-d6) DTCWT based technique; (e1-e6) curvelet based technique; (f1-f6) NSCT based technique; (g1-g6) DTCWT-PSO based technique; (h1-h6) NSCT-PCNN based technique; (i1-i6) proposed technique.

Table 1: Evaluation performance for fused medical images by various quality metrics

Image Modality	Quality Metrics	PCA	DWT	SWT	DTCWT	Curvelet	NSCT	DTCWT PSO	NSCT PCNN	Proposed
Data Set I CT and MRI	SD	62.884	55.0227	55.847	58.5727	75.736	70.658	56.9724	77.2038	72.8881
	NMI	0.826	0.7169	0.715	0.6729	0.5861	0.5967	0.6851	0.7702	0.8411
	SSIM	4.607	4.6522	3.819	3.1969	3.0688	3.948	3.1142	3.2844	4.0761
	ESIM	0.401	0.3406	0.455	0.5068	0.4746	0.4897	0.5003	0.448	0.5717
Data Set II CT and MRI	SD	63.467	56.7274	57.426	60.6093	79.482	72.7865	56.8767	79.817	74.805
	NMI	0.838	0.7665	0.782	0.7301	0.6181	0.6452	0.7563	0.7327	0.8849
	SSIM	3.935	4.0307	3.46	3.0475	3.1377	3.324	2.9442	3.2801	4.0905
	ESIM	0.378	0.3493	0.454	0.5223	0.5179	0.5185	0.5068	0.4829	0.5677
Data Set III CT and MRI	SD	63.153	60.4157	61.312	64.5094	81.59	70.6423	63.2617	80.0196	75.8832
	NMI	0.826	0.7426	0.747	0.697	0.5934	0.5825	0.712	0.7882	0.801
	SSIM	3.965	3.8432	3.28	2.9357	3.0886	3.2749	2.8732	3.1825	4.0091
	ESIM	0.369	0.359	0.436	0.4884	0.4531	0.4659	0.4817	0.4376	0.5692
Data Set IV MRT1 and MRT2	SD	59.079	58.3354	58.88	62.4244	76.8882	71.231	62.313	72.6492	77.2225
	NMI	0.791	0.7696	0.792	0.767	0.6736	0.6834	0.7743	0.7242	0.8238
	SSIM	3.462	3.3427	3.124	2.8843	3.0368	3.2398	2.8944	3.0745	2.9086
	ESIM	0.337	0.3331	0.417	0.5154	0.4787	0.4946	0.5176	0.4414	0.5419
Data Set V MRT1 and MRT2	SD	76.316	74.2201	74.686	76.6255	95.4531	73.462	74.9361	93.2302	97.2543
	NMI	0.825	0.7503	0.739	0.6919	0.7147	0.7351	0.7017	0.8612	0.8931
	SSIM	4.126	3.8884	3.558	3.3027	3.4823	3.5127	3.2398	3.6406	4.4269
	ESIM	0.449	0.4394	0.473	0.5068	0.4688	0.4759	0.5007	0.5027	0.5618
Data Set VI MRT1 and MRT2	SD	57.28	57.1453	57.836	60.7211	72.9397	67.359	60.9295	68.6153	74.8084
	NMI	0.752	0.7779	0.775	0.7737	0.6875	0.6938	0.7745	0.7323	0.8502
	SSIM	3.829	3.9184	3.582	3.2526	3.3334	3.239	3.2672	3.3183	4.3012
	ESIM	0.437	0.4385	0.467	0.5282	0.5015	0.5128	0.5297	0.4705	0.5677

(a)

(b)

(c)

(d)
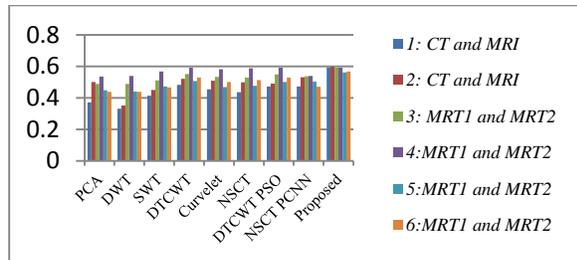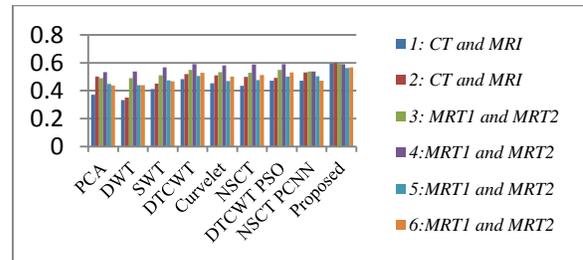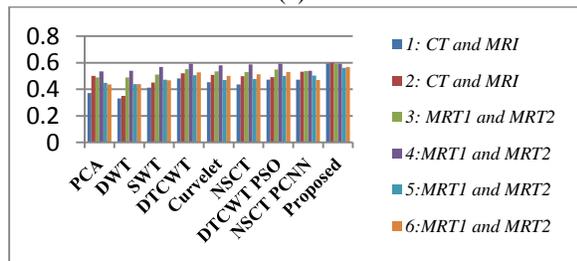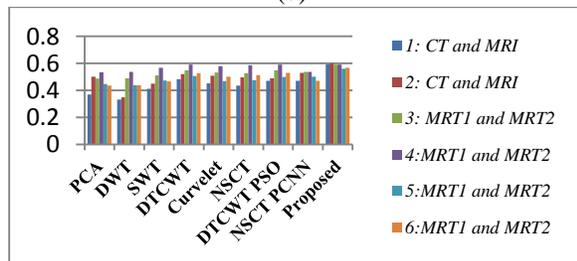
Fig. 7. (a) Variation of performance parameters with various fusion methods based on standard deviation. (b) Variation of performance parameters with various fusion methods based on NMI. (c) Variation of performance parameters with various fusion methods based on SSIM. (d) Variation of performance parameters with various fusion methods based on ESIM.

By the experimental images, PCA based schemes offer underprivileged results comparative to other techniques. Because it has no scale selectivity and it is not obvious to deal properly with incomplete data set, in which some of the points are missing. To overcome this inadequacy it satisfied the pyramid and multi resolution based algorithms. However, the fused image contrast will be reduced comparatively less in multi resolution based algorithms. With multi

resolution based algorithms, the NSCT based algorithm performs better result because the NSCT is a multi-scale geometric analysis tool which utilizes the geometric regularity in the image and provides an asymptotic optimal representation in the terms of better localization, multi-direction and shift invariance. This is also justified by the fact that shift-invariant decomposition overcomes successfully and improves the quality of the fused image around the edges. This approach is to perform some extent well supported multi-focus images. However, in this algorithm the medical images give not as much of performance. For the reason that, it is not able to present in the low-frequency efficiently by prominent information and to obtain the poor results [15].

The performance of this proposed method [26] is close to each other, it is to furnish the fine quality fused images compared to other fused results that suffers to others the obtained fused result which suffers something noticeably to reduce the visual quality, time consuming and also missing some information due to initial level decomposition process. In this proposed approach it is based on spatial frequency and pulse coupled neural network [16]. By looking carefully in the fused image the internal edges are missing (weak edges) and also computational time is very long. So, the key motivation of the proposed approach gives a better performance to extract a more accurate and prominent information from low and high frequency coefficients, the time reducing and the supplementary accepted output with improved visual quality. Thus, it can be concluded from Fig. 6 and Table 1 proves the superiority of the proposed method over existing methods based on visual and statistical assessment.

C. Real clinical examples on CT/MRI, and MR-T1/MR-T2 image fusion

The performance of clinical diagnosis, the CT and MRI image fusion at the semi-oval center area is essential. CT images hold anatomical information, and MRI images offer the normal and pathological soft tissue. The proposed fusion rules in multimodal medical image fusion becomes a growing study and analysis for doctors to find a more precise diagnosis. Figure 8 shows the real clinical images of the two sets of CT and MRI and the MRT1 and MRT2 are considered to demonstrate the practical value of the proposed scheme. The first case of a 25 year young human who is investigated through the CT scan for neuroestithelical tumor but not in the clear visible for those scanned in Fig. 8 (i). However, in the MRI image of the same patient will find some notable symptoms but recovery is critical because of visual difficultly. In the second case is of a 47 year old woman who one day was not able to speak and was weak on the right side of the body. Then she was admitted in the hospital and the doctors investigated through the CT image but it indicated as normal. However, the doctors had a doubt for this patient and also the image. After 3 days the doctors were initiate acquired in the MRI. They observed large area of abnormal signal in the region in MRI image. Here in early analysis is compared with the existing techniques, the proposed technique can be observed in the all information in the fused image and also gives a better quality within the high contrast image shown in the Table 2, visually displayed in Fig. 9, and the illustration by the graph in the Figs. 10 (a), 10 (b), 10 (c) and 10 (d) independently on the basis of standard deviation, NMI, SSIM and ESIM.
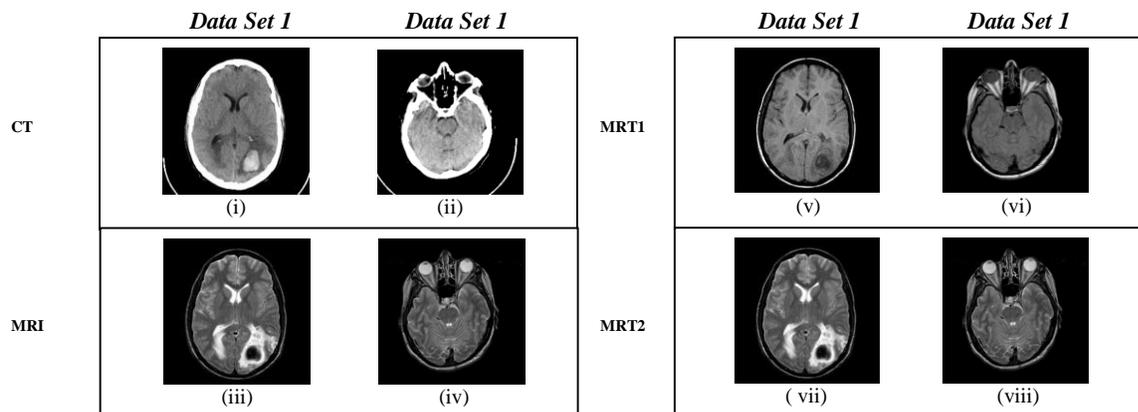
Fig. 8. Real clinical multimodal medical image data sets: (i) and (iii) CT image; (ii) and (iv) MRI image; (v) and (vii) MR-T1 image; (vi) and (viii) MR-T2 image.
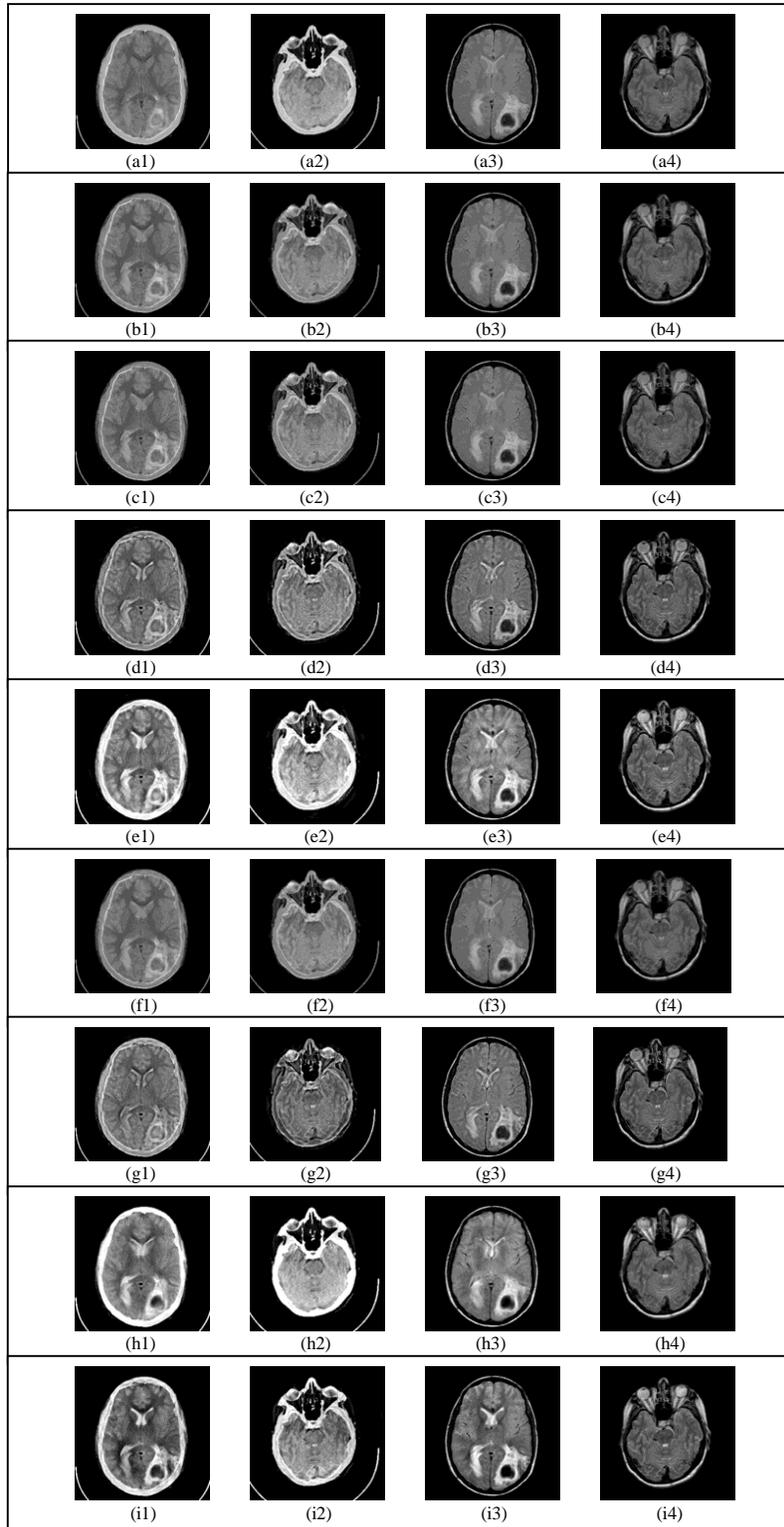
Fig. 9. The multimodal medical image fusion results of different fusion algorithms: fused images from (a1-a4) PCA based technique; (b1-b4) DWT based technique; (c1-c4) SWT based technique; (d1-d4) DTCWT based technique; (e1-e4) curvelet based technique; (f1-f4) NSCT based technique; (g1-g4) DTCWT-PSO based technique; (h1-h4) NSCT-PCNN based technique; (i1-i4) proposed technique.

Table 2: Evaluation performance for fused medical images by various quality metrics

Image Modality	Quality Metrics	PCA	DWT	SWT	DTCWT	Curvelet	NSCT	DTCWT PSO	NSCT PCNN	Proposed
Data Set I CT and MRI	SD	65.541	61.4685	61.959	63.7885	75.4965	70.7653	66.9167	76.1149	75.3883
	NMI	0.848	0.7625	0.76	0.7005	0.6456	0.6574	0.6898	0.8063	0.8872
	SSIM	3.922	3.782	3.397	3.0492	3.3196	3.9724	3.1482	3.5409	4.3167
	ESIM	0.371	0.3315	0.413	0.4827	0.4535	0.4354	0.4723	0.4717	0.5943
Data Set II CT and MRI	SD	77.253	63.4617	64.19	67.3	80.6006	72.3864	58.6839	81.6084	84.0422
	NMI	4.001	3.6725	3.031	2.6375	2.8586	3.0585	2.5432	3.1672	3.7301
	SSIM	3.9530	3.5482	3.6548	3.0682	3.4231	3.9832	3.3652	3.6384	4.5372
	ESIM	0.501	0.3502	0.451	0.5203	0.5093	0.4982	0.491	0.5312	0.5981
Data Set III MRT1 and MRT2	SD	58.012	58.1103	58.617	60.6151	60.9098	56.4582	60.7721	61.7255	64.5669
	NMI	0.816	0.821	0.809	0.7792	0.7276	0.6894	0.7783	0.8169	0.8863
	SSIM	3.599	3.6302	3.382	3.124	3.2239	3.5632	3.118	3.1891	4.1816
	ESIM	0.489	0.4893	0.511	0.5501	0.5338	0.5287	0.549	0.5379	0.5915
Data Set IV MRT1 and MRT2	SD	46.64	46.684	47.023	48.4167	49.4354	43.5734	48.4333	50.5065	51.4235
	NMI	0.894	0.9	0.912	0.891	0.8616	0.7943	0.8906	0.879	0.9854
	SSIM	3.671	3.7543	3.515	3.1996	3.2501	3.8734	3.1966	3.3043	4.1543
	ESIM	0.534	0.5381	0.567	0.5911	0.5805	0.5873	0.5908	0.5382	0.5909

(a)

(b)

(c)

(d)
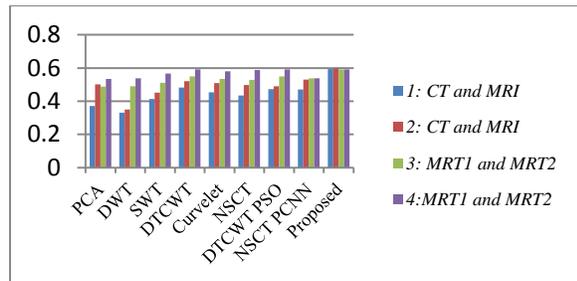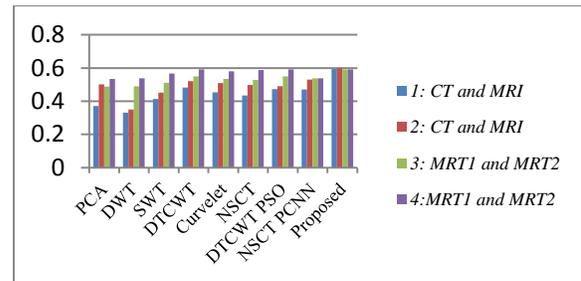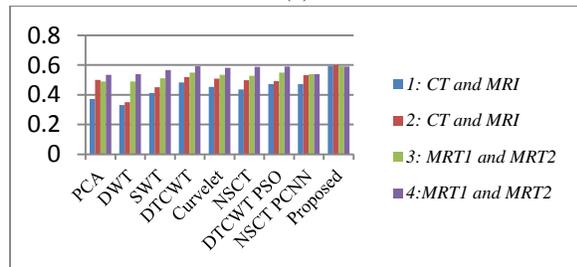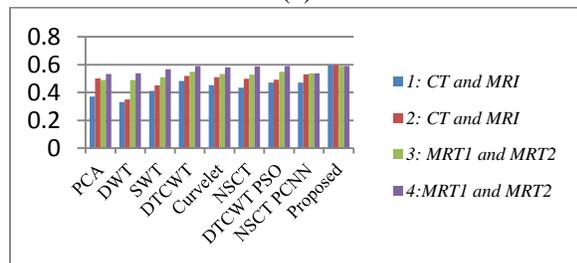
Fig. 10. (a) Variation of performance parameters with various fusion methods based on standard deviation. (b) Variation of performance parameters with various fusion methods based NMI. (c) Variation of performance parameters with various fusion methods based SSIM. (d) Variation of performance parameters with various fusion methods based ESIM.

IV. CONCLUSION

In this paper, new unique image fusion rules are proposed for multi-modal medical images, which is based on dual tree complex wavelet transform with modified LOA and ICV for the low pass sub-bands and high pass sub-bands. In our experimental results, several groups of CT and MRI and MRT1and MRT2 images are fused based on a few standard acceptable existing algorithms and the new unique proposed systems. The visual and statistical comparisons

demonstrate that the performance of the proposed algorithm is superior to the existing state-of-the-art methods. Proposed approach can improve the details of the fused image, and can get better effect of the visual quality with a smaller amount information distortion than existing methodologies. In the real applications, it will precisely offer an additional detail for diagnosis by doctors based on our new approach with the properties of high quality, high flexibility and time consumption. However, all modality of imaging has its own sensible limitations. In the follow-up study, a numerous work can be implemented in the new medical image fusion approach. From the variety of image quality estimation table and graphs, it has been obvious that the proposed fusion technique outperforms in terms of standard deviation, normalized mutual Information, structure similarity index measure and edge similarity index measure.

REFERENCES

[1] J. H. Teng, X. Wang, J. Zhang, S. Wang, and P. Huo, "A multimodality medical image fusion algorithm based on wavelet transform," *International Conference on Advances in Swarm Intelligence*, 6146:627-633, 2010.

[2] S. Das and M. K. Dundu, "A neuro-fuzzy approach for medical image fusion," *IEEE Transaction on Bio-medical Engineering*, vol. 60, no. 12, pp. 3347-3353, 2013.

[3] Z. Lu, H.-P. Yiu, Y. Chai, S. X. Yang, "A novel approach for multi-modal medical image fusion," *Experts Systems with Applications*, vol. 41, no. 16, pp. 7425-7435, 2014.

[4] V.S. Retronic and S. Xydias, "Gradient based multi-resolution image fusion," *IEEE TIP*, vol. 13, no. 2, pp. 228-237, 2004.

[5] Z. Wang and Y. Ma, "Medical image fusion using m-PCNN," *Information Fusion*, vol. 9, no. 2, pp. 176-185, 2008.

[6] S. Das and M. K. Kund, "NSCT based multi-modal medical image fusion using pulse coupled neural network and modified spatial frequency," *Medical and Biological Engineering and Computing*, vol. 50, no. 10, pp. 1145-1114, 2012.

[7] T. Yong, S. S. Park, S. Huang, and N. Rao, "Medical image fusion via an effective wavelet based approach," *EURASIP Journal of Advance in Signal Processing*, pp. 1-13, 2010.

[8] Kingsbury, "The dual-tree complex wavelet transform: A new technique for shift invariance and directional filters," *IEEE Digital Signal Processing Workshop*, 1998.

[9] V. P. S. Naidu and J. R. Raol, "Pixel-level image fusion using wavelets and principal component analysis," *Defense Science Journal*, vol. 58, no. 3, pp. 338-352, 2008.

[10] Q. Guihong, Z. Dali, and Y. Pingfan, "Medical image fusion by wavelet transform modulus maxima," *Opt. Express*, vol. 9, pp. 184-190, 2001.

[11] T. J. Li and Y. Y. Wang, "Biological image fusion uses a SWT based variable-weights selection scheme," *In Proc. of the 3rd International Conference on Bioinformatics and Biomedical Engineering*, pp. 1-4, 2009.

[12] I. W. Selesnick, R. G. Baraniuk, and N. G. Kingsbury, "The dual tree complex wavelet transform: A coherent framework for multi-scale signal and image processing," *IEEE Signal Processing Magazine*, vol. 22, no. 6, pp. 123-151, 2005.

[13] F. E. Ali, I. M. El-Dokany, A. A. Saad, and F. E. Abd El-Samie, "Curvelet fusion of mr and ct images," *Progr. Electromagn. Res. C*, vol. 3, pp. 215-224, 2008.

[14] M Q. Zhang and B. L. Guo, "Multi-focus image fusion using the non-sub-sampled contourlet transform," *Signal Process*, vol. 89, no. 7, pp. 1334-1346, 2009.

[15] J. Tao, S. Li, and B. Yang, "Multimodal image fusion algorithm using dual-tree complex wavelet transform and particle swarm optimization," *Advanced Intelligent Computing Theories and Application Communications in Computer and Information Science*, vol. 93, pp. 296-303, 2010.

[16] M. Yazdani and F. Jolai, "Lion optimization algorithm (LOA): A nature-inspired meta heuristic algorithm," *Journal of Computational Design and Engineering*, vol. 1, pp. 1-12, 2015.

[17] C. C. Lai, C. H. Wu, and M. C. Tsai, "Feature selection using particle swarm optimization with application in spam filtering," *International Journal of Innovative Computing Information and Control*, vol. 5, pp. 423-432, 2009.

[18] G. Piella and H. Heijmans, "A new quality metric for image fusion," *In Proc. of International Conference on Image Processing*, 2:173-6-III, 2003.

[19] R. Xu and D. Wunsch, "Survey of clustering algorithms," *IEEE Transactions on Neural Networks*, vol. 6, no. 3, pp. 645-678, 2005.

[20] J. Shi and J. Malik, "Normalized cuts and image segmentation," *IEEE Transactions on Pattern Analysis and Machine Intelligence*, vol. 22, no. 8, pp. 888-905, 2000.

[21] S. Li and B. Yang, "Multi-focus image fusion using region segmentation and spatial frequency," *Image and Vision Computing, Elsevier*, vol. 26, pp. 971-979, 2008.

[22] G. N. Raut, P. L. Paikrao, and D. S. Chaudhari, "Study of quality assessment techniques for fused images," *International Journal of Innovative*

Technology and Exploring Engineering, vol. 2, pp. 290-294, 2013.

[23] C. Yang, J. Zhang, X. Wang, and X. Liu, "A novel similarity based quality metric for image fusion," *Inf. Fusion*, vol. 9, pp. 156-160, 2008.

[24] G. Bhatnagar, Q. M. J. Wu, and Z. Liu, "Directive contrast based multimodal medical image fusion in NSCT domain," *IEEE Transaction on Multimedia*, vol. 15, no. 5, pp. 1014-1024, 2013.

[25] http://www.med.harvard.edu/AANLIB/

[26] Y. Chai, H. Li, and X. Zhang, "Multi-focus image fusion based on features contrast of multi-scale products in non sub-sampled contourlet transform domain," *Optik*, vol. 123, pp. 569-581, 2012.

Rubesh Selvakumar received the MCA degree from MK Universities, Madurai, TamilNadu, India in 2001 and M.E. degree from Anna University, Chennai, TamilNadu, India in 2005. He was a part time Research Fellowship with the Image Processing, Anna University, and Chennai. He has published many papers and presented in the conference in various areas like image processing, MANET and Wireless Communications. He is currently an Asst. Professor with the Department of Computer Science and Engineering, MIET, Madurai, TamilNadu, India. His research interests lie on the broad area of image processing with application in medical image fusion and noising analysis.

C. G. Ravichandran received his B.E. degree in Electronics and Communication Engineering from Bharathiyar University in 1988 and M.E. degree in Electronics Engineering and Ph.D. degree in Information and Communication Engineering (Medical Image Processing) from Anna University, Chennai during 1991 & 2009 respectively. Currently he is the Professor & Principal of SCAD Institute of Technology, Palladam, Tamilnadu, India. He has produced Four Ph.D.'s so far and currently guiding Eight Ph.D. candidates in Anna University Chennai. He has published around 20 articles in various reputed international Journals. His research interests include image segmentation, medical image processing, network architecture, distributed systems and web services.